materials

Advances in Polymeric Materials for Biomedical Applications

Edited by
Iza Radecka and Marek M. Kowalczuk

Printed Edition of the Special Issue Published in *Materials*

www.mdpi.com/journal/materials

MDPI

Advances in Polymeric Materials for Biomedical Applications

Advances in Polymeric Materials for Biomedical Applications

Editors

Iza Radecka
Marek M. Kowalczuk

MDPI • Basel • Beijing • Wuhan • Barcelona • Belgrade • Manchester • Tokyo • Cluj • Tianjin

Editors
Iza Radecka
University of Wolverhampton
UK

Marek M. Kowalczuk
Polish Academy of Sciences
Poland
University of Wolverhampton
UK

Editorial Office
MDPI
St. Alban-Anlage 66
4052 Basel, Switzerland

This is a reprint of articles from the Special Issue published online in the open access journal *Materials* (ISSN 1996-1944) (available at: https://www.mdpi.com/journal/materials/special_issues/polym_Mater_Biomedical).

For citation purposes, cite each article independently as indicated on the article page online and as indicated below:

LastName, A.A.; LastName, B.B.; LastName, C.C. Article Title. *Journal Name* **Year**, *Volume Number*, Page Range.

ISBN 978-3-0365-3206-6 (Hbk)
ISBN 978-3-0365-3207-3 (PDF)

Contents

About the Editors

Iza Radecka is a Professor in Biotechnology at the School of Sciences at the University of Wolverhampton, UK. After graduating in 1990 with an MSc in Biological Sciences from the University of Silesia, Poland, she undertook a research position in the Institute of Polymer Chemistry at the Polish Academy of Sciences in Zabrze, Poland. After this, she decided to take a PhD post at the Department of Biochemistry, University of Silesia, with a special interest in microbial biotechnology. After completing her PhD in 1998, Iza joined the School of Sciences at the University of Wolverhampton. Iza teaches a wide variety of microbiology and biotechnology courses, both at undergraduate and postgraduate level. Her research is focused on cost-effective synthesis of new biomaterials using bacterial biopolymers produced from bacteria and using eco-sustainable feedstock and their chemical derivatization. She has published numerous research papers in highly ranked scientific journals, as well as authored several chapters in biotechnological books. Iza has also presented several invited lectures at international conferences. Iza is a Fellow of the Royal Society of Biology.

Marek M. Kowalczuk is Professor at the Centre of Polymer and Carbon Materials at the Polish Academy of Sciences, Zabrze, Poland, and Emeritus Professor in synthetic/polymer chemistry at the University of Wolverhampton, UK. He received his PhD in 1984 from the Faculty of Chemistry, Silesian University of Technology, Gliwice, Poland, and his DSc in 1994 from the same university. Since 2010, he has been Professor of Chemistry, nominated by the President of Poland. He has been Visiting Professor at Ohio State University, Columbus, USA; Visiting Lecturer at the University of Massachusetts, Amherst, USA; and a Marie Curie fellow at the University of Bologna, Italy. Recently, he was elected as a member of the Chemistry Committee of the Polish Academy of Sciences. He is author and co-author of over 200 scientific papers and several patents. His main scientific interests are biodegradable and functional polymer biomaterials, novel initiators and mechanisms of anionic polymerisation related to the synthesis of biodegradable polymers possessing the desired architecture, the biodegradation of polymers, polymer mass spectrometry, and forensic engineering of advanced polymeric materials.

materials

MDPI

Communication

Electrospinning of Fish Gelatin Solution Containing Citric Acid: An Environmentally Friendly Approach to Prepare Crosslinked Gelatin Fibers

Anna Liguori [1,†], Jone Uranga [2,†], Silvia Panzavolta [1], Pedro Guerrero [2], Koro de la Caba [2,*] and Maria Letizia Focarete [1,*]

[1] Department of Chemistry "Giacomo Ciamician" and INSTM UdR of Bologna, University of Bologna, via Selmi 2, 40126 Bologna, Italy

[2] BIOMAT research group, University of the Basque Country (UPV/EHU), Engineering College of Gipuzkoa, Plaza de Europa 1, 20018 Donostia-San Sebastián, Spain

* Correspondence: koro.delacaba@ehu.eus (K.d.l.C.); marialetizia.focarete@unibo.it (M.L.F.); Tel.: +34-943-017188 (K.d.l.C.); +39-051-2099577 (M.L.F.)

† Both authors contribute equally to this work.

Received: 31 July 2019; Accepted: 30 August 2019; Published: 1 September 2019

Abstract: The majority of the crosslinking approaches employed to confer water resistance properties to electrospun gelatin mats are based on the use of potential cytotoxic agents, turning out to be not suitable for biomedical applications. Environmentally friendly chemical strategies based on the use of non-toxic agents are, therefore, strongly demanded. In the present work, the possibility to produce crosslinked electrospun fish gelatin mats by electrospinning an aqueous solution, containing citric acid as a crosslinking agent, is reported. The effect of pH on solution rheological properties, as well as on the electrospun mat morphology, chemistry, and crosslinking degree, is assessed. The increase of solution pH from 1.8 to 3.7 allows for obtaining fibers that maintain the fibrous morphology also in the mat. Subsequent thermal treatment of the electrospun mat (80 °C for 30 min) turns out to increase the crosslinking degree and morphological stability of the mat.

Keywords: fish gelatin; citric acid; electrospinning; pH; thermal treatment; gelatin structure; crosslinking degree

1. Introduction

Gelatin is a polymer obtained from the thermal denaturation or chemical degradation of collagen. These processes involve the loss of the collagen triple-helix structure and the formation of random coil structure typical of gelatin. Gelatin macromolecules can rearrange, under certain conditions, thus forming again sequences of the triple helix, even if the fibrillar collagen structure cannot be recovered and the material becomes highly soluble in an aqueous environment. Gelatin is employed in different fields, such as food industry, tissue engineering, medical applications [1–4], thanks to its biocompatibility, biodegradability, and low cost. Moreover, gelatin shows binding sites for cell adhesion, signaling, and differentiation, which make this polymer suitable in tissue engineering, wound dressing, and drug delivery [5–9]. In these sectors, electrospun nanofibrous mats are highly demanded, since they mimic the extracellular matrix and promote cell adhesion and proliferation due to their high porosity and surface area.

However, due to water solubility, gelatin nanofibrous mats do not maintain their morphology when they come in contact with water. In order to improve water resistance, physical [10] and chemical [11–13] crosslinking methods have been proposed. Focusing on chemical crosslinking approaches, agents such as genipin, diisocyanate, glutaraldehyde, and carbodiimide, have been

successfully employed, being included in the gelatin solution prior to spinning [8,11,14–16]. Chemical methods also include post-treatment strategies based on the introduction of crosslinking agents after the spinning of the solution [13,16–20]. However, this approach demands a further step and, in some cases, has been reported to induce the flattening of the fibers, fusing them together [17,20]. Furthermore, some of the above-mentioned agents cause cytotoxicity [13,17] and are not suitable for applications in the medical field.

Citric acid is a natural acid and it has been already demonstrated to be suitable for the crosslinking of proteins [21–24]. The carboxylic groups of citric acid can undergo nucleophilic acyl substitution with the ε-amines of lysine, leading to the formation of stable amide bonds [21]. Saito et al. reported the use of a citric acid derivative, obtained through the modification of citric acid carboxyl groups with N-hydroxysuccinimide in presence of 1-ethyl-3-(3-dimethyl aminopropyl)carbodiimide hydrochloride, for the preparation of crosslinked type A porcine skin gelatin gels [25]. More recently, Shafagh et al. reported the use of citric acid to crosslink porcine skin gelatin in presence of Ag nanoparticles to produce, through a green approach in which water was used as a solvent, gelatin/Ag nanocomposite hydrogels with swelling and a drug release behavior both depending on pH [26]. Uranga et al. developed citric acid-crosslinked fish gelatin films, starting from an aqueous solution containing also glycerol and chitosan, with potentials for packaging applications since the presence of citric acid in the films did not produce any change of color, but improved both the light barrier and mechanical properties of the obtained films [27].

Among the different techniques for the production of polymeric substrates, electrospinning enables to develop micro- and nano-materials, and has been successfully used also to process fish-derived proteins [28], suitable for biomedical applications [29]. Citric acid has been used to crosslink collagen electrospun nanofibers. Cumming et al. successfully produced intra-fibrillar crosslinked marine collagen nanofibers by using the optimized citric acid: collagen molar ratio of 260:1 at pH 3.5 and performing a thermal treatment at 160 °C for 16 h after the mat fabrication [21]. Jiang et al. employed citric acid to produce crosslinked electrospun gelatin fibers using acetic acid as solvent and sodium hypophosphite as a catalyst of the citric acid, followed by a thermal treatment at 150 °C for 4 h to induce crosslinking [30].

To the best of our knowledge, no works have dealt so far with the production of crosslinked fish gelatin electrospun fibers by using an aqueous solution of citric acid, avoiding acetic acid or other chemicals. Indeed, only one previous work is present in the literature on the investigation of fish gelatin electrospinning in water/citric acid solution [31], but in this work the authors demonstrated that it was possible to obtain electrospun fibers only in the presence of additional acetic acid in the solution. Moreover, no studies or considerations are reported in this paper on the strategies to crosslink the as-produced mats.

The aim of the present work is to develop a protocol to make feasible, for the first time, the electrospinning process of fish gelatin by using only a natural and non-toxic crosslinker, such as citric acid, in aqueous solution to obtain crosslinked fibers, as illustrated in Scheme 1. The effect of the solution's pH on electrospinnability and morphological and chemical properties of the resulting fibers was investigated. Furthermore, the effect of a subsequent thermal treatment of the mat on its morphological and chemical properties was also assessed.

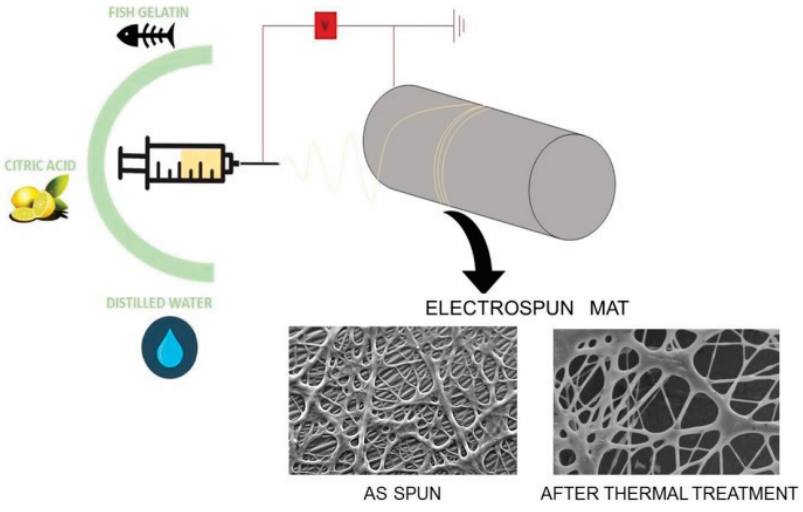

Scheme 1. Scheme of the proposed approach to produce electrospun crosslinked gelatin fish fibrous mats.

2. Materials and Methods

2.1. Materials

240 bloom type A fish gelatin (FG), with an average molar mass of 125–250 kDa and a lysine content of 2.62%, was obtained from Healan Ingredients, North Newbald, UK, 280 Bloom type A gelatin from porcine skin (PG) was obtained from Italgelatine SpA, Via Statale, Italy. Anhydrous citric acid was provided by Panreac, Barcelona, Spain, sodium hydroxide, hydrochloric acid, 2,4,6-trinitrobenzenesulfonic acid (TNBS) and diethyl ether were purchased from Sigma-Aldrich, Milano, Italy. All chemicals were used as received without further purification.

2.2. Preparation of Solutions

FG solution was prepared by dissolving citric acid and gelatin in 3 mL of distilled water with citric acid/gelatin/water weight ratio of 0.9:1.0:3.0. The components were mixed together and kept at 50 °C under constant stirring (200 rpm) for 40 min. In order to modify the pH of FG solution, an FG+NaOH solution was obtained by dissolving citric acid and gelatin in 2.3 mL of distilled water with a citric acid/gelatin/water weight ratio of 0.9:1.0:2.3 and then adding 0.7 mL of NaOH 5 M. The compositions of FG solutions were optimized on the basis of rheological measurements, taking as a reference a PG solution. PG solution was prepared as previously described [8], in particular, PG was dissolved in a solution of acetic acid and distilled water (60/40 vol% acetic acid/distilled water) at a concentration of 30% (w/v). The obtained solution was stirred at 50 °C for 60 min. The pH of the solutions was measured by a calibrated pH meter (XS Instrument pH7, Carpi, Italy). In this work, the pH of the FG solution was 1.8, while the pH of FG+NaOH solution was 3.7.

2.3. Rheological Assessment of Solutions

The rheological measurements were performed using a rotational rheometer (Anton Paar MCR 102, Graz, Austria) operating in a plate-plate configuration. Experiments were performed keeping the temperature constant at 25 °C through the integrated Peltier system and a Julabo AWC100 cooling system, Seelbach, Germany. The sample was kept hydrated during the measurements through the use of a solvent trap (H-PTD200). Time-sweep oscillatory tests were carried out at a fixed strain amplitude of 0.3% and an angular frequency of 1 rad s^{-1}

2.4. Electrospun Mat Fabrication

Mats were prepared by the electrospinning technique. The electrospinning apparatus consisted of a Spellman SL 50 P 10/CE/230 high-voltage power supply (Hauppauge, NY, USA), a KD Scientific 200 series syringe pump, and a glass syringe containing the polymer solution connected to a stainless-steel blunt-ended needle with an inner diameter of 0.51 mm through a PTFE tube. Electrospinning was performed at room temperature and relative humidity of 40–50%. FG solution was electrospun by using the following conditions: applied voltage = 20 kV, feed rate = 0.3 mL h^{-1}, and needle-to-collector distance = 15 cm. The electrospinning of FG+NaOH solution was carried out using the same parameters employed for FG solution, except for the voltage and flow rate which were increased up to 23 kV and decreased up to 0.1 mL h^{-1}, respectively, due to the higher solution viscosity conferred by NaOH. After fabrication, some mats were subjected to a thermal treatment carried out at 80 °C for 30 min under vacuum. The obtained mats were stored in a desiccator at 4 °C until further analysis.

2.5. Characterization Methods

A polarized optical microscope (OM) (Zeiss Axioscop, Zaventem, Belgium) was used to detect electrospun fibers directly collected on glass slides during electrospinning. Scanning electron microscope (SEM) observations were performed 24 h after mat fabrication at an acceleration voltage of 15 kV. Samples were mounted on a stub with double-side adhesive tape and sputter-coated with gold before observation. The distribution of fiber diameters (average and standard deviation) was measured on the SEM images of about 50 fibers by means of ImageJ software. Wide-angle X-ray diffraction (WAXD) analysis was carried out using a PANalytical powder diffractometer (Almelo, Netherlands) endowed with a fast X'Celerator detector. The radiation was generated from a CuKα (λ = 0.15418 nm) source (40 mA, 40 kV). WAXD data were obtained from 2θ values from 5° to 60°, where θ is the incidence angle of the X-ray beam on the sample. Fourier transforms infrared (FTIR) spectroscopy was carried out on a Nicolet 380 FTIR spectrometer (Thermo Scientific, Waltham, MA, USA) using ATR Golden Gate. 32 scans were performed with a resolution of 4 cm^{-1} in the range 4000–800 cm^{-1}. Spectra were smoothed using the Savitzky–Golay function and second-derivative spectra of the amide I region were used at peak position guides for the curve fitting procedure, using OriginPro 9.1 software.

2.6. Crosslinking Extent

The crosslinking extent was measured according to the method of Panzavolta and coworkers [8]. Briefly, an UV assay of uncrosslinked ε-amino groups was performed on differently treated mats and on fish gelatin as reference. After the reaction with 0.5% TNBS, gelatin was hydrolyzed with 6 M HCl and extracted with diethyl ether. The solution's absorbance was measured against a blank at 346 nm. The moles of free ε-amino groups per gram of gelatin were calculated by the following Equation (1):

$$\text{Moles of } \varepsilon\text{–amino groups/g of gelatin } = \frac{2 \cdot A \cdot V}{\varepsilon \cdot b \cdot x} \quad (1)$$

where A is the sample absorbance, B is the final sample volume (L), ε is the TNP-lys molar absorptivity (1.46×10^4 L mol^{-1} cm^{-1}), b is the cell path length (cm), x is the sample weight (g).

The cross-linking extent (CE) was determined from the ratio between the moles of crosslinked ε–amino groups of treated gelatin mats (obtained as a difference between uncrosslinked groups before and after crosslinking) with respect to ε–amino groups measured in fish gelatin.

3. Results and Discussion

3.1. Electrospinning of Fish Gelatin

It has been widely reported that the addition of an acid to water solutions, or the use of solvents such as 1,1,3,3,3-hexafluoro-2-propanol, is required for gelatin electrospinning to prevent gelation

that hinders and even blocks the solution flow through the syringe needle and capillary during the spinning process [32,33]. Due to the possible toxicity of the most employed acids or organic solvents, efforts have been devoted to the fabrication of gelatin electrospun fibers using solutions of benign acids in water. Acetic acid, malic acid, and citric acid water solutions, as binary, ternary, and quaternary solvents, were recently used to manufacture FG based electrospun mats [31,32]. Although positive results on the feasibility of the process were achieved for water/acetic acid solvents, citric acid based binary solvent was reported to be non-suitable for developing fibers [31].

Considering both the absence of toxicity of citric acid and its potential crosslinking action, in this work efforts have been carried out to identify a procedure for the production of crosslinked FG electrospun mats using a spinning solution containing only citric acid in an aqueous solution. In particular, the effect of solution's pH on the electrospinning process, mat properties, and crosslinking degree was investigated by adding NaOH to the FG citric acid/water solution in order to increase the pH of the FG solution from 1.8 to 3.7, on the basis of a previous study on collagen electrospun fibers crosslinked with citric acid [21]. In the mentioned paper the highest crosslinking extent was achieved from a solution containing collagen and citric acid with a pH 3.5, a result that was attributed by the authors to the more effective formation of citric anhydride at this pH [21,34].

Given the importance of flow properties and viscoelastic behavior of the solution in the electrospinning process, FG solution composition was optimized on the basis of rheological measurements, taking as a reference a PG solution whose electrospinnability was previously demonstrated by some of the Authors [8]. Figure 1 reports the storage modulus (G′) and the loss modulus (G″) over 1 h 40 min period for the analyzed solutions. FG shows a rheological behavior similar to that of PG. Indeed, although FG moduli are slightly lower than those of PG, both solutions behave as viscoelastic liquids (G′ < G″) at initial times (up to 12 min for PG and up to 23 min for FG), then they switch to a solid-phase dominated behavior (G′ > G″), as demonstrated by the achievement of the cross-over, referred to as the "gel point" attributed to the increased molecular association. Finally, the moduli reach a fairly constant value. The presence of NaOH affects the viscoelastic properties of the solutions. Indeed, FG+NaOH presents higher values of G′ and G″ than FG, even higher than PG, and it shows no cross-over and a solid-phase dominated behavior since the beginning of the measurement. This result might indicate that crosslinking reactions due to citric acid are more likely to happen in the solution at pH 3.7 rather than in that at pH 1.8.

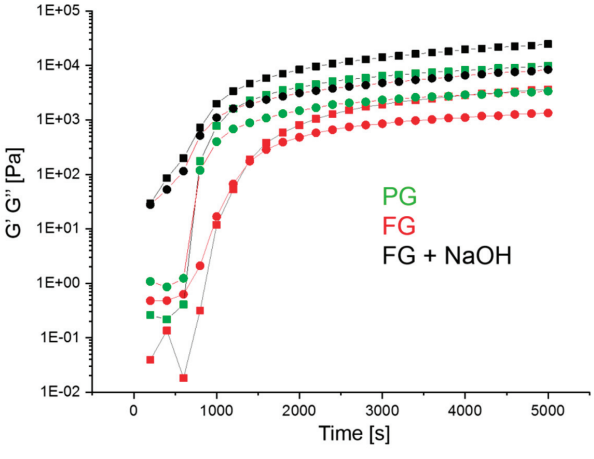

Figure 1. Time dependence of storage modulus G′ (square) and loss modulus G″ (circle) of PG (green curves), FG (red curves), and FG+NaOH (black curves) solutions.

For all the solutions, even if a gel point was observed and the solid-like behavior dominated over time, the small differences between G′ and G″ indicate the formation of a weak gel that did not hinder electrospinnability of the solutions.

3.2. Characterization of Fish Gelatin Electrospun Mats

The OM and SEM images of the electrospun mats obtained from FG and FG+NaOH solutions are reported in Figure 2. Interestingly, the OM images (Figure 2a,d) show that bead-free and regular microfibers were obtained for both FG and FG+NaOH solutions. In contrast to previous findings [31], our results demonstrate that electrospinning of FG from a citric acid/water solution without the addition of acetic acid to form microfibers was possible. However, although both the solutions turned out to be electrospinnable, the fibrous morphology of mats obtained from FG solution was not preserved over time, since the mats turned into films, with a barely recognizable fibrous structure, in few hours, as demonstrated by the SEM micrographs (Figure 2b).

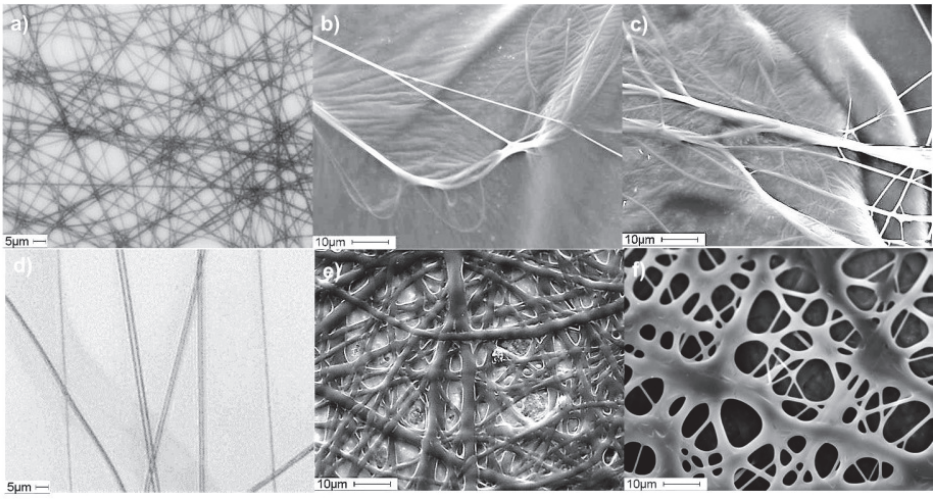

Figure 2. OM (**a**,**d**) and SEM images (**b**,**c**,**e**,**f**) of electrospun mats from FG (**a**,**b**,**c**) and FG+NaOH (**d**,**e**,**f**) solutions: mats as spun (**a**,**b**,**d**,**e**) and after the thermal treatment (**c**,**f**).

Addition of NaOH to FG solutions increased the pH values from 1.8 to 3.7 and improved the fiber stability over time. The obtained fibrous mat was able to preserve its morphology better than fibers obtained from FG solution (compare Figure 2b,e), although fiber fusion at their contact points could be noticed.

In agreement with previous literature findings [21,30], the thermal treatment performed on these mats immediately after their fabrication came out to get a beneficial effect on the resulting morphology, since the fibrous morphology of the mats is better maintained with respect to the as spun mats (Figure 2c,f). It is pointed out that, even if the fiber diameter was hardly measurable due to the many fusion points among fibers, after the thermal treatment a fiber diameter of 2.19 ± 0.07 μm and 4.42 ± 0.05 μm was evaluated for FG mats and FG+NaOH mats, respectively.

To assess the extent of the crosslinking reaction between gelatin and citric acid, the amount of ε-amino groups of gelatin reacted with citric acid was calculated. In line with the morphological results, only a small amount of ε-amino groups was crosslinked with citric acid in the mats obtained from FG solution, leading to a crosslinking extent of 12%. On increasing the pH up to 3.7 in the FG+NaOH solution, crosslinking extents of 25% and 38% were achieved for FG+NaOH mat as spun and thermally treated, respectively. These results are in agreement with previous findings [35], and highlight that the

crosslinking reactions can take place also at room temperature in the water solution of FG with citric acid, even if an increase of temperature up to 80 °C is needed to speed up such crosslinking reaction.

On the basis of the above-described results, the following considerations can be drawn. For the mat obtained from FG solution, the obtained morphology is well explained by the low crosslinking extent of the fibers and it is mainly ascribed to the low pH of the solution, since at pH 1.8 the crosslinking reactions can difficultly take place. Moreover, the widely reported mechanism driving the crosslinking of proteins or molecules containing amino groups in the presence of citric acid lies in the formation of reactive citric anhydride from citric acid and in the nucleophilic substitution occurring between the carboxyl groups of the anhydride and the amino groups of the considered protein or molecule [21,34,35]. Since type-A fish gelatin is employed in this work and its isoelectric point is in the pH range of 6.0–9.5 [36], the protonation of the amine groups takes place in the strong acidic conditions of FG solutions (pH 1.8), thus limiting the crosslinking reaction. An increase of pH up to 3.7, even if lower than fish gelatin isoelectric point, would favor the deprotonation of $-NH_3^+$ groups in $-NH_2$, and the above described nucleophilic substitution was more likely to occur with the formation of amide groups. The pH value of 3.7 was, thus, selected in order to achieve the best compromise between the number of amine groups available for crosslinking and the known crosslinking mechanism of citric acid, which has been reported to occur at the highest extent at pH 3.5 [21].

The influence of the electrospinning process on structural properties of gelatin was investigated on fish gelatin powder and on the obtained mats through wide-angle WAXD analysis. In that way, the relative triple-helix content of fish gelatin materials was analyzed in detail (Figure 3). It is well known that the collagen WAXD pattern includes two broad diffraction bands. The first one, centered at about 8°, related to the triple helix diameter, while the second one at around 21° is related to the distance between amino acidic residues in the helix. These reflections are typically observed also in the pattern of partially renaturated gelatin powder and gelatin films [37].

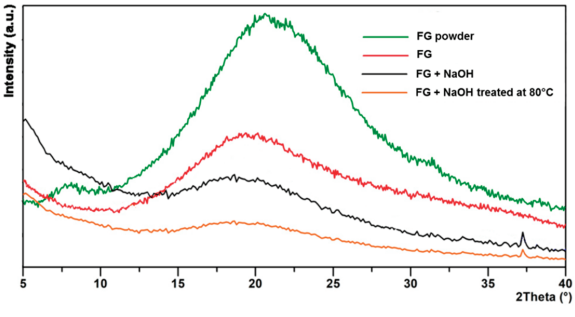

Figure 3. WAXD patterns of FG powder, FG, FG+NaOH, and thermal treated FG+NaOH electrospun mats.

In agreement with these data, results reported in Figure 3 show that fish gelatin powder exhibits the two reflections centered at about 8° and 21°, as previously reported [38,39]. However, reflection at 8° disappears after the electrospinning process of both FG and FG+NaOH solutions, as a consequence of acidic pH. This result can be explained considering that, as previously observed for gelatin solubilized in acetic acid solutions [8], citric acid prevents the gelatin's partial renaturation which takes place during gelling from aqueous solution and a random coil conformation is favored, decreasing the number of single left-hand helix chains and residual triple-helix conformations. Furthermore, citric acid also influences the diffraction reflection located at about 21°, whose intensity decreases as a consequence of the decrease of the single left-hand helix chain content. Addition of NaOH to FG solution, with a consequent increase of pH from 1.8 to 3.7, does not change the diffraction pattern significantly, whereas the thermal treatment performed on FG+NaOH mat further decreases the broad band at about 21°.

Figure 4 shows the ATR-FTIR spectra of the electrospun mats obtained from FG and FG+NaOH solutions before and after the thermal treatment, FG powder is also reported for the sake of comparison. The broad band above 3000 cm^{-1}, observed in all spectra shown in Figure 4a, corresponds to the hydroxyl and amino groups [40]. Some changes can be observed in FTIR spectra, in particular, in those bands associated to the peptide bonds in gelatin: amide I (C=O stretching), amide II (N–H bending), and amide III (C–N stretching). As can be seen in Figure 4b), there was a shift of these bands to higher wavenumbers from FG mat to FG+NaOH mats, indicating that the citric acid incorporated into the formulation causes new interactions between the amino groups of gelatin and the carboxyl groups of citric acid [27,41], in accordance with the shift of the characteristic band related to the carboxyl group in citric acid from 1748 cm^{-1} to 1715 cm^{-1} [42].

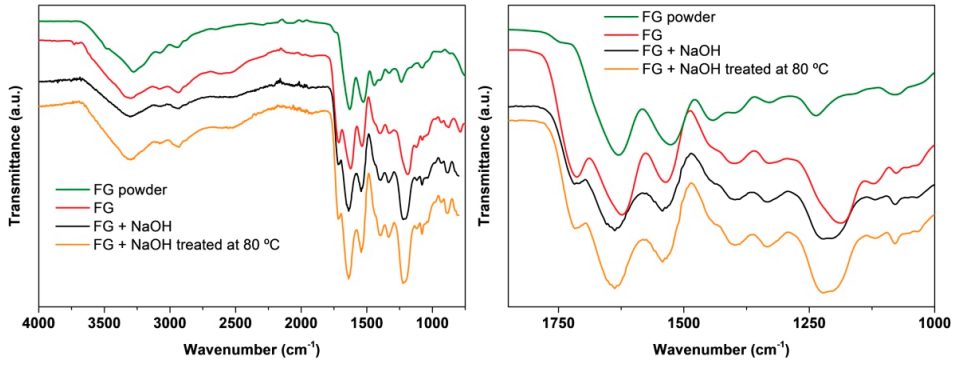

Figure 4. ATR-FTIR spectra of FG powder, FG, FG+NaOH, and thermally treated FG+NaOH electrospun mats (**a**) from 4000 to 800 cm^{-1} and (**b**) from 1850 to 1000 cm^{-1}.

The band corresponding to amide I is related to the secondary structure of the protein backbone and it is generally used for the quantitative analysis of the secondary structures. Hydrogen bonding plays a significant role in stabilization of protein secondary structure. Indeed, inter-peptide hydrogen bonding stabilizes secondary structures (i.e., α-helix and β-sheet conformations), while peptide-water hydrogen bonding competes against peptide bond-peptide bond hydrogen bonding. Due to the central role of hydrogen bonding in protein folding, the analysis of this band is of great importance (Figure 5).

The assignment of absorption peaks in amide I band is as follows: two peaks from 1603 to 1616 cm^{-1} support β-sheet conformation, the peak at 1634 cm^{-1} corresponds to random coil conformation, the peak from 1641 to 1650 cm^{-1} is associated to α-helix conformation, and the peak centered at 1670–1678 cm^{-1} is assigned to the β-turn conformation of the hairpin-folded antiparallel β-sheet structure (Table 1).

As shown in Figure 5 and Table 1, electrospinning causes changes in the secondary structure of gelatin. While FG powder shows α-helix conformation, a random coil is the predominant conformation for electrospun mats, in accordance with the results found by XRD, which show amorphous structure with no remaining triple helix structure.

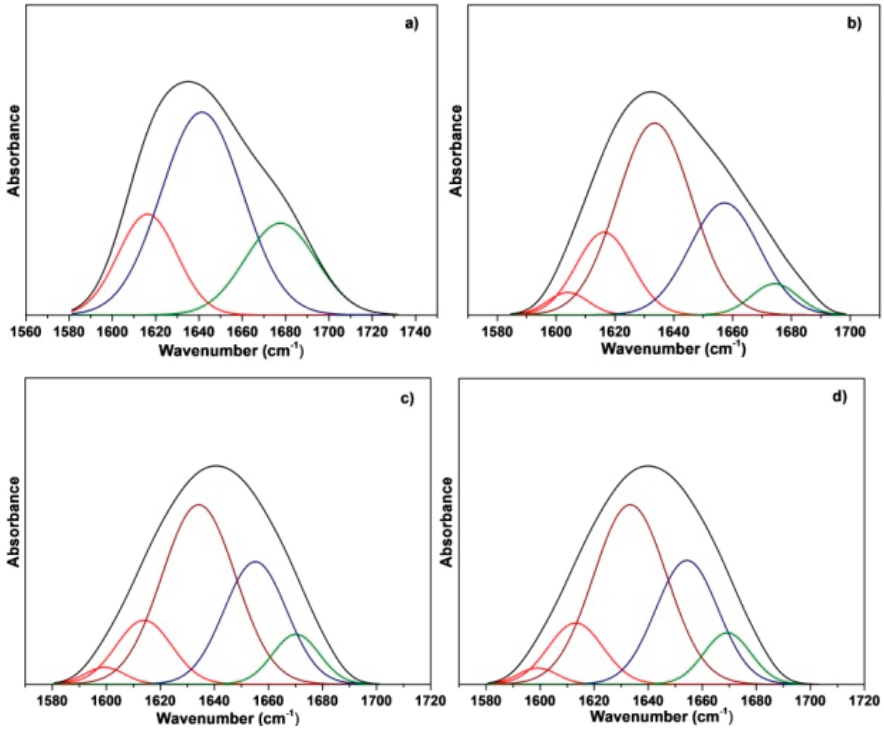

Figure 5. Curve fitting spectra of amide I band (black curve) for (**a**) FG powder, (**b**) FG, (**c**) FG+NaOH, and (**d**) thermal treated FG+NaOH electrospun mats (β-sheet conformation, red curve; random coil conformation, brown curve; α-helix conformation, blue curve; β-turn conformation, green curve).

Table 1. Resulting percentage of the curve fitting of amide I for FG powder, FG, FG+NaOH, and thermal treated FG+NaOH electrospun mats.

Amide I Area	1603–1616 cm^{-1} (%)	1634 cm^{-1} (%)	1641–1650 cm^{-1} (%)	1670–1678 cm^{-1} (%)
FG powder	20.37	-	57.00	22.63
FG	18.75	48.73	26.54	5.98
FG+NaOH	16.94	44.70	29.79	8.57
FG+NaOH treated at 80 °C	16.16	44.29	30.84	8.71

4. Conclusions

An environmentally friendly chemical strategy to successfully electrospin fish gelatin from a solution containing only citric acid in an aqueous solution was demonstrated. Citric acid was used as a benign acid to solubilize gelatin and allow the electrospinning process and, at the same time, as a crosslinking agent. The pH of the spinning solutions turned out to have a strong influence on the viscoelastic behavior of the solutions, as well as on the crosslinking extent that, in turn, influenced the fiber morphology stability. Rheological measurements provided evidence that in all solutions the solid-like behavior dominated over time, but the weak gel formed did not hinder electrospinnability of the solution. The solution at pH 3.7, showing higher values of G′ and G″ moduli, was characterized by a higher extent of crosslinking with respect to the solution at pH 1.8. Although microfibers were obtained for both FG and FG+NaOH solutions, the increase of solution pH from 1.8 to 3.7 was necessary to maintain the fibrous morphology also in the mat. A subsequent thermal treatment at 80 °C of the electrospun mat turned out to significantly increase the morphological stability of the

mat. The crosslinking degrees of the mats were in line with the morphological results (FG mat = 12%, FG+NaOH mat = 25%, thermally treated FG+NaOH mat = 38%). Gelatin denaturation after the electrospinning process was demonstrated by the absence of the diffraction band related to the triple helix diameter, as expected since gelatin solubilization in acidic solvents is known to prevent the partial renaturation of gelatin. ATR-FTIR characterization confirmed this result and demonstrated that the gelatin structure changed from α-helix to random coil conformation as a consequence of the electrospinning process. Although further studies are necessary to find the best solution composition to further optimize the final morphology as well as the crosslinking extent of the produced mats, this work is the first successful attempt to produce crosslinked electrospun fish gelatin fibers through the use of a citric acid/water solution.

Author Contributions: All authors contributed to the conceptualization and the methodology of this article; investigation, J.U., A.L., S.P.; data curation, J.U., A.L., S.P., M.L.F., P.G., K.d.l.C.; writing—original draft preparation, J.U., A.L.; writing—review and editing, M.L.F., S.P., K.d.l.C.; supervision, M.L.F., S.P., P.G., K.d.l.C.

Funding: This research was funded by the Spanish Ministry of Science, Innovation and Universities (RTI2018-097100-B-C22), the Basque Government (Department of Quality and Food Industry), the Provincial Council of Gipuzkoa (Department of Economic Development, the Rural Environment and Territorial Balance) and the Italian Ministry of University and Research (MIUR).

Acknowledgments: Jone Uranga thanks the Basque Government (PRE_2015_1_0205) for her fellowship and for the mobility grant (EP_2018_1_0050).

Conflicts of Interest: The authors declare no conflict of interest.

References

1. Gómez-Estaca, J.; Gavara, R.; Hernández-Muñoz, P. Encapsulation of curcumin in electrosprayed gelatin microspheres enhances its bioaccessibility and widens its uses in food applications. *Innov. Food Sci. Emerg. Technol.* **2015**, *29*, 302–307. [CrossRef]
2. Su, K.; Wang, C. Recent advances in the use of gelatin in biomedical research. *Biotechnol. Lett.* **2015**, *37*, 2139–2145. [CrossRef] [PubMed]
3. Dolci, L.S.; Liguori, A.; Panzavolta, S.; Miserocchi, A.; Passerini, N.; Gherardi, M.; Colombo, V.; Bigi, A.; Albertini, B. Non-equilibrium atmospheric pressure plasma as innovative method to crosslink and enhance mucoadhesion of econazole-loaded gelatin films for buccal drug delivery. *Colloids Surf. B* **2018**, *163*, 73–82. [CrossRef] [PubMed]
4. Khor, E. Methods for the treatment of collagenous tissues for bioprostheses. *Biomaterials* **1997**, *18*, 95–103. [CrossRef]
5. Aduba, J.; Hammer, J.A.; Yuan, Q.; Andrew Yeudal, W.; Bowlin, G.L.; Yang, H. Semi-interpenetrating network (sIPN) gelatin nanofiber scaffolds for oral mucosal drug delivery. *Acta Biomater.* **2013**, *9*, 6576–6584. [CrossRef] [PubMed]
6. Angarano, M.; Schulz, S.; Fabritius, M.; Vogt, R.; Steinberg, T.; Tomakidi, P.; Friedrich, C.; Mulhaupt, R. Layered gradient nonwovens of in situ crosslinked electrospun collagenous nanofibers used as modular scaffold systems for soft tissue regeneration. *Adv. Funct. Mater.* **2013**, *23*, 3277–3285. [CrossRef]
7. Li, M.; Mondrinos, M.J.; Gandhi, M.R.; Ko, F.K.; Weiss, A.S.; Lelkes, P.I. Electrospun protein fibers as matrices for tissue engineering. *Biomaterials* **2005**, *26*, 5999–6008. [CrossRef]
8. Panzavolta, S.; Gioffrè, M.; Focarete, M.L.; Gualandi, C.; Foroni, L.; Bigi, A. Electrospun gelatin nanofibers: Optimization of genipin cross-linking to preserve fiber morphology after exposure to water. *Acta Biomater.* **2011**, *7*, 1702–1709. [CrossRef]
9. Mano, J.F.; Reis, R.L. Osteochondral defects: Present situation and tissue engineering approaches. *J. Tissue Eng. Regen. Med.* **2007**, *1*, 261–273. [CrossRef]
10. Liguori, A.; Bigi, A.; Colombo, V.; Focarete, M.L.; Gherardi, M.; Gualandi, C.; Oleari, M.C.; Panzavolta, S. Atmospheric pressure non-equilibrium plasma as a green tool to crosslink gelatin nanofibers. *Sci. Rep.* **2016**, *6*, 38542. [CrossRef]
11. Gualandi, C.; Torricelli, P.; Panzavolta, S.; Pagani, S.; Focarete, M.L.; Bigi, A. An innovative co-axial system to electrospin in situ crosslinked gelatin nanofibers. *Biomed. Mater.* **2016**, *11*, 025007. [CrossRef] [PubMed]

12. Ratanavaraporn, J.; Rangkupan, R.; Jeeratawatchai, K.; Kanokpanont, S.; Damrongsakkul, S. Influences of physical and chemical crosslinking techniques on electrospun type A and B gelatin fiber mats. *Int. J. Biol. Macromol.* **2010**, *47*, 431–438. [CrossRef] [PubMed]
13. Zhang, Y.Z.; Venugopal, J.; Huang, Z.M.; Limab, C.T.; Ramakrishna, S. Crosslinking of the electrospun gelatin nanofibers. *Polymer* **2006**, *47*, 2911–2917. [CrossRef]
14. Kishan, A.P.; Nezarati, R.M.; Radzicki, C.M.; Renfro, A.L.; Robinson, J.L.; Whitely, M.E.; Cosgriff-Hernandez, E.M. In situ crosslinking of electrospun gelatin for improved fiber morphology retention and tunable degradation. *J. Mater. Chem. B* **2015**, *3*, 7930–7938. [CrossRef]
15. Nguyen, T.H.; Lee, B.T. Fabrication and characterization of cross-linked gelatin electro-spun nano-fibers. *J. Biomed. Sci. Eng.* **2010**, *3*, 1117–1124. [CrossRef]
16. Agheb, M.; Dinar, M.; Rafienia, M.; Salehi, H. Novel electrospun nanofibers of modified gelatin-tyrosine in cartilage tissue engineering. *Mater. Sci. Eng. C* **2017**, *71*, 240–251. [CrossRef] [PubMed]
17. Sisson, K.; Zhang, C.; Farach-Carson, M.C.; Bruce Chase, D.; Rabolt, J.F. Evaluation of cross-linking methods for electrospun gelatin on cell growth and viability. *Biomacromolecules* **2009**, *10*, 1675–1680. [CrossRef]
18. Correia, D.M.; Padrão, J.; Rodrigues, L.R.; Dourado, F.; Lanceros-Méndez, S.; Sencadas, V. Thermal and hydrolytic degradation of electrospun fish gelatin membranes. *Polym. Test.* **2013**, *32*, 995–1000. [CrossRef]
19. Lu, W.; Ma, M.; Xu, H.; Zhang, B.; Cao, X.; Guo, Y. Gelatin nanofibers prepared by spiral-electrospinning and cross-linked by vapor and liquid-phase glutaraldehyde. *Mater. Lett.* **2015**, *140*, 1–4. [CrossRef]
20. Chou, S.F.; Luo, L.J.; Lai, J.Y.; Hui-Kang Ma, D. Role of solvent-mediated carbodiimide cross-linking in fabrication of electrospun gelatin nanofibrous membranes as ophthalmic biomaterials. *Mater. Sci. Eng. C* **2017**, *17*, 1145–1155. [CrossRef]
21. Cumming, M.H.; Leonard, A.R.; Le Corre-Bordes, D.S.; Hofman, K. Intra-fibrillar citric acid crosslinking of marine collagen electrospun nanofibers. *Int. J. Biol. Macromol.* **2018**, *114*, 874–881. [CrossRef] [PubMed]
22. Jiang, Q.; Reddy, N.; Yang, Y. Cytocompatible cross-linking of electrospun zein fibers for the development of water-stable tissue engineering scaffolds. *Acta Biomater.* **2010**, *6*, 4042–4051. [CrossRef] [PubMed]
23. Reddy, N.; Warner, K.; Yang, Y. Low-temperature wet-cross-linking of silk with citric acid. *Ind. Eng. Chem. Res.* **2011**, *50*, 4458–4463. [CrossRef]
24. Jiang, Q.; Reddy, N.; Zhang, S.; Roscioli, N.; Yang, Y. Water-stable electrospun collagen fibers from a non-toxic solvent and crosslinking system. *Ind. Eng. Chem. Res* **2011**, *50*, 4458–4463. [CrossRef] [PubMed]
25. Saito, H.; Taguchi, T.; Kobayashic, H.; Kataoka, K.; Tanaka, J.; Murabayashi, S.; Mitamura, Y. Physicochemical properties of gelatin gels prepared using citric acid derivative. *Mater. Sci. Eng. C* **2004**, *24*, 781–785. [CrossRef]
26. Shafagh, N.; Sabzi, M.; Afshari, M.J. Development of pH-sensitive and antibacterial gelatin/citric acid/Ag nanocomposite hydrogels with potential for biomedical applications. *J. Polym. Res.* **2018**, *25*, 1661–1669. [CrossRef]
27. Uranga, J.; Leceta, I.; Etxabide, A.; Guerrero, P.; de la Caba, K. Cross-linking of fish gelatins to develop sustainable films with enhanced properties. *Eur. Polym. J.* **2016**, *78*, 82–90. [CrossRef]
28. Setta, S.; Stephansen, K.; Yarin, L. Solution-blown nanofiber mats from fish sarcoplasmic protein. *Polymer* **2016**, *93*, 78–87. [CrossRef]
29. Pawłowska, S.; Kowalewski, T.A.; Pierini, F. Fibrous polymer nanomaterials for biomedical applications and their transport by fluids: An overview. *Soft Matter* **2018**, *14*, 8421–8444. [CrossRef]
30. Jiang, Q.; Xu, H.; Cai, S.; Yang, Y. Ultrafine fibrous gelatin scaffolds with deep cell infiltration mimicking 3D ECMs for soft tissue repair. *J. Mater. Sci. Mater. Med.* **2014**, *25*, 1789–1800. [CrossRef]
31. Mahmood, K.; Kamilah, H.; Sudesh, K.; Karim, A.A.; Ariffin, F. Study of electrospun fish gelatin nanofilms from benign organic acids as solvents. *Food Packag. Shelf* **2019**, *19*, 66–75. [CrossRef]
32. Erencia, M.; Cano, F.; Tornero, J.A.; Fernandes, M.M.; Tzanov, T.; Macanas, J.; Carrillo, F. Electrospinning of gelatin fibers using solutions with low acetic acid concentration: Effect of solvent composition on both diameter of electrospun fibers and cytotoxicity. *J. Appl. Polym. Sci.* **2015**, *132*, 42115. [CrossRef]
33. Djabourov, M.; Leblond, J.; Papon, P. Gelation of aqueous gelatin solutions. I. Structural investigation. *J. Phys. Fr.* **1988**, *49*, 319–332. [CrossRef]
34. Higuchi, T.; Eriksson, S.; Uno, H.; Windheuser, J.J. Facilitated Reversible Formation of Amides from Carboxylic Acids in Aqueous Solutions. Intermediate production of acid anhydride. *J. Am. Chem. Soc.* **1963**, *85*, 3655–3660. [CrossRef]

35. Xu, H.; Shen, L.; Xu, L.; Yang, Y. Low-temperature crosslinking of proteins using non-toxic citric acid in neutral aqueous medium: Mechanism and kinetic study. *Ind. Crops Prod.* **2015**, *74*, 234–240. [CrossRef]
36. Alfaro, A.T.; Balbinot, E.; Weber, C.I.; Tonial, I.B.; Machado-Lunkes, A. Fish Gelatin: Characteristics, Functional Properties, Applications and Future Potentials. *Food Eng. Rev.* **2015**, *7*, 33–44. [CrossRef]
37. Gioffrè, M.; Torricelli, P.; Panzavolta, S.; Rubini, K.; Bigi, A. Role of pH on stability and mechanical properties of gelatin films. *J. Bioact. Compat. Polym.* **2012**, *27*, 67–77. [CrossRef]
38. Etxabide, A.; Leceta, I.; Cabezudo, S.; Guerrero, P.; de la Caba, K. Sustainable fish gelatin films: From food processing waste to compost. *ACS Sustain. Chem. Eng.* **2016**, *4*, 4626–4634. [CrossRef]
39. Sha, X.M.; Tu, Z.C.; Liu, W.; Wang, H.; Shi, Y.; Huang, T.; Man, Z.Z. Effect of ammonium sulfate fractional precipitation on gel strength and characteristics of gelatin from bighead carp (Hypophthalmichthysnobilis) scale. *Food Hydrocoll.* **2014**, *36*, 173–180. [CrossRef]
40. Baniasadi, H.; Ramazani, S.A.A.; Mashayekhan, S. Fabrication and characterization of conductive chitosan/gelatin-based scaffolds for nerve tissue engineering. *Int. J. Biol. Macromol.* **2015**, *74*, 360–366. [CrossRef]
41. Cui, Z.; Beach, E.S.; Anastas, P.T. Modification of chitosan films with environmentally benign reagents for increased water resistance. *Green Chem. Lett. Rev.* **2011**, *4*, 35–40. [CrossRef]
42. Francisco, C.R.L.; Heleno, S.A.; Fernandes, I.P.M.; Barreira, J.C.M.; Calhelha, R.C.; Barros, L.; Gonçalves, O.H.; Ferreira, I.C.F.R.; Barreiro, M.F. Functionalization of yogurts with Agaricusbisporus extracts encapsulated in spray-dried maltodextrin crosslinked with citric acid. *Food Chem.* **2018**, *245*, 845–853. [CrossRef] [PubMed]

materials

MDPI

Article

New Poly(Propylene Imine) Dendrimer Modified with Acridine and Its Cu(II) Complex: Synthesis, Characterization and Antimicrobial Activity

Paula Bosch [1,*], Desislava Staneva [2], Evgenia Vasileva-Tonkova [3], Petar Grozdanov [3], Ivanka Nikolova [3], Rositsa Kukeva [4], Radostina Stoyanova [4] and Ivo Grabchev [5,*]

1 Institute of Science and Technology of Polymers, Institute of Science and Technology of Polymers-Spanish National Research Council (ICTP-CSIC), Juan de la Cierva 3, 28006 Madrid, Spain
2 Department of Chemical Technology, University of Chemical Technology and Metallurgy, 1756 Sofia, Bulgaria
3 The Stephan Angeloff Institute of Microbiology, Bulgarian Academy of Sciences, 1113 Sofia, Bulgaria
4 Institute of General and Inorganic Chemistry, Bulgarian Academy of Sciences, 1113 Sofia, Bulgaria
5 Faculty of Medicine, Sofia University "St. Kliment Ohridski", 1407 Sofia, Bulgaria
* Correspondence: pbosch@ictp.csic.es (P.B.); i.grabchev@chem.uni-sofia.bg (I.G.); Tel.: +359-28161319

Received: 21 July 2019; Accepted: 16 September 2019; Published: 18 September 2019

Abstract: A second-generation poly(propylene imine) dendrimer modified with acridine and its Cu(II) complex have been synthesized for the first time. It has been found that two copper ions form complexes with the nitrogen atoms of the dendrimeric core by coordinate bonds. The new compounds have been characterized by nuclear magnetic resonance (NMR), electron paramagnetic resonance (EPR), fourier-transform infrared spectroscopy (FTIR) and fluorescence spectroscopy. The spectral characteristics of the modified dendrimer have been measured in different organic solvents, and a negative fluorescence solvatochromism has been observed. The antimicrobial activity of the dendrimers has been tested against model pathogenic microorganisms in agar and by broth dilution method. The cotton fabric treated with both dendrimers has been evaluated towards pathogenic microorganisms. The obtained modified cotton fabrics have been shown to hamper bacterial growth and to prevent biofilm formation. Dendrimer cytotoxicity has been investigated in vitro in the model HEp-2 cell line.

Keywords: dendrimer; metallodendrimer; acridine; antimicrobial activity; antibacterial cotton

1. Introduction

Antibacterial surfaces are very important with regard to minimizing infectious diseases which are one of the main causes of mortality worldwide [1]. This problem is mainly due to the increasing resistance of pathogenic microorganisms to antibiotics applied in clinical practice [2] Heterocyclic compounds have major role in the design and investigations of new bioactive drugs [3,4] Therefore acridine derivatives are one of the intensively exploited organic fluorophores in which fluorescence color intensity depends strongly on the polarization of their chromophoric system [5,6]. Possessing a heteroaromatic polycyclic molecule acridine derivatives are well known for their DNA intercalating abilities and pharmacological activity. That has led to the design and preparation of acridine compounds with anticancer, antimalarial, antiviral and antifungal activities [5–10].

Dendrimers are macromolecules with well-defined molecular weight and a high degree of branching units containing different reactive functional groups to which substances with biological activity may be attached by a chemical bond or by weak intermolecular interactions [11]. Compared to the low molecular weight bioactive compounds, dendrimers have the potential to deliver a large dose

of biologically active substances, depending on the dendrimer generation. [12,13]. On the other hand, dendrimers containing metal ions, or metal nanoparticles also exhibit good biological activity [14–17].

Cotton fabrics are natural polymers, that have properties, such as high water absorptivity and air permeability and which are used for the production of textile products with different applications [18,19]. One of the major drawbacks of ordinary cotton fabrics is the possibility of being colonized by pathogenic microorganisms forming biofilms leading to undesired hygienic problems [20,21]. In the medical and clinical practice, cotton materials are used to obtain antibacterial textiles like wound dressings, hospital linen, sterile surgical materials, etc. [22]. Therefore, the improvement of their antimicrobial resistance is of major importance.

In this paper, the peripheral modification of a second-generation poly (propylene imine) dendrimer with acridine fluorophores has been described for the first time. Its copper complex has also been obtained and characterized. The spectral characteristics of the new fluorescent dendrimer have been investigated in different organic solvents. The antimicrobial activity of the dendrimers in agar, liquid medium and after their deposition on a textile material has also been tested. The cytotoxicity of the dendrimers has been evaluated in vitro in the model HEp-2 cell line.

2. Materials and Methods

2.1. Materials

Poly(propylene imine) dendrimer second-generation, phenol, 9-chloroacridine, ammonia solution (32%) and anhydrous magnesium sulfate were obtained from Sigma-Aldrich and used as received. All organic solvents: tetrahydrofurane, ethylacetat, chloroform, dichloromethane, acetonitrile, methanol, ethanol, used in this study were used as obtained from Sigma-Aldrich without any additional purifications. Dimethyl sulfoxide (DMSO) for molecular biology was used for antibacterial screening (Sigma–Aldrich). The antibacterial activity of the compounds was tested in vitro with Gram (+) bacterial strain *Bacillus cereus* (*B. cereus*) ATCC 11778 and Gram (−) bacterial strain *Pseudomonas aeruginosa* (*P. aeruginosa*) 1390, and the antifungal activity was screened on fungi strain *Candida lipolytica* (*C. lipolytica*) 7618. Microorganisms were obtained from the collection of the Institute of Microbiology, Bulgarian Academy of Sciences, Sofia, Bulgaria. Before experimental use, cultures from solid medium were sub cultivated in a liquid medium (meat-peptone broth, MPB), incubated (orbital shaker incubator) and used as a source of inoculums for each experiment.

2.2. Synthesis of Acridine Dendrimer (ACR)

A two-neckle round bottom flask, provided with a reflux cooler, magnetic stirring and N_2 atmosphere was loaded with 0.5 g of 9-chloroacridine (2.3 mmol) and 1.15 g of distilled phenol. The reaction was maintained refluxing at 110 °C for 1 h. Then, 182.8 L of dendrimer (0.181 g, 0.23 mmol) was added, and reflux at 110 °C was maintained for 6 h. The reaction was then allowed to cool at room temperature, and 30 mL of acetone were added, under stirring, to the brown slurry obtained. The slurry solidified, and the yellow-orange solid obtained was washed with acetone. The solid was dissolved in water/NH_4OH (pH 8) and extracted with dichloromethane (4 × 20 mL). The organic extracts were dried over anhydrous $MgSO_4$ and evaporated under vacuum. 0.25 g (yield = 52%) of a yellow-orange solid were obtained. Tdecomp: 254 °C

FT-IR cm^{-1}: 3240, 1615, 1594, 1558, 1518, 1466, 1138, 1020, 752, 647.

^{1}H-RMN ($CDCl_3$) ppm: 1.22 (s, $4H^{15}$, C-CH_2-CH_2-C), 1.57 (bs, $16H^9$ and $8H^{12}$, C-CH_2-C), 1.91–2.07 (bs, $8H^{11}$, $8H^{13}$ and $4H^{14}$, N-CH_2), 2.28 (bs, $16H^{10}$, N-CH_2), 3.60 (bs, $16H^8$, NH-CH_2-), 7.03 (bs, $16H^2$, Ar-H), 7.43 (bs, $16H^3$, Ar-H), 7.89 (sa, $16H^4$ and $16H^1$, Ar-H).

^{13}C-NMR ($CDCl_3$) ppm: 23, 25, 29, 45, 51, 55, 115, 117, 121, 126, 129, 133, 141, 152.

API-ES-MS (positive) *m*/*z*: found: 2191.6 (100, $[M + H]^+$), 1096.1 (65, $[M + H]^+/2$).

2.3. Synthesis of [Cu_2(ACR)(NO_3)$_2$]

ACR dendrimer (0.219 g, 0.1 mmol) was dissolved in 20 mL of ethanol and $Cu(NO_3)_2 \cdot 3H_2O$ (0.113 g, 0.6 mmol) was added to the solution. The mixture was stirred for 2 h, and the solid formed was filtered, washed with ethanol three times, and dried under vacuum. Yield: 0.225 g, 88.1%

FT-IR cm^{-1}: 1638, 1691, 1531, 1466, 1367, 1298, 1173, 1037, 826, 754, 661.

Analysis: $C_{144}H_{152}N_{26}O_{12}Cu_2$ (2564.8 g mol^{-1}) Calculated (%): C 67.43, H 5.93, N 14.20; Found (%): C 67.54, H 5.88, N 14.28

2.4. Dendrimers Characterization

The UV-Vis spectrophotometric investigations of the dendrimers were performed on a UV-Vis "Thermo Spectronic Unicam UV 500" double beam spectrophotometer. Fluorescence spectra were taken on a "Cary Eclipse" fluorimeter. The absorption and fluorescence spectra were recorded using 10^{-6} mol/L solutions of the dendrimers. The quantum yield of fluorescence was determined by comparing the areas underneath the fluorescence spectra of the dendrimers. Standard quinine bisulfate/H_2SO_4 1N ($\Phi_f = 0.546$) was used as standard material to calculate the dendrimer fluorescence quantum yields. ATR FT-IR spectroscopic analyses of dendrimers were performed using an IRAffinity-1 spectrophotometer (Shimadzu Co., Kyoto, Japan) equipped with a MIRacleTM ATR (diamond crystal, depth of penetration of the infrared (IR) beam into the sample was about 2 mm) accessory (PIKE Technologies, Cottonwood, WI, USA). The spectra were recorded from 4000 cm^{-1} to 500 cm^{-1} with a spectral resolution of 4 cm^{-1} using a DLATGS detector equipped with a temperature controller. All spectra were corrected for H_2O and CO_2 using IR solution internal software. ^1H (600.13 MHz) and ^{13}C (150.92 MHz) NMR spectra were acquired on an BRUKER, AVANCE AV600 II+NMR spectrometer (Rheinstetten, Germany). The measurements were carried out in a $CDCl_3$ solution at ambient temperature. The chemical shifts were referenced to a tetramethylsilane (TMS) standard. The EPR spectra of Cu(II) complexes were recorded as the first derivative of the absorption signal by using a Bruker EMXplus EPR spectrometer (Rheinstetten, Germany), operating in the X-band (9.4 GHz). The recording temperature was varied within the range of 120–450 K. The quantitative EPR calculations were performed by SpinCountTM software module (Bruker, Hamburg, Germany). The spectra were simulated using the program SIMFONIA (Bruker, Hamburg, Germany). The effect of the metal cations upon the fluorescence intensity was examined by adding a few L of stock solution of the metal cations to a known volume of the tripod solution (3 mL). The addition was limited to 0.1 mL, so that dilution remained insignificant.

2.5. Cotton Fabric Functionalization with ACR and [Cu_2(ACR)(NO_3)$_2$]

0.005 g of each dendrimer was dissolved in 5 mL of a N,N-dimethylformamide(DMF)–water 1:4 (*v*/*v*) solution. The cotton fabric sample (1 g) (weight 140 g m^{-2}) was immersed into the solution at 25 °C for 30 min, washed with water and dried at ambient temperature. The dyed cotton fabric is yellow in color and resistant to water treatment. In this case, the fixation of the dendrimer on the surface of the textile material is accomplished by van der Waals forces and possible hydrogen bonds between hydroxyl groups from the cellulose structure and tertiary nitrogen atoms from the dendrimer molecule.

2.6. Cellular Toxicity

HEp-2 cells (National Bank for Industrial Microorganisms and Cell Cultures, No. NBIMCC-95, Sofia, Bulgaria) were grown in medium containing 10% heated calf serum in DMEM (Gibco BRL, Red Bank, NJ, USA) supplemented with 10 mmol/L HEPES buffer (Gibco BRL, Red Bank, NJ, USA) and antibiotics (penicillin, 100 U/mL; streptomycin, 100 µg/mL).

Monolayer cells in 96-well plates (Costar®, Corning Inc., Kennebunk, ME, USA) were inoculated with 0.1 mL/well-containing concentrations (in logarithmic intervals) of the compounds diluted in a maintenance medium. Cells were incubated in a humidified atmosphere at 37 °C and 5% CO_2 for 48 h.

After microscopic evaluation, the maintenance medium containing the test compound was removed, cells were washed, and 0.1 mL maintenance medium supplemented with 0.005% neutral red dye was added to each well and cells were incubated at 37 °C for 3 h. After incubation, the neutral red day was removed, and cells were washed once with PBS, and 0.15 mL/well desorb solution (1% glacial acetic acid and 49% ethanol in distilled water) was added. The optical density (OD) of each well was read at 540 nm in a microplate reader (Organon Teknika Reader model 530, Organon, West Chester, PA, USA). The 50% cytotoxic concentration (CC_{50}) was defined as the material concentration that reduced the cell viability by 50% when compared to untreated control.

2.7. Antimicrobial Activity Test

The antimicrobial activity of the compounds was firstly tested by the agar diffusion method using 0.2% solutions of the investigated compounds in dimethyl sulfoxide (DMSO). Plates containing Mueller-Hinton agar (MHA) were inoculated with aliquots of suspensions of microbial cultures. An equal amount (30 μL, 0.06 μg) of each sample solution was introduced into wells (8 mm in diameter) punched in MHA following a sterile procedure. Standard commercial discs with gentamicin (G, antibacterial agent) and nystatin (Ns, antifungal agent) were used as references. A positive control using only inoculation and negative control using only DMSO in wells were also prepared. The plates were incubated at the appropriate temperature for 24−48 h, and the resulting inhibition zones (diameter, mm) were recorded.

Broth dilution method was performed for in vitro determination of the minimum inhibitory concentration (MIC) of the compounds [23]. Stock solutions of the investigated compounds (0.1% in DMSO) were serially diluted in MPB to final concentrations ranging from 2 to 200 μg/mL. After inoculation, the test tubes were incubated at the appropriate temperature for 24 h under shaking. Positive controls (compounds and MPB, without inoculum) and negative controls (MPB and inoculum, without compounds) were also prepared. Growth of the strains was assayed by monitoring the turbidity at 600 nm (OD_{600}). Microbial growth (%) was determined on the basis of the positive control, which was considered as 100%. The MIC was considered to be the lowest concentration of the tested sample to inhibit the visible growth of microorganisms. All assays were performed in triplicate, and the average was taken; standard deviations were less than 5%.

2.8. Antibacterial Activity of Cotton Fabrics

The antibacterial activity of cotton fabrics treated with ACR and $[Cu_2(ACR)(NO_3)_2]$ was tested against *B. cereus* and *P. aeruginosa* as model strains. Test tubes containing MPB and square cotton specimens (10 mm × 10 mm) were inoculated with a suspension of each bacterial culture. Untreated cotton and without specimens were used as controls. After incubation for 24 h at the appropriate temperature, the bacterial growth was determined by measuring OD_{600}. Antimicrobial activity of the treated cotton samples was evaluated by the reduction of OD_{600} after incubation compared to the control sample. All antimicrobial tests were done in triplicate, and the average was taken.

2.9. Scanning Electron Microscopy (SEM)

The adhesion and biofilm formation over the cotton fabric were assessed by SEM. The tubes containing MPB and specimens of untreated and treated cotton fabrics were inoculated with a suspension of *P. aeruginosa.* After incubation for 24 h, the specimens were washed with phosphate-buffered saline, dried and coated with gold with Jeol JFC-1200 fine coater (Jeol Ltd., Tokyo, Japan) and then investigated by Jeol JSM-5510 SEM (Jeol Ltd., Tokyo, Japan).

2.10. Hydrophilicity of Cotton Fabrics

Static immersion test was carried out to measure the amount of water absorbed by the cotton fabrics. The tested cotton samples were weighed and immersed into distilled water, taken out after

about 3 min and tapped to remove excess water and then weighed once again. The absorption percentage was determined by the following formula [24]:

$$\text{Absorption (\%)} = (\text{mass of water absorbed/original mass}) \times 100$$

3. Results

3.1. Synthesis of Acridine Dendrimer

To obtain a polypropylene imine dendrimer modified with acridine fluorophores, we used a second-generation dendrimer containing eight primary amino groups in its periphery, thus enabling eight acridine fragments to be coupled into one molecule. Fully functionalized acridine dendrimer (ACR) was obtained in a moderate yield by modification of a previously described procedure, [25] as depicted in Scheme 1. As the acridine dendrimer was obtained as a protonated species in the reaction medium, the solid was dissolved in water/NH_4OH (pH 8) wherefrom it was extracted in its neutral form. The copper complex, $[Cu_2(ACR)(NO_3)_2]$, was subsequently synthesized easily by a reaction run in ethanol at room temperature.

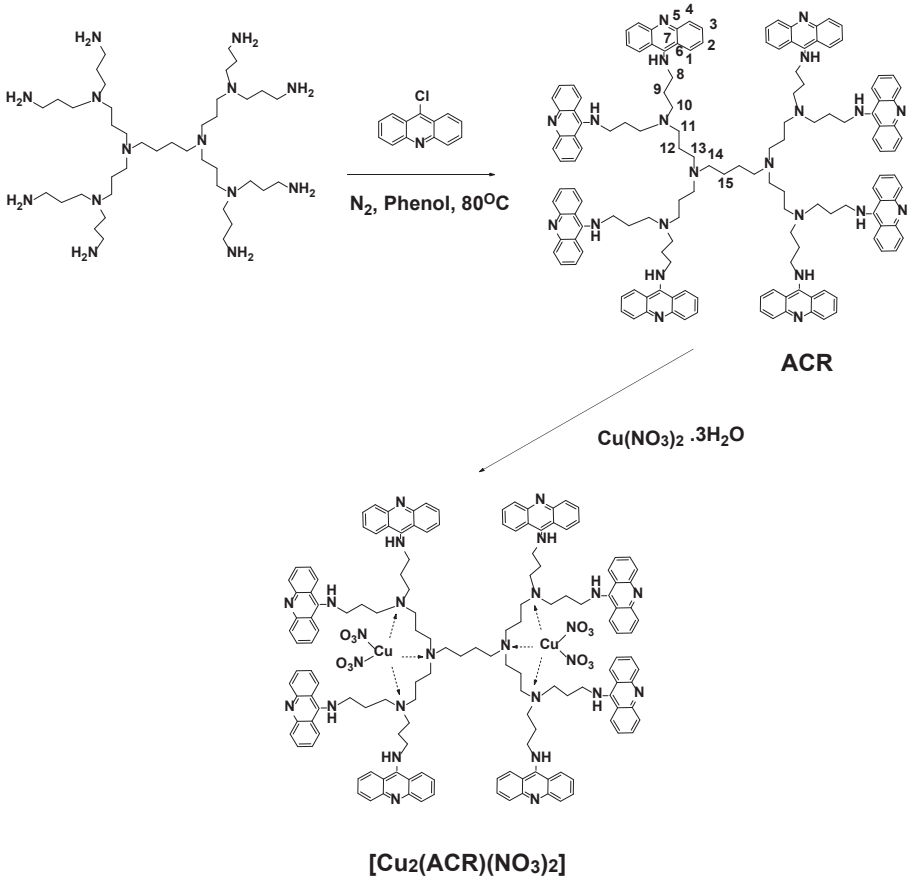

Scheme 1. Synthesis of acridine dendrimer (ACR) dendrimer.

3.2. Spectral Characterizations

The dendrimer is insoluble in water, but it is very well soluble in organic solvents. The basic spectral characteristics of ACR dendrimer: Absorption (λ_A) and fluorescence (λ_F) maxima, Stoke's shift $\nu_A - \nu_F$), the quantum yield of fluorescence (Φ_F) have been investigated in seven organic solvents of different polarity, and the main results are summarized in Table 1.

Table 1. Photophysical characteristics of ACR dendrimer in organic solvents of different polarity (see text).

Solvent	λ_A nm	λ_F nm	$\nu_A - \nu_F$ cm^{-1}	Φ_F
Acetonitrile	414	467	2741	0.010
Ethanol	414	458, 481[s]	2320	0.040
Methanol	412	455, 480 [s]	2294	0.023
Ethyl acetate	392	467	4096	0.012
Chloroform	402	471	3644	0.004
Tetrahydrofurane	396	480	4420	0.003
Dichloromethane	408	469	3188	0.007

s: Shoulder.

The spectrum of the acridine dendrimer has absorption maxima between 396–412 nm, ascribed to an internal charge transfer (ICT) transition. It emits fluorescence with maxima at 455–480 nm region. In most solvents, the spectra are composed by a single broadband, whereas, in hydrogen bonding solvents (alcohols) a shoulder can be distinguished [26–29]. The results show solvent polarity dependence. Comparing the absorption maxima of the spectra taken in non-polar solvents with those taken polar ones, a positive solvatochromism has been obtained, while the respective maxima in polar environments do not change their position. In the case of fluorescence maxima, it is seen that with increasing the medium polarity, their values decrease and a negative solvatochromism has been found (Figure 1). The lower values of Stokes shift ($\nu_A - \nu_F$) in a polar medium can be explained by the dipole-dipole interactions and possibility of the formation of hydrogen bonds. That probably stabilizes the acridine molecules in the excited state, and conformational changes are slightly pronounced. This is also confirmed by the results obtained for the quantum fluorescence yield, where the values in polar media are several times higher (Table 1). Similar results have been obtained when acridine functionality has been bonded to a hyperbranched polymer [30].

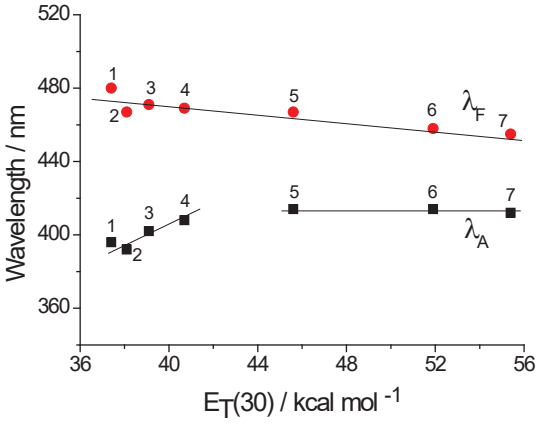

Figure 1. Solvent polarity dependence of absorption and fluorescence maxima: 1-tetrahydrofurane, 2-ethylacetate, 3-chloroform, 4-dichloromethane, 5-acetonitrile, 6-methanol, 7-ethanol.

In order to elucidate the formation of a copper complex, titration of ACR dendrimer with Cu(II) ions has been carried out in acetonitrile solution. Figure 2A shows the decrease of fluorescence intensity with increasing concentration of Cu(II) ions. Figure 2A also shows that Cu(II) forms a complex with a dendrimer molecule at a 1:2 stoichiometry. The possible formation of the coordination of Cu(II) is with the tertiary amino groups in the dendrimer core. IR spectroscopy has been used for the characterization of the isolated solid complex (Figure 2B). The difference is observed in the range 1200–1340 cm^{-1}, where is the absorption of nitrate groups ($-NO_3$).

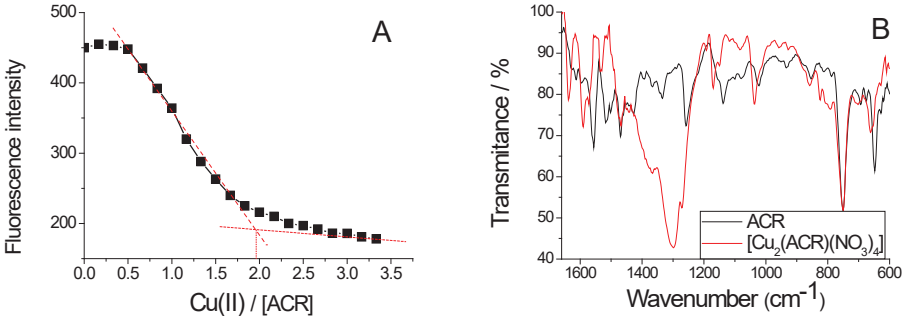

Figure 2. Fluorescence (**A**) and infrared (IR) (**B**) spectral characterization of $[Cu_2(ACR)(NO_3)_2]$.

3.3. EPR Analysis

Figure 3 display the EPR spectra of the dendrimer complexes $[Cu_2(ACR)(NO_3)_2$ and EPR spectrum of ACR ligand is shown for the comparison, The EPR spectrum of the copper complex consists of an anisotropic signal with *g*-components of $g_1 = 2.238$, $g_2 = 2.075$, $g_3 = 2.065$ between 120 and 295 K. The *g*-components are not sensitive towards the recording temperature. In the range of g_1-component, a hyperfine structure is hardly resolved, the constant hyperfine being $A_1 = 16.5$ mT. The analysis of EPR parameters of the Cu(II) complex reveals that the g_1-component adopts a relatively low value, whereas, the magnitude of the hyperfine constant A_1 is relatively high. On the basis of Peisach-Blumberg diagram [31], the relation between the values of *g*- and *A*-components can be used as an experimental measure on the composition of the coordination shell around Cu(II) ions: The coordination of nitrogen to Cu(II) provokes a decrease of the $g_{\|}$-value and a corresponding increase in $A_{\|}$ value, while the opposite trend is observed when oxygen is coordinated around Cu(II). The comparison shows that for the complexes of Cu(II) with ACR, the ligand is coordinated to Cu(II) ions mainly through nitrogen atoms (Scheme 1).

The ligand displays a narrow symmetrical signal with a *g*-factor of 2.003, in comparison with the copper complex. The *g*-value and the extremely narrow line width (less than 0.5 mT) implies that the signal comes, most probably, from free radicals. It should be taken into account that the origin of this signal is unclear. It is of importance that the signal, due to the ligand is not observed in the EPR spectrum of the copper complex; hence, all ligand molecules are involved in the complexation.

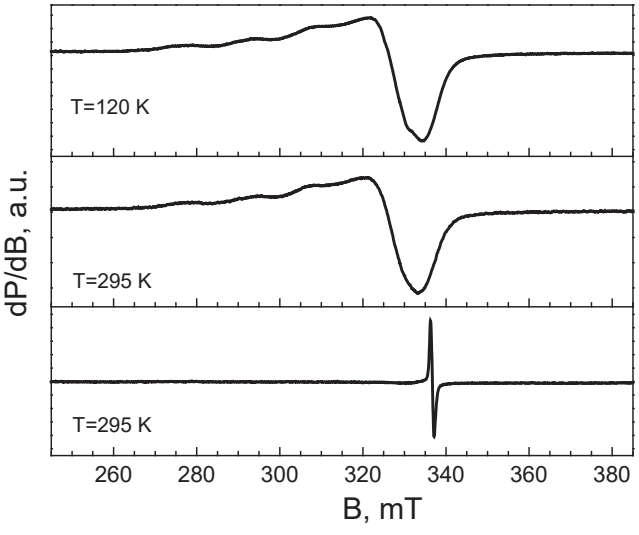

Figure 3. EPR spectra of the complex of $[Cu_2(ACR)(NO_3)_2]$) and dendrimer ligand ACR (bottom). The recording temperature is indicated.

3.4. NMR Characterization of Dendrimer ACR

The chemical structure of the dendrimer ACR was confirmed by ^{1}H and ^{13}C NMR spectroscopy. The ^{1}H NMR data show the evidence for the bonding of acridine fluorophore to the primary amino group from the dendrimer structure. From Scheme 1 it is clearly seen that the chemical structure of the polypropylene imine dendrimer is composed only of methylene groups ($-CH_2-$) and their characteristic signals are in the spectral range δ = 1.22–3.60 ppm. These signals were observed at polypropylene imine dendrimers modified with 1,8-naphthalimide or benzanthrone fluorophores [32,33]. The aromatic proton (Ar−H) signals from the acridine structure are recorded in the δ = 7.03–7.89 ppm region as broad singlets. The carbon signals for acridine ring (Ar−C) are at δ = 115–152 ppm and that of the methylene groups $-CH_2-$ group of the poly(propylene imine) dendrimer framework are between δ = 23–55 ppm.

3.5. Antimicrobial Activity of ACR and $[Cu_2(ACR)(NO_3)_2]$

Figure 4 plots the inhibition zones formed by the ACR and $[Cu_2(ACR)(NO_3)_2]$) against three different model pathogens. Both the free ligand and $[Cu_2(ACR)(NO_3)_2]$ showed strong activity against the used Gram (+) *B. cereus* and the yeasts *Candida*; the complex exhibited about 30% higher activity than the ligand and standard drug. The low activity has been observed against Gram negative *P. aeruginosa*.

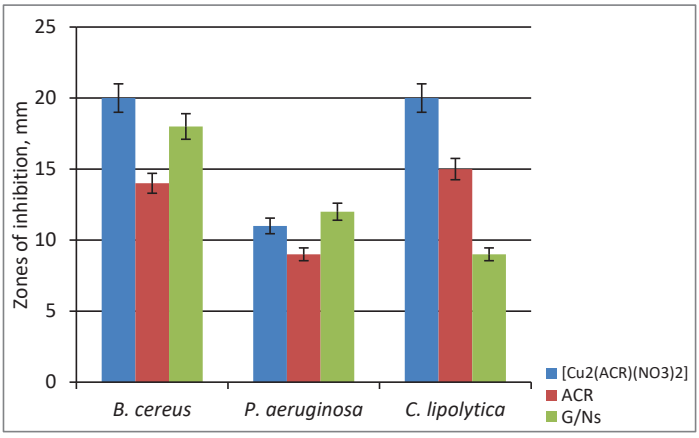

Figure 4. Zones of inhibition of the model strains by 0.06 g of the investigated ACR and $[Cu_2(ACR)(NO_3)_2]$. G, Gentamicin; Ns, Nystatin.

The MICs of the compounds have been determined by serial dilution in MPB, and the results are shown in Table 2. Obviously, complexation with Cu(II) ions enhances the antimicrobial effect of the ligand to a different extent, depending on the tested strain.

Table 2. Minimum inhibitory concentration (MIC) values of the compounds ACR and $[Cu_2(ACR)(NO_3)_2]$ towards the tested strains.

Strain	MIC, μg/mL	
	ACR	**$[Cu_2(ACR)(NO_3)_2]$**
Bacillus cereus	40	10
Pseudomonas aeruginosa	120	80
Candida lipolytica	80	40

MIC s of the $[Cu_2(ACR)(NO_3)_2]$ vary from 10 to 80 μg/mL, and from 40 to 120 μg/mL for the ligand. Both the ligand and its Cu(II) complex exhibit the highest effectiveness in inhibiting the growth of *B. cereus* (the lowest MICs 10 and 40 μg/mL, respectively) followed by *C. lipolytica* with MICs of 40 and 80 μg/mL, respectively. Gram (−) *P. aeruginosa* displays the highest resistance to the compounds with the highest MIC values. The observed difference in the susceptibility of both type of bacteria to the investigated substances is due to the different structure of the bacterial cell walls. [34].

Dendrimer interior is a binding site for Cu(II) ions, and after its complexation, the polarity of the Cu(II) is reduced which can be explained to the partial sharing of positive charges with the nitrogen groups that increase the lipophilicity of the $[Cu_2(ACR)(NO_3)_2]$ complex. The enhanced lipophilicity increases penetration of the metal complex through the lipid membranes and consequently blocking metal-binding sites in the targeted enzymes of the microorganisms [35].

According to Holetz theory MICs values can be used to classify the microbiological activity of the compounds against pathogenic microorganisms [36]. Compounds with MICs less than 100 μg/mL exhibit good antimicrobial activity, in the range 100 to 500 μg/mL have moderate activity, weak activity demonstrate compounds in the range from 500 to 1000 μg/mL, and compounds over 1000 μg/mL are considered inactive. Depending on those criteria, our results exhibit a good antimicrobial activity of the tested compounds against the used model strains.

3.6. Antibacterial Activity of Cotton Fabric

Various methods have been proposed for the antimicrobial modification of material surfaces as an alternative way of preventing the formation of highly resistant biofilms [37]. The antimicrobial activity of cotton fabrics treated with the compounds has been investigated by reduction of the growth of Gram (+) *B. cereus* and Gram (−) *P. aeruginosa* used as model strains. The results demonstrate good antimicrobial effect of both ACR and $[Cu_2(ACR)(NO_3)_2]$ treated cotton fabrics (Figure 5). They are highly effective inhibiting about 90% of the growth of *B. cereus* and more than 50% of the growth of *P. aeruginosa*. Slow diffusion of the compounds from the cotton fabric into the medium and the direct contact with bacterial cells may contribute to the antimicrobial effect of the modified cotton fabrics.

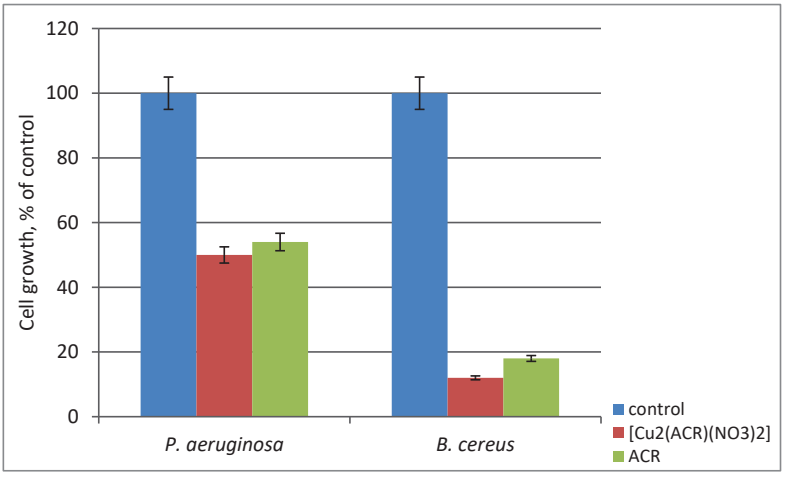

Figure 5. Reduction of the growth of model bacteria by untreated (control) and treated cotton fabrics.

3.7. Hydrophilicity of Cotton Fabrics

Hydrophilicity of cotton fabrics has been assessed by the amount of absorbed water. Hydrophilicity of untreated cotton fabric and cotton fabrics treated with ACR and $[Cu_2(ACR)(NO_3)_2]$ complex has been determined to be 112%, 95% and 86%, respectively. The results clearly indicated that the compounds induce an increase in hydrophobicity when applied to cotton fabric may be due to an increase in the number of hydrophobic groups on the surface of the treated cotton fabric. More effective hydrophobicity has been achieved with the cotton fabric treated with $[Cu_2(ACR)(NO_3)_2]$, if compared to that of ACR treated fabric, which effect can be explained by the enhanced lipophilicity of the $[Cu_2(ACR)(NO_3)_2]$ complex.

3.8. SEM Analysis

Pseudomonas aeruginosa is an excellent biofilm producer, and it has been selected to investigate the efficacy of the cotton fabrics treated with the ACR and $[Cu_2(ACR)(NO_3)_2]$ in preventing the adhesion and biofilm formation [38]. In Figure 6 are presented SEM micrographs of untreated cotton fabrics and cotton fabrics treated with ACR and its $[Cu_2(ACR)(NO_3)_2]$ complex after 24 h of incubation. From the SEM images, it is clearly seen that a formation of P. aeruginosa biofilm on the untreated cotton fabric (Figure 6B). In this case, many bacterial cells are adhered to the cotton surface and embedded into extracellular bio matrix. On the other hand, a significant reduction of biofilm formation and bacterial the adhesion has been observed on the surface of the cotton fabric treated with ACR (Figure 6D). Only single bacterial cells are attached to the cotton surface of the cotton fabric treated with the complex $[Cu_2(ACR)(NO_3)_2]$ (Figure 6C). Thus, the deposition of ACR and $[Cu_2(ACR)(NO_3)_2]$ complex on the

cotton fabric prevents the formation and proliferation of a bacterial biofilm, allowing the production of antibacterial cotton fabric.

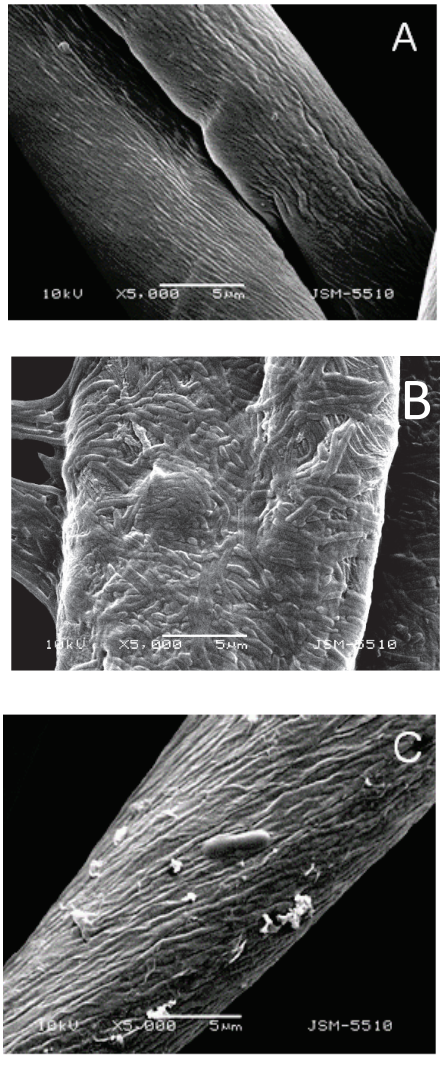

Figure 6. Scanning Electron Microscopy (SEM) micrograph of cotton fabrics tested against *P. aeruginosa* at magnification X 5000: (**A**) Cotton textile before treatments; (**B**) biofilm on untreated cotton textile; (**C**) absence of biofilm on cotton textile treated with $[Cu_2(ACR)(NO_3)_2]$; (**D**) reduced biofilm formation on cotton textile treated with ACR.

3.9. In Vitro Cytotoxicity Assay

The evaluation of cytotoxicity of antimicrobials is a critical step to guarantee their safe use. The results for the cytotoxicity of the newly synthesized dendrimers are shown in Figure 7. It has been found that both acridine dendrimer and its Cu-complex affected HEp-2 cells at similar doses, with CC_{50} values of 19.5 μg/mL and 19.4 μg/mL, respectively. At the active concentration of the $[Cu_2(ACR)(NO_3)_2]$

against Gram-positive *B. cereus* (MIC 10 μg/mL) cell viability is near 75%, while other tests did not detect viable cells at the active concentrations of the dendrimers (MICs 40–120 μg/mL). The results also show that the binding of copper ions to the dendrimer molecule does not additionally increase the cytotoxicity of the dendrimer ligand ACR.

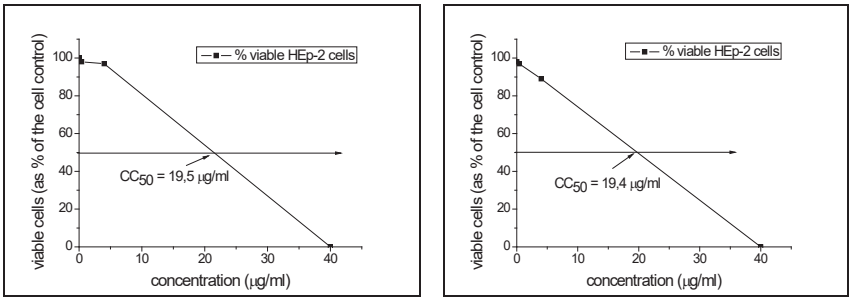

Figure 7. Cytotoxicity values of the compounds ACR (**A**), and $[Cu_2(ACR)(NO_3)_2]$ (**B**) towards HEp-2 cells.

4. Conclusions

For the first time, acridine has been used for the modification of a poly(propylene imine) dendrimer (ACR). The new fluorescent dendrimer has been used as a ligand to obtained its Cu(II) complex $[Cu_2(ACR)(NO_3)_2]$. EPR, FTIR, and fluorescent spectroscopy have been used to confirm the structure of metallodendrimer. It has been found that two copper ions are included in the dendrimer core by coordination with the inner tertiary nitrogen atoms. The basic photophysical characteristics of dendrimer have been examined in different organic solvents, and a negative fluorescence solvatochromism has been observed. The antimicrobial activity of dendrimers has been tested in vitro against some model Gram positive and Gram negative bacteria and yeasts. The results demonstrated enhancement in the antimicrobial activity of acridine dendrimer via complexation with copper ions against *B. cereus* and *C. lipolytica*. Deposition of dendrimers on the surface of cotton fabric has led to an increase in hydrophobicity of the textile. That prevents the formation of bacterial biofilm and makes these compounds useful for the production of antibacterial cotton fabrics.

Author Contributions: Conceptualization, P.B. and I.G.; methodology, synthesis, characterization and supervision P.B. and I.G.; textile investigation, D.S.; microbiological E.V.-T.; cytotoxicity assay P.G. and I.N.; EPR analysis R.K. and R.S.; project administration I.G. and P.B.

Funding: This research was funded by Fund "Scientific Research", Ministry of Education and Science of Bulgaria, grant number KOCT01/24-2017" and "Ministry of Economy and Competitively of Spain", grand number RTI2018-096328-B-I00

Acknowledgments: IG and PB acknowledge COST CA15114 action "Anti-MIcrobial Coating Innovations to prevent infectious diseases (AMICI)".

Conflicts of Interest: The authors declare no conflict of interest.

References

1. Kaur, R.; Liu, S. Antibacterial surface design - Contact kill. *Prog. Surf. Sci.* **2016**, *91*, 136–153. [CrossRef]
2. Bin, W.; Ho, S.; Park, J.; Hak, S.; Finn, J.; Yoon, S. Discovery of torezolid as a novel 5-hydroxymethyl-oxazolidinone antibacterial agent. *Eur. Med. Chem.* **2011**, *46*, 1027–1039.
3. Venepally, V.; Jala, R.C.R. An insight into the biological activities of heterocyclic-fatty acid hybrid molecules. *Eur. J. Med. Chem.* **2017**, *141*, 113–137. [CrossRef] [PubMed]

4. Gong, H.H.; Addla, D.; Lv, J.S.; Zhou, C.H. Heterocyclic Naphthalimides as New Skeleton Structure of Compounds with Increasingly Expanding Relational Medicinal Applications. *Curr. Top. Med. Chem.* **2016**, *16*, 3303–3364. [CrossRef] [PubMed]
5. Sharma, V.K.; Sahare, P.D.; Rastogi, R.C.; Ghoshal, S.K.; Mohan, D. Excited state characteristics of acridine dyes: Acriflavine and acridine orange. *Spectrochim. Acta A* **2003**, *59*, 1799–1804. [CrossRef]
6. Pietrzak, M.; Szabelski, M.; Kasparek, A.; Wieczorek, Z. Interactions of hypericin with a model mutagen - Acridine orange analyzed by light absorption and fluorescence spectroscopy. *Chem. Phys. Lett.* **2017**, *669*, 85–91. [CrossRef]
7. Novak, K. Chemical structures and biological activities of bis- and tetrakis-acridine derivatives: A review. *J. Mol. Struct.* **2017**, *1146*, 562–570.
8. Cholewiński, G.; Dzierzbicka, K.; Kołodziejczyk, A.M. Natural and synthetic acridines/acridones as antitumor agents: Their biological activities and methods of synthesis. *Pharmacol. Rep.* **2011**, *63*, 305–336. [CrossRef]
9. Palaniraja, J.; Kumar, S.S.; Ramki, S.; Arunachalam, P.; Roopan, S.M. Conventional spectroscopic identification of biologically activeimidazo-pyrimido fused acridines: In vitroanti-bacterial andanti-feedant activity. *J. Mol. Liq.* **2017**, *230*, 634–640. [CrossRef]
10. Gensicka-Kowalewska, M.; Cholewinski, G.; Dzierzbicka, K. Recent developments in the synthesis and biological activity of acridine/acridone analogues. *RSC Adv.* **2017**, *7*, 15776–15804. [CrossRef]
11. Mintzer, M.A.; Grinstaff, M.W. Biomedical applications of dendrimers: A tutorial. *Chem. Soc. Rev.* **2011**, *40*, 173–190. [CrossRef] [PubMed]
12. Rolland, O.; Turrin, C.-O.; Caminade, A.-M.; Majoral, J.-P. Dendrimers and nanomedicine: Multivalency in action. *New J. Chem.* **2009**, *33*, 1809–1824. [CrossRef]
13. Oliveira, J.M.; Salgado, A.J.; Sousa, N.; Mano, J.F.; Reis, R.L. Dendrimers and derivatives as a potential therapeutic tool in regenerative medicine strategies. *Prog. Polym. Sci.* **2010**, *35*, 1163–1194. [CrossRef]
14. Staneva, D.; Vasileva-Tonkova, E.; Makki, M.S.I.; Sobahi, T.R.; Abdel-Rahman, R.M.; Boyaci, I.H.; Asiri, A.M.; Grabchev, I. Synthesis and spectral characterization of a new PPA dendrimer modified with 4-bromo-1,8-naphthalimide and in vitro antimicrobial activity of its Cu(II) and Zn(II) metal complexes. *Tetrahedron* **2015**, *71*, 1080–1087. [CrossRef]
15. Grabchev, I.; Vasileva-Tonkova, E.; Staneva, D.; Bosch, P.; Kukeva, R.; Stoyanova, R. Synthesis, spectral characterization, and in vitro antimicrobial activity in liquid medium and applied on cotton fabric of a new PAMAM metallodendrimer. *Int. J. Polym. Anal. Ch.* **2018**, *23*, 45–57. [CrossRef]
16. Grabchev, I.; Staneva, D.; Vasileva-Tonkova, E.; Alexandrova, R.; Cangiotti, M.; Fattori, A.; Ottaviani, M.F. Antimicrobial and anticancer activity of new poly (propyleneamine) metallodendrimers. *J. Polym. Res.* **2017**, *24*, 210. [CrossRef]
17. Staneva, D.; Vasileva-Tonkova, E.; Bosch, P.; Grozdanov, P.; Grabchev, I. Synthesis and Characterization of a New PAMAM Metallodendrimer for Antimicrobial Modification of Cotton Fabric. *Macromol. Res.* **2018**, *26*, 332–340. [CrossRef]
18. Rahnev, I.; Rimini, G. Isotropy Equilibrium of The Double Woven Fabric with Cotton Face and Wool Reverse Fibrous Compositions. In Proceedings of the IOP Conference Series: Materials Science and Engineering, 17th World Textile Conference (AUTEX), Corfu, Greece, 29–31 May 2017; Volume 254, pp. 675–683.
19. Rahnev, I. Comparative Analysis of Single, Twisted and Sirospun Cotton. In Proceedings of the 12th World Textile Conference (AUTEX), Zadar, Yugoslavia, 13–15 June 2012; ISBN 978-2-7466-2858-8.
20. Schmidt-Emrich, S.; Stiefel, P.; Rupper, P.; Katzenmeier, H.; Amberg, C.; Maniura-Weber, K.; Ren, Q. Rapid assay to assess bacterial adhesion on textiles. *Materials* **2016**, *9*, 249. [CrossRef] [PubMed]
21. Roy, R.; Tiwari, M.; Donelli, G.; Tiwari, V. Strategies for combating bacterial biofilms: A focus on anti-biofilm agents and their mechanisms of action. *Virulence* **2018**, *9*, 522–554. [CrossRef]
22. Staneva, D.; Grabchev, I. *Encyclopedia of Polymer Applications*; CRC Press: Boca Raton, FL, USA, 2018; pp. 2545–2562.
23. Wikler, M.A. *Methods for Dilution Antimicrobial Susceptibility Tests for Bacteria That Grow Aerobically: Approved Standard*, 5th ed.; Clinical and Laboratory Standards Institute: Wayne, PA, USA, 2000.
24. Vaideki, K.; Jayakumar, S.; Rajendran, R.; Thilagavathi, G. Investigation on the effect of RF plasma and neem leaf extract treatment on the surface modification and antimicrobial activity of cotton fabric. *Appl. Surf. Sci.* **2008**, *254*, 2472–2478. [CrossRef]

25. Denny, W.A.; Atwell, G.J.; Baguley, B.C.; Wakelin, L.P.G. The Acridines. *J. Med. Chem.* **1985**, *28*, 1568–1574. [CrossRef] [PubMed]
26. Albert, A. *The Acridines*, 2nd ed.; Edward Arnold Ltd.: London, UK, 1966.
27. Aaron, J.J.; Maafi, M.; Párkányi, C.; Boniface, C. Quantitative treatment of the solvent effects on the electronic absorption and fluorescence spectra of acridines and phenazines. The ground and first excited singlet-state dipole moments. *Spectrochim. Acta A* **1995**, *51*, 603–615. [CrossRef]
28. Ebead, Y.; Roshal, A.D.; Wróblewska, A.; Doroshenko, A.O.; Błażejowski, J. Tautomerism of acridin-9-amines substituted at the exocyclic nitrogen atom: Spectroscopic investigations and theoretical studies. *Spectrochim. Acta A* **2007**, *66*, 1016–1023. [CrossRef] [PubMed]
29. Said, A.; Karaky, K.; Chreim, Y.; Brown, R.; Blanc, S.; Lacombe, S.; Save, M.; Billon, L. From solutions to porous film: Influence of the media on fluorescent acridine endcapped polystyrene photophysic properties. *Mater. Today Commun.* **2015**, *3*, 27–35. [CrossRef]
30. Medel, S.; Martínez-Campos, E.; Acitores, D.; Vasileva-Tonkova, E.; Grabchev, I.; Bosch, P. Synthesis and spectroscopic properties of a new fluorescent acridine hyperbranched polymer: Applications to acid sensing and as antimicrobial agent. *Eur. Polym. J.* **2018**, *102*, 19–29. [CrossRef]
31. Peisach, J.; Blumberg, W.E. Structural implications derived from the analysis of electron paramagnetic resonance spectra of natural and artificial copper proteins. *Arch. Biochem. Biophys.* **1974**, *165*, 691–708. [CrossRef]
32. Grabchev, I.; Bosch, P.; McKenna, M.; Nedelcheva, A. Synthesis and spectral properties of new green fluorescent poly(propyleneimine) dendrimers modified with 1,8-naphthalimide as sensors for metal cations. *Polymer* **2007**, *48*, 6755–6762. [CrossRef]
33. Staneva, D.; Grabchev, I. Heterogeneous sensors for ammonia, amines and metal ions based on a dendrimer modified fluorescent viscose fabric. *Dyes Pigments* **2018**, *155*, 164–170. [CrossRef]
34. Russell, A.D. Similarities and differences in the responses of microorganisms to biocides. *J. Antimicrob. Chemother.* **2003**, *52*, 750–763. [CrossRef]
35. Elshaarawy, R.F.; Janiak, C. Antibacterial susceptibility of new copper (II) N-pyruvoyl anthranilate complexes against marine bacterial strains–In search of new antibiofouling candidate. *Arabian J. Chem.* **2016**, *9*, 825–834. [CrossRef]
36. Holetz, F.B.; Pessini, G.L.; Sanches, N.R.; Cortez, D.A.; Nakamura, C.V.; Filho, B.P.D. Screening of some plants used in the Brazilian folk medicine for the treatment of infectious diseases. *Mem. I. Oswaldo Cruz* **2002**, *97*, 1027–1031. [CrossRef] [PubMed]
37. Adlhart, C.; Verran, J.; Azevedo, N.F.; Olmez, H.; Keinänen-Toivola, M.M.; Gouveia, I.; Melo, L.F.; Crijns, F.J. Surface modifications for antimicrobial effects in the healthcare setting: A critical overview. *Hosp. Infect.* **2018**, *99*, 239–249. [CrossRef] [PubMed]
38. Rasamiravaka, T.; Labtani, Q.; Duez, P.; El Jaziri, M. The formation of biofilms by *Pseudomonas aeruginosa*: A review of the natural and synthetic compounds interfering with control mechanisms. *BioMed. Res. Int.* **2015**, *2015*, 759348. [CrossRef] [PubMed]

materials

MDPI

Communication

Hierarchical Composite Meshes of Electrospun PS Microfibers with PA6 Nanofibers for Regenerative Medicine

Zuzanna J. Krysiak, Małgorzata Z. Gawlik, Joanna Knapczyk-Korczak, Łukasz Kaniuk and Urszula Stachewicz *

International Center of Electron Microscopy for Material Science, Faculty of Metals Engineering and Industrial Computer Science, AGH University of Science and Technology, 30-059 Cracow, Poland; krysiak@agh.edu.pl (Z.J.K.); mg.gawlik@gmail.com (M.Z.G.); jknapczyk@agh.edu.pl (J.K.-K.); kaniuk@agh.edu.pl (Ł.K.)

* Correspondence: ustachew@agh.edu.pl; Tel.: +48-12-617-5230

Received: 30 March 2020; Accepted: 21 April 2020; Published: 23 April 2020

Abstract: One of the most frequently applied polymers in regenerative medicine is polystyrene (PS), which is commonly used as a flat surface and requires surface modifications for cell culture study. Here, hierarchical composite meshes were fabricated via electrospinning PS with nylon 6 (PA6) to obtain enhanced cell proliferation, development, and integration with nondegradable polymer fibers. The biomimetic approach of designed meshes was verified with a scanning electron microscope (SEM) and MTS assay up to 7 days of cell culture. In particular, adding PA6 nanofibers changes the fibroblast attachment to meshes and their development, which can be observed by cell flattening, filopodia formation, and spreading. The proposed single-step manufacturing of meshes controlled the surface properties and roughness of produced composites, allowing governing cell behavior. Within this study, we show the alternative engineering of nondegradable meshes without post-treatment steps, which can be used in various applications in regenerative medicine.

Keywords: polystyrene; nylon 6; electrospun fibers; composite mesh; proliferation; roughness

1. Introduction

The vastly growing field of regenerative medicine is continuously looking for new materials and novel ways to improve currently used materials for cell culture studies. Many studies showed the importance of cells–materials interactions and how to modify the surface to enhance cell adhesion and proliferation, which are responsible for tissue growth [1–3]. In regenerative medicine, one of the most frequently used polymers is polystyrene (PS), which is hydrophobic and thus, often, its surface needs modification by entering hydroxyl groups to achieve hydrophilic behavior [4]. This modified PS is a so-called tissue culture polystyrene (TCPS) that enables easy cell attachment and proliferation. Therefore, it is widely used in cell culture experiments in the form of a flat surface [5,6]. Films, which are 2D structures, are mostly applied for in vitro tests, whereas for tissue engineering, 3D porous constructs are more preferable for cell development. A variety of methods can be applied for 3D meshes manufacturing [7]. Those produced via electrospinning have a structure with high porosity and a high surface area to volume ratio [8,9]. The porosity can be controlled via fiber size governed by electrospinning parameters, as well as the application of various collectors [10]. This technique allows the fabrication of both random and aligned fibers for different applications with a wide range of sizes from nano to micrometers, which influence different cell behavior on manufactured material [7,11–13]. Aligned fibers fabricated via electrospinning were applied to build the ligament tissue based on the hierarchical structure [14]. A combination of nano with micro electrospun fibers in the scaffold was

found to be a promising material for bone tissue regeneration [15]. A two-nozzle electrospinning set-up [16] can be used to obtain composite structures [17] made of nano and microfibers [18].

Polyamides are commercially used as surgical struts [19], in many cardiovascular applications [20], and also for the production of artificial tendons, ligaments, joints [21] and inguinal meshes [22]. PS with nylon 6 (PA6) is known for its high mechanical strength, biocompatibility, flexibility, and similarity to the peptides concerning amide bonds. Electrospun PA6 fibers were blended with other polymer fibers [23,24], which resulted in increased cell proliferation [25,26] applied in the wound and burn treatment [27]. Additionally, the wetting behavior of PA6 fibers can be controlled via electrospinning itself [28,29], and the wetting properties of a material are crucial factors in biomedical applications. Both the chemistry in the meaning of hydrophobicity or hydrophilicity and roughness influence surface wettability [30,31].

PS is mostly used for in vitro studies [4,5,32], but without any surface modification, for example, sliver negative ion implementation [33], protein absorption [34], or plasma treatment [35,36], does not enhance cell development. PS fibers have been already combined with PA6 fibers [37] in the fog collector's meshes, comparing fiber diameter, roughness, contact angle, and the showing mechanical properties of PS, PA6, and PS-PA6 mats of maximum stress 0.03, 1.24 and 0.07 MPa, respectively [38]. Similar designs of nondegradable polymers have the potential to be used in vascular tissue engineering [39] or hernia meshes [40,41]. Moreover, electrospinning was often used to produce highly porous materials with controlled morphology and mechanical properties for vascular grafts [42].

Therefore, the goal of this study was to electrospin hierarchical constructs containing PS in the form of microfibers with the addition of hydrophilic PA6 nanofibers to produce 3D structures. To fabricate our meshes, we applied a two-nozzle system to electrospun both polymers at the same time, aiming towards the biomimetic extracellular matrix (ECM) in terms of wetting and roughness [43]. Importantly, we showed that the chemical or oxidation modifications of hydrophobic PS modification can be replaced by adding hydrophilic PA6 nanofibers into meshes. The engineered hierarchical and fibers-based composite meshes can be applied in regenerative medicine to control cell behavior and to firmly integrate with living tissue.

2. Materials and Methods

2.1. Solutions Preparation

Prior to the solution's preparation, polymers were dried in an oven (SLN32STD, POL-EKO-APARATURA sp.j., Wodzisław Śląski, Poland) for 3 h at T = 30 °C. PS (Sigma Aldrich, Gillingham, UK, Mw = 350,000 g·mol^{-1}) was dissolved in dimethylformamide (DMF, 99.8%, POCH, Gliwice, Poland) at a concentration of 25 wt%, PA6 (BASF, Ludwigshafen, Germany, Mw = 24,000 g·mol^{-1}) was dissolved in formic acid (85%, POCH, Gliwice, Poland), and acetic acids (99.5%, POCH, Gliwice, Poland) mixed in a volume ratio of 1:1 at 12 wt%. Both solutions were stirred at 500 rpm for 4 h at 20 °C (IKA RCT basic, Staufen, Germany). The concentration of the polymer solution was adjusted according to the molecular weight of the polymer to obtain suitable viscosity, allowing it to produce beadles' fibers.

2.2. Electrospinning and Meshes Characterization

Fibers were electrospun using a set-up with the climate-controlled chamber (IME Technologies, Waalre, The Netherlands) at T = 25 °C and H = 40%, then deposited on the slowly rotating (10 rpm) collector covered with an Al foil; see the schematic in Figure 1. Three different fiber mats were produced: PS, PA6, and PS-PA6. For the first two mats, only one nozzle was used. High voltage with positive voltage polarity in the range of 13–20 kV was applied to the needle kept at a distance of 15–22 cm from the collector, with all the other parameters listed in Table 1. The quality of the electrospun fibers was analyzed with the scanning electron microscope (SEM, Merlin Gemini II, Zeiss, Oberkochen, Germany) after the samples were sputtered with gold (Q150RS, Quorum Technologies, Laughton, UK). The diameters of the fibers were measured using ImageJ (v1.51s, USA), and the average fiber diameter was calculated from 100 measurements in the SEM images. Additionally, the contact

angles were measured on the electrospun mats using deionized water. Pictures of water droplets were taken with a Canon EOS 700D camera (Tokyo, Japan) with an EF-S 60 mm f/2.8 Macro USM zoom lens 3 s after placing the 3-μL droplets on the mats. The contact angles were measured using MB-Ruler (version 5.3, Germany) based on the sessile drop method and the mean value was calculated as the average of 10 droplets. The roughness of the electrospun samples was analyzed in our previous reports [38], where a laser microscope (Olympus OLS4000, Tokyo, Japan) was used. Prior to the roughness analysis, the electrospun samples were deposited on glass slides and covered with the 5-nm gold layer. Ten measurements per sample type were performed, with the investigated area of 646×646 μm^2 for PS and PS-PA6 composites, and 130×130 μm^2 for PA6.

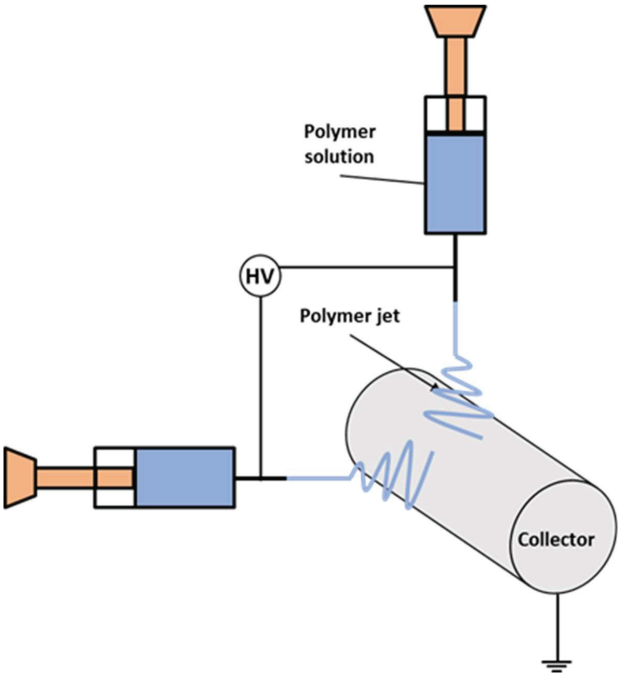

Figure 1. The electrospinning set-up consisting of two nozzles to produce polystyrene (PS) and PS with nylon 6 (PA6) fibers at the same time to obtain the composite meshes.

Table 1. Electrospinning parameters of PS, PA6, and with two nozzles spinning at the same time to produce PS-PA6 composite meshes.

Polymer	Voltage Applied to the Needle (kV)	Voltage Applied to the Collector (kV)	Distance Between Needle and Collector (cm)	Flow Rate (mL·h^{-1})
PS	13	0	15	1.5
PA6	18	−2	15	0.2
PS-PA6	20	0	22/17	1.8/0.1

2.3. Cell Culture Studies

NIH 3T3 murine fibroblast cells (Sigma Aldrich, Gillingham, UK) were used for proliferation and adhesion assay on the meshes sterilized with UV light. Cells were seeded on PS, PA6, and PS-PA6 composite fibers, and on the bottom of a 24-well plate (TCPS) as a reference, with a concentration of 2×10^4 cells per sample. Samples with cells were incubated at H = 90%, T = 37 °C, and CO_2 set

to 5% up to 7 days. Cell proliferation and adhesion assays were performed using MTS (CellTiter 96®® AQueous One Solution Cell Proliferation Assay, MTS, Promega, Madison, WI, USA). The cell morphology was examined with SEM. NIH 3T3 cells were cultured in Dulbecco's Modified Eagle Medium (DMEM with 4.5 g/L D-Glucose, Gibco, Paisley, UK), supplemented with 10% of Fetal Bovine Serum (FBS, Sigma Aldrich, St. Louis, MO, USA), 1% of L-Glutamine solution (Sigma Aldrich, St. Louis, MO, USA), 2% of antibiotics (Penicillin-Streptomycin, Sigma Aldrich, St. Louis, MO, USA), and 1% of amino acids (Mem non-essential Amino Acid solution 100x, Sigma Aldrich, St. Louis, MO, USA). The medium was changed three times a week.

2.3.1. Adhesion Test

Adhesion assay was performed 1.5, 2, and 4 h after cell seeding. Samples were washed with PBS prior to MTS reagent, added to rinse unattached cells. Next, 80 µL MTS reagent and 400 µL of fresh cell culture medium were added to each sample and reference. It was incubated for 4 h at 37 °C, H = 90% and a CO_2 concentration of 5%. After that time, 100 µL of the reaction solution from every sample was transferred to a 96-well plate in triplicates. The absorbance at a wavelength of 490 nm was measured using a Microplate Reader (LT-4000, Labtech, Aylesbury, UK).

2.3.2. MTS Proliferation Assay

Proliferation was assessed after 1, 3, and 7 days of fibroblast culture. After each time point, the culture medium was removed, and meshes were transferred to the new 24-well plate. Then, 80 µL of MTS reagent and 400 µL of cell culture medium were added, and assay was proceeded as described above. For proliferation assessment with SEM, after the defined time of 1, 3, and 7 days, cell culture samples were transferred to the new 24-well plate and rinsed 3 times with PBS. Next, they were fixed with a 2.5% formaldehyde solution for 2 h at 4 °C. The solution was removed and the samples were again rinsed with PBS solution, then dehydrated using a series of ethanol solutions with the concentrations: 50%, 70%, 96%, and 99.9%. The meshes were left to dry under the hood. Before the SEM observation, the samples were coated with a 5 nm layer of Au.

2.3.3. Statistical Analyses

The statistical analyses were performed using OriginPro (v2019 SR2, OriginLab, USA). Analysis of variance (ANOVA) with a Tukey test was performed with significance at $p < 0.02$. For fiber diameter and contact angle measurement, errors are based on standard deviation calculation.

3. Results and Discussion

3.1. Fibers Characterization

Prior to the cell culture study, the quality and morphology of the produced electrospun fibers were verified with SEM; see Figure 2. The average fiber diameter for PS was 4.62 ± 0.3 µm (Figure 2C) and 0.101 ± 0.018 µm for PA6 (Figure 2D). The size of PS fibers was similar in the fibrous composite. However, the average fiber diameter of PA6 fibers was increased to 0.145 ± 0.030 µm, due to the slight adjustment of the electrospinning parameters; see Table 1 and Figure 2G,H, as previously described [44]. The water contact angle measurement confirmed PA6 hydrophilicity (45.9 ± 4.9°) and PS (139.7 ± 4.7°) hydrophobicity and also showed the hydrophobic character of produced composite (132.8 ± 3.5°); see Figure 2. According to the previous study, the larger the average fiber diameter, the higher the surface roughness (R_a), which reached 15.535 ± 2.197 µm for PS, 0.205 ± 0.222 µm for PA6, and 8.848 ± 0.960 µm for PS-PA6 [38]. Additionally, R_a strongly influences the wetting behavior of electrospun membranes [31]. Here, the hydrophobic character was obtained for PS-PA6 composite mesh mainly due to the roughness effect [44], and the water droplets still kept the contact points with PS fibers. The presence of PS and PA6 fibers was already confirmed by the X-ray photoelectron microscopy analysis (XPS) reported in our studies previously [38], where also the roughness and water contact angle were investigated according

to PA6 content. Based on the reported data in [38], the increased PA6 fraction of nanofibers that usually forms a compact layer of membrane lowers the surface roughness once combined with PS microfibers. The increase in PA6 nanofibers fraction, controlled with a longer electrospinning time, decreased the roughness and water contact angle only slightly. Importantly, the PA6 meshes are characterized by relatively small pore sizes of 1.7 µm, and a very high porosity of 96% in meshes [45]. In addition to the morphology, the mechanical properties of manufactured PS-PA6 hierarchical composite meshes were also investigated in various configurations, showing higher tensile stress for PA6 (1.24 MPa) than for PS (0.3 MPa) fibers. The incorporation of PA6 fibers into PS meshes significantly improved the mechanical properties of composite meshes reaching 0.6 MPa [38].

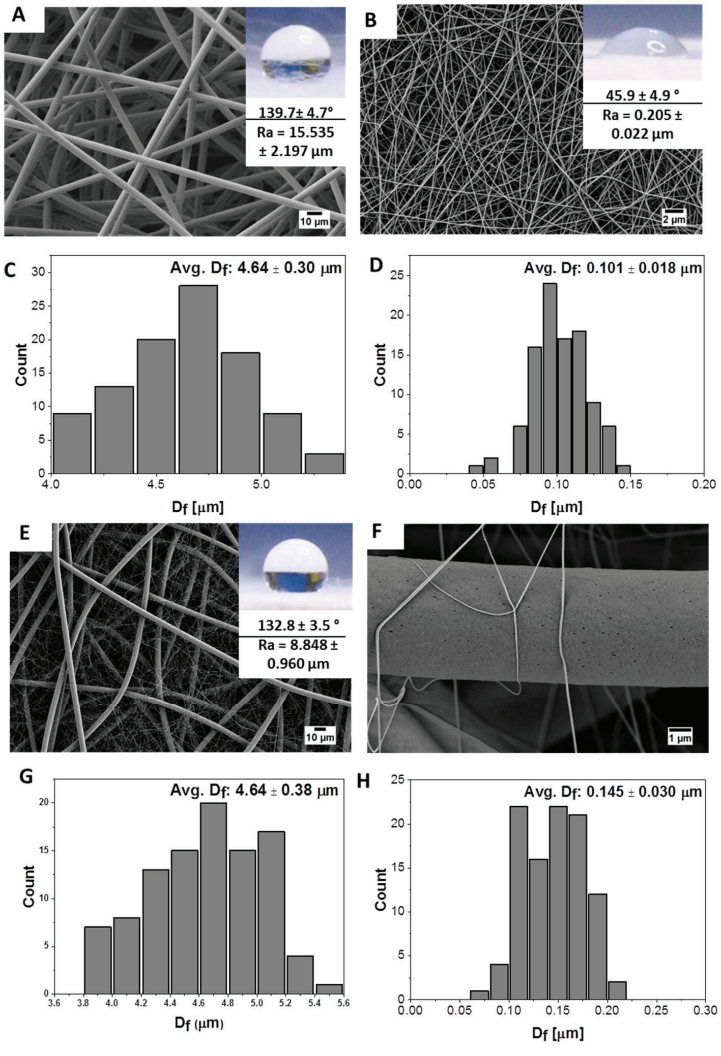

Figure 2. SEM micrographs of electrospun fibers of (**A**) PS, (**B**) PA6, (**E**) PS-PA6 composites, and (**F**) PS-PA6 composite with the higher magnification showing a few PA6 nanofibers on the individual PS microfiber. The fiber diameter distribution showed in histograms for (**C**) -PS; (**D**) -PA6, (**G**) -PS in the composite, and (**H**) -PA6 in the composite meshes.

3.2. Cell Culture Study

The SEM micrographs of fibroblast on electrospun fibers and composites shown in Figure 3 indicate a clear difference in cell behavior on the three types of tested meshes. After one day of incubation, cells started to attach to the fibers, but still kept spherical shapes (Figure 3A,D,G). The cells on the PS mats did not flatten even after 7 days of culturing (Figure 3C), in contrast to PA6 nanofibers and PS-PA6 composite meshes, where cells clearly started already spreading on the fibers after the third day. The cells' attachment and spreading prove their integration with the mesh [15,46]. Importantly, by incorporating PA6 nanofibers to PS fibers, we decreased the surface roughness of meshes significantly, as the PA6 fibers were 100 nm in diameter [44]. Fibroblasts prefer a lower surface roughness [43,47] for spreading and migration [48]. Additionally, the hydrophilic character of PA6 fibers leads to evident cell spreading and attachment, causing further enhanced cell development [30,31]. The SEM observations, shown in Figure 3 prove that PS-PA6 composite meshes were enhancing cell flattening and proliferation.

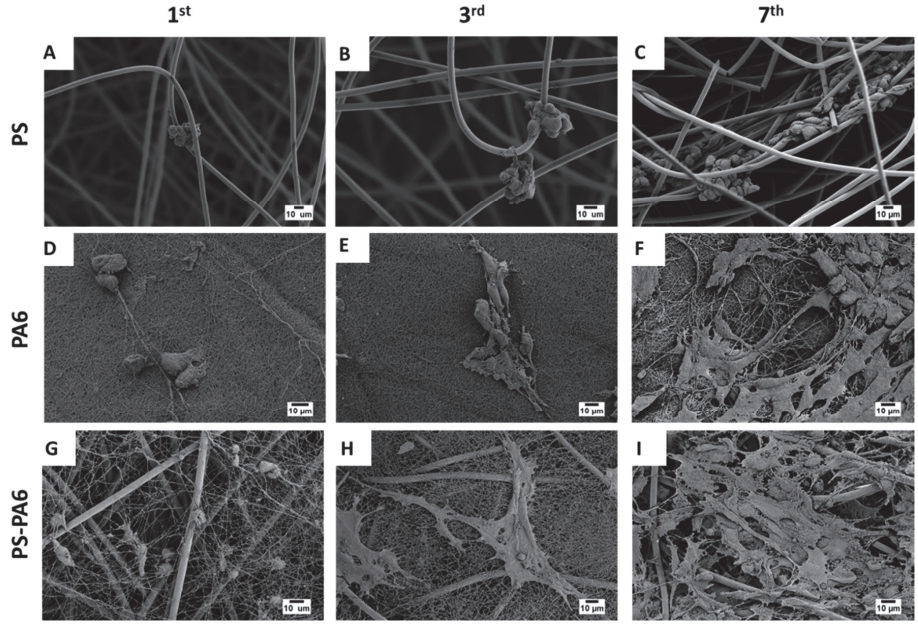

Figure 3. SEM micrographs showing fibroblasts growth on electrospun fiber after the 1st, 3rd, and 7th day in cell culture on (**A**–**C**) PS meshes, (**D**–**F**) PA6 meshes and (**G**–**I**) PS-PA6 composite meshes, respectively.

The surface properties of meshes are essential for cell attachment. In the first few hours, the process of cell anchoring already begins, leading to further cell development and proliferation [49–51]. The adhesion test performed during the first 4 h of cell culture indicates no significant difference in cell attachment between all fibrous meshes and TCPS, see Figure 4A. Interestingly, cell geometry and attachment to PS, PA6, and PS-PA6 composite varied. In Figure 5, we show the SEM images focused on cell filopodia anchoring to fibers. Additionally, the shape of the created filopodia and the cell flattening were different between the three types of samples. The cells kept the round shape on PS fibers (Figure 5A) and PA6 nanofibers, but PS-PA6 composites were flattened (Figure 5B,C). Moreover, the changes in filopodia's morphology defined totally different cells spreading, which is crucial for tissue regeneration and biomaterials integration with the living system. The further proliferation assay in Figure 4B shows no differences between materials after 1 day of cell culture. However, after the third day, the absorbance

values started to increase for PA6, especially for the PS-PA6 composite, which continued up to the seventh day. The MTS test for PS meshes was close to constant over one-week of cell culture, indicating that the cell proliferation was only kept at a minimal level. Importantly, after 7 days, the number of cells on PS-PA6 composite meshes was greater than on any other tested samples and TCPS (Figure 4B). Even though the statistical analysis showed differences between materials after the same period, SEM images of cells also have to be taken into consideration to conclude which material has the most suitable properties for cell proliferation. It was previously shown that decreasing the surface roughness and hydrophobicity enhances cell proliferation [52]. In our study, the incorporation of PA6 nano-sized fibers into PS fibers decreased the roughness by half $R_{a,}$ and only slightly decreased the water contact angle values; see Figure 2. However, cell proliferation was visibly higher, as presented in Figure 4B. Indeed, the decreased R_a and hydrophilic character of PA6 fibers enhanced cell proliferation. As Ansleme et al. described, the short-term adhesion and proliferation were more influenced by surface chemistry, while surface roughness affects long-term behavior [31]. We noticed a better adhesion for more hydrophilic materials, such as PA6 meshes or TCPS. The PS-PA6 composite meshes were characterized by a water contact angle above 130°, thus showing that hydrophobic behavior does not have a straightening effect. Noticeably, by adding PA6 to meshes, we also changed the surface chemistry by including the oxygen groups that were eventually detected by XPS [38]. This type of surface with increased oxygen content is preferable for cell adhesion [31]. Indeed, after one week of cell culture, the R_a decreased by half for PS-PA6 composite meshes in comparison to PS showed the highest value of absorbance for cell proliferation. Interestingly, the size of PS fibers in order of magnitude was higher than for PA6, with increased cell penetration into meshes and growth inside them, whereas in just PA6 meshes, the small distances between nanofibers were limiting cells to the top surface of the samples. The increase of PA6 fraction decrees the spacing between fibers as the smaller fiber diameter in electrospun random meshes cause the smaller distance between fibers [53]. The fiber diameters also control the roughness of meshes [44]. Therefore, the content of PA6 nanofibers was selected not to limit the cell's integration with electrospun meshes. We showed previously on PMMA nanofibers, microfibers, ribbons, and films how the cell morphology is changing according to the surface topography. A diameter of fiber exceeding 3.5 μm is required to provide enough spacing for cell migration into the 3D meshes and enhance the filopodia attachments to fibers underneath [53]. The increased fraction of nanofibers facilitates more cell spreading on the top of the surface in comparison to the microfibers; therefore, in our PS-PA6 hierarchical scaffolds, the layering electrospinning providing a higher number of PA6 fibers were not investigated in vitro in this study.

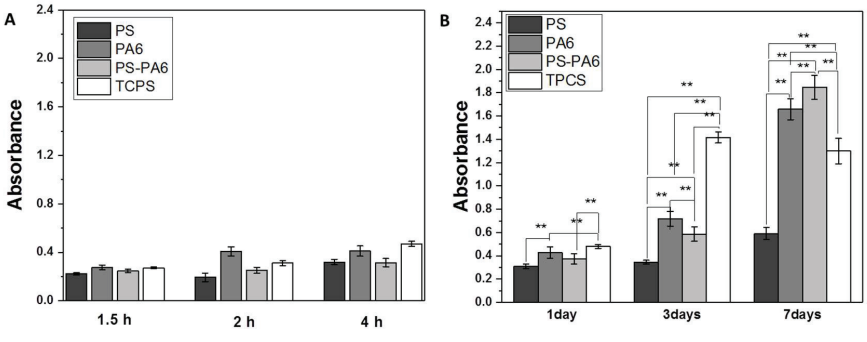

Figure 4. Cell culture study on electrospun PS, PA6 and PS-PA6 composite meshes showing (**A**) the adhesion test: 1.5 h, 2 h, and 4 h and (**B**) proliferation assay after 1, 3 and 7 days after cell seeding. ** statistical significance calculated with ANOVA, followed by Tukey's post-hoc test, $p < 0.02$, error bars are based on standard deviation.

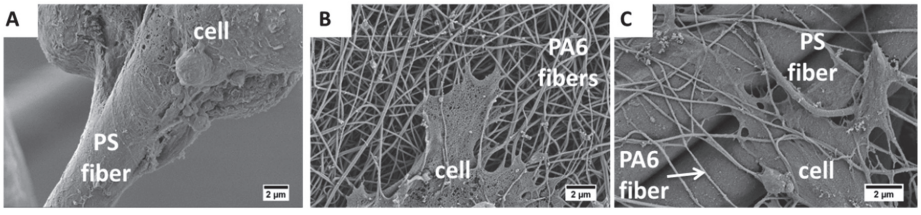

Figure 5. SEM micrographs focused on cell–fiber attachment after the 3rd day of cell culture on (**A**) PS microfibers; (**B**) PA6 nanofibers and (**C**) hierarchical PS-PA6 composite meshes.

4. Conclusions

Within this study, we were able to fabricate a hierarchically structured composite consisting of PS microfibers and PA6 nanofibers using a two-nozzle electrospinning set-up in the single-step manufacturing method. We showed that controlling the surface morphology, chemistry, and roughness of composite meshes guided fibroblasts behavior and development. The filopodia formation and their further proliferation were affected by the size of fibers. The micronized PS fibers allowed deeper penetration of cells, allowing enhanced material integration with the living systems. Moreover, nanosized PA6 fibers with hydrophilic wetting behavior by itself promoted cell development and spreading, despite the fact that the obtained composites were, in general, hydrophobic. Manipulating the rate of PA6 nanofibers in the PS network of fibers allows us to tailor mechanical properties [37] and roughness of meshes [38], thus designing the environment for desired cell types [30,39]. The proposed combination of polymers and its structure is leading to multiple application strategies of nondegradable meshes supporting tissue in regenerative medicine.

In summary, we introduced a novel way to produce PS-PA6 composite meshes in a single-step manufacturing method to enhance cell proliferation and development. These nondegradable polymer composite meshes are able to create a favorable environment for cells reminding ECM with a perspective use in regenerative medicine and for in vitro studies of disease models as 3D constructs.

Author Contributions: Conceptualization, U.S.; methodology, J.K.-K., Z.J.K and U.S.; validation, U.S. and Z.J.K.; formal analysis, Z.J.K. and M.Z.G.; investigation, Z.J.K., J.K.-K., M.Z.G. and Ł.K.; resources, U.S.; data curation, Z.J.K., M.Z.G. and U.S.; writing—original draft preparation, Z.J.K. and U.S.; writing—review and editing, Z.J.K. and U.S.; visualization, Z.J.K., M.Z.G. and U.S.; supervision, U.S.; project administration, U.S.; funding acquisition, U.S. All authors have read and agreed to the published version of the manuscript.

Funding: This research was part of the "Nanofiber-based sponges for atopic skin treatment" project carried out within the First TEAM program of the Foundation for Polish Science co-financed by the European Union under the European Regional Development Fund, project no POIR.04.04.00-00- 4571/18-00 and supported by the infrastructure at International Centre of Electron Microscopy for Materials Science (IC-EM) at AGH University of Science and Technology. Joanna Knapczyk-Korczak thanks Sonata Bis 5 project, No 2015/18/E/ST5/00230 for PhD scholarship.

Conflicts of Interest: The authors declare no conflict of interest.

References

1. Kooten, T.G.; Spijker, H.T.; Busscher, H.J. Plasma-treated polystyrene surfaces: Model surfaces for studying cell–biomaterial interactions. *Biomaterials* **2004**, *25*, 1735–1747. [CrossRef] [PubMed]
2. Szewczyk, P.; Metwally, S.; Karbowniczek, J.E.; Marzec, M.M.; Stodolak-Zych, E.; Gruszczynski, A.; Bernasik, A.; Stachewicz, U.; Stodolak, E. Surface-Potential-Controlled Cell Proliferation and Collagen Mineralization on Electrospun Polyvinylidene Fluoride (PVDF) Fiber Scaffolds for Bone Regeneration. *ACS Biomater. Sci. Eng.* **2018**, *5*, 582–593. [CrossRef]
3. Metwally, S.; Karbowniczek, J.; Szewczyk, P.; Marzec, M.M.; Gruszczyński, A.; Bernasik, A.; Stachewicz, U. Single-Step Approach to Tailor Surface Chemistry and Potential on Electrospun PCL Fibers for Tissue Engineering Application. *Adv. Mater. Interfaces* **2018**, *6*, 1–12. [CrossRef]

4. Curtis, A.S.; Forrester, J.V.; McInnes, C.; Lawrie, F. Adhesion of cells to polystyrene surfaces. *J. Cell Boil.* **1983**, *97*, 1500–1506. [CrossRef]
5. Steele, J.G.; Dalton, B.A.; Johnson, G.; Underwood, P.A. Polystyrene chemistry affects vitronectin activity: An explanation for cell attachment to tissue culture polystyrene but not to unmodified polystyrene. *J. Biomed. Mater. Res.* **1993**, *27*, 927–940. [CrossRef]
6. Baker, S.; Atkin, N.; Gunning, P.A.; Granville, N.; Wilson, K.; Wilson, D.; Southgate, J. Characterisation of electrospun polystyrene scaffolds for three-dimensional in vitro biological studies. *Biomaterials* **2006**, *27*, 3136–3146. [CrossRef]
7. Simonet, M.; Schneider, O.D.; Neuenschwander, P.; Stark, W.J. Ultraporous 3D polymer meshes by low-temperature electrospinning: Use of ice crystals as a removable void template. *Polym. Eng. Sci.* **2007**, *47*, 2020–2026. [CrossRef]
8. Ma, P.X. Biomimetic materials for tissue engineering. *Adv. Drug Deliv. Rev.* **2007**, *60*, 184–198. [CrossRef]
9. Stachewicz, U.; Szewczyk, P.; Kruk, A.; Barber, A.H.; Czyrska-Filemonowicz, A. Pore shape and size dependence on cell growth into electrospun fiber scaffolds for tissue engineering: 2D and 3D analyses using SEM and FIB-SEM tomography. *Mater. Sci. Eng. C* **2019**, *95*, 397–408. [CrossRef]
10. Pham, Q.P.; Sharma, U.; Mikos, A.G. Electrospinning of Polymeric Nanofibers for Tissue Engineering Applications: A Review. *Tissue Eng.* **2006**, *12*, 1197–1211. [CrossRef]
11. Li, X.; Wang, X.; Yao, D.; Jiang, J.; Guo, X.; Gao, Y.; Li, Q.; Shen, C. Effects of aligned and random fibers with different diameter on cell behaviors. *Colloids Surfaces B Biointerfaces* **2018**, *171*, 461–467. [CrossRef] [PubMed]
12. Stachewicz, U.; Qiao, T.; Rawlinson, S.; Almeida, F.; Li, W.; Cattell, M.J.; Barber, A. 3D imaging of cell interactions with electrospun PLGA nanofiber membranes for bone regeneration. *Acta Biomater.* **2015**, *27*, 88–100. [CrossRef] [PubMed]
13. Kaniuk, Ł.; Krysiak, Z.J.; Metwally, S.; Stachewicz, U. Osteoblasts and fibroblasts attachment to poly(3-hydroxybutyric acid-co-3-hydrovaleric acid) (PHBV) film and electrospun scaffolds. *Mater. Sci. Eng. C* **2020**, *110*, 110668. [CrossRef]
14. Sensini, A.; Gualandi, C.; Focarete, M.L.; Belcari, J.; Zucchelli, A.; Boyle, L.; Reilly, G.C.; Kao, A.; Tozzi, G.; Cristofolini, L. Multiscale hierarchical bioresorbable scaffolds for the regeneration of tendons and ligaments. *Biofabrication* **2019**, *11*, 035026. [CrossRef]
15. Tuzlakoglu, K.; Bölgen, N.; Salgado, A.J.; Gomes, M.E.; Pişkin, E.; Reis, R.L. Nano- and micro-fiber combined scaffolds: A new architecture for bone tissue engineering. *J. Mater. Sci. Mater. Electron.* **2005**, *16*, 1099–1104. [CrossRef]
16. Theron, S.; Yarin, A.; Zussman, E.; Kroll, E. Multiple jets in electrospinning: Experiment and modeling. *Polymer* **2005**, *46*, 2889–2899. [CrossRef]
17. Bolbasov, E.N.; Buznik, V.M.; Stankevich, K.S.; Goreninskii, S.I. Composite Materials Obtained via Two-Nozzle Electrospinning from Polycarbonate and Vinylidene Fluoride/Tetrafluoroethylene Copolymer. *Inorg. Mater. Appl. Res.* **2018**, *9*, 184–191. [CrossRef]
18. Zhang, C.; Li, Y.P.; Wang, W.; Zhan, N.; Xiao, N.; Wang, S.; Li, Y.; Yang, Q. A novel two-nozzle electrospinning process for preparing microfiber reinforced pH-sensitive nano-membrane with enhanced mechanical property. *Eur. Polym. J.* **2011**, *47*, 2228–2233. [CrossRef]
19. Karaca, E.; Hockenberger, A.S. Analysis of the fracture morphology of polyamide, polyester, polypropylene, and silk sutures before and after implantationin vivo. *J. Biomed. Mater. Res. Part B Appl. Biomater.* **2008**, *87*, 580–589. [CrossRef]
20. Jaganathan, S.K.; Supriyanto, E.; Murugesan, S.; Balaji, A.; Asokan, M.K. Biomaterials in Cardiovascular Research: Applications and Clinical Implications. *BioMed Res. Int.* **2014**, *2014*, 1–11. [CrossRef]
21. Shen, J.; Li, Y.; Zuo, Y.; Zou, Q.; Cheng, L.; Zhang, L.; Gong, M.; Gao, S. Characterization and cytocompatibility of biphasic calcium phosphate/polyamide 6 scaffolds for bone regeneration. *J. Biomed. Mater. Res. Part B Appl. Biomater.* **2010**, *95*, 330–338. [CrossRef] [PubMed]
22. Wisniewski, N.; Rajamand, N.; Adamsson, U.; Lins, P.E.; Reichert, W.M.; Klitzman, B.; Ungerstedt, U. Analyte flux through chronically implanted subcutaneous polyamide membranes differs in humans and rats. *Am. J. Physiol. Metab.* **2002**, *282*, E1316–E1323. [CrossRef]
23. Panthi, G.; Barakat, N.A.M.; Risal, P.; Yousef, A.; Pant, B.; Unnithan, A.R.; Kim, H.Y. Preparation and Characterization of Nylon-6/Gelatin Composite Nanofibers Via Electrospinning for Biomedical Applications. *Fibers Polym.* **2013**, *14*, 718–723. [CrossRef]

24. Pant, H.R.; Risal, P.; Park, C.H.; Tijing, L.D.; Jeong, Y.J.; Kim, C.S. Core–shell structured electrospun biomimetic composite nanofibers of calcium lactate/nylon-6 for tissue engineering. *Chem. Eng. J.* **2013**, *221*, 90–98. [CrossRef]
25. Pant, H.R.; Kimc, H.J.; Bhatt, L.R.; Joshi, M.K.; Kima, E.K.; Kima, J.I.; Abdal-haya, A.; Hui, K.S.; Kim, C.S. Applied Surface Science Chitin butyrate coated electrospun nylon-6 fibers for biomedical applications. *Appl. Surf. Sci.* **2013**, *285*, 538–544. [CrossRef]
26. Abdal-hay, A.; Khali, K.A.; Al-Jassir, F.F.; Gamal-Eldeen, A.M. Biocompatibility properties of polyamide 6/PCL blends composite textile scaffold using EA. hy926 human endothelial cells. *Biomed. Mater.* **2017**, *12*, 035002. [CrossRef] [PubMed]
27. Winnacker, M. Polyamides and their functionalization: Recent concepts for their applications as biomaterials. *Biomater. Sci.* **2017**, *5*, 1230–1235. [CrossRef]
28. Stachewicz, U.; Stone, C.A.; Willis, C.R.; Barber, A. Charge assisted tailoring of chemical functionality at electrospun nanofiber surfaces. *J. Mater. Chem.* **2012**, *22*, 22935. [CrossRef]
29. Stachewicz, U.; Barber, A. Enhanced Wetting Behavior at Electrospun Polyamide Nanofiber Surfaces. *Langmuir* **2011**, *27*, 3024–3029. [CrossRef]
30. Oliveira, S.; Alves, N.; Mano, J.F. Cell interactions with superhydrophilic and superhydrophobic surfaces. *J. Adhes. Sci. Technol.* **2012**, *28*, 843–863. [CrossRef]
31. Anselme, K.; Ploux, L.; Ponche, A. Cell/Material Interfaces: Influence of Surface Chemistry and Surface Topography on Cell Adhesion. *J. Adhes. Sci. Technol.* **2010**, *24*, 831–852. [CrossRef]
32. Chauvel-Lebret, D.; Pellen-Mussi, P.P.O.; Auroy, P.; Bonnaure-Mallet, M. Evaluation of the in vitro biocompatibility of various elastomers. *Biomaterials* **1999**, *20*, 291–299. [CrossRef]
33. Tsuji, H.; Satoh, H.; Ikeda, S.; Ikemoto, N.; Gotoh, Y.; Ishikawa, J. Surface modification by silver-negative-ion implantation for controlling cell-adhesion properties of polystyrene. *Surf. Coatings Technol.* **1998**, *103*, 124–128. [CrossRef]
34. Shen, M.; Horbett, T.A. The effects of surface chemistry and adsorbed proteins on monocyte / macrophage adhesion to chemically modified polystyrene surfaces. *J. Biomed. Res.* **2001**, *57*, 336–345. [CrossRef]
35. Dowling, D.P.; Miller, I.; Ardhaoui, M.; Gallagher, W.M. Effect of Surface Wettability and Topography on the Adhesion of Osteosarcoma Cells on Plasma-modified Polystyrene. *J. Biomater. Appl.* **2010**, *26*, 327–347. [CrossRef] [PubMed]
36. Metwally, S.; Stachewicz, U. Surface potential and charges impact on cell responses on biomaterials interfaces for medical applications. *Mater. Sci. Eng. C* **2019**, *104*, 109883. [CrossRef]
37. Yoon, J.W.; Park, Y.; Kim, J.; Park, C.H. Multi-jet electrospinning of polystyrene/polyamide 6 blend: Thermal and mechanical properties. *Fash. Text.* **2017**, *4*, 1438. [CrossRef]
38. Knapczyk-Korczak, J.; Ura, D.P.; Gajek, M.; Marzec, M.M.; Berent, K.; Bernasik, A.; Chiverton, J.P.; Stachewicz, U. Fiber-Based Composite Meshes with Controlled Mechanical and Wetting Properties for Water Harvesting. *ACS Appl. Mater. Interfaces* **2019**, *12*, 1665–1676. [CrossRef]
39. Lourenço, B.N.; Marchioli, G.; Song, W.; Reis, R.L.; Van Blitterswijk, C.; Karperien, M.; Van Apeldoorn, A.; Mano, J.F. Wettability Influences Cell Behavior on Superhydrophobic Surfaces with Different Topographies. *Biointerphases* **2012**, *7*, 46–11. [CrossRef]
40. Berger, D.; Bientzle, M. Polyvinylidene fluoride: A suitable mesh material for laparoscopic incisional and parastomal hernia repair! *Hernia* **2008**, *13*, 167–172. [CrossRef]
41. Schumpelick, V.; Klinge, U.; Junge, K.; Stumpf, M. Incisional abdominal hernia: The open mesh repair. *Langenbeck's Arch. Surgery* **2004**, *389*, 1–5. [CrossRef] [PubMed]
42. Khan, A.; Shah, M.H.; Nauman, M.; Hakim, I.; Shahid, G.; Niaz, P.; Sethi, H.; Aziz, S.; Arabdin, M. In vitro evaluation of electrospun nanofiber scaffolds for vascular graft application. *J. Pak. Med. Assoc.* **2017**, *67*, 1180–1185. [PubMed]
43. Kunzler, T.P.; Drobek, T.; Schuler, M.; Spencer, N.D. Systematic study of osteoblast and fibroblast response to roughness by means of surface-morphology gradients. *Biomaterials* **2007**, *28*, 2175–2182. [CrossRef] [PubMed]
44. Szewczyk, P.; Ura, D.; Metwally, S.; Knapczyk-Korczak, J.; Gajek, M.; Marzec, M.M.; Bernasik, A.; Stachewicz, U. Roughness and Fiber Fraction Dominated Wetting of Electrospun Fiber-Based Porous Meshes. *Polymers* **2018**, *11*, 34. [CrossRef]

45. Stachewicz, U.; Modaresifar, F.; Bailey, R.J.; Peijs, T.; Barber, A.H. Manufacture of Void-Free Electrospun Polymer Nanofiber Composites with Optimized Mechanical Properties. *ACS Appl. Mater. Interfaces* **2012**, *4*, 2577–2582. [CrossRef]
46. Knight, E.; Przyborski, S.A. Advances in 3D cell culture technologies enabling tissue-like structures to be created in vitro. *J. Anat.* **2014**, *227*, 746–756. [CrossRef]
47. Dalby, M.J.; Riehle, M.; Johnstone, H.; Affrossman, S.; Curtis, A. Polymer-Demixed Nanotopography: Control of Fibroblast Spreading and Proliferation. *Tissue Eng.* **2002**, *8*, 1099–1108. [CrossRef]
48. Oliveira, S.M.; Song, W.; Alves, N.M.; Mano, J.F. Chemical modification of bioinspired superhydrophobic polystyrene surfaces to control cell attachment/proliferation. *Soft Matter* **2011**, *7*, 8932–8941. [CrossRef]
49. Wei, J.; Igarashi, T.; Okumori, N.; Igarashi, T.; Maetani, T.; Liu, B.; Yoshinari, M. Influence of surface wettability on competitive protein adsorption and initial attachment of osteoblasts. *Biomed. Mater.* **2009**, *4*, 45002. [CrossRef]
50. Liu, W.; Zhan, J.; Su, Y.; Wu, T.; Wu, C.; Ramakrishna, S.; Mo, X.; Al-Deyab, S.S.; El-Newehy, M. Biointerfaces Effects of plasma treatment to nanofibers on initial cell adhesion and cell morphology. *Colloids Surf. B Biointerfaces* **2014**, *113*, 101–106. [CrossRef]
51. Chen, M.; Patra, P.K.; Warner, S.B.; Bhowmick, S. Role of Fiber Diameter in Adhesion and Proliferation of NIH 3T3 Fibroblast on Electrospun Polycaprolactone Scaffolds. *Tissue Eng.* **2007**, *13*, 579–587. [CrossRef] [PubMed]
52. Kim, C.H.; Khil, M.S.; Kim, H.Y.; Lee, H.U.; Jahng, K.Y. An improved hydrophilicity via electrospinning for enhanced cell attachment and proliferation. *J. Biomed. Mater. Res. Part B Appl. Biomater.* **2006**, *78*, 283–290. [CrossRef] [PubMed]
53. Ura, D.; Karbowniczek, J.; Szewczyk, P.; Metwally, S.; Kopyściański, M.; Stachewicz, U. Cell Integration with Electrospun PMMA Nanofibers, Microfibers, Ribbons, and Films: A Microscopy Study. *Bioengineering* **2019**, *6*, 41. [CrossRef] [PubMed]

materials

MDPI

Article

Polydopamine Linking Substrate for AMPs: Characterisation and Stability on Ti6Al4V

Zuzanna Trzcińska [1], Marc Bruggeman [1], Hanieh Ijakipour [1], Nikolas J. Hodges [2], James Bowen [3] and Artemis Stamboulis [1,*]

[1] School of Metallurgy and Materials, University of Birmingham, Edgbaston, Birmingham B15 2TT, UK; zutrzcinska@outlook.com (Z.T.); MXB1082@student.bham.ac.uk (M.B.); HXI756@student.bham.ac.uk (H.I.)
[2] School of Biosciences, University of Birmingham, Edgbaston, Birmingham B15 2TT, UK; n.hodges@bham.ac.uk
[3] School of Chemical Engineering, University of Birmingham, Edgbaston, Birmingham B15 2TT, UK; james.bowen@open.ac.uk
* Correspondence: a.stamboulis@bham.ac.uk

Received: 15 May 2020; Accepted: 19 August 2020; Published: 22 August 2020

Abstract: Infections are common complications in joint replacement surgeries. Eradicated infections can lead to implant failure. In this paper, analogues of the peptide KR-12 derived from the human cathelicidin LL-37 were designed, synthesised, and characterised. The designed antimicrobial peptides (AMPs) were attached to the surface of a titanium alloy, Ti6Al4V, by conjugation to a polydopamine linking substrate. The topography of the polydopamine coating was evaluated by electron microscopy and coating thickness measurements were performed with ellipsometry and Atomic Force Microscopy (AFM). The subsequently attached peptide stability was investigated with release profile studies in simulated body fluid, using both fluorescence imaging and High-Performance Liquid Chromatography (HPLC). Finally, the hydrophobicity of the coating was characterised by water contact angle measurements. The designed AMPs were shown to provide long-term bonding to the polydopamine-coated Ti6Al4V surfaces.

Keywords: Ti6Al4V; polydopamine; antimicrobial peptides; cathelicidin; KR-12

1. Introduction

Infection are the most common complications of joint replacement surgery, with nosocomial or hospital-acquired infections ranking as the sixth leading cause of death, presenting a major healthcare challenge [1]. Infection can lead to extended inflammation at the site of the surgery, thus causing the rejection and failure of the implant [2]. Although the administration of antibiotics significantly reduces the risk of postsurgical infections, bacterial biofilm production on the implant surface or untimely administration of antibiotics will reduce their effectiveness [3].

The use of titanium in dental and orthopaedic implants is well established due to titanium's strength, stiffness, and corrosion resistance. Titanium also shows seamless integration with the surrounding tissues due to its excellent biocompatibility [4,5]. The drawback of using titanium implants is their susceptibility to bacterial colonisation on the surfaces of the implants [6]. To combat the formation of biofilms on implant surfaces, the time-controlled release of various antibiotic coatings has previously been investigated [7,8]. However, the release of the antibiotics below the level of the minimum inhibitory concentration (MIC) is known to produce antibiotic-resistant strains of bacteria. Higher levels of antibiotic release have been shown to be toxic to the surrounding tissues. The increase of antibiotic-resistant bacteria has led to the search for an alternative method of antimicrobial protection [9].

Antimicrobial peptides, which are a part of the innate immune system of all living organisms, have broad-spectrum activity against many microorganisms, such as Gram-positive bacteria, Gram-negative

bacteria, viruses, and fungi [10–13]. Moreover, they can inhibit biofilm formation and induce its dissolution, as well as attract phagocytes to further induce natural defence mechanisms [14]. The mechanisms of action of antimicrobial peptides (AMPs) against bacteria are not fully understood due to the high diversity of these peptides. Nevertheless, it is widely accepted that bacterial cell death is due to the interaction of cationic AMPs with negatively charged phospholipids on the bacterial membrane, which lead to the loss of membrane structural integrity, and eventually cell death [10–13]. AMPs exhibit a strong preference for specific membrane compositions, allowing them to be selective towards bacterial cell membranes, but not mammalian or plant cells [14]. Currently, only a few AMPs are used clinically due to limiting factors, such as the high cost of peptide synthesis, their susceptibility to proteolytic degradation, and their unknown long-term toxicology profiles [1,14,15]. Here, analogues of the peptide KR-12 derived from the human cathelicidin LL-37 were designed due to its established antimicrobial activity and lack of mammalian cell toxicity, as originally found by Jacob et al. [16].

To introduce the antimicrobial peptides stably on a surface, different types of coatings can be employed. A popular approach is the use of polydopamine (pDA), a strong adhesive mussel-inspired polymer, due to its low cost, simplicity of application, and improved biocompatibility [17–19]. Similarly to mussel adhesive proteins, the adhesive properties of the pDA are owed to quinine and catechol groups, which create chelating structures with metals. Additionally, after polymerisation, pDA can be further functionalised with amine-containing nucleophiles, such as proteins and peptides. This allows the application of a pDA coating to Ti6Al4V, where the in-house designed analogues of the peptide KR-12 are subsequently covalently bonded to the pDA coating.

2. Materials and Methods

2.1. Peptide Design

The shortest active peptide fragment derived from cathelicidin LL-37, KR12, was used as a template to design three peptides of varying antimicrobial activity. The peptide sequences and various properties are summarised in Table 1.

Table 1. Table showing the used peptides sequences, including their charge, hydrophobicity, and amphiphacity, determined by hydrophobic characteristics. Within the sequences, positively charged residues are marked in blue, the negatively charged in red, and highly hydrophobic sequences are underlined.

Peptide	Sequence	Length of Sequence	Net Charge	Charge Density	Mean Hydrophobicity [H]	Helical Hydrophobic
KR12	KRIVQRIKDFLR	12 aa	+4	0.33	0.193	0.782
KR12/32	KIRVQRIKDFLR	12 aa	+4	0.33	0.193	0.429
KR12-5911	KRIVRIKFR	9 aa	+5	0.56	0.178	0.395
KR12/32-5911	KIRVRIKFR	9 aa	+5	0.56	0.178	0.092

2.2. Peptide Synthesis, Purification

Peptides dyed with carboxyfluorescein (5(6)-FAM) were synthesised in-house following conventional solid-phase peptide synthesis (SPPS). After synthesis, the peptides were purified to show a minimum purity of >95%. Peptides without the dye exhibited a purity of >98% and were purchased from ProteoGenix, Schiltigheim, France. All the amino acids used in SPPS (i.e., Fmoc–Ala–OH, Fmoc–Asp(OtBu)–OH, Fmoc–Glu(OtBu)–OH, Fmoc–Phe–OH, Fmoc–Gly–OH, Fmoc–Ile–OH, Fmoc–Lys(Boc)–OH, Fmoc–Leu–OH, Fmoc–Asn–OH, Fmoc–Gln–OH, Fmoc–Pro–OH, Fmoc–Arg(Pbf)–OH) were purchased from AGTC Bioproducts Ltd., Itlings Lane Hessle, UK, with a purity of >98 % purity, which were side-chain protected where appropriate. Preloaded Wang resin with Fmoc-protected amino acids (Fmoc–Arg(Pbf) Wang, Fmoc–Glu(OtBu) Wang, Fmoc–Lys(Boc)–OH) with peptide substitutions in the range of 0.21–5.3 mmol/g and o-benzotriazole–N,N,N′,N′–tetramethyl–uronium–hexafluoro-phosphate (HBTU) of >98% purity

were purchased from NovaBiochem, Merck Life Science UK Limited, Watford, UK. Anhydrous N,N dimethylformide (DMF), anhydrous dichloromethane (DCM), 5(6)-FAM, piperidine/DMF 20% mix (*v*/*v*), ninhydrin, trifluoroacetic acid (TFA), and triisopropylsilane (TIPS) were all HPLC grade with >99% purity, which were purchased from Sigma Aldrich, Merck Life Science UK Limited, Dorset, UK. Anhydrous diethyl ether of HPLC grade used for precipitation of peptides was purchased from Fisher Scientific UK Ltd., Loughborough, UK. SPPS reactions were carried out in Aldrich® System 45™ vessels with caps and fritted discs purchased from Sigma Aldrich, Merck Life Science UK Limited, Dorset, UK. Acetonitrile and TFA used for peptide purification and for purity analysis with high-pressure liquid chromatography (HPLC) were of HPLC grade and were purchased from Sigma Aldrich, Merck Life Science UK Limited, Dorset, UK.

Once ready for cleavage, the dried Wang resin beads were weighed and transferred from the reaction vessel into a 50 mL round-bottom flask equipped with a magnetic stirrer. A fresh cleavage mixture made of TFA, dH_2O, and TIPS (*v*/*v*/*v* = 95/2.5/2.5) was then prepared and 10 mL per 0.1 g of dried resin beads was added to the Wang resin beads in the round-bottom flask. The flask was then carefully closed and wrapped with aluminium foil to prevent photo-bleaching. The reagents were left to react under gentle and continuous stirring for 3–5 h. Subsequently, the Wang resin beads were removed by vacuum filtration and the peptides were dissolved in the cleavage mixture. The peptides were then precipitated by adding the solution dropwise to ice-cold diethyl ether. To ensure maximum precipitation, the diethyl ether was kept overnight at −20 °C. The precipitate was then separated from the supernatant by centrifugation at 13,500 rpm and air-drying overnight at −20 °C. The dried crude peptide powder was dissolved in dH_2O and then freeze-dried using a LyoDry Midi freeze dryer (MechaTech Systems Ltd., Bristol, UK).

Labelling of the synthesised peptides with the fluorescence dye 5(6)-FAM was performed while the molecules were still attached to the Wang resin. The reaction is similar to the amino acid coupling. A mixture of 5 equiv 5(6)-FAM and 4.9 equiv HBTU dissolved in DMF (≈3 mL) was placed in a reaction vessel containing a known amount of washed Wang resin with a previously deprotected N-terminal peptide sequence. The reaction vessel was wrapped with aluminium foil to prevent photo-bleaching and was placed on an orbital shaker. The reaction mixture was left to react overnight under continuous shaking (≈200 rpm). It was then washed three times with DMF (6 mL) and three times with DCM (6 mL). After the washing procedure, the resin beads were dried under vacuum until all of the DCM was removed.

2.3. Peptide Characterisation

2.3.1. High-Pressure Liquid Chromatography

All peptides were purified with preparative HPLC using a Thermo Scientific Dionex Summit preparative HPLC system (Thermo Fisher Scientific Ltd., Loughborough, UK). Their purity was tested with a Thermo Scientific Dionex Summit analytical HPLC system. Both systems were equipped with C18 columns, water with 0.05% TFA was used as the hydrophilic medium, and acetonitrile with 0.05% TFA was used as the hydrophobic medium. The detection of molecules was conducted by measuring the UV absorbance of the amide bond at a wavelength of 210 nm. For preparative HPLC, a total of 2 mL of crude peptide dissolved in a mixture of acetonitrile and water (*v*/*v* = 1) was injected into the C18 column, while for analytical HPLC 100 µL of a similar peptide solution was added to the C18 column. In both cases, the columns were run for 60 min with a linear gradient of solvents starting at 100% dH_2O and 0% acetonitrile, finishing at 0% water and 100% acetonitrile.

2.3.2. Mass Spectrometry

After purification, acetonitrile was evaporated with the use of a rotary evaporator and the peptides were recovered by freeze-drying. Subsequently, the peptides were analysed on a Waters Micromass LCT TOF spectrometer (Waters UK, Wilmslow, UK) using electrospray ionisation in the School of Chemistry Mass Spectrometry facility. Prior to mass analysis, the peptide samples were dissolved in

water. After the purification of the crude peptides, a purity of ≥95% was achieved and the theoretical mass agreed with the calculated mass displayed in Table 2.

Table 2. Purity and mass analysis of peptides.

Peptide	Theoretical Molecular Weight (g/mol)	Molecular Weight M Measured by MS (g/mol)	Purity Calculated by HPLC (%)
KR12	1572	M = 1574 $[M + 2H]^{2+}$ = 788 $[M + Na + H]^{2+}$ = 799	95
5(6)-FAM-labelled KR12	1904	M = 1903 $[M + 2H]^{2+}$ = 952	95
KR12/32	1572	M = 1572 $[M + 2H]^{2+}$ = 787 $[M + 3H]^{3+}$ = 525	99
5(6)-FAM-labelled KR12/32	1904	M = 1903 $[M + H]^{+}$ = 1904 $[M + 2H]^{2+}$ = 952	95
KR12-5911	1216	M = 1215 $[M + 2H]^{2+}$ = 609	97
5(6)-FAM-labelled KR12-5911	1548	M = 1547 $[M + H]^{+}$ = 1549 $[M + 2H]^{2+}$ = 775	95
KR12/32-5911	1216	M = 1215 $[M + 2H]^{2+}$ = 609	98
5(6)-FAM-labelled KR12/32-5911	1548	M = 1547 $[M + 2H]^{2+}$ = 775	96
KR12	1572	M = 1574 $[M + 2H]^{2+}$ = 788 $[M + Na + H]^{2+}$ = 799	95
5(6)-FAM-labelled KR12	1904	M = 1903 $[M + 2H]^{2+}$ = 952	95

2.3.3. Minimum Inhibitory Concentration (MIC) Values of Peptides

The minimum inhibition concentration (MIC) is used to determine the lowest concentration of antimicrobial agent needed to inhibit the visible growth of a bacteria strain after overnight incubation. All the bacteria strains were kindly provided by Dr Mark Webber of the Quadram Institute Bioscience (Norwich, UK; *Escherichia coli* (*E. coli*, I364), *Pseudomonas aeruginosa* (*P. aeruginosa*, PAO1) and *Staphylococcus aureus* (*S. aureus*, F77/NCTC8532)). Lysogen broth (LB broth) and agar were purchased from Sigma-Aldrich, Merck Life Science UK Limited, Dorset, UK. Fresh LB agar culture plates were prepared by pouring ≈10 mL of an autoclaved warm mixture of LB broth (2.5%) and bacteriological agar (1.5%) dissolved in dH_2O. The agar plate was streaked and incubated overnight at 36 °C. A single bacterial colony was chosen and grown in 5 mL broth overnight under agitation at 36 °C. Subsequently, 50 μL of LB broth was added to wells 2–12 of a 96-well culture plate. AMPs were diluted to a concentration of 256 μg/mL, added to well 1, and diluted two-fold down to column 11. Column 12 was left empty, with no AMPs added. Then, 50 μL of the diluted overnight bacteria culture was added to the wells and incubated at 36 °C for 18 h to allow bacteria to grow. After incubation, the well plates were examined for bacterial growth and the lowest concentration of AMPs where clear liquid was observed was assumed to be the minimum inhibitory concentration. Three measurements for each peptide and against each type of bacteria were performed and the average values were obtained.

2.4. Sample Preparation

Titanium alloy grade 5 (Ti6Al4V) plates with dimensions of 15 cm × 15 cm and a thickness of 0.1 cm were purchased from William Gregor Ltd., London, UK, and cut into 1 cm × 1 cm plates. Then, the plates were mounted in conducting Bakelite and polished to mirror finish. Three steps were used during polishing of the plates. First, Bakelite-mounted Ti6Al4V plates were ground with MD-Piano of 220 grit, with water used as a lubricant. Then, a DiaDuo-2 diamond of 9 μm grain size suspended in water and an MD-Largo polishing plate were used. Finally, a colloidal suspension (OP-S) activated with ammonia solution was used and polished on MD-Chem polishing disc. All the polishing materials and equipment were purchased from Struers Ltd., Rotherham, UK. After polishing the plates to a mirror finish, the highly polished surfaces were secured with electrical tape to prevent the introduction of scratches and Bakelite was broken down to release the mounted Ti6Al4V plates. The tape was then removed from the plates and any impurities introduced on the Ti6Al4V surfaces during the previous steps were removed by cleaning the plates in an ultrasonic bath with water (15 min) and acetone (15 min). The plates were dried overnight in a desiccator and were used within 48 h after cleaning.

Having been cleaned and polished to a mirror finish, Ti6Al4V plates were placed inside a 24-well cell culture plate with the polished side facing upwards. Dopamine, purchased from Sigma-Aldrich, was dissolved to a final concentration of 5 mg/mL in 50 mM Tris buffer (Fisher Scientific UK Ltd., Loughborough, UK) at pH = 8.5. Then, 1.5 mL of dopamine solution was transferred into the cell culture plates containing the Ti6Al4V plates. Subsequently, the prepared plates were placed in the dark for 24 h without a cover to allow simultaneous dopamine polymerisation in air and metallic surface coating. Ti6Al4V plates coated with polydopamine (pDA) were washed to remove any loose pDA particles and placed in a new set of 24-well cell culture plates. The AMP solution was then prepared by dissolving peptides in a concentration equal to the MIC value for each peptide in 50 mM Tris buffer at pH 7.4. Then, 1.5 mL of this solution was transferred into the cell culture plates with the pDA-coated Ti6Al4V plates. The cell culture plates were then kept in the dark without a cover for 24 h to allow conjugation of the peptides with the pDA. Finally, the plates were washed several times with dH_2O to remove unconjugated peptides. The prepared plates were stored in the dark in a desiccator to dry and used within 7 days of preparation.

2.5. Topography of Coating

The topography analysis of the pDA- and AMP-conjugated pDA coatings was performed with a Bruker Icon Atomic Force Microscope (Bruker UK Ltd., Coventry, UK). A silicone probe was passed over the surface of the coatings and its displacement was recorded. This generated a three-dimensional plot of the surface topography. In this research, images were recorded in static mode over a 20 μm × 20 μm area. Ellipsometry was performed on a Jobin-Yvon UVISEL ellipsometer (HORIBA UK Ltd., Northampton, UK) with a xenon light source. First, the light reflection of the uncoated surface of the sample was measured to set the measurement baseline, then the height of the coated surface was measured relative to the baseline.

2.6. Fluorescence Microscopy

Fluorescence microscopy was used to determine the conjugation of AMPs to the pDA with a Leica DM6000B widefield epifluorescence microscope (Leica Microsystems Ltd., Milton Keynes, UK), equipped with a 100 W short-arc epifluorescence mercury burner and a Leica DFL350 FX firewire camera (Leica Microsystems Ltd., Milton Keynes, UK) located at the Institute of Biomedical Research (IBR) in the School of Medicine, University of Birmingham. Measurements were performed with an epifluorescence filter set at an excitation wavelength of 480 nm and a green emission wavelength of 527 nm, corresponding to the green fluorescence associated with 5(6)-FAM. For each sample, a set of five random points were recorded for comparison and the brightness of the green light was analysed using the ImageJ 1.46r analysis program.

2.7. Scanning Electron Microscopy

Imaging of the uncoated and pDA-coated surfaces was performed on a Zeiss Supra 55VP scanning electron microscope (Carl Zeiss Ltd., Zeiss House, Cambridge, UK). All measurements were conducted on samples coated with ≈1 nm of the electrodeposited carbon film. A 10 kV electron beam and various magnifications were used.

2.8. Coating Stability

In order to prepare the simulated body fluid (SBF), sodium chloride (NaCl), sodium bicarbonate ($NaHCO_3$), potassium chloride (KCl), potassium phosphate dibasic trihydrate ($K_2HPO_4{\cdot}3H_2O$), magnesium chloride hexahydrate ($MgCl_2{\cdot}6H_2O$), hydrochloric acid (HCl) 32%, calcium chloride ($CaCl_2$), sodium sulfate (Na_2SO_4), and tris(hydroxymethyl)aminomethane (Tris, $(CH_2OH)_3CNH_2$) were purchased from Sigma Aldrich, Merck Life Science UK Limited, Dorset, UK. The SBF was prepared as described by Kokubo and Takadama [20]. The stability of the AMPs on the surface of Ti6Al4V was performed in SBF by submerging and keeping AMP-coated plates in SBF at 37 °C for a total of 30 days. Analysis of the released AMPs to the solution was performed using two methodologies. Firstly, the change in green light intensity of the pDA Ti6Al4V surfaces coated with 5(6)-FAM-labelled peptides was analysed after 1 and 6 h, then at 1, 3, 7, 14, and 30 days of submersion in SBF, imaged under fluorescence microscopy. Secondly, plates with no labelled peptides were immersed in SBF solution and analysed by HPLC at the same time intervals. However, in this method, 100 μL of the SBF solution was withdrawn to determine the cumulative absorbance at the same retention time for every individual peptide.

2.9. Dynamic Contact Angle Analysis

Hydrophobicity was determined by a dynamic contact angle technique on a Dyne Technology ThetaLite optical tensiometer (Dyne Testing Ltd., Lichfield, UK) located in the Science City Lab at the School of Chemical Engineering, University of Birmingham. Deionised water was used as a liquid medium to perform the contact angle measurements. The measurements were performed by recording the contact and retraction angles of a 5 μL droplet released on and removed from the studied surface. The recording time of each incident was set to 20 s and the camera recorded 10 frames/s. The droplets were released and then removed at a speed of 5 mL/min. All surfaces were kept in a desiccator prior to measurements and were each measured three times.

2.10. Cell Culture Studies

Human osteosarcoma cells (HOS) were purchased from the European Collection of Authenticated Cell Cultures (catalogue number 87070202). Cultured cells were grown in RPMI medium supplemented with 10% *v*/*v* fetal calf serum, 100 U/mL penicillin, 100 μg/mL streptomycin, and 2 mM glutamine as a monolayer in T75 cell culture flasks in a humidified atmosphere (5% CO_2 incubator; 95% air) at 37 °C. Cells were sub-cultured at approximately 80% confluency twice-weekly using a standard trypsin-EDTA protocol. All cell cultures were confirmed as being free from Mycoplasma sp. contamination using the EZ-PCR mycoplasma detection kit according to the manufacturer's instructions (Biological Industries USA, Cromwell, CT, USA). All cells were cultured up to passage 20 before being discarded. Before cell culture, coated surfaces were placed flat with the coated surface facing upwards into a 6-well cell culture dish. Surfaces were sterilised with 2 mL of 70% *v*/*v* ethanol for 30 min. Subsequently, surfaces were washed with sterile phosphate-buffered saline (PBS, 3 × 2 mL). HOS cells (100,000) were added and left to attach for 4 h. The medium was changed and cells were incubated for 5 and 7 days before being prepared for analysis by electron microscopy.

3. Results

3.1. Antimicrobial Characterisation

The MIC values of the peptides KR12, KR12/32, KR12-5911, and KR12/32-5911 against *E. coli*, *P. aeruginosa*, and *S. aureus* are shown in Figure 1 and compared against LL-37 in Table 3. The most effective peptide against *E. coli* was peptide KR12-5911 at 0.5 μM, followed by KR12 at 2 μM, and KR12/32 and KR12/32-5911 at 4 μM. The lowest MIC values against *P. aeruginosa* were observed for peptides KR12 and KR12-5911 at 2 μM, whilst peptides KR12/32 and KR12/32-5911 showed MIC values of 4 μM. For *S. aureus*, the most effective was peptide KR12/32-5911 with an MIC of 2 μM, followed by KR12-5911 and KR12 at 8 μM and KR12/32 at 32 μM. All peptides show similar MIC values against Gram-negative bacteria. Additionally, the peptides were more effective against Gram-negative bacteria when compared to the Gram-positive bacteria, apart from KR12/32-5911.

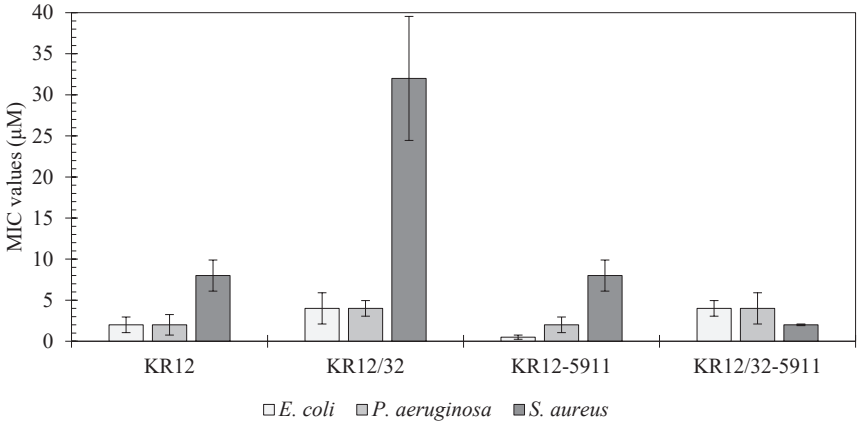

Figure 1. Minimum inhibitory concentration (MIC) values for the designed KR12 analogues.

Table 3. MIC values for the designed KR12 analogues compared to the LL-37 human cathelicidin.

Sequence	MIC Values (μM)			
	***E. coli* (I364)**	***P. aeruginosa* (PAO1)**	***S. aureus* (F77)**	**Geometric Mean**
KR12	2	2	8	4.0
KR12/32	4	4	32	13.33
KR12-5911	0.5	2	8	3.5
KR12/32-5911	4	4	2	3.33
LL-37 [14]	8	8	4	6.67

3.2. Polymerisation of Dopamine

Dissolution of dopamine in the Tris buffer resulted in an immediate colour shift to light brown. As the polymerisation proceeded, the colour became darker until the solution was black, as shown in Figure 2. As can be observed, once the polymerisation took place for 96 h, a film formed between the surface of the liquid and the air, resulting in a different reflection of light. Scanning electron microscopy (SEM) micrographs of the pDA coatings are shown in Figure 3. Figure 3a shows a clear boundary between the uncoated and uniformly coated Ti6Al4V surfaces, while Figure 3b shows the bead-like structure of the polydopamine (pDA) coating. The beads display a circular shape with an average diameter of 86 ± 20 nm. It can be observed that the beads are in fact constructed of clusters of even smaller particles with an average diameter of 10 ± 1 nm. Even though the clusters are densely packed, there are visible inequalities in the shapes of the grooves in between the clusters.

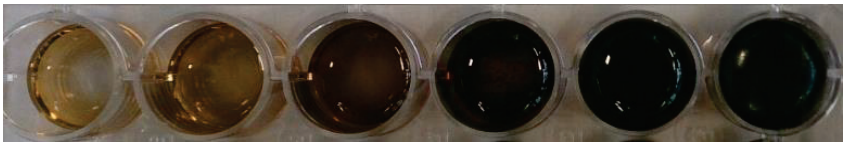

Figure 2. A photograph of s 24-well plate showing the change in colour of the alkaline dopamine solutions over 6 h, 12 h, 24 h, 48 h, 72 h, and 96 h, shown from left to right, respectively.

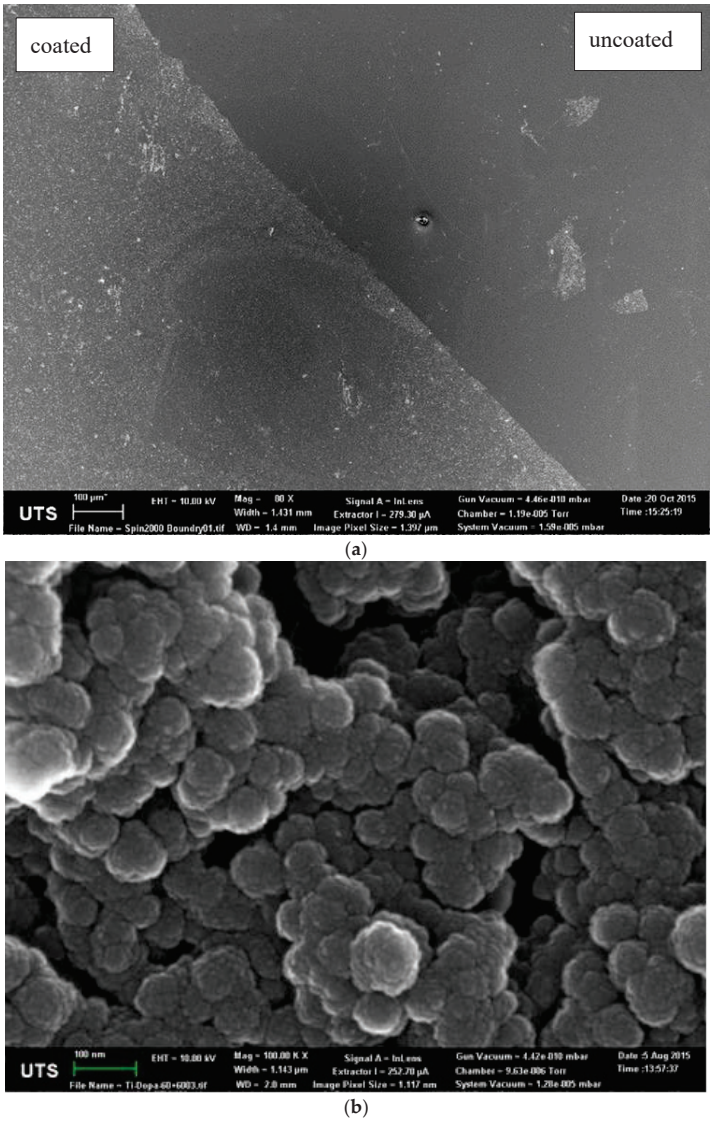

(**a**)

(**b**)

Figure 3. SEM micrographs showing (**a**) the Ti6Al4V surface with a polydopamine (pDA) coating (left) and uncoated (right) at a magnification of 1000×, as well as (**b**) the pDA coating at 100,000× magnification.

The thickness of the pDA coating was measured by both ellipsometry and AFM, the results of which are shown in Table 4. The results for the thickness of the coating measured by both ellipsometry and AFM agreed with one another. A 24-h immersion of Ti6Al4V plates in the dopamine solution resulted in the growth of an approximately 10-nm-thick layer. The thickness of the coating steadily increased to reach around 55 nm after 72 h, after which the growth plateaued.

Table 4. Polydopamine coating thickness as measured by ellipsometry and Atomic Force M.icroscopy (AFM).

Time of Immersion	24 h	48 h	72 h	96 h
Coating thickness measured by ellipsometry (nm)	10.2 ± 1.1	32.8 ± 1.1	52.4 ± 7.0	54.7 ± 6.4
Coating thickness measured by AFM (nm)	10.3 ± 0.5	34.1 ± 2.0	55.4 ± 9.0	57.1 ± 6.8

3.3. Fluorescence Microscopy

Fluorescence microscopy images of the various coated Ti6Al4V surfaces are shown in Figure 4a–f, while the subsequent fluorescence intensities are shown below in Table 5. From the fluorescence intensities of the peptide coating without the polydopamine, it can be observed that the peptide KR12 (Figure 4a) was present on the surface in the smallest quantities, while the lines presented in the image originated from the surface roughness and defects of the unpolished Ti6Al4V surface prior to coating. For the Ti6Al4V surfaces with a pDA linking substrate (Figure 4b–e), the green colour of the carboxyfluorescein (5(6)-FAM)-labelled peptides was generally distributed uniformly across the surface of Ti6Al4V, indicating a uniform peptide coating.

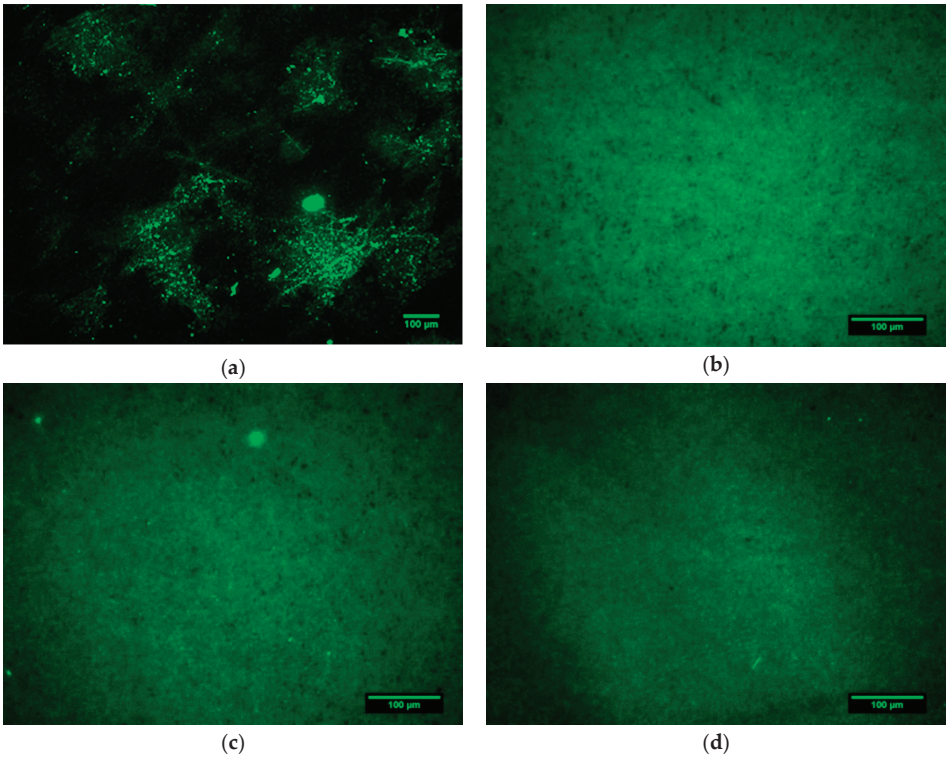

(**a**) (**b**)

(**c**) (**d**)

Figure 4. *Cont.*

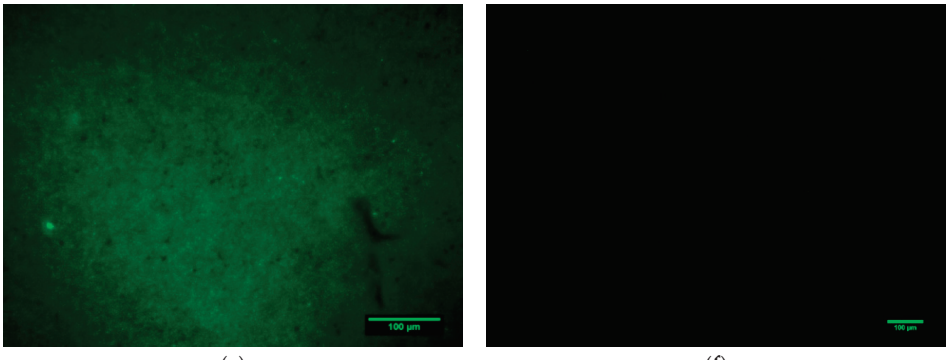

(**e**) (**f**)

Figure 4. Fluorescence microscopy images of the Ti6Al4V surface coated for 24 h with 5(6)-FAM-labelled (**a**) KR12, (**b**) pDA-KR12, (**c**) pDA-KR12/32, (**d**) pDA-KR12-5911, and (**e**) pDA-KR12/32-5911; and (**f**) for Ti6Al4V without coating.

Table 5. Fluorescent intensity values of various Ti6Al4V peptide-coated surfaces over 24 h.

	5(6)-FAM-KR12	pDA-5(6)-FAM-KR12	pDA-5(6)-FAM- KR12/32	pDA-5(6)-FAM-KR12-5911	pDA-5(6) -FAM-KR12/ 32-5911
Fluorescence intensity (FI)	868 ± 144	1204 ± 37	1198 ± 44	1227 ± 42	1189 ± 52

3.4. Peptide Release Studies

The peptide release profiles were all studied in simulated body fluid (SBF) over a total period of 30 days. The fluorescence-based release profiles of the pDA-attached peptides on the Ti6Al4V surface are shown in Figure 5. Roughly 30% of the peptides were released from the surface in the initial 6 h and 40–50% was released after 30 days. To verify the release profiles based on fluorescence, the studies were repeated with no labelled peptides and analysed by HPLC. The release profiles based on cumulative absorbance measured by HPLC are shown in Figure 6, which indicated that roughly 70% of the cumulative peptides were released in the first 6 h.

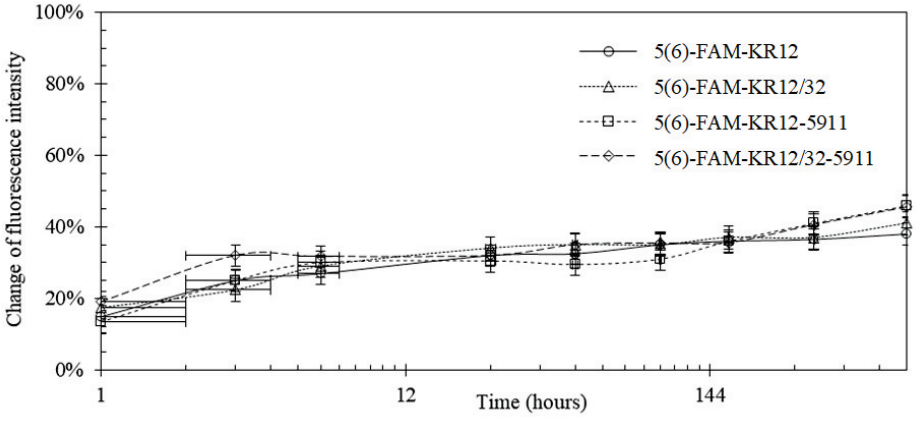

Figure 5. Release profile of 5(6)-FAM-labelled peptides that were released from the Ti6Al4V-coated surface based on fluorescence measurements; x-axis displayed in logarithmic scale (base = 12).

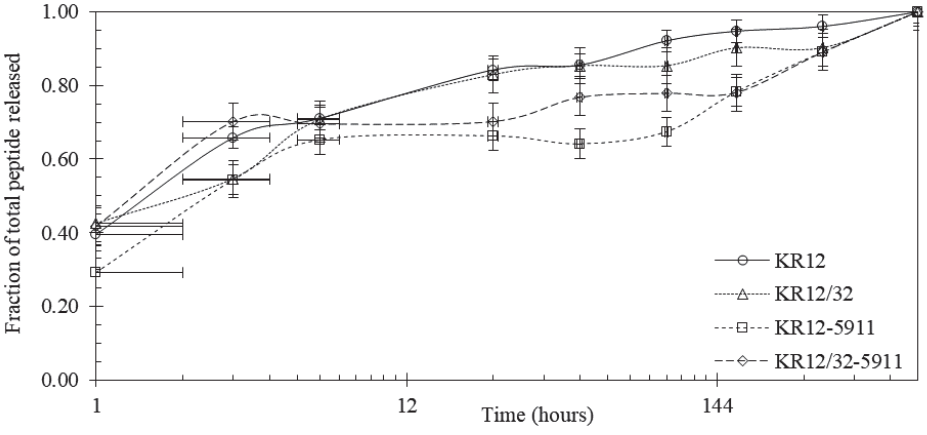

Figure 6. Release profile showing the percentage of the total peptides released in SBF from the pDA-coated Ti6Al4V surface based on HPLC; x-axis displayed in logarithmic scale (base = 12).

3.5. Wettability of the Surface

The changes of the water droplet contact angles on the uncoated and coated Ti6Al4V with pDA and conjugated with KR12, KR12/32, KR12-5911, and KR12/32-5911 are shown in Figure 7. Three main events can be observed in the graphs: expansion of the droplet's volume from 1 μL to 6 μL, the droplet's volume of 6 μL remaining steady, and shrinkage of droplet's volume from 6 μL to 1 μL. The application of the pDA and conjugation of the peptides all decreased the water contact angle of the surface of the Ti6Al4V, as shown in Table 6. Peptides KR12 and KR12/32 showed similar decreases in contact angles of roughly 1.3° and 7.8° when compared to pDA and Ti6Al4V, respectively. The coating containing peptide KR12/32-5911 had a contact angle about 1.0° smaller than those with peptides KR12 and KR12/32. However, the surface coated with the peptide KR12/32-5911 showed the biggest contact angle changes of roughly 2.7° and 9.7° when compared to the Ti6Al4V sample with pDA coating and the uncoated Ti6Al4V sample that was polished to mirror finish, respectively.

Table 6. Overview of the water contact angles during the steady droplet volume.

Surface	Contact Angle at Steady Volume of the Droplet
Mirror polished Ti6Al4V	65.4° ± 1.6
Ti6Al4V coated with pDA	59.0° ± 1.2
Ti6Al4V coated with pDA and peptide KR12	57.7° ± 0.9
Ti6Al4V coated with pDA and peptide KR12/32	57.5° ± 0.7
Ti6Al4V coated with pDA and peptide KR12-5911	55.6° ± 1.1
Ti6Al4V coated with pDA and peptide KR12/32-5911	56.3° ± 0.5

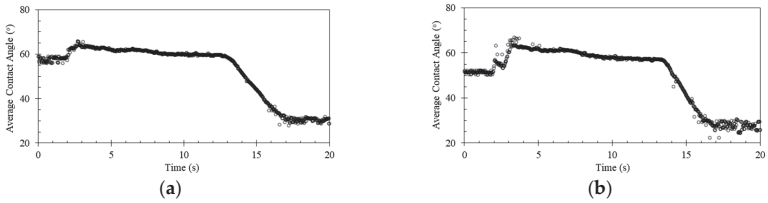

Figure 7. *Cont.*

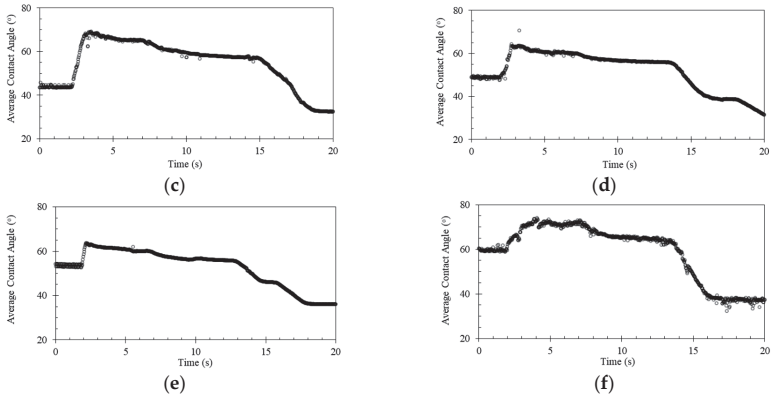

Figure 7. Changes of the water contact angles of the Ti6Al4V surface coated with (**a**) pDA, (**b**) pDA-KR12, (**c**) pDA-KR12/32, (**d**) pDA-KR12-5911, (**e**) pDA-KR12/32-5911, and (**f**) Ti6Al4V without coating, showing the changes in the water droplet's volume.

3.6. Cell Studies

The micrographs presented in Figure 8a–l show the attachment of human osteosarcoma cells (HOS) on the coated and uncoated Ti6Al4V surfaces taken at days 5 and 7 of incubation. HOS showed consistent growth on all of the surfaces, except for the Ti/pDA surface decorated with the peptide KR12/32-5911 shown in Figure 8k–l, where cells were observed to be detached on day 7 of culture. On the Ti/pDA KR12/32 sample shown Figure 8g–h, the surface cells showed a flatter morphology compared to the other surfaces. On all of the other surfaces, although minor differences in the densities of cells can be seen, there is little change between the growth of cells and there is clear evidence of an increase in the number of cells from day 5 to day 7 of culture.

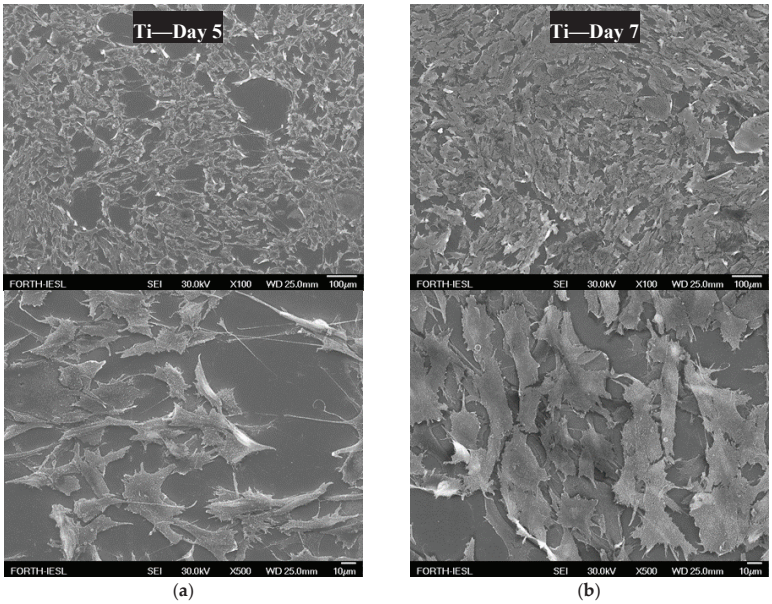

Figure 8. *Cont.*

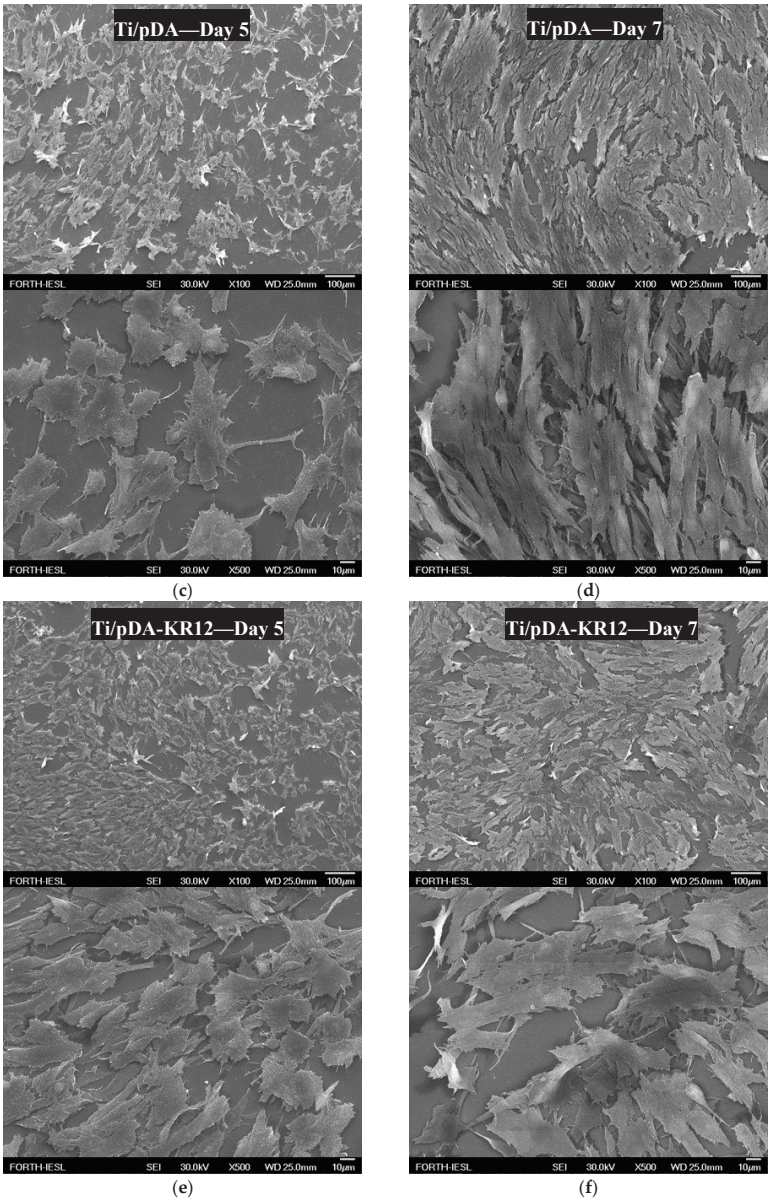

Figure 8. *Cont.*

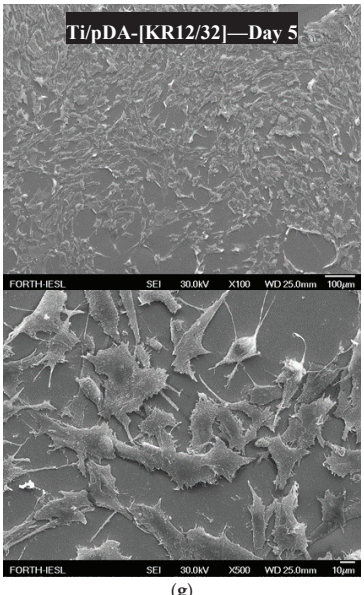

(**g**)

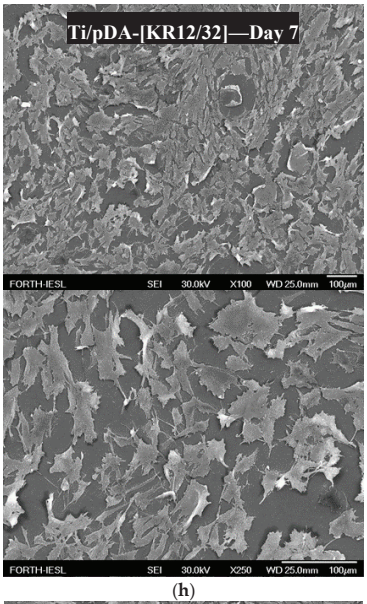

(**h**)

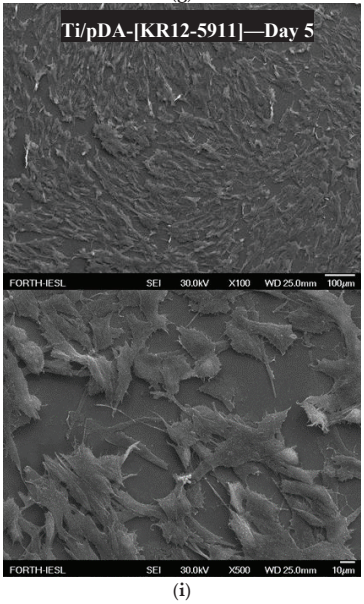

(**i**)

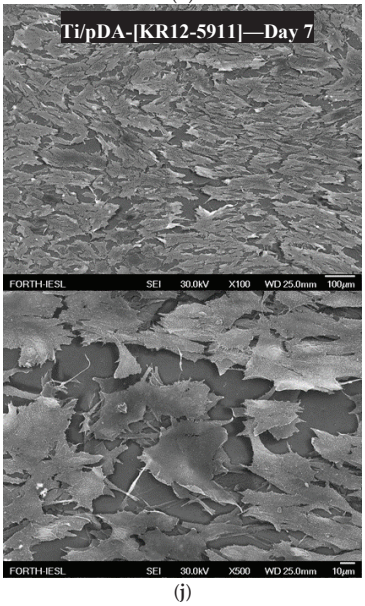

(**j**)

Figure 8. *Cont.*

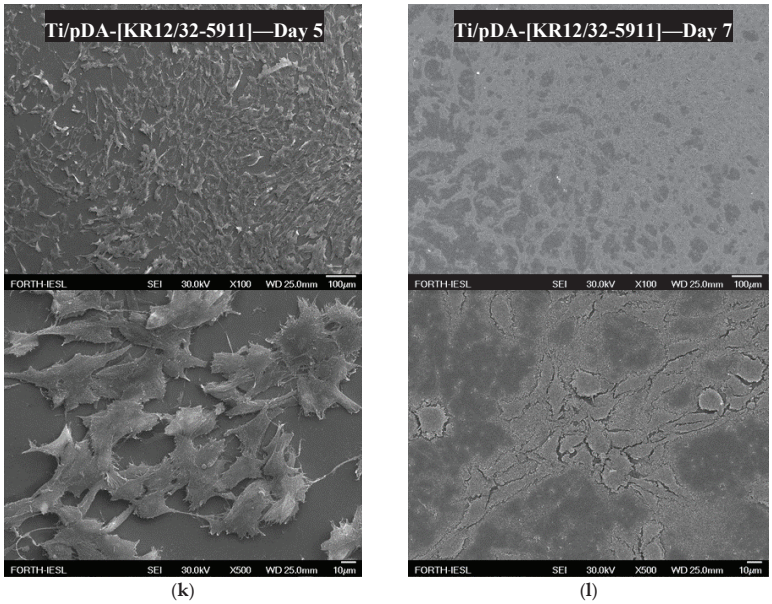

Figure 8. SEM micrographs showing the growth of the seeded human osteosarcoma cells (HOS) on day 5 and 7 for (**a**,**b**) Ti6Al4V, (**c**,**d**) Ti6Al4V/pDA, (**e**,**f**) Ti6Al4V/pDA-KR12, (**g**,**h**) Ti6Al4V/pDA-KR12/32, (**i**,**j**) Ti6Al4V/pDA-KR12/5911, and (**k**,**l**) Ti6Al4V/pDA-KR12/32-5911 at 100× and 500× magnification, respectively.

4. Discussion

4.1. Peptide MIC Characterisation

Infections caused by the investigated bacteria are some of the most commonly occurring incidences during orthopaedic joint replacement surgeries [21]. Factors such as prolonged antibiotic treatment or administration below the MIC value have been shown to increase bacterial resistance towards antibiotics [22]. Thus, it is important to design antimicrobial peptides with low MIC values that are effective against orthopaedic bacteria. When comparing the MIC values of the human cathelicidin LL-37 with the designed peptides, as summarised in Table 3, the KR12 peptide showed promising MIC values with a higher antimicrobial tendency towards Gram-negative bacteria.

LL-37 was shown to have antimicrobial activity against fungi [23], bacteria [24], and viruses [23,25]. Additionally, it has immunostimulatory and immunomodulatory functions against infections [26] and stimulates angiogenesis [27] during the wound healing process [28]. LL-37 immobilised on polymer surfaces has also been proven to retain its antimicrobial activity [29]. Therefore, the designed KR12 analogous peptide may share similar properties with LL-37, but this remains to be investigated.

4.2. Polydopamine Coating of Ti6Al4V

Dissolving dopamine in a solution of alkaline pH changes the colour of the solution from translucent white to brown, then eventually to black, as shown in Figure 2. This colour change can be explained by the structure of dopamine. Dopamine contains phenol groups, and when polymerised it creates polyphenols structures that contain many aromatic rings joined together [30]. Multiple aromatic rings in close proximity in one molecule are known as charge transfer complexes, whereby the charge is delocalised between the rings [31]. These complexes promote absorption of visible light, causing electron transition from a lower electron state to higher electron state, as a result of which a dark colour is observed [32]. Immersing Ti6Al4V plates in a solution of dopamine resulted in the

formation of a thin film on the surface of the metallic plate, which agrees with Messersmith et al. [33], who reported that pDA was able to adhere to virtually any surface and that its polymerisation in slightly basic solution resulted in a film formation on the surface. The SEM morphology and topology studies showed that the surface of the pDA coating was built from small round particles of ≈100 nm diameter. It was proposed by Jiang et al. that the pDA first polymerises in nanoaggregates, which over time attach themselves on the surface, creating a uniform coating [34,35].

The attachment of the nanoaggregates to the surface could potentially have been driven by the sedimentation of the particles towards the bottom of the container where the substrate to be coated was located. The coating then accumulated with more beads and increased the thickness of the coating, which varied depending on the size of the beads accumulated. This could explain the ≈10 nm coating thickness after the initial 24 h, and the increases of the thickness to 32 nm after 48 h and to 57 nm after 52 h of pDA polymerisation. Similar film thickness growth was reported by Jiang et al. [33,35]. In this study, a thickness plateau was reached after 72 h of polymerisation. This pattern of growth was also previously reported by Bensmann et al. [36], where the pDA film reached 62.8 nm in thickness after 72 h and did not increase in thickness afterwards. Formation of the plateau can be explained by the lack of oxygen after the formation of the first pDA layer. Since oxidation is a common reaction of polyphenols [37], it can be assumed that the polymerisation required oxygen to continue and the presence of the film limited the accessibility to oxygen. In addition, as oxidation on the surface will continue as oxygen is available on the surface, polymerisation will eventually stop when dopamine is consumed.

4.3. Peptide Attachment to Polydopamine

The KR12 analogous peptide labelled with 5(6)-FAM at the N-terminal was conjugated to an already pDA-coated Ti6Al4V surface. The presence of the peptides was confirmed by the emitted fluorescence, showing only small variations in the measured fluorescence intensities between the different peptides. The quinone group of pDA is known to undergo a Schiff base reaction or Michael addition without the use of any other reagent or catalyst, allowing the conjugation of biomolecules to pDA [38]. The catechol group of the pDA is known to oxidise to quinone at a pH above 7.5 in excess of oxygen, which is necessary for successful conjugation to nucleophiles [39]. Here, the designed peptides contained two lysine residues that should be able to conjugate to pDA, but the first lysine was presumed to be shielded by the bulky 5(6)-FAM label at the N-terminus. Therefore, it was expected that pDA was conjugated with the second lysine residue relative to the N-terminus. It was observed that the initial burst of peptides released approximately 25–35% of the peptides from the surface after 6 h, and approximately 40–50% was released after 30 days. The fluorescence release profile studies in SBF indicated that 50–60% of the peptides potentially remained conjugated to the pDA after 30 days. The initial burst of peptide release could be attributed to the release of unattached peptides to the pDA that were not successfully removed during the wash step. After the initial burst, the rate of release of the peptides decreased and was only reduced further by roughly 5–10% after the final 30 days. The release profile from the fluorescence was confirmed by HPLC using non-fluorescent peptides. An initial ≈70% burst of cumulative peptide was released in the first 6 h, and a slower subsequent release for the remaining period was observed. These release studies clearly showed that these peptides were conjugated to the pDA-coated Ti6Al4V surface in a very stable manner through the lysine residues.

4.4. Wettability of the Surface

New implants within the body come into immediate contact with extracellular fluid and moieties, such as proteins, which are some of the first molecules to interact with the surfaces of an implant [40,41]. The optimal water contact angle of a biomaterial reported for bone-forming cells to attach to a surface was reported to be 55° [42]. Metallic surfaces are very hydrophobic, resulting in slow integration rates of the implant with the body. A water contact angle study of pDA-coated titanium surfaces

by Nijhuis et al. reported that coated Ti6Al4V surfaces were much less hydrophobic (≈47°) than the uncoated surfaces (≈75°) [43], presumably resulting in an improvement of the implant integration [44]. In this paper, we report that the introduction of pDA coating on the surface of Ti6Al4V resulted in a decrease in the water contact angle from 65.4° ± 1.6 to 59.0° ± 1.2. The experimental values are in agreement with prior research performed by Luo et al. [45], who reported on the water contact angle of a pDA-coated Ti6Al4V surface. The water contact angle was further reduced to approximately 56.8° when the pDA coating was decorated with the peptides—the results varied depending on the used peptide, but they all showed a reduction relative to the pDA-coated Ti6Al4V surface.

4.5. Cell Culture Studies

All surfaces showed attachment of cells on day 5, with no evidence of toxicity (which is determined by any change of cell morphology or density compared to the plain titanium surface), with one exception for the KR12/32-5911 surface. The cell morphology was generally "flattened" and fibroblast-like, typical of the described HOS morphology in the literature [46]. The density of attached cells increased over time, confirming that cells were viable and able to proliferate. In contrast, there was evidence that the surface of KR12/32-5911 was toxic to the cells, and at day 7 there were no longer any cells.

5. Conclusions

In the present research, KR12 and three new analogous peptides were successfully synthesised and showed promising antimicrobial activity against *E. coli*, *P. aeruginosa*, and *S. aureus*, with MIC values generally being lower than that of their native peptide, the human cathelicidin LL-37. The titanium surfaces were coated with pDA and characterised. Subsequently, the pDA-coated surfaces were decorated with KR12 and the other three designed analogous peptides. The pDA coating provided a long-term linking substrate for the peptides, which was confirmed by fluorescence microscopy and HPLC. Cultured HOS cells showed good attachment and cell growth on the material surfaces, with no visible toxicity towards the cells, except for the KR12/32-5911 peptide. This surface treatment shows potential to provide long-term antimicrobial activity on many metallic and organic material surfaces and could be used in biomedical materials and implants.

Author Contributions: Conceptualization, A.S. and Z.T.; methodology, A.S., J.B., N.J.H.; software, M.B.; validation, A.S. and Z.T.; formal analysis Z.T. and A.S.; investigation Z.T.; resources, Z.T., M.B. and H.I.; data curation, Z.T., M.B., H.I., J.B., N.J.H. and A.S.; writing—original draft preparation, Z.T., M.B. and H.I.; writing—review and editing, A.S., N.J.H.; visualization, Z.T., M.B., H.I.; supervision, A.S., J.B. and N.J.H.; project administration, A.S.; funding acquisition, A.S. All authors have read and agreed to the published version of the manuscript.

Funding: This project has been partially funded by the European Union's Horizon 2020 research and innovation programme under the Marie Sklodowska-Curie grant agreement No. 645749. The project has been also financially supported by a studentship provided by the School of Metallurgy and Materials, University of Birmingham, UK.

Conflicts of Interest: The authors declare no conflict of interest.

References

1. Cloutier, M.; Mantovani, D.; Rosei, F. Antibacterial Coatings: Challenges, Perspectives, and Opportunities. *Trends Biotechnol.* **2015**, *33*, 637–652. [CrossRef]
2. Goodman, S.B.; Yao, Z.; Keeney, M.; Yang, F. The future of biologic coatings for orthopaedic implants. *Biomaterials* **2013**, *34*, 3174–3183. [CrossRef]
3. Romanò, C.L.; Scarponi, S.; Gallazzi, E.; Romanò, D.; Drago, L. Antibacterial coating of implants in orthopaedics and trauma: A classification proposal in an evolving panorama. *J. Orthop. Surg. Res.* **2015**, *10*, 157. [CrossRef]
4. Geetha, M.; Singh, A.K.; Asokamani, R.; Gogia, K.A. Ti based biomaterials, the ultimate choice for orthopaedic implants—A review. *Prog. Mater. Sci.* **2009**, *54*, 397–425. [CrossRef]
5. Bauer, J.; Siala, W.; Tulkens, P.M.; Van Bambeke, F. A combined pharmacodynamic quantitative and qualitative model reveals the potent activity of daptomycin and delafloxacin against Staphylococcus aureus biofilms. *Antimicrob. Agents Chemother.* **2013**, *57*, 2726–2737. [CrossRef]

6. Mishra, B.; Wang, G. Titanium surfaces immobilised with the major antimicrobial fragment FK-16 of human cathelicidin LL-37 are potent against multiple antibiotic-resistant bacteria. *Biofouling* **2017**, *33*, 544–555. [CrossRef] [PubMed]
7. Stigter, M.; Bezemer, J.; De Groot, K.; Layrolle, P. Incorporation of different antibiotics into carbonated hydroxyapatite coatings on titanium implants, release and antibiotic efficacy. *J. Control. Release* **2004**, *99*, 127–137. [CrossRef]
8. Rathbone, C.R.; Cross, J.D.; Brown, K.V.; Murray, C.; Wenke, J.C. Effect of various concentrations of antibiotics on osteogenic cell viability and activity. *J. Orthop. Res.* **2011**, *29*, 1070–1074. [CrossRef]
9. Mor, A. Peptide-based antibiotics: A potential answer to raging antimicrobial resistance. *Drug Dev. Res.* **2000**, *50*, 440–447. [CrossRef]
10. Alves, D.; Olívia Pereira, M. Mini-review: Antimicrobial peptides and enzymes as promising candidates to functionalise biomaterial surfaces. *Biofouling* **2014**, *30*, 483–499. [CrossRef]
11. Bazaka, K.; Jacob, M.V.; Chrzanowski, W.; Ostrikov, K. Anti-bacterial surfaces: Natural agents, mechanisms of action, and plasma surface modification. *RSC Adv.* **2015**, *5*, 48739–48759. [CrossRef]
12. Zasloff, M. Antimicrobial peptides of multicellular organisms. *Nature* **2002**, *415*, 389–395. [CrossRef] [PubMed]
13. Guilhelmelli, F.; Vilela, N.; Albuquerque, P.; Derengowski, L.D.S.; Pereira, I.S.; Kyaw, C.M. Antibiotic development challenges: The various mechanisms of action of antimicrobial peptides and of bacterial resistance. *Front. Microbiol.* **2013**, *4*, 353. [CrossRef]
14. Fjell, C.D.; Hiss, J.A.; Hancock, R.E.W.; Schneider, G. Designing antimicrobial peptides: Form follows function. *Nat. Rev. Drug Discov.* **2011**, *11*, 37–51. [CrossRef]
15. Lazzaro, B.P.; Zasloff, M.; Rolff, J. Antimicrobial peptides: Application informed by evolution. *Science* **2020**, *368*, eaau5480. [CrossRef]
16. Jacob, B.; Park, I.-S.; Bang, J.-K.; Shin, S.Y. Short KR-12 analogs designed from human cathelicidin LL-37 possessing both antimicrobial and antiendotoxic activities without mammalian cell toxicity. *J. Pept. Sci.* **2013**, *19*, 700–707. [CrossRef]
17. Jia, L.; Han, F.; Wang, H.; Zhu, C.; Guo, Q.; Li, J.; Zhao, Z.; Zhang, Q.; Zhu, X.; Li, B. Polydopamine-assisted surface modification for orthopaedic implants. *J. Orthop. Transl.* **2019**, *17*, 82–95. [CrossRef]
18. Zhu, Y.; Liu, D.; Wang, X.; He, Y.; Luan, W.; Qi, F.; Ding, J. Polydopamine-mediated covalent functionalisation of collagen on a titanium alloy to promote biocompatibility with soft tissues J. *Mater. Chem. B* **2019**, *7*, 2019–2031. [CrossRef]
19. Wang, Y.; Qi, H.; Miron, R.J.; Zhang, Y. Modulating macrophage polarisation on titanium implant surface by poly(dopamine)-assisted immobilisation of IL4. *Clin. Implant Dent. Relat. Res.* **2019**, *21*, 977–986. [CrossRef]
20. Kokubo, T.; Takadama, H. How useful is SBF in predicting in vivo bone bioactivity? *Biomaterials* **2006**, *27*, 2907–2915. [CrossRef]
21. Ribeiro, M.; Monteiro, F.J.; Ferraz, M.P. Infection of orthopedic implants with emphasis on bacterial adhesion process and techniques used in studying bacterial-material interactions. *Biomaterials* **2013**, *2*, 176–194. [CrossRef] [PubMed]
22. Levison, M.E.; Levison, J.H. Pharmacokinetics and Pharmacodynamics of Antibacterial Agents. *Infect. Dis. Clin. N. A.* **2009**, *23*, 791–815. [CrossRef] [PubMed]
23. Wong, J.H.; Łęgowska, A.; Rolka, K.; Ng, T.B.; Hui, M.; Cho, C.H.; Lam, W.W.L.; Au, S.W.-N.; Gu, O.W.; Wan, D.C.C. Effects of cathelicidin and its fragments on three key enzymes of HIV-1. *Peptides* **2011**, *32*, 1117–1122. [CrossRef]
24. Overhage, J.; Campisano, A.; Bains, M.; Torfs, E.C.W.; Rehm, B.H.A.; Hancock, R.E.W. Human Host Defense Peptide LL-37 Prevents Bacterial Biofilm Formation. *Infect. Immun.* **2008**, *76*, 4176–4182. [CrossRef]
25. Barlow, P.G.; Svoboda, P.; Mackellar, A.; Nash, A.A.; York, I.A.; Pohl, J.; Davidson, D.J.; Donis, R.O. Antiviral Activity and Increased Host Defense against Influenza Infection Elicited by the Human Cathelicidin LL-37. *PLoS ONE* **2011**, *6*, e25333. [CrossRef]
26. Davidson, D.J.; Currie, A.J.; Reid, G.S.D.; Bowdish, D.M.E.; MacDonald, K.L.; Ma, R.C.; Hancock, R.E.W.; Speert, D.P. The Cationic Antimicrobial Peptide LL-37 Modulates Dendritic Cell Differentiation and Dendritic Cell-Induced T Cell Polarization. *J. Immunol.* **2004**, *172*, 1146–1156. [CrossRef]

27. Koczulla, R.; Von Degenfeld, G.; Kupatt, C.; Krötz, F.; Zahler, S.; Gloe, T.; Issbrücker, K.; Unterberger, P.; Zaiou, M.; Lebherz, C.; et al. An angiogenic role for the human peptide antibiotic LL-37/hCAP-18. *J. Clin. Investig.* **2003**, *111*, 1665–1672. [CrossRef]
28. Duplantier, A.J.; Van Hoek, M.L. The Human Cathelicidin Antimicrobial Peptide LL-37 as a Potential Treatment for Polymicrobial Infected Wounds. *Front. Immunol.* **2013**, *4*, 1–14. [CrossRef]
29. Dutta, D.; Kumar, N.; Willcox, M.D.P. Antimicrobial activity of four cationic peptides immobilised to poly-hydroxyethylmethacrylate. *Biofouling* **2016**, *32*, 429–438. [CrossRef]
30. Alfieri, M.L.; Panzella, L.; Oscurato, S.L.; Salvatore, M.; Avolio, R.; Errico, M.E.; Maddalena, P.M.; Napolitano, A.; D'Ischia, M. The Chemistry of Polydopamine Film Formation: The Amine-Quinone Interplay. *Biomimetics* **2018**, *3*, 26. [CrossRef]
31. Kim, J.H.; Lee, M.; Park, C.B. Polydopamine as a Biomimetic Electron Gate for Artificial Photosynthesis. *Angew. Chem. Int. Ed.* **2014**, *53*, 6364–6368. [CrossRef] [PubMed]
32. Dreyer, D.R.; Miller, D.J.; Freeman, B.D.; Paul, D.R.; Bielawski, C.W. Perspectives on poly(dopamine). *Chem. Sci.* **2013**, *4*, 3796. [CrossRef]
33. Lee, H.; Dellatore, S.M.; Miller, W.M.; Messersmith, P.B. Mussel-Inspired Surface Chemistry for Multifunctional Coatings. *Science* **2007**, *318*, 426–430. [CrossRef] [PubMed]
34. Jiang, J.; Zhu, L.; Zhu, L.; Zhu, B.; Xu, Y. Surface Characteristics of a Self-Polymerised Dopamine Coating Deposited on Hydrophobic Polymer Films. *Langmuir* **2011**, *27*, 14180–14187. [CrossRef] [PubMed]
35. Zhang, W.; Yang, F.K.; Han, Y.; Gaikwad, R.; Leonenko, Z.; Zhao, B. Surface and Tribological Behaviors of the Bioinspired Polydopamine Thin Films under Dry and Wet Conditions. *Biomacromolecules* **2013**, *14*, 394–405. [CrossRef] [PubMed]
36. Bernsmann, F.; Ponche, A.; Ringwald, C.; Hemmerle, J.; Raya, J.; Bechinger, B.; Voegel, J.C.; Schaaf, P.; Ball, V. Characterisation of Dopamine−Melanin Growth on Silicon Oxide. *J. Phys. Chem. C* **2009**, *113*, 8234–8242. [CrossRef]
37. Lynge, M.E.; Van Der Westen, R.; Postma, A.; Städler, B. Polydopamine-a nature-inspired polymer coating for biomedical science. *Nanoscale* **2011**, *3*, 4916. [CrossRef]
38. Shin, Y.M.; Jun, I.; Lee, J.Y.; Rhim, T.; Shin, H. Bio-inspired Immobilization of Cell-Adhesive Ligands on Electrospun Nanofibrous Patches for Cell Delivery. *Macromol. Mater. Eng.* **2012**, *298*, 555–564. [CrossRef]
39. Li, H.; Cui, D.; Cai, H.; Zhang, L.; Chen, X.; Sun, J.; Chao, Y. Use of surface plasmon resonance to investigate lateral wall deposition kinetics and properties of polydopamine films. *Biosens. Bioelectron.* **2013**, *41*, 809–814. [CrossRef]
40. Lee, H.J.; Koo, A.N.; Lee, S.W.; Lee, M.H.; Lee, S.C. Catechol-functionalised adhesive polymer nanoparticles for controlled local release of bone morphogenetic protein-2 from titanium surface. *J. Control. Release* **2013**, *170*, 198–208. [CrossRef]
41. Ku, S.H.; Ryu, J.; Hong, S.K.; Lee, H.; Park, C.B. General functionalisation route for cell adhesion on non-wetting surfaces. *Biomaterials* **2010**, *31*, 2535–2541. [CrossRef] [PubMed]
42. Ponsonnet, L.; Reybier, K.; Jaffrezic, N.; Comte, V.; Lagneau, C.; Lissac, M.; Martelet, C. Relationship between surface properties (roughness, wettability) of titanium and titanium alloys and cell behaviour. *Mater. Sci. Eng. C* **2003**, *23*, 551–560. [CrossRef]
43. Nijhuis, A.W.G.; Van den Beucken, J.J.J.P.; Boerman, O.C.; Jansen, J.A.; Leeuwenburgh, S.C.G. 1-Step Versus 2-Step Immobilisation of Alkaline Phosphatase and Bone Morphogenetic Protein-2 onto Implant Surfaces Using Polydopamine. *Tissue Eng. Part C Methods* **2013**, *19*, 610–619. [CrossRef] [PubMed]
44. Liu, X.; Chu, P.K.; Ding, C. Surface modification of titanium, titanium alloys, and related materials for biomedical applications. *Mater. Sci. Eng. R Rep.* **2004**, *47*, 49–121. [CrossRef]
45. Luo, R.; Tang, L.; Zhong, S.; Yang, Z.; Wang, J.; Weng, Y.; Tu, Q.; Jiang, C.; Huang, N. In Vitro Investigation of Enhanced Hemocompatibility and Endothelial Cell Proliferation Associated with Quinone-Rich Polydopamine Coating. *ACS Appl. Mater. Interfaces* **2013**, *5*, 1704–1714. [CrossRef]
46. Jun, I.-K.; Jang, J.-H.; Kim, H.-W.; Kim, H.-E. Recombinant osteopontin fragment coating on hydroxyapatite for enhanced osteoblast-like cell responses. *J. Mater. Sci.* **2005**, *40*, 2891–2895. [CrossRef]

materials

MDPI

Article

Bioactive (Co)oligoesters as Potential Delivery Systems of p-Anisic Acid for Cosmetic Purposes

Magdalena Martinka Maksymiak [1,*], Magdalena Zięba [1], Arkadiusz Orchel [2], Monika Musiał-Kulik [1], Marek Kowalczuk [1] and Grazyna Adamus [1,*]

[1] Centre of Polymer and Carbon Materials, Polish Academy of Sciences, M. Curie-Skłodowskiej 34 Str., 41–819 Zabrze, Poland; mzieba@cmpw-pan.edu.pl (M.Z.); mmusial@cmpw-pan.edu.pl (M.M.-K.); marek.kowalczuk@cmpw-pan.edu.pl (M.K.)

[2] Department of Biopharmacy, Faculty of Pharmaceutical Sciences in Sosnowiec, Medical University of Silesia, Katowice, Poland, Jednosci 8 Str., 41–208 Sosnowiec, Poland; aorchel@sum.edu.pl

* Correspondence: mmaksymiak@cmpw-pan.edu.pl (M.M.M.); grazyna.adamus@cmpw-pan.edu.pl (G.A.)

Received: 3 July 2020; Accepted: 11 September 2020; Published: 18 September 2020

Abstract: This article reports the studies on bioactive (co)oligoesters towards their use as controlled delivery systems of p-anisic acid. The objects of the study were oligo[3-hydroxy-3-(4-methoxybenzoyloxymethyl)propionate], $(p\text{-AA-}CH_2\text{-HP})_n$ oligoester, and oligo[(3-hydroxy-3-(4-methoxybenzoyloxymethyl)propionate)-co-(3-hydroxybutyrate)] $[(p\text{-AA-}CH_2\text{-HP})_x\text{-co-}(HB)_y$ (co)oligoesters containing p-anisic acid moiety (p-AA, as the bioactive end and side groups) connected to the polymer backbone through the susceptible to hydrolysis ester bonds. A thorough insight into the hydrolysis process of the bioactive (co)oligoesters studied has allowed us to determine the release profile of p-AA as well as to identify polymer carrier degradation products. The p-AA release profiles determined on the basis of high-performance liquid chromatography (HPLC) measurements showed that the release of the bioactive compound from the developed (co)oligoester systems was regular and no burst effect occurred. Biological studies demonstrated that studied (homo)- and (co)oligoesters were well tolerated by HaCaT cells because none of them showed notable cytotoxicity. They promoted keratinocyte growth at moderate concentrations. Bioactive (co)oligoesters containing p-anisic acid moiety had somewhat decreased cell proliferation at the highest concentration (100 μg/mL). The important practical inference of the current study is that the (co)oligoesters developed have a relatively large load of the biologically active substance (p-AA) per polymer macromolecule, which unlocks their potential application in the cosmetic industry.

Keywords: polyhydroxyalkanoates; oligo(3-hydroxy-3-(4-methoxybenzoyloxymethyl)propionate); bioactive (co)oligoesters; p-anisic acid derivatives; hydrolytic degradation; cosmetic delivery system; ESI-MS; multistage mass spectrometry

1. Introduction

Natural antioxidants offer a host of benefits, especially for our health and general well-being, including anti-aging, anti-carcinogenic, anti-inflammatory, and anti-microbial properties, which promote a growing use in cosmetic products. The antioxidant activities of natural antioxidants have been largely ascribed to the presence of phenolic content [1,2].

Additionally, antioxidants possess very strong preservative properties and they may prevent lipid oxidation in cosmetic products. Besides, sunlight, air and vehicle pollution, and other environmental factors produce free radicals, which could be neutralized by antioxidants. The use of antioxidants in cosmetics aims to create a barrier that helps protect the skin against free radicals produced by oxidative stressors [3].

Among phenols, which are a well-known group of biologically active compounds, the best known are flavonoids, tannins, and phenolic acids. The last ones belong to aromatic secondary plant metabolites, are widespread in vegetation, and provide a wealth of anti-aging benefits. They can be readily absorbed in the human body and demonstrate strong preserving properties, which include anti-bacterial and anti-fungal effects [4]. The main function of phenolic antioxidants is retardation oxidation of unsaturated oils that may affect the final color and smell of cosmetic products [5].

p-Anisic acid (4-Methoxybenzoic acid) reveals antioxidant, anti-inflammatory, and anti-tumor properties, and is a proven antiseptic, which makes it suitable as a preservative in cosmetic products [5]. Over the past few years, p-AA became progressively substantial when used as a multi-functional material in the cosmetics and food sectors [6]. Among various cosmetic ingredients with antimicrobial properties, there are some commercially available ones (p-anisic acid and levulinic acid), which were found in number in several herbs (e.g., *Pimpinella anisum*) and as a by-product in the preparation of diosgenin from wild yam (*Dioscorea villosa*) [7].

The other developed cosmetic products, consisting of these alternative anti-microbial substances, are characterized as preservative-free or naturally preserved cosmetics [8].

Nevertheless, antioxidants encounter some difficulties, especially concerning the stability problems when they penetrate the transdermal barrier [9]. The use of controlled release systems in cosmetics contributes to the improvement of antioxidants' skin penetration. Moreover, it is a further challenge that the developed delivery systems (DSs) are readily integrated into the final cosmetic product formulation, thus leading to a consistent product for the customers' use. Furthermore, the use of DS enhances the protection of sensitive active ingredients and guarantees their targeted controlled release. It was proved that cosmetic DSs demonstrate a positive impact on the permeation of the bioactive compounds throughout the skin layers, and thus the concentration of the active species may be well controlled in both the obtained formulation and in the skin, respectively. So far, several types of DSs (e.g., niosomes, transfersomes, liposomes, lipid nanoparticles, polymeric microparticles, and nanoparticles) have been applied in cosmetic products. Skin interaction with the various DSs depends mostly on such factors as size, flexibility, and composition [10].

Many works have demonstrated that the improvement of the skin penetration of indigenously applied drugs can be achieved using particle-based formulations. However, a more rational approach needs to be considered when the transfer of the promising results to the clinical application is planned. Moreover, the different properties of diseased skin and the fate of these polymeric materials should be taken into account. Ideally, depending on the nature of the polymer, decomposition of a biodegradable polymer into non-toxic products and its degradation in a controlled manner after topical applications on the skin surface is highly desired [11].

The emergence of a broad spectrum of biodegradable polymers dedicated specifically for biomedical applications has resulted from the development of macromolecules with well determined structure and properties. The synthetic aliphatic polyesters possess a unique position among biodegradable polymers. They show the possibility of many health-related applications thanks to their good biodegradability and biocompatibility [12,13].

β-Lactones are considered as attractive substrates in organic synthesis [14] that can be used as monomers for the synthesis of aliphatic polyesters via ring-opening polymerization (ROP) [15,16]. Quite recently, selective and highly active catalysts that might be used for epoxide carbonylation have been described [17–19]. Thus, a new source of bioactive β-lactone monomers that contain in their structure a biologically active substance has been established. They proved to be very valuable and helpful for the synthesis of new polyesters, including polymeric DS with bioactive moieties. Polymer-bioactive compound conjugates offer countless benefits over free drugs such as increased water solubility, controlled and targeted drug delivery, more bioavailability, and thus enhanced therapeutic efficacy [20].

In our previous studies, we provided an overview of the approach for synthesizing bioactive (co)oligoesters on the basis of anionic homo- and co-polymerization of selected β-substituted β-lactones

that contain bioactive species selectively chosen from compounds commonly used in cosmetic industry. The molecular-level structure of the obtained bioactive (co)oligoesters, as well as their abilities in the prospective application in cosmetology, were also demonstrated [21–25].

In the present contribution, we present a further extension study on bioactive (co)oligoesters that contain p-anisic acid moieties bound along oligomer chains. Considering the future use of developed biomaterials as controlled DS of p-AA, the current research has been focused on detailed studies of hydrolytic degradation of the resulting bioactive (co)polyesters.

The results of studies on the hydrolytic degradation of the obtained materials allowed us to gain full knowledge of the hydrolysis process and examine the p-AA release profile. In addition, applying mass spectrometry has enabled to identify the products of degradation of the biomaterials studied and determine their molecular structure.

Moreover, both bioactive (homo)- and (co)oligoesters were found to be cytocompatible when in contact with human HaCaT cells and they seem to be optimal to support keratinocyte functions. Especially, (p-AA-CH_2-HP)$_n$ oligoester did not exert any inhibitory impact on cell growth, even at a relatively high concentration. Incubation with (co)oligoester had beneficial effects on HaCaT cells at concentrations below 100 μg/mL.

2. Materials and Methods

2.1. Materials

p-Anisic acid sodium salt (sodium p-anisate, 4-methoxybenzoic acid sodium salt for synthesis, Merck KGaA, Darmstadt, Germany) was used without further treatment. LC-MS grade methanol, chloroform, acetonitrile and 0.1% formic acid in water were purchased from Merck (Merck KGaA, Darmstadt, Germany). (*R,S*)-β-Butyrolactone (β-BL, Sigma-Aldrich Chemie GmbH, Steinheim, Germany) was distilled over CaH_2 and the fraction boiling at 56 °C (9 mmHg) was collected. The 4-Methoxybenzoyloxymethythylpropiolactone (p-AA-CH_2-PL) was synthesized at the Institute of Organic Chemistry, Polish Academy of Sciences by carbonylation of the respective epoxide under ambient CO pressure [26].

The oligo(3-hydroxy-3-(4-methoxybenzoyloxymethyl)propionate) (p-AA-CH_2-HP)$_n$ oligoesters (sample 1; $M_{n,GPC}$ = 700, M_w/M_n = 1.15) and oligo[(3-hydroxy-3-(4-methoxybenzoyloxymethyl)-propionate)-co-(3-hydroxybutyrate)], [(p-AA-CH_2-HP)$_x$-co-(HB)$_y$] (co)oligoesters (sample 2; $M_{n,GPC}$ = 900 M_w/M_n = 1.23) were obtained via anionic ring-opening oligomerization of (p-AA-CH_2-PL) and via anionic ring-opening (co)oligomerization of β-BL with p-AA-CH_2-PL, respectively. The synthesis was performed according the procedure described in [25]. The resulting (co)oligoesters were purified and characterized by ^{1}H nuclear magnetic resonance (^{1}H NMR), gel permeation chromatography (GPC), and multistage mass spectrometry (ESI-MS^n).

2.2. Measurements

2.2.1. Performance of Electrospray Mass Spectrometry (ESI-MS^n) Analyses

Electrospray mass spectra were acquired by directly infusing the polyester sample into the ESI source of a Finnigan LCQ ^{TM} ion trap mass spectrometer (Finnigan, San Jose, CA, USA) with a syringe pump at a flow rate of 10 mL min^{-1}. Nitrogen was used as the nebulising gas. The LCQ ESI source was operated at 4.5 kV, and the capillary heater was set to 200 °C. The polyester samples were diluted in a chloroform/methanol system (1:1; *v/v*). For fragmentation experiments, the ions of interest were isolated monoisotopically in the ion trap and were collisionally activated. The helium damping gas that was present in the mass analyzer acted as the collision gas. The ring electrode radio-frequency (RF) amplitude with a significant voltage range was set to a value that caused the peak height of the molecular ion to decrease by at least 50%. The analyses were accomplished in the negative-ion mode.

2.2.2. Performing of HPLC Analyses

Qualitative and quantitative analyses by high-performance liquid chromatography (HPLC—VWR/Hitachi LaChrom Elite®, Tokyo, Japan) on the release of p-AA from the respective (homo)- and (co)oligoesters were performed. The samples were filtered through syringe filters Iso-Disc™ (0.2 µm, Supelco®) (Sigma-Aldrich Chemie GmbH, Steinheim, Germany) and separated on a LiChrospher® RP-18 column (250 mm × 4 mm, 5 µm, Merck) protected by guard column LiChrospher® RP-18 (4 mm × 4 mm, 5 µm, Merck KGaA, Darmstadt, Germany). The mobile phase consisted of 0.1% formic acid in water and acetonitrile. Table 1 shows the solvent gradient used for separation. The flow rate was set at 1 mL/min. The evaluation was performed using diode array detector (DAD) at 254 nm. The samples were analyzed in triplicate. The standard curve of peak area versus acid concentration was constructed over the range from 0.03 to 125 µg/mL and subjected to linear regression analysis (R^2 = 0.9953). The calibration curve used for HPLC measurements is presented in Figure 1.

Table 1. Solvent gradient used for high-performance liquid chromatography (HPLC) analysis.

Time (min)	Mobile Phase (%)	
	A	B
0	75	25
5	75	25
20	60	40
25	55	45
45	45	55
50	75	25

A is 0.1% formic acid in water and B is acetonitrile.

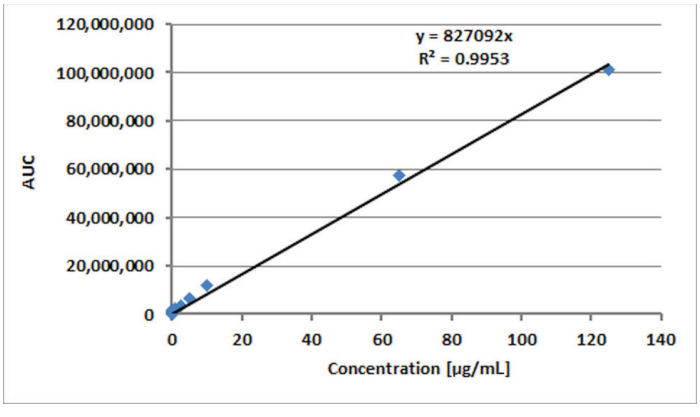

Figure 1. High-performance liquid chromatography (HPLC) calibration curve for p-anisic acid.

2.3. Assessment of Cytocompatibility of (Homo) and (Co)oligoesters Containing the p-Anisic Acid Moiety

2.3.1. Statistical Analysis

The data were analyzed by use of a one-way analysis of variance (ANOVA) followed by a Tukey post hoc test. All of the obtained results were expressed as means ± SD. *p*-value of <0.05 was considered statistically significant. The analysis was performed with a use of Statistica 13.3 software (StatSoft, Kraków, Poland).

2.3.2. SRB (Sulforhodamine B) Cell Proliferation Assay

The human keratinocyte HaCaT cell line (nontumorigenic, spontaneously immortalized cells) was purchased from Cell Lines Service (Eppelheim, Germany). Cells were cultured in DMEM (Dulbecco's Modified Eagle's Medium, Sigma-Aldrich, Chemie GmbH, Steinheim, Germany) containing 10% fetal bovine serum (PAN Biotech), 100 U/mL penicillin, 100 µg/mL streptomycin, and 20 mM HEPES (pH 7.3; Sigma-Aldrich, Chemie GmbH, Steinheim, Germany). Cell cultures were incubated at 37 °C in a humidified atmosphere with 5% CO_2. The synthesized (co)oligoesters (samples 1–2) and unconjugated p-anisic acid were dissolved in dimethyl sulfoxide (DMSO) to obtain stock solutions. Working solutions were made by combining stock solutions with a complete culture medium, and sterile filtered. The final concentration range of the studied compounds was 1–100 µg/mL. DMSO concentration in every culture medium (including control) was adjusted to 0.2%. As a positive control, treatment with 5% DMSO in the culture medium was applied.

In Vitro Toxicology Assay Kit, Sulforhodamine B Based (Sigma-Aldrich, Chemie GmbH, Steinheim, Germany) was utilized to study cell proliferation. Keratinocytes were seeded into 96-well plates at an initial density of 3×10^3 cells/well in 200 µL of medium. Cells were allowed to adhere and grow for 24 h. Then, the medium was replaced with working solutions, and keratinocytes were cultured for the next 72 h. After treatment, the culture medium was aspirated, and keratinocytes were fixed with 10% trichloroacetic acid, washed with deionized water, and stained with 0.4% SRB (sulforhodamine B) dissolved in 1% acetic acid. The unincorporated stain was washed out with 1% acetic acid and the incorporated sulforhodamine B was solubilized in 200 µL of 10 mM tris(hydroxymethyl)aminomethane solution. Absorbance was measured at 570 and 690 nm (reference wavelength) using the MRX Revelation plate reader (Dynex Technologies, Chantilly, VA, USA).

2.4. Hydrolytic Degradation Tests of Bioactive (p-AA-CH_2-PL)$_n$ Oligoester and [(p-AA-CH_2-HP)$_x$-co-(HB)$_y$] (Co)oligoester With the p-AA Moiety

Hydrolytic degradation tests were performed, according to our previously elaborated protocol [21,23], the specimens were inserted into a thermo-regulated incubator (Memmert GmbH, Schwabach, Germany) set at 37 °C in deionized water (pH = 7) in 15 mL screw-capped vials with an air-tight Polytetrafluoroethylene (PTFE)/silicone septum in a period of 14 days. Approximately 20 mg of (p-AA-CH_2-HP)$_n$ or [(p-AA-CH_2-HP)$_x$-co-(HB)$_y$] and 10 mL of aqua were mixed in glass vials. At different time intervals (24, 30, 48, 72 168, and 336 h), the aliquots were removed from the controlled environment and analyzed with the use of ESI-MS measurements accomplished in negative ion mode and by means of HPLC. The tests were carried out in triplicate.

3. Results and Discussion

We have recently developed an effective protocol for the preparation and characterization of (co)oligoesters containing bioactive moieties that were linked as pendant groups along oligomer backbones. The purpose of the current research was the preliminary assessment of the developed (co)oligoesters for their use as controlled DS for p-AA. The objects of this study were as follows: (p-AA-CH_2-HP)$_n$ (sample 1; see Section 2.1. Materials) oligoester and [(p-AA-CH_2-HP)$_x$-co-(HB)$_y$] (co)oligoesters (sample 2, see Section 2.1. Materials) containing p-AA (as the bioactive end and side groups) connected to the polymer backbone through the susceptible to hydrolysis and ester bonds [25].

3.1. Characterization of (p-AA-CH_2-HP)$_n$ Oligoester Degradation Products

To evaluate the future use of synthesized (co)oligoesters as delivery and release systems for specific antioxidants, we examined hydrolytic degradation and the release profile of p-anisic acid. We used ESI-mass spectrometry for monitoring of hydrolytic degradation progress, identification of released p-anisic acid, as well as analysis of water fractions collected after defined hydrolysis time

intervals that contained soluble in water degradation products formed during the hydrolysis process of the studied oligoesters.

Water solutions collected before (Figure 2a) and after 2 weeks (Figure 2b) of incubation of the (p-AA-CH_2-HP)$_n$ in water at a temperature of 37 °C were analyzed. ESI-mass spectra of the respective aliquots were acquired in the negative ion mode and are depicted in Figure 2.

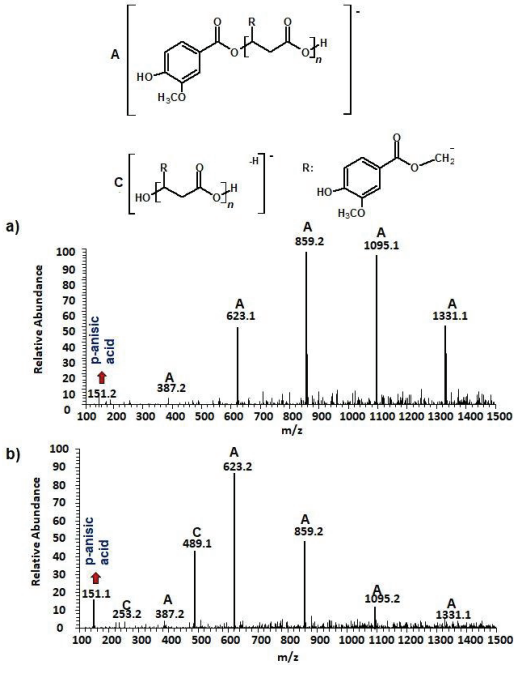

Figure 2. The negative electrospray (ESI) mass spectra of aqua solutions of the (p-AA-CH_2-HP)$_n$ (sample 1) (**a**) and medium collected after hydrolytic degradation (14 days) of the (p-AA-CH_2-HP)$_n$ at 37 °C together with chemical structures of the ions derived from series A and C (**b**).

One main series A of singly charged ions that occurred at 236 Da in a regular manner, which represent oligo(3-hydroxy-3-(4-methoxybenzoyloxymethyl)propionate) terminated by carboxylic and p-AA end groups, was observed in the mass spectrum depicted in Figure 2a. The shift of the distribution of ion patterns to the lower *m/z* values on the spectrum recorded after 2 weeks of the hydrolysis process was observed (Figure 2b). Furthermore, the intensity of the signals corresponding to oligoesters with lower molecular weights increased as a function of hydrolysis time (see Figure 2b). Thus, data obtained from ESI-MS analysis demonstrated that shorter (p-AA-CH_2-HP)$_n$ chains were formed. Additionally, the formation of oligo(3-hydroxy-3-(4-methoxy benzoyloxymethyl)-propionate) terminated by carboxylate and hydroxyl end groups (Series C) upholds the assumption that the hydrolysis process continued throughout the whole time-span regularly (Figure 2b). Moreover, the higher intensity signal at *m/z* 151 (corresponding to free p-AA) was observed, which confirms the hydrolysis process and release of the p-AA from the oligoester into the water fraction. The chemical structures of soluble in water degradation products (Series A and C) are depicted in Figure 2.

3.2. Characterization of [(p-AA-CH_2-HP)$_x$-co-(HB)$_y$] (Co)oligoester Degradation Products

The chemical structure of [(p-AA-CH_2-HP)$_x$-co-(HB)$_y$] (co)oligoesters, which were subjected to incubation in water after a specific period of time, was determined with the aid of ESI-MS analysis.

Figure 3 shows the negative ESI mass spectrum in a spectral expansion in the range *m/z* 600–1100 of the water fractions before (Figure 3a) and after 2 weeks (Figure 3b) of incubation of the (co)oligoesters samples in water at 37 °C. The resulting ESI mass spectrum in the case of (co)oligoester consisted of a large number of ions and is much more complex owing to the various combinations of two (p-AA-CH_2-HP) and (HB) comonomer units. To simplify the figures and Table 2, the abbreviation for the (p-AA-CH_2-HP) comonomer unit was used, that is, $(\text{p-AA-CH}_2\text{-HP})_x = A_x$. The peaks represented the individual (co)polyester chains at different polymerization degrees and their chemical composition has a tendency to group themselves in clusters. The major mass spacing that occurred between the signals belonging to the neighboring series was equal to 86 Da. These values correspond to the molecular weights of 3-hydroxybutyrate repeating units (86 Da).

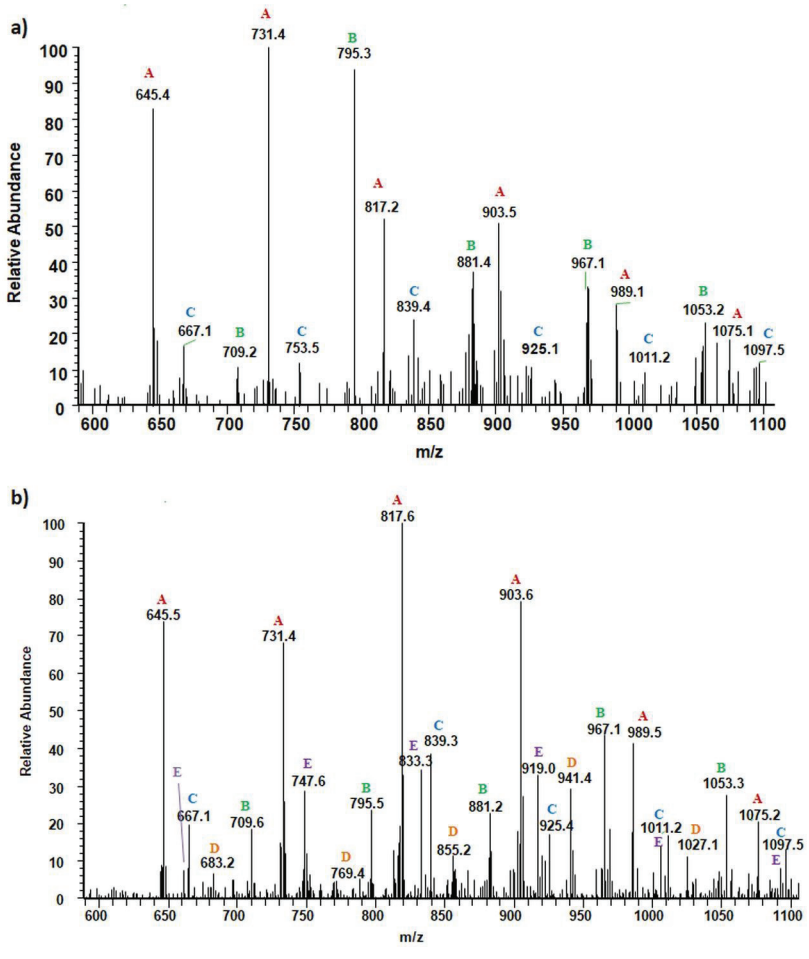

Figure 3. Spectral expansion in the range *m/z* 600–1100 of ESI-mass spectra (performed in negative ion-mode) of water solution of the $[(\text{p-AA-CH}_2\text{-HP})_x\text{-co-(HB)}_y]$ (co)oligoesters collected before incubation (sample 2) (**a**) and aqua-soluble degradation products collected after hydrolytic degradation (14 days) of the $[(\text{p-AA-CH}_2\text{-HP})_x\text{-co-(HB)}_y]$ (co)oligoesters at 37 °C (**b**).

Table 2. Structural assignments of ions present in the enlarged region (*m/z* 600–1100) of the electrospray mass spectrometry (ESI-MS) of the degradation products of [(p-AA-CH_2-HP)$_x$-co-(HB)$_y$]. Spectra depicted in Figures 3 and 4.

Series	Chemical Structure of the Ions	Composition of the Comonomers	*m/z*
		(p-AA-CH_2-HP)$_x$ = A$_x$	
A	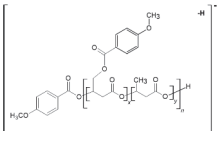	p-AA-A$_1$/HB$_3$	645
		p-AA-A$_1$/HB$_4$	731
		p-AA-A$_1$/HB$_5$	817
		p-AA-A$_1$/HB$_6$	903
		p-AA-A$_1$/HB$_7$	989
		p-AA-A$_1$/HB$_8$	1075
B	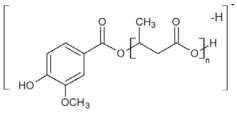	p-AA-A$_2$/HB$_1$	709
		p-AA-A$_2$/HB$_2$	795
		p-AA-A$_2$/HB$_3$	881
		p-AA-A$_2$/HB$_4$	967
		p-AA-A$_2$/HB$_5$	1053
C	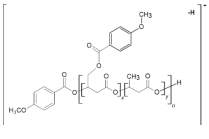	p-AA-HB$_6$	667
		p-AA-HB$_7$	753
		p-AA-HB$_8$	839
		p-AA-HB$_9$	925
		p-AA-HB$_{10}$	1011
		p-AA-HB$_{11}$	1097
D	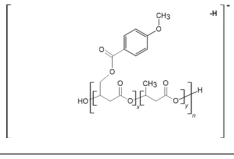	A$_1$/HB$_5$OH	683
		A$_1$/HB$_6$OH	769
		A$_1$/HB$_7$OH	855
		A$_1$/HB$_8$OH	941
		A$_1$/HB$_9$OH	1027
E	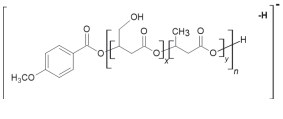	A$_2$/HB$_2$OH	661
		A$_2$/HB$_3$OH	747
		A$_2$/HB$_4$OH	833
		A$_2$/HB$_5$OH	919
		A$_2$/HB$_6$OH	1005
		A$_2$/HB$_7$OH	1091

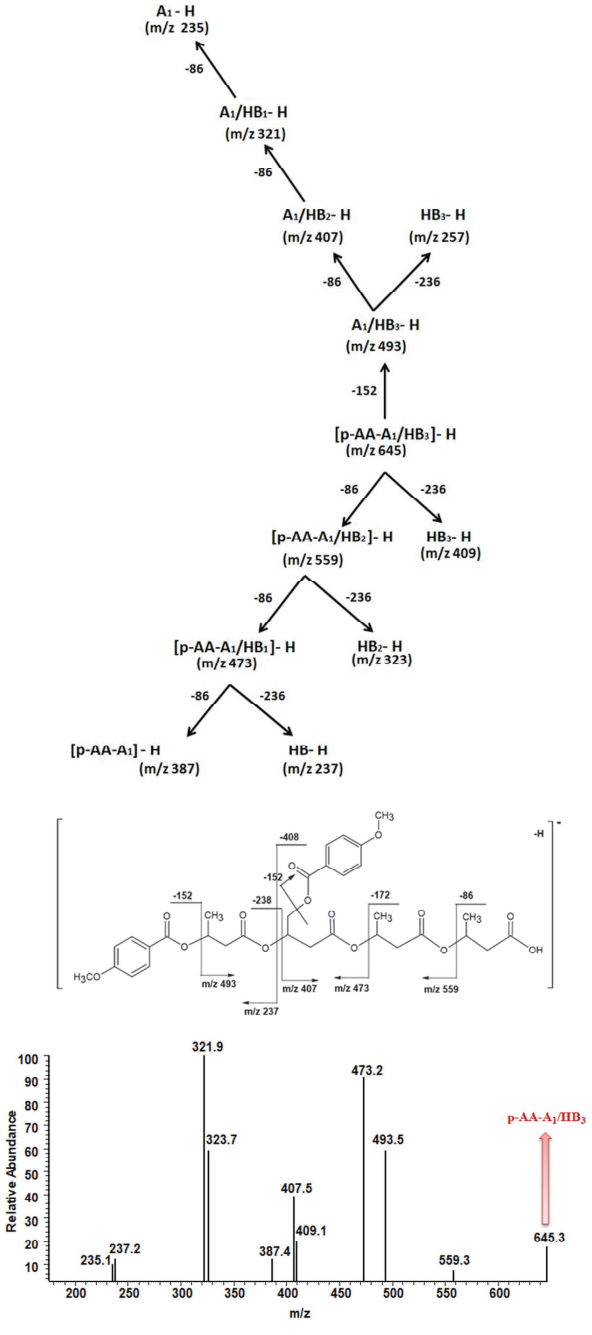

Figure 4. ESI-MS^2 spectrum (performed in negative-ion mode) of [p-AA-A_1/HB_3] (co)oligoester ion at *m/z* 645 with carboxylic and p-anisate end groups and possessing one p-AA-CH_2-HP comonomer unit together with the theoretical fragmentation pathway.

Two main series of ions present in the ESI mass spectra, which appear at $m/z = 151 + (n \times 86) + 236$ and $m/z = 151 + (n \times 86) + (2 \times 236)$ (Series A and B, Figure 3a and Table 2), correspond to the (co)oligoester chains terminated by carboxylic and p-anisate end groups. The above mentioned (co)oligoester chains contain one (Series A) or two (Series B) (p-AA-CH_2-HP) comonomer units arranged in a different combination with HB comonomer units along the oligomer backbone, (Series A) and (Series B), in Figure 3a and Table 2, respectively. In the mass spectra, we can observe a third and less abundant (with lower relative intensity) series of ions Series C (see Figure 3a and Table 2) at $m/z = 151 + (n \times 86)$. This series was ascribed to oligo(3-hydroxybutyrate) terminated by carboxyl and p-anisate moiety end groups. Table 2 contains the data with the ascribed structures of the ions presented in the ESI-MS spectra (Figure 3).

Additionally, in the mass spectra shown in Figure 3b, two series of anions, marked as Series D–E, were distinguished. These signals correspond to [(p-AA-CH_2-HP)$_x$-co-(HB)$_y$] chains terminated by hydroxyl and carboxylate end groups, which were formed during the hydrolysis process of the (co)oligoester studied. However, the formation of oligo-3-hydroxybutyrate terminated by carboxylate and hydroxyl end groups was not detected in the spectrum. Most probably, the lack of the detection of these signals was due to too low intensity of peaks, below the detection limit. The chemical structures of the identified oligomers (Series A–E) are depicted in Table 2.

A deeper knowledge of the structure of individual (co)oligoester chains was gained with the use of tandem ESI-MS/MS. This technique was also previously applied by us for structural studies of individual molecular ions selected from different types of copolymers and allowing differentiation of the individual molecular chains of the random and diblock copolyesters [27,28].

We applied tandem mass spectrometry (ESI-MS/MS) in order to confirm the structural assignment of the ions present in the obtained ESI-MS spectra. In particular, the acquired data were crucial to verify the distribution of p-AA-CH_2-HP and HB comonomers along the [(p-AA-CH_2-HP)$_x$-co-(HB)$_y$] (co)oligoester chains. Herein, we show as an example ESI-MS/MS spectrum (in negative ion mode) of the precursor ion at m/z 645, representing oligomers terminated by carboxyl and p-anisate moiety end groups. The verified ion of interest contained three 3-hydroxybutyrate repeating units and one p-AA-CH_2-HP unit distributed randomly in the (co)oligoester chain. The fragment ion at m/z 493 corresponds to the oligomer formed by the loss of p-AA (152 Da), which can be derived from the terminal group and/or from the pendant group of the p-AA-CH_2-HP comonomer unit. The product ion at m/z 559 represents the oligomer formed by the loss of the 3-hydroxybutyrate unit (crotonic acid; 86 Da) in the oligoester chains. The product ion at m/z 409 corresponds to the oligomer formed by the loss of the last, in the oligoester chain, p-AA-CH_2-HP comonomer unit in the form of 4-methoxybenzoyloxycrotonic acid (236 Da, see Scheme in Figure 4). The ESI-MS/MS spectrum and proposed fragmentation pathway clearly confirm that the p-AA-CH_2-HP comonomer units are arranged in a random manner in the oligomer chain.

Fragmentation of the precursor ion at m/z 645 (Series A, Figure 3 and Table 2) proceeds as a result of random cleavage of ester bonds along the oligomer chain and ester bonds between the chain and of p-anisate pendant group. In the case of solutions containing both acids and oligomers, the intensity of signals in the ESI spectra corresponding to acid molecules is lower than in the case of oligomers [29]. For a quantitative estimation of (co)oligoesters and acid content, based on ESI mass spectra obtained for mixtures, a separate calibration for each type of ingredient is required. Therefore, the release profile of p-anisic acid was determined separately by HPLC (see Section 3.3, *Comparative studies of the release of p-anisic acid from* (p-AA-CH_2-HP)$_n$ *oligoester and [(p-AA-CH_2-HP)$_x$*-co-*(HB)$_y$] (co)oligoesters*)).

3.3. Comparative Studies of the Release of p-Anisic Acid from (p-AA-CH_2-HP)$_n$ Oligoester and [(p-AA-CH_2-HP)$_x$-co-(HB)$_y$] (Co)oligoesters

The release studies of p-anisic acid from both (p-AA-CH_2-HP)$_n$ oligoester and [(p-AA-CH_2-HP)$_x$-co-(HB)$_y$] (co)oligoesters were performed in aqua solutions at 37 °C for the period of 14 days. To determine the amount and profile of the p-anisic acid release from

[(p-AA-CH_2-HP)$_x$-co-(HB)$_y$] copolymers, the mediums collected after a specific period of degradation of (co)oligoesters were analysed by high-performance liquid chromatography (HPLC) equipped with a DAD detector. The results of HPLC analysis, including the presence of p-anisic acid and calculated based on the calibration curve of the amount of acid released from the studied (co)oligoesters over time, are presented in Figure 5.

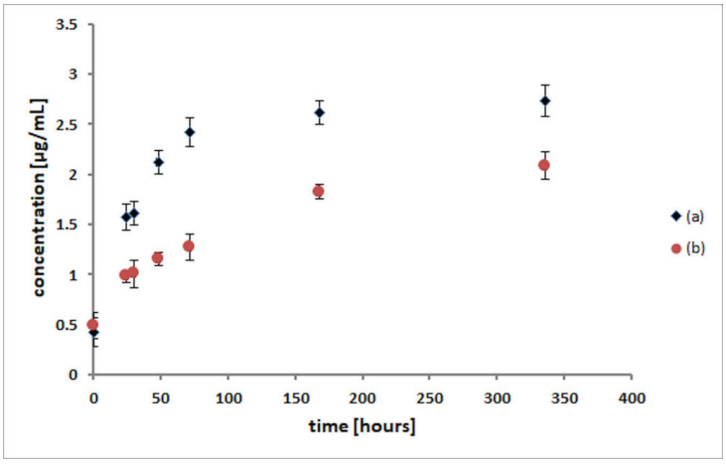

Figure 5. Comparative release profiles of p-anisic acid from (p-AA-CH_2-HP)$_n$ homo(oligoester) (**a**) and [(p-AA-CH2-HP)$_x$-co-(HB)$_y$] (co)oligoesters (**b**).

The amount of p-AA released from (p-AA-CH_2-HP)$_n$ oligoester and [(p-AA-CH_2-HP)$_x$-co-(HB)$_y$] (co)oligoesters was determined for 14 days. Initially, a slightly higher release rate was observed, but after 3 days, p-AA showed a relatively slower release rate. From the p-AA release profile, it is clear that almost 50% of the bioactive compound studied was released from the carrier in the first 3 days in the case of [(p-AA-CH_2-HP)$_x$-co-(HB)$_y$] and, in the case of (p-AA-CH_2-HP)$_n$, it was more than 75%. Additionally, we consider such concentrations as achievable in the epidermis, taking into account possible cosmetic formulations, as well as release and absorption rates described in our previous work in this field [23]. We should highlight that the release of a bioactive agent proceeded regularly. However, the release rate of p-AA was much faster for (p-AA-CH_2-HP)$_n$, which is an expected result as this carrier possessed a higher loading of p-AA per polymer macromolecule compared with (co)oligoester carrier (Figure 5). As we described previously, bioactive oligoesters that contain from 1 to 8 of p-AA molecules and (co)oligoesters that contain from 2 to 3 molecules of the p-AA moiety (as the bioactive end and side groups) were synthesized [25].

3.4. Cytocompatibility of (Homo)- and (Co)oligoesters Containing p-AA Moiety

SRB Assay for Cell Proliferation

To study the cytocompatibility of the synthesized (homo)- and (co)oligoesters with biosystems, their effects on cell growth were measured using sulforhodamine B staining. The HaCaT cell line was derived from normal human epidermis and the cells underwent spontaneous immortalization during successive passages [30]. These cells are not tumorigenic and they retained some properties of normal keratinocytes such as contact inhibition of proliferation or the ability to differentiate [31]. Therefore, the HaCaT cell line has become a popular model for testing dermal drugs and cosmetics. In the culture flask, this cell line grows as a monolayer of densely packed cells (Figure 6). The substances tested in our study were applied over a relatively wide concentration range (1–100 µg/mL). The concentration range of p-anisic acid (and its conjugates) was set up based on data referring to the biological

activities of that compound. It has been shown to influence the enzymatic activity of proteasome and lysosomal cathepsins at such low concentrations as 5 μM (0.76 μg/mL) [32]. Inhibition of tyrosinase activity was detectable from 0.1 mM (15 μg/mL), with an IC50 value 0.6 mM (91 μg/mL) [33]. Antiproliferative activity of p-anisic acid against HepG2 cancer cell line was observed for the concentration range of 1–100 μM, with IC50 coming to 25 μM (3.8 μg/mL) [34]. On the other hand, we consider such concentrations as achievable in the epidermis, taking into account possible cosmetic formulations, as well as release and absorption rates [23].

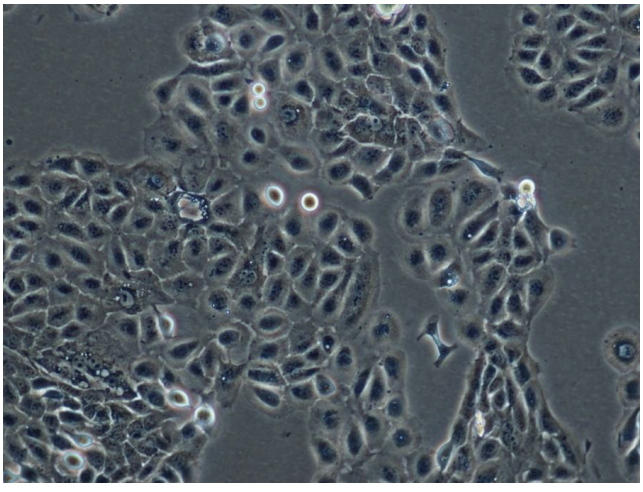

Figure 6. Phase-contrast micrograph of HaCaT keratinocytes in culture flask (original magnification: ×100).

As shown in Figure 7A, (p-AA-CH_2-HP)$_n$ did not exert any detrimental effect on keratinocyte proliferation. In fact, in treated wells, average cell numbers were greater than in the control. The statistical analysis revealed significant differences in cultures treated with (p-AA-CH_2-HP)$_n$ at concentrations of 10 and 30 μg/mL. As shown in Figure 7C, free p-anisic acid exerted a significant cell growth promotion effect at the concentration of 100 μg/mL. Mechanisms responsible for that effect are unknown as only scant information exists on the p-methoxybenzoic acid impact on human cell functions. It has been previously suggested that the conjugates of drugs and oligo-(R,S)-(3-hydoxybutyrate) (OHB) are more efficiently taken up by cells, compared with non-conjugated molecules [35]. More efficient accumulation inside cells would explain the ability of our (homo)oligoester to stimulate keratinocyte proliferation at lower concentrations, compared with the free acid.

A pattern of keratinocyte response to [(p-AA-CH_2-HP)$_x$-co-(HB)$_y$] was slightly different (Figure 7B). That is, (co)oligoester increased cell proliferation at concentrations of 3, 10, and 30 μg/mL, but inhibited cellular growth at the highest dose (100 μg/mL). In our previous research [23], we demonstrated some growth inhibitory properties of oligo(3-hydroxybutyrate) carriers in HaCaT cells. Zawidlak-Wegrzynska et al. [35] demonstrated that conjugation of ibuprofen with OHB increased its antiproliferative effects in colon cancer HT-29 and HCT 116 cell lines. OHB oligomer alone also exhibited some growth inhibitory action, though at relatively large concentrations. Oligo(3-hydroxybutyrate) loaded into liposomes reduced the growth of L929 cells and induced cell death and cell cycle arrest at the G_1/G_0 phase [36]. On the basis of these observations, we suggest that the presence of HB units in the [(p-AA-CH_2-HP)$_x$-co-(HB)$_y$] chain and somewhat greater molecular mass could possibly favour the revealing of its antiproliferative activity in the present study. The mechanism underlying the antiproliferative effect of OHB is currently unknown. However, it is worth pointing out that 3-hydroxybutyrate dose-dependently decreased proliferation of the human kidney HK-2 cell line [37]. It was accompanied by cell cycle arrest at the G_0/G_1 phase and increased $p21^{WAF1}$ as well as $p27^{kip1}$

protein expression. These changes were mediated by oxidative stress, Smad3, and TGF-β. It has been shown that mammalian cells or body fluids (as serum) are able to hydrolyse dimers and trimers of 3-hydroxybutyrate owing to the action of enzymes, for example, carboxylesterase [38]. Therefore, 3-hydroxybutyrate could mediate the growth inhibitory effects of [(p-AA-CH_2-HP)$_x$-co-(HB)$_y$]. After all, mild inhibition of HaCaT cell growth was seen solely at a very high concentration of the studied (co)oligoester, which allows considering it biocompatible. In practice, it is advisable to carefully adjust its concentration in cosmetic preparation to obtain an optimal effect on epidermal cells.

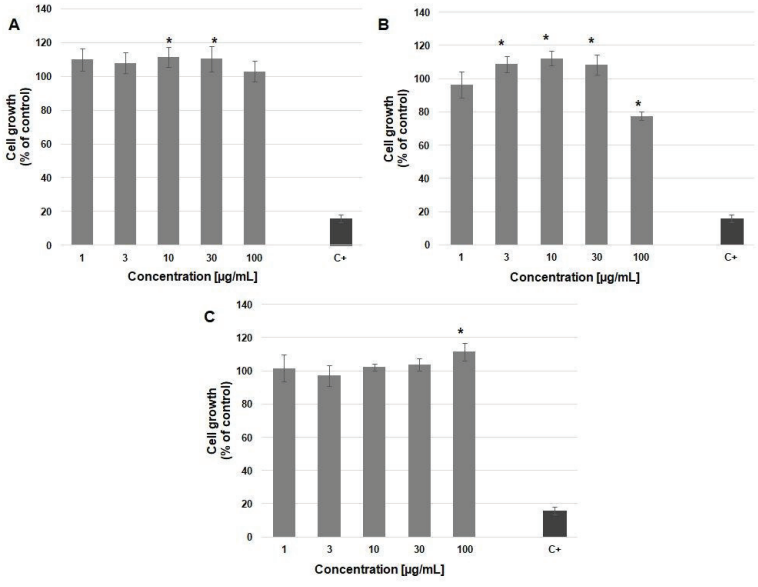

Figure 7. Growth of HaCaT cells in the presence of (**A**) (p-AA-CH_2-HP)$_n$; (**B**) [(p-AA-CH_2-HP)$_x$-co-(HB)$_y$]; and (**C**) p-anisic acid. Each bar represents the mean ± SD; * $p < 0.05$ versus the control group (analysis of variance, ANOVA); C+—positive control.

4. Conclusions

With regard to likely applications of the developed (p-AA-CH_2-HP)$_n$ and [(p-AA-CH_2-HP)$_x$-co-(HB)$_y$] (co)oligoesters in the area of biomaterials, especially in cosmetology, comprehensive in vitro cytotoxicity tests as well as hydrolytic degradation under laboratory conditions were performed.

The application of ESI-mass spectrometry to characterize aqua-soluble hydrolytic degradation products of (p-AA-CH_2-HP)$_n$ oligoesters and [(p-AA-CH2-HP)$_x$-co-(HB)$_y$] (co)oligoesters allowed us to determine their molecular level chemical structure and helped us to confirm the release of bioactive p-AA from the developed systems.

Biological comparative in vitro studies showed that the synthesized (co)oligoesters were non-toxic and were well tolerated by the HaCaT cells. Both (homo)- and (co)oligoesters exerted a beneficial effect on keratinocyte growth, especially at moderate concentrations. The highest concentration of the (co)oligoester caused only a mild inhibition of cell proliferation. The presented study shows the potential of the developed (homo)- and (co)oligoesters as novel controlled release and delivery systems for future applications in the cosmetics industry.

Author Contributions: Conceptualization, G.A. and M.M.M.; Methodology, M.M.M., G.A., A.O., and M.M-K.; Formal Analysis, M.M.M., M.Z., and A.O.; Investigation, M.M.M., M.Z., A.O., and M.M.-K.; Writing—Original Draft Preparation, M.M.M., G.A., and A.O.; Writing—Review & Editing, G.A. and M.M.M.; Supervision, G.A. and M.K. All authors have read and agreed to the published version of the manuscript.

Funding: This research was partially funded by the European Union's Horizon 2020 research and innovation program under the Marie Sklodowska-Curie grant agreement No 872152, project GREEN-MAP.

Acknowledgments: The authors are grateful to the late Tomasz Balakier for the synthesis of monomer (p-AA-CH_2-PL), conducted under the guidance of Janusz Jurczak from the Institute of Organic Chemistry, Polish Academy of Sciences.

Conflicts of Interest: The authors declare no conflict of interest.

References

1. Pandey, K.B.; Rizvi, S.I. Plant polyphenols as dietary antioxidants in human health and disease. *Oxid. Med. Cell Longev.* **2009**, *2*, 270–278. [CrossRef] [PubMed]
2. Parrado, C.; Mascaraque, M.; Gilaberte, Y.; Juarranz, A.; Gonzalez, S. Fernblock (*Polypodium leucotomos* Extract): Molecular Mechanisms and Pleiotropic Effects in Light-Related Skin Conditions, Photoaging and Skin Cancers, a Review. *Int. J. Mol. Sci.* **2016**, *17*, 1026. [CrossRef] [PubMed]
3. Othman, A.; Norton, L.; Finny, S.; Andreescu, S. Easy-to-use and inexpensive sensors for assessing the quality and traceability of cosmetic antioxidants. *Talanta* **2020**, *208*, 120473. [CrossRef] [PubMed]
4. Herman, A. Antimicrobial Ingredients as preservative booster and components of self-preserving cosmetic products. *Curr. Microbiol.* **2019**, *76*, 744–754. [CrossRef]
5. Papageorgiou, S.; Varvaresou, A.; Tsirivas, E.; Demetzos, C. New alternatives to cosmetics preservation. *J. Cosmet. Sci.* **2010**, *61*, 107–123.
6. Straetmans, U.; Janichen, J.; Petersen, W.; Kinder, M.; Johnson, C.; Reynolds, G. Concentrated, aqueous solutions of p-methoxybenzoic acid for use in cosmetic and dermatologic formulations. U.S. Patent 20060229291 A1, 12 October 2006.
7. Sautour, M.; Mitaine-Offer, A.-C.; Lacaille-Dubois, M.-A. The *Dioscorea* genus: A review of bioactive steroid saponins. *J. Nat. Med.* **2007**, *61*, 91–101. [CrossRef]
8. Varvaresou, A.; Papageorgiou, S.; Tsirivas, E.; Protopapa, E.; Kintziou, H.; Kefala, V.; Demetzos, C. Self-preserving cosmetics. *Int. J. Cosm. Sci.* **2009**, *31*, 163–175. [CrossRef]
9. Lupo, M.P. Antioxidants and vitamins in cosmetics. *Clin. Dermatol.* **2001**, *19*, 467–473. [CrossRef]
10. Costa, R.; Santos, L. Delivery systems for cosmetics—From manufacturing tothe skin of natural antioxidants. *Powder Technol.* **2017**, *322*, 402–416. [CrossRef]
11. Rancan, F.; Blume-Peytavi, U.; Vogt, A. Utilization of biodegradable polymeric materials as delivery agents in dermatology. *Clin. Cosmet. Investig. Dermatol.* **2014**, *7*, 23–34. [CrossRef]
12. Albertsson, A.-C.; Varma, I.K. Recent developments in ring opening polymerization of lactones for biomedical applications. *Biomacromolecules* **2003**, *4*, 1466–1486. [CrossRef]
13. Michalak, M.; Jurczyk, S.; Jelonek, K.; Hakkarainen, M.; Kurcok, P. Polyhydroxyalkanoates as promising materials in biomedical systems. In *Frontiers in Drug Design and Discovery*; Rahman, A., Choudhary, I., Eds.; Bentham Science Publishers: Sharjah, UAE, 2017; Volume 8, Chapter 5; pp. 242–288.
14. Pommier, A.; Pons, J.M. Recent Advances in β-Lactone Chemistry. *Synthesis* **1993**, *5*, 441–459. [CrossRef]
15. Rieth, L.R.; Moore, D.R.; Lobkovsky, E.B.; Coates, G.W. Single-Site ß-Diiminate Zinc Catalysts for the Ring-Opening Polymerization of ß-Butyrolactone and ß-Valerolactone to Poly(3-hydroxyalkanoates). *J. Am. Chem. Soc.* **2002**, *124*, 15239–15248. [CrossRef] [PubMed]
16. Adamus, G.; Kowalczuk, M. Synthesis of Poly(2-methyl-3-hydroxyoctanoate) via Anionic Polymerization of α-Methyl-β-pentyl-β-propiolactone. *Biomacromolecules* **2008**, *9*, 696–703. [CrossRef] [PubMed]
17. Getzler, Y.D.Y.L.; Mahadevan, V.; Lobkovsky, E.B.; Coates, G.W. Synthesis of ß-Lactones: A highly active and selective catalyst for epoxide carbonylation. *J. Am. Chem. Soc.* **2002**, *124*, 1174–1175. [CrossRef] [PubMed]
18. Schmidt, J.A.R.; Mahadevan, V.; Getzler, Y.D.Y.L.; Coates, G.W. A readily synthesized and highly active epoxide carbonylation catalyst based on a chromium porphyrin framework. Expanding the range of available ß-Lactones. *Org. Lett.* **2004**, *6*, 373–376. [CrossRef]
19. Kramer, J.W.; Lobkovsky, E.B.; Coates, G.W. Practical ß-Lactone Synthesis: Epoxide Carbonylation at 1 atm. *Org. Lett.* **2006**, *8*, 3709–3712. [CrossRef]
20. Mundlia, J.; Ahuja, M.; Kumar, P. Enhanced biological activity of polyphenols on conjugation with gellan gum. *Int. J. Polym. Mater.* 2020. [CrossRef]

21. Maksymiak, M.; Dębowska, R.; Jelonek, K.; Kowalczuk, M.; Adamus, G. Structural characterization of biocompatible lipoic acid–oligo-(3-hydroxybutyrate) conjugates by electrospray ionization mass spectrometry. *Rapid Commun. Mass Spectrom.* **2013**, *27*, 773–783. [CrossRef]
22. Maksymiak, M.; Kowalczuk, M.; Adamus, G. Electrospray tandem mass spectrometry for the structural characterization of p-coumaric acid–oligo(3-hydroxybutyrate) conjugates. *Int. J. Mass Spectrom.* **2014**, *359*, 6–11. [CrossRef]
23. Maksymiak, M.; Debowska, R.; Bazela, K.; Dzwigalowska, A.; Orchel, A.; Jelonek, K.; Dolegowska, B.; Kowalczuk, M.; Adamus, G. Designing of Biodegradable and Biocompatible Release and Delivery Systems of Selected Antioxidants Used in Cosmetology. *Biomacromolecules* **2015**, *16*, 3603–3612. [CrossRef] [PubMed]
24. Adamus, G.; Kwiecień, I.; Maksymiak, M.; Bałakier, T.; Jurczak, J.; Kowalczuk, M. Molecular level structure of novel synthetic analogues of aliphatic biopolyesters as revealed by multistage mass spectrometry. *Anal. Chim. Acta.* **2014**, *808*, 104–114. [CrossRef]
25. Maksymiak, M.; Bałakier, T.; Jurczak, J.; Kowalczuk, M.; Adamus, G. Bioactive (co)oligoesters with antioxidant properties—Synthesis and structural characterization at the molecular level. *RSC Adv.* **2016**, *6*, 57751–57761. [CrossRef]
26. Bałakier, T.; Chaładaj, W.; Jurczak, J.; Adamus, G.; Kowalczuk, M. An effective protocol for the synthesis enantiomerically pure 4-substituted oxetane-2-ones. *Tetrahedron* **2013**, *69*, 4990–4993. [CrossRef]
27. Adamus, G. Molecular Level Structure of (R,S)-3-hydroxybutyrate/(R,S)-3-hydroxy-4-ethoxybutyrate Copolyesters with Dissimilar Architecture. *Macromolecules* **2009**, *42*, 4547–4557. [CrossRef]
28. Kowalczuk, M.; Adamus, G. Mass spectrometry for the elucidation of the subtle molecular structure of biodegradable polymers and their degradation products. *Mass Spectrom. Rev.* **2016**, *35*, 188–198. [CrossRef]
29. Adamus, G.; Hakkarainen, M.; Höglund, A.; Kowalczuk, M.; Albertsson, A.C. MALDI-TOF-MS reveals the molecular level structures of different hydrophilic-hydrophobic polyether-esters. *Biomacromolecules* **2009**, *10*, 1540–1546. [CrossRef]
30. Boukamp, P.; Petrussevska, R.T.; Breitkreutz, D.; Hornung, J.; Markham, A.; Fusenig, N.E. Normal keratinization in a spontaneously immortalized aneuploid human keratinocyte cell line. *J. Cell Biol.* **1988**, *106*, 761–771. [CrossRef]
31. Schoop, V.M.; Mirancea, N.; Fusenig, N.E. Epidermal organization and differentiation of HaCaT keratinocytes in organotypic coculture with human dermal fibroblasts. *J. Investig. Dermatol.* **1999**, *112*, 343–353. [CrossRef]
32. Georgousaki, K.; Tsafantakis, N.; Gumeni, S.; Lambrinidis, G.; González-Menéndez, V.; Tormo, J.R.; Genilloud, O.; Trougakos, I.P.; Fokialakis, N. Biological evaluation and in silico study of benzoic acid derivatives from *Bjerkandera adusta* targeting proteostasis network modules. *Molecules* **2020**, *25*, 666. [CrossRef]
33. Kubo, I.; Chen, Q.X.; Nihei, K.; Calderón, J.S.; Céspedes, C.L. Tyrosinase inhibition kinetics of anisic acid. *Z. Naturforsch. C J. Biosci.* **2003**, *58*, 713–718. [CrossRef] [PubMed]
34. El-Hawary, S.S.; Sayed, A.M.; Mohammed, R.; Hassan, H.M.; Zaki, M.A.; Rateb, M.E.; Mohammed, T.A.; Amin, E.; Abdelmohsen, U.R. Epigenetic modifiers induce bioactive phenolic metabolites in the marine-derived fungus *Penicillium brevicompactum*. *Mar. Drugs* **2018**, *16*, 253. [CrossRef] [PubMed]
35. Zawidlak-Wegrzyńska, B.; Kawalec, M.; Bosek, I.; Łuczyk-Juzwa, M.; Adamus, G.; Rusin, A.; Filipczak, P.; Głowala-Kosińska, M.; Wolańska, K.; Krawczyk, Z.; et al. Synthesis and antiproliferative properties of ibuprofen-oligo(3-hydroxybutyrate) conjugates. *Eur. J. Med. Chem.* **2010**, *45*, 1833–1842. [CrossRef] [PubMed]
36. Sun, J.; Dai, Z.; Zhao, Y.; Chen, G.Q. In vitro effect of oligo-hydroxyalkanoates on the growth of mouse fibroblast cell line L929. *Biomaterials* **2007**, *28*, 3896–3903. [CrossRef] [PubMed]
37. Guh, J.Y.; Chuang, T.D.; Chen, H.C.; Hung, W.C.; Lai, Y.H.; Shin, S.J.; Chuang, L.Y. Beta-hydroxybutyrate-induced growth inhibition and collagen production in HK-2 cells are dependent on TGF-beta and Smad3. *Kidney Int.* **2003**, *64*, 2041–2051. [CrossRef]
38. Tasaki, O.; Hiraide, A.; Shiozaki, T.; Yamamura, H.; Ninomiya, N.; Sugimoto, H. The dimer and trimer of 3-hydroxybutyrate oligomer as a precursor of ketone bodies for nutritional care. *JPEN J. Parenter. Enteral. Nutr.* **1999**, *23*, 321–325. [CrossRef]

materials

MDPI

Article

pH-Sensitive Dairy-Derived Hydrogels with a Prolonged Drug Release Profile for Cancer Treatment

Oksana A. Mayorova [1,*], Ben C. N. Jolly [2], Roman A. Verkhovskii [1], Valentina O. Plastun [1], Olga A. Sindeeva [1,3] and Timothy E. L. Douglas [2,4,*]

[1] Institute of Nanostructures and Biosystems, Saratov State University, 83 Astrakhanskaya st., 410012 Saratov, Russia; r.a.verhovskiy@mail.ru (R.A.V.); voplastun@gmail.com (V.O.P.); o.sindeeva@skoltech.ru (O.A.S.)
[2] Engineering Department, Lancaster University, Gillow Av., Lancaster LA1 4YW, UK; bcnjolly001@gmail.com
[3] Skolkovo Institute of Science and Technology, Skolkovo Innovation Center, Building 3, 143026 Moscow, Russia
[4] Materials Science Institute (MSI), Lancaster University, Gillow Av., Lancaster LA1 4YW, UK
* Correspondence: Beloousova011@yandex.ru (O.A.M.); t.douglas@lancaster.ac.uk (T.E.L.D.)

Abstract: A novel versatile biocompatible hydrogel of whey protein isolate (WPI) and two types of tannic acid (TAs) was prepared by crosslinking of WPI with TAs in a one-step method at high temperature for 30 min. WPI is one common protein-based preparation which is used for hydrogel formation. The obtained WPI-TA hydrogels were in disc form and retained their integrity after sterilization by autoclaving. Two TA preparations of differing molecular weight and chemical structure were compared, namely a polygalloyl glucose-rich extract-ALSOK 02-and a polygalloyl quinic acid-rich extract-ALSOK 04. Hydrogel formation was observed for WPI solutions containing both preparations. The swelling characteristics of hydrogels were investigated at room temperature at different pH values, namely 5, 7, and 9. The swelling ability of hydrogels was independent of the chemical structure of the added TAs. A trend of decrease of mass increase (MI) in hydrogels was observed with an increase in the TA/WPI ratio compared to the control WPI hydrogel without TA. This dependence (a MI decrease-TA/WPI ratio) was observed for hydrogels with different types of TA both in neutral and acidic conditions (pH 5.7). Under alkaline conditions (pH 9), negative values of swelling were observed for all hydrogels with a high content of TAs and were accompanied by a significant release of TAs from the hydrogel network. Our studies have shown that the release of TA from hydrogels containing ALSOK04 is higher than from hydrogels containing ALSOK 02. Moreover, the addition of TAs, which display a strong anti-cancer effect, increases the cytotoxicity of WPI-TAs hydrogels against the Hep-2 human laryngeal squamous carcinoma (Hep-2 cells) cell line. Thus, WPI-TA hydrogels with prolonged drug release properties and cytotoxicity effect can be used as anti-cancer scaffolds.

Keywords: whey protein isolate; hydrogel; tannic acid; anticancer scaffold

Citation: Mayorova, O.A.; Jolly, B.C.N.; Verkhovskii, R.A.; Plastun, V.O.; Sindeeva, O.A.; Douglas, T.E.L. pH-Sensitive Dairy-Derived Hydrogels with a Prolonged Drug Release Profile for Cancer Treatment. *Materials* **2021**, *14*, 749. https://doi.org/10.3390/ma14040749

Academic Editor: Franz E. Weber
Received: 16 December 2020
Accepted: 29 January 2021
Published: 5 February 2021

1. Introduction

Recently, much attention has been paid to hydrogels in drug delivery. In this regard, hydrogels must comply with principles such as biocompatibility, biodegradation, and non-toxicity. One common protein-based preparation used for hydrogel formation in the food industry is whey protein isolate (WPI), which we have recently begun to investigate as a hydrogel biomaterial for biomedical applications [1–4]. The major component of WPI is ß-lactoglobulin (approximate composition 74.1%) and the second major component is α-lactalbumin (23.0%) [5]. Whey proteins have been identified to have desirable properties because they consist of branched-chain amino acids which promote highly hydrated three-dimensional polymer networks in hydrogels [6]. Gelation occurs by increasing the temperature due to denaturation of native ß-lactoglobulin protein [7]. The process of whey protein aggregation consists of three stages, including conformational changes of the native

protein structure, chemical reactions typically through disulfide bridges between intra- and interchain bonds and physical interactions like hydrophobic interactions, which leads to aggregation clustering and the formation of a spatial gel network [8]. The increased comparison of ß-lactoglobulin allows to fabricate more elastic WPI hydrogels with far superior mechanical properties compered to hydrogels based on whey protein concentrate. The important functional property of a WPI hydrogels is its high ability to retain water or body fluids within its structure. The WPI denaturing permits exposure of hydrophobic regions of the protein molecule, to which the hydrophobic regions of hydrophobic drugs can bind, resulting in increased drug solubility. Cytocompatible hydrogels have been successfully used to develop drug delivery systems due to their stimulus-sensitive response to external triggers, such as pH [9]. Hence, it would be desirable to combine the ability of WPI hydrogels to solubilize and carry hydrophobic drugs with pH responsiveness.

One class of hydrophobic molecules with biological activity are tannic acids (TAs). TAs are polyphenols closely related to our daily life: They are found in many fruits and vegetables consumed by humans and are used in the food industry and herbal medicine. Hydrolyzable tannins are one of three types of TAs that are formed by a carbohydrate (glucose, quinic acid, or other), in which OH-groups are partially or completely esterified with gallic acid or related compounds [10–12]. In this context hydrolyzable means that ester hydrolysis can occur, as opposed to acid-base hydrolysis (deprotonation). Hydrolyzable tannins can be extracted from various vegetable plants and trees. As a rule, TAs are considered non-toxic in small doses [13,14] and exhibit antitumor effects [15]. The presence of TA in natural components can reduce tumor necrosis factor levels [16] and weaken the inflammatory cytokine expression [17]. Previously, it was shown that TA crosslinked into a compacting collagen gel predominantly inhibited proliferation of high-melanoma A375 cells with metastatic potential [18]. In addition, ternary composite nanofibers containing tannic acid can be used as wound dressings in the case of recessive dystrophic epidermolysis bullosa, which often leads to the development of an aggressive form of squamous cell carcinoma [19]. TA has been shown to help crosslinking of gelatin and pectin derivatives due to the presence of a large number of hydroxyl groups in the polyphenol structure due to intermolecular H-bond formation, in which the polyphenols act as electron pair donors [20]. From the physicochemical point of view, polyphenols stabilize the secondary structure of proteins, increase their thermal stability and significantly reduce their biodegradability [21]. Recently, a comparative analysis was carried out of the ability of gellan gum hydrogels enhanced with polyphenols (including the ones investigated in our research, ALSOK 02 and ALSOK 04), to enzymatic mineralization and the hydroxyapatite formation [22]. TA inclusion inhibited the growth of human osteoblast-like Saos-2 cells on substrates of mineralized gellan gum hydrogel biomaterials with calcium phosphate and did not confer antibacterial activity against *Escherichia coli*.

In this study, we combined the beneficial properties of TAs and WPI to create new pH-sensitive cytocompatible hydrogels which display an anticancer affect. Two TAs of differing molecular weight and chemical structure (polygalloyl glucoses—ALSOK 02 and polygalloyl quinic acids—ALSOK 04) were compared using swelling tests at different pH values. We hypothesized that the addition of TAs would reduce the swelling of WPI hydrogels due to the aforementioned interactions between polyphenols and proteins. To our best knowledge, this combination of components has not yet been tested for biomaterial-related applications. We focused on the dependence of the swelling ability of hydrogels on pH of the medium, chemical structure, and concentration of TAs, which allowed a more prolonged release of TAs over several days. The behavior of hydrogels that are sensitive to external pH are especially in demand in the development of anticancer scaffolds. The cytotoxic activity of TA and WPI-based hydrogels were evaluated in vitro against the Hep-2 human laryngeal squamous carcinoma cell line (Hep-2 cells).

2. Materials and Methods

2.1. Materials

Phosphate buffered saline (PBS, 0.01 M), iron(III) chloride (tetrahydrate) were obtained from Sigma-Aldrich (Steinheim, Germany). AlamarBlue (Cell Viability Reagent) was obtained from Invitro-gen (Waltham, MS, USA). Hydrochloric acid and sodium hydroxide was purchased from Reakhim (Moscow, Russia) and used without further purification. WPI (BiPRO, Davisco Foods Int., Inc., Eden Prairie, MN, USA) with 97.7% protein and 75% BGL in dry matter (according to the specification) was used as described previously [6]. TAs (ALSOK 02; MW 1040 D; pentagalloyl glucose 20% by weight; ALSOK 04; MW 850 D) was purchased from Omnichem NV Belgium (Wetteren, Belgium). Millipore Milli Q water (18.2 MΩ cm^{-1}) was used as an aqueous medium during all sets of experiments.

2.2. Methods

2.2.1. Hydrogel Preparation

The hydrogel preparation was carried out by thermally-induced gelation. Hydrogels were fabricated with four different concentrations of TAs: 1.5, 3.0, 6.0, and 12.0 mg per mL which corresponds to the TA/WPI ratios were 0.0375/0.075/0.15/0.30 in the hydrogels; a control sample without the TA addition was also prepared. The required amount of TAs was added to the initial solution consisting of 40 mg per mL WPI [23]. All WPI hydrogels were prepared from a solution at pH 7.0. The protein–polyphenol solutions were left in the refrigerator overnight to remove excess air bubbles present. The solutions were transferred to plastic Petri dishes. Gelation was carried out at 90 °C for 30 min in an oven. Each cm^2 of the Petri dish surface area was occupied by 0.31 mL hydrogel. The resulting hydrogels were then transferred to glass Petri dishes for further autoclaving at 121 °C for 15 min before any further characterization.

2.2.2. Swelling Study in Phosphate Buffered Saline (PBS) with Different pH Values

The behavior of the swelling of the hydrogel samples was carried out in PBS at different pH values (pH 5, 7, 9). The desired basic and acidic pH values were obtained by pH adjustment using NaOH and HCl solutions, respectively. To measure the swelling, after autoclaving, samples of the excised hydrogel discs (diameter 3 mm) were dried at 80 °C for 1 h, then a dried sample with known weight was placed in 24-well plates and incubated in a solution (1:10). The swelling process took place at room temperature for up to 48 h. Swollen gels were periodically (1, 24, and 48 h) removed, blotted on dry filter paper to remove excess water and immediately weighed. Then, the mass increase (*MI*) was calculated as:

$$MI\ (\%) = ((Mt - Mo)/Mo) \times 100$$

where *Mt* is the weight of the hydrogel at a certain time, *Mo* is the initial hydrogel weight. All experiments were carried out with $n = 6$.

2.2.3. Fourier Transform Infrared (FTIR) Spectroscopy

The chemical structure of the synthesized WPI hydrogels was investigated by using Fourier Transform Infrared spectroscopy using a Fourier-transform infrared (FTIR) spectrophotometer (Agilent Technology, Oxfordshire, UK) in attenuated total reflectance (ATR) mode. Spectra were collected in the 500–4000 cm^{-1} spectral range with a resolution of 4 cm^{-1} and an average of 8 scans.

2.2.4. In Vitro Release Studies

The TA release from WPI hydrogels was measured using a spectrophotometer (Multi-Mode Reader Synergy H1, BioTek, Winooski, VT, USA) at 48 h after incubation. A dried hydrogel sample was weighed accurately and then incubated in PBS at room temperature for up to 48 h. At the indicated time, a few drops of 0.5 N iron(III) chloride were added

to the selected aliquot, and the optical density of the solutions was measured at 586 nm (Figures S1 and S2) [24]. The tests were conducted on six independent replicates.

2.2.5. Cell Viability Test

Cells were seeded in 96-well plates at the density described in the individual experiments. The following day, the excised hydrogel discs (diameter 3 mm) were added to triplicate wells. Fresh medium was added to each of 96 wells. Subsequently, the cells were incubated (Innova CO-170, New Brunswick Scientific, Enfield, CT, USA) at 37 °C for 48 h, together with the added materials. In the last step, 10 µL of AlamarBlue dye was added to each well and the intensity was measured using a spectrophotometer (Multi-Mode Reader Synergy H1). The experiment showed the capability of metabolically active cells to convert the AlamarBlue reagent into a fluorescent and colorimetric indicator. [25].

A commercially available laryngeal cancer cell line, Hep-2 (ATCC, CCL-23) was kindly provided by the center "Symbiosis" IBPPM RAS (Saratov, Russia).

2.2.6. Statistical Analysis

The statistical data on the WPI-TA hydrogels' swelling under conditions with different pH, both with and without TA, the TA release and the cytotoxic activity of the hydrogels were calculated using Microsoft Excel. Means and standard deviations were obtained from 3–6 independent experiments.

The data on the kinetics of swelling of hydrogels loaded with TA incubated in PBS at different pH values were plotted as "mean ± standard error" (n = 6). The viability of Hep2 cells incubated for 24 and 48 h with hydrogels containing different TA/WPI ratio was presented as "mean ± standard error" (n = 4). Differences between treatments were analyzed using two-way analysis of variance (ANOVA, Microsoft Excel 2016). [26] Calculations were carried out using Microsoft Excel software. Values of $p \leq 0.05$ were considered significant (Tables S1–S4).

3. Results and Discussion

3.1. Preparation and Characterization of WPI Hydrogels Containing TAs

WPI is a promising cross-linking component for the preparation of hydrogels containing various biologically active compounds. Previously, hydrogels based on various WPI concentrations were synthesized and their properties were studied. [6]. Two types of TAs (polygalloyl glucoses—ALSOK 02, polygalloyl quinic acids—ALSOK 04) were used for the fabrication of the WPI hydrogels. The main differences in these preparations are varying amounts of hydroxyl groups and chemical structure. Based on the literature data, TA concentrations in WPI hydrogels were selected and hydrogels with differing TAs contents were synthesized 1.5; 3.0; 6.0 and 12.0 mg per mL, which corresponds to the TA/WPI ratios were 0.0375/0.075/0.15/0.30 in the hydrogels. [27,28]. Hydrogels were obtained by heating the solution to 90 °C for 30 min. Such a short exposure to high temperatures does not lead to pathological changes in the TA structure [29].

The gelification process of WPI-TAs solutions was carried out at pH 7 in deionized water. It is assumed that the incorporation of an additional small TAs amount into the WPI hydrogel structure (maximum TA/WPI ratio of 0.30) does not affect the hydrogel pI, since WPI is the prevailing constituent of hydrogels. According to previously published studies [30] the pI of hydrogels obtained at a pH above the native protein pI (pI 5.2) shifts to a more acidic range (pI 4.1) due to the electrostatic repulsion of negatively charged groups of glutamic and aspartic acids and corresponding deprotonation of lysine amino acid residues.

To understand the functional properties of WPI-TA hydrogels, it is necessary to determine their structure and identify the binding nature of the protein and polyphenols. FTIR measurements are a sensitive tool for detecting conformational changes in the secondary structure of a protein [31]. In the present study FTIR-spectra of WPI-TAs hydrogels were measured from a solid dried condition to exclude pronounced stretching vibrations of

water molecules in the 3673–2942 cm^{-1} range and a deformation band of water in the 1644 cm^{-1} region. Figure 1 shows the FTIR spectra of unmodified WPI hydrogel and hydrogels with various TA concentrations. In the spectrum of the unmodified WPI hydrogel (burgundy line), we observed three strong bands at 3208, 1673, and 1545 cm^{-1}, which correspond to vibrations for amide A, amide I, and amide II, respectively [32]. In the vibrational spectrum region of amide I, stretching vibrations of the COO^- of the Asn and Gln side residues and NH_3^+ deformation vibrations of amino acids containing additional NH_2-groups in the side chain (Asp, Glu, Lys, and Arg) are manifested. This overlap of the amino acid residues absorption bands with the Amide I absorption band makes it very sensitive to the intermolecular H-bonds manifestation. A signal change of the amide I absorption band makes it possible to determine the conformational protein change.

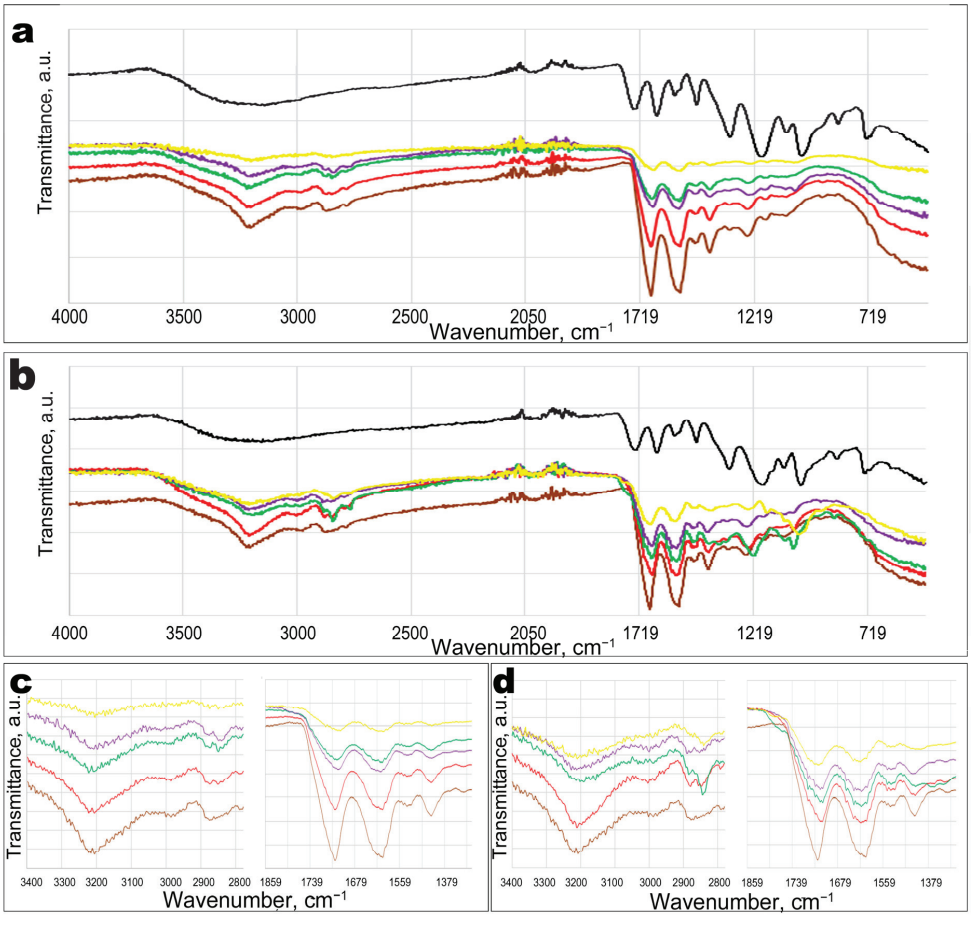

Figure 1. FTIR spectra of whey protein isolate (WPI) hydrogels with ALSOK 02 (**a**) and ALSOK 04 (**b**). Tannic acid (TA)/WPI ratio: 0.0 (burgundy line); 0.0375 (red line); 0.075 (green line); 0.15 (purple line); 0.30 (yellow line), TA (black line). The main diagnostic bands are magnified for FTIR spectra of WPI-ALSOK 02 (**c**) and WPI-ALSOK 04 (**d**) hydrogels. The dotted lines (**c**,**d**) indicate the main vibration signals (amide A, amide I, amide II) of the control WPI hydrogel without TAs (burgundy lines).

FTIR spectra of hydrogels with different TA contents showed similar bands to that of the WPI hydrogel control spectrum. It indicates that new covalent bonds were not

created. A similar result was reported by Ferraro, et al. (2015), who studied the nature of the interaction between rosmarinic acid (natural polyphenol) and milk whey proteins through non-covalent bonds in detail [33].

The spectral lines of hydrogels with TAs revealed broadening of the vibrational signal at 3208 cm^{-1}, which indicates the formation of intermolecular H-bonds (Figure 1c,d). For hydrogels containing polygalloyl glucose (ALSOK 02) the broadening of the symmetric vibration signal of -NH and -OH groups into Amide A is more pronounced than for hydrogels with the same content of the polygalloyl quinine acid (ALSOK 04). H-bonds are the main binding force of WPI and hydrophilic substances [34]. Vibrational signals of Amide I and Amide II are considered the basis of the WPI signal and confirm the presence of whey proteins. A change in the secondary structure of the protein is usually explained by broadening of Amide I and a shift of Amide II. When more ALSOK 02 is added into hydrogels, the peaks of Amide I bending vibrations are shifted by 7 cm^{-1} (from 1545 cm^{-1} to 1538 cm^{-1}) towards a lower wavenumber (Figure 1c). This indicates a change in the nature of the side amino group vibrations of Asp, Glu, Lys, and Arg due to the formation of intermolecular H-bonds with the polyphenols. The same phenomenon occurred for Amide II; the maximum shift was observed from 1673 cm^{-1} to 1657 cm^{-1} for a hydrogel with ALSOK 02/WPI ratio 0.30 (Figure 1b,d). For hydrogels containing ALSOK 04, the shifts of stretching vibrations of Amide I and Amide II groups were more significant than for hydrogels with ALSOK 02, perhaps due to the contribution of closely spaced signals of stretching vibrations of carboxyl groups and stretching of the C=C aromatic bonds of uncrosslinked ALSOK 04. The maximum shift was up to 25 cm^{-1} and was observed also for hydrogels with ALSOK 04/WPI ratio 0.30 (Figure 1d). The shift of Amide I and Amide II indicates the presence of an electrostatic interaction between WPI and TA, and not chemical reactions [31]. For the WPI-ALSOK 02 complex, the formation of intermolecular H-bonds is more characteristic than for the WPI-ALSOK 04, which directly depends on the chemical structure of TAs and their ability to ionize in water. Thus, a hydrolysable polygalloyl glucose (ALSOK 02) with a large number of hydroxyl groups interacts better with protein than polygalloyl quinic acid (ALSOK 04). Thus, in all cases, non-specific binding between polyphenols and WPI is confirmed, without additional covalent bond formation during the hydrogels' preparation.

3.2. Swelling Kinetics of WPI Hydrogels

The swelling characteristics play an important role in the absorption of body fluids and the transfer of nutrients and cellular metabolites. One of the main strategies for releasing captured drugs is controlled hydrogel swelling. It is known that an osmotic pressure is also defined as the measure of the tendency of a solution to take in pure solvent by osmosis. Under an action of a solvent diffusion and hydrogel network osmotic pressure, an increase of the pore size is observed that results in mixing between the solvent and the WPI segments and, as a consequence, swelling of hydrogels [35]. The swelling degree of hydrogels depends on the stretching of the polymer chains, which exert a pressure inside the hydrogel through their elasticity.

A swelling test was performed for WPI hydrogels containing different amounts of TAs and a control hydrogel without TAs in PBS solution (pH 7) for six repetitions within 48 h. The swelling degree of hydrogels depends on the hydrogel composition and the surrounding aqueous medium, as well as the degree of protein–protein, protein–water or protein–polyphenol interactions. [7] The increase of the mass increasing (MI) was observed for all hydrogels at the first 1 h of the swelling experiment (Figure 2). It indicates that all hydrogels absorbed and retained a certain amount of water in their structure. According to two-way analysis of variance (ANOVA), the swelling data of WPI-TA hydrogels are statistically significantly different ($p < 0.05$) between hydrogels with different TA/WPI ratio compared to the control hydrogels without TA. (Table S1).

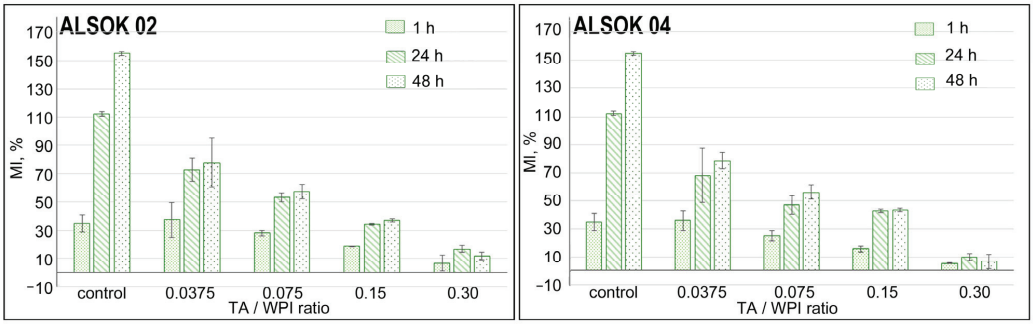

Figure 2. Mass increase (MI) of WPI hydrogels with TAs (ALSOK 02 (**left**), ALSOK 04 (**right**)) in PBS (pH 7). WPI hydrogel (control); TA/WPI ratios are 0.0375/0.075/0.15/0.30. $p < 0.05$ compared with the control groups (within each pH-dependence swelling group).

As shown in Figure 2, the presence of TAs which are bound to WPI proteins by non-covalent electrostatic interaction in the hydrogel structure significantly reduces its swelling ability. The inability of TAs to absorb water reasons for the decrease in the MI of hydrogels thereby preventing swelling. Thus, a high polyphenol content in hydrogels can inhibit the penetration of various proteins and, therefore, it is believed that bioactive drugs will be protected from premature degradation due to the hindrance of enzyme diffusion into pores in the hydrogels. Also, the correlation between the swelling ratio of the hydrogel and the TA concentration will allow hindrance of drug diffusion into the body and, as a consequence, slow the kinetics of drug release [36]. The highest MI was observed for hydrogels with the lowest TAs/WPI ratio—0.0375.

In general, for hydrogels containing TAs with a high content of hydroxyl groups (ALSOK 02), the MI is higher than for hydrogels with the same concentration of polygalloylquinic acids (ALSOK 04). This is primarily due to the chemical structure of the added compounds. Addition of greater numbers of the hydroxyl groups to the hydrogel network allows an increase in the number of formed intermolecular H-bonds. As a rule, such bonds are labile and are easily stretched and broken by exposure to external stimuli. The osmotic pressure generated during the swelling process can be responsible for such spatial changes in the hydrogel networks.

An increase of the TA concentration in the WPI hydrogels reduces and limits the mobility of the hydrogel network, which leads to resistance to diffusion and water uptake. [37] So the smallest MI is observed for the hydrogels containing the maximum amount of ALSOK 02 and ALSOK 04. For hydrogels with a maximum TA content (TA/WPI ratio 0.30), complete swelling by water is observed 24 h after the incubation start. After 48 h, the MI decrease is observed (Figure 2) due to the subsequent reduction in the hydrogel mass, provoked, probably, by TA release from the hydrogel networks.

3.3. pH-Dependent Swelling Behaviors and TA Release from WPI Biohydrogels

We also focused on studying the pH dependence of hydrogel swelling. The prepared hydrogel compositions were immersed in acidic (pH 5, Figure 3 above) and basic (pH 9, Figure 3 below) phosphate buffered saline (PBS), incubated for 48 h at room temperature.

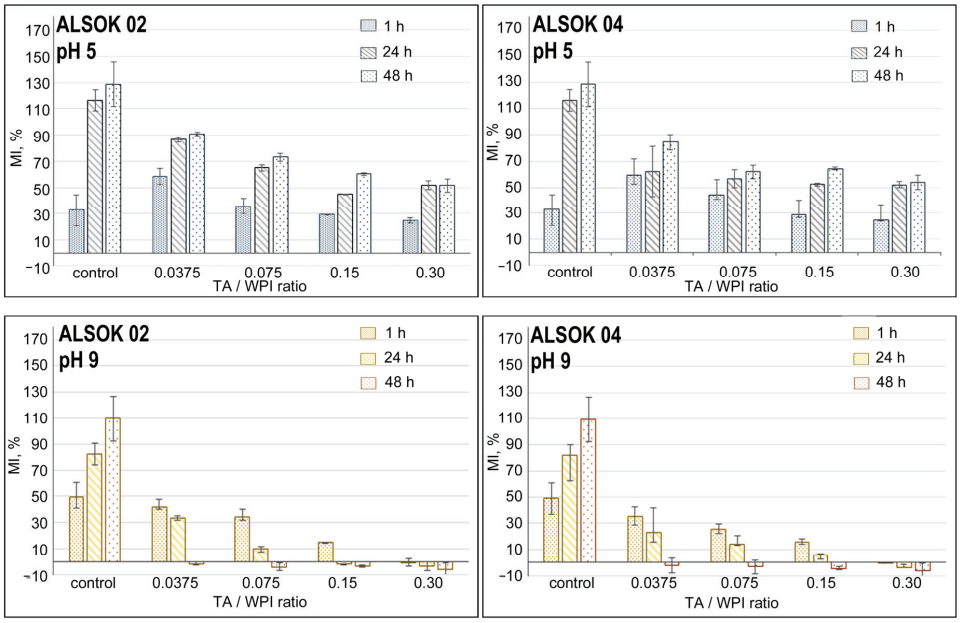

Figure 3. Mass increase (MI) of WPI hydrogels with TAs (ALSOK 02 (**left, up**) ALSOK 04 (**right, up**)) in PBS (pH 5). Mass increase (MI) of WPI hydrogels with TAs (ALSOK 02 (**left, down**) ALSOK 04 (**right, down**)) in PBS (pH 9). $p < 0.05$ compared with the control groups (within each pH-dependence swelling group).

For 48 h after a storage, the solutions became more opaque in the basic state (pH 9), but transparent at acidic medium (pH 5). This is due to TA hydrolysis and the subsequent oxidation by decarboxylation of the hydrolysis products in the presence of base. Usually, hydrogels formed from amphoteric polyelectrolytes (for example, WPI) have a small MI at a pH equal to their isoelectric point (pI of native ß-lactoglobulin is 5.1) [38]. The presence of a high TAs content affects the diffusion of ions, reducing the elasticity of the hydrogel network. Such a low ability of hydrogels to take up water is associated with less interaction or absence of WPI hydrophilic sites with water due to the formation of numerous bonds between the protein and TAs. Due to this, the formation of denser and more rigid structures occurs, which leads to a decrease in the flexibility of protein chains. In PBS solutions, the swelling capacity of hydrogels is lower compared to the values in distilled water. This can be explained by the uneven distribution of ions in the hydrogel network and solution. This causes a decrease in the equilibrium water absorption of the hydrogel and a swelling decrease over time.

It is interesting to note the behavior of hydrogels in the basic medium (Figure 4 left, down; right, down). The MI value for hydrogels at pH 9 is higher than at pH 2 during the first hour of the experiment. So the higher the pH, the more surface charges, the higher the electrostatic repulsive force, and higher MI value [30,39]. For the control WPI sample that does not contain TAs, the MI value continues to grow throughout the duration of the experiment. However, the presence of TA in the hydrogel results in lower MI values. According to two-way analysis of variance (ANOVA), statistically significant differences ($p < 0.05$) in the swelling data of hydrogels are observed between hydrogels with different TA/WPI ratio compared to the control hydrogels without TA (Tables S2 and S3). A decrease of MI values is observed with increasing TA concentration in the hydrogels. Due to the hydrolysis of TAs under basic conditions and partial deprotonization, the destruction of intermolecular H-bonds is possible and, as a consequence, the release of TA hydrolysis products from hydrogels with subsequent weight loss. We do not exclude the possibility

that WPI material may be diffusing out of the hydrogels too. Future work will investigate the possible simultaneous release of hydrogel material.

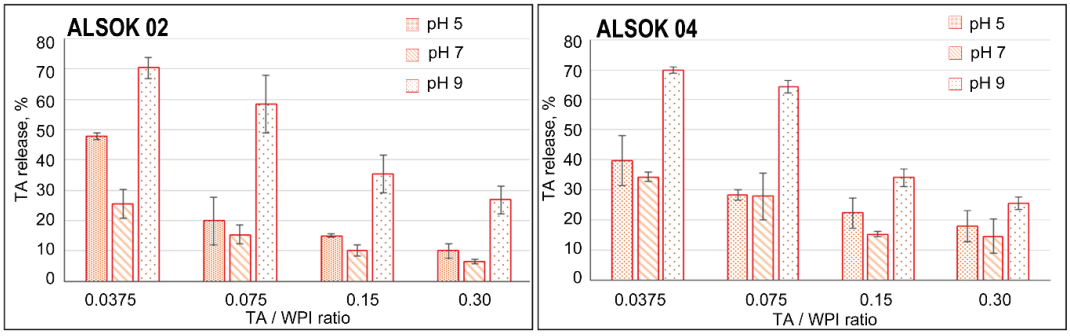

Figure 4. Histograms of the released TA amount (ALSOK 02 (**left**) ALSOK 04 (**right**)) from the WPI hydrogel at 48 h after incubation. Error bars show standard errors.

Targeted drug release from hydrogels in combination with a controlled release rate is a desirable property of pH-sensitive hydrogels. To confirm its hypothesis, the TA release from hydrogels was studied at different pH. Figure 4 shows the TA release profiles from hydrogels 48 h after their incubation in PBS solution at pH 5, 7, and 9, respectively.

According to Figure 4, TA release was the smallest when the samples were immersed in a neutral medium (pH 7). It is believed that the strongest ionic interaction between polyphenols and protein occurs in the solution at pH was close to the isoelectric point of native whey proteins (pI 5.1) [40], which leads to the formation of a denser hydrogels.

The highest TAs release 48 h after incubation is observed for hydrogels in the basic medium (pH 9), which is consistent with the swelling test data. An increase in pH will lead to deprotonation of WPI and TAs. As a result, a large TA release percentage is observed, which is associated with a violation of intermolecular H-bonds [41]. For hydrogels containing a small TA weight (TAs/WPI ratio—0.0375) the TA release percentage reaches high values, up to 80%. However, for WPI hydrogels with the highest TA content (TAs/WPI ratio—0.30), only 40% of the TA initially present is released from the hydrogel network. It leads to the formation of a denser hydrogel. We do not exclude the possibility that WPI material may be diffusing out of the hydrogels. Our future work will investigate the possibility of simultaneous release of hydrogel material. This aspect is important for the development of hydrogel scaffold with controlled release of drugs and nutrients, as well as the case of wound healing, absorption of wound exudates.

In an acidic medium (pH 5), a high TAs release value is observed, which is also associated with protein dissociation and protonation. This may be a positive sign for effective cancer therapy, since the local and endosomal pH is significantly lower than that of normal tissue [42].

Thus, the pH-dependent drug release from hydrogels allows hydrogels to be used locally, as anticancer scaffolds for the treatment or palliative treatment of serious gastrointestinal malignancies where pH values range from acidic (in the stomach) to basic (in the intestine).

3.4. Anticancer Activity of WPI Hydrogels Containing TA

Cytotoxicity of WPI hydrogels was estimated on the laryngeal cancer cell line (Hep 2) using the Alamar Blue assay, which measures the metabolic activity of cells.

The cultivation of Hep 2 cells during 48 h in the presence of WPI hydrogel discs without and with the addition of TAs (ALSOK 02, ALSOK 04) showed that samples without TAs exerted an inconsiderable cytotoxic effect on the cell line whereas hydrogels contained TAs caused a significant inhibition of metabolic processes (Figure 5).

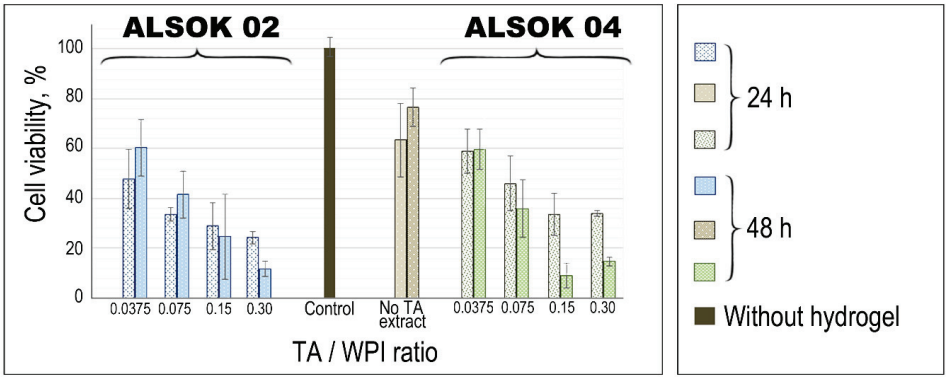

Figure 5. Results of cytotoxicity tests of WPI hydrogels without and with addition of TAs (ALSOK 02 and ALSOK 04) on the Hep 2 cell line. The Hep 2 cells were cultured in the presence of WPI hydrogels containing TAs (blue—ALSOK 02, green—ALSOK 04), hydrogels without TAs (brown). Cell culture without adding WPI hydrogels (black) was the control throughout the experiment. $p < 0.05$ compared with the control groups without adding TA.

Hydrogels with TA/WPI ratio 0.0375 produced a similar effect in comparison to pure hydrogel samples. The increase of TAs concentration led to more significant cytotoxic effects, correspondingly. Samples with maximum TA/WPI ratio 0.3 after 24 h incubation exhibited to 50% inhibition of metabolic processes whereas after 48 h this value increased to 80%. Previously, the ability of polyphenol derivatives to induce apoptosis and cell cycle termination was shown for cancer cell lines in vitro [43,44]. However, the cytotoxic effect of hydrogels with ALSOK 02 was higher than for the sample containing ALSOK 04 (Figure 5). Significant differences in cell viability between WPI hydrogels with different TA/WPI ratio were observed ($p < 0.05$) compared with the control groups without adding TA for each one of TA types (Table S4). In previous work on mineralized gellan gum hydrogels containing ALSOK 02 and ALSOK 04, greater cytotoxicity towards osteosarcoma-derived Saos-2 cells was observed after 2 h [22]. Thus, the use of WPI hydrogels containing TAs at 3 mg per mL (TA/WPI ratio 0.075) concentration is the most promising for provision of a prolonged anti-cancer effect.

4. Conclusions and Outlook

WPI hydrogels containing two types of TA have been produced, which withstand autoclaving. The greatest influence on the swelling change is exerted by the amount of TAs contained in the WPI hydrogels. An increase of the TA/WPI ratio in the hydrogels to 0.30 (for ALSOK 02 and ALSOK 04 both) leads to a significant decrease in MI compared with the control hydrogel without TA in neutral conditions (pH 7). The pH lowering leads to a MI decrease and an increase in the amount of released TAs by 1.5–2 times compared with incubation at neutral pH (pH 7) for all WPI hydrogels with and without TAs. The maximum TAs release was observed for hydrogels with the TA/WPI ratio 0.0375 (for ALSOK 02 and ALSOK 04 both) in alkaline pH (pH 9) and amounted to almost 80% 48 h after the incubation start. According to the swelling data, at this time point, the hydrogels begin to destruct, since their MI have negative values at 48 h. Future work will investigate the possible simultaneous release of hydrogel material. Also, measurements of the pH and zeta potential of the hydrogel dependence on pH gelification will be investigated in our future work. All obtained hydrogels containing TAs have cytotoxic properties against the human laryngeal cell carcinoma (Hep-2) Hep-2 cell line. An increase in the concentration of TAs in hydrogels leads to an increase in the cytotoxic effect. Thus, a WPI hydrogels can be used as anti-cancer scaffolds with a prolonged release profile of TAs.

Supplementary Materials: The following are available online at https://www.mdpi.com/1996-1944/14/4/749/s1, Figure S1: Linearity using ALSOK 02 demonstrating the line equation and the linear correlation coefficient (R2), Figure S2: Linearity using ALSOK 04 demonstrating the line equation and the linear correlation coefficient (R2), Table S1: *p*-Values for two-way analysis of variance (ANOVA) statistics for the WPI-TA hydrogel's swelling data (TA/WPI ratio–0.0375/0.075/0.15/0.3) at pH 7 compared to the swelling data of the WPI hydrogel without TA, Table S2: *p*-Values for two-way analysis of variance (ANOVA) statistics for the WPI-TA hydrogel's swelling data (TA/WPI ratio–0.0375/0.075/0.15/0.3) at pH 5 compared to the swelling data of the WPI hydrogel without TA, Table S3: *p*-Values for two-way analysis of variance (ANOVA) statistics for the WPI-TA hydrogel's swelling data (TA/WPI ratio–0.0375/0.075/0.15/0.3) at pH 9 compared to the swelling data of the WPI hydrogel without TA, Table S4: *p*-Values for two-way analysis of variance (ANOVA) statistics for the cell viability data of WPI-TA hydrogels (TA/WPI ratio–0.0375/0.075/0.15/0.3) compared to the WPI hydrogel without TA.

Author Contributions: Conceptualization, design, planning, O.A.M.; methodology, O.A.M., B.C.N.J.; and R.A.V.; inves-tigation, O.A.M., B.C.N.J.; and R.A.V., and V.O.P.; data curation, O.A.M. and R.A.V.; writing—original draft preparation, O.A.M. and R.A.V.; writing—review and editing, T.E.L.D. and V.O.P.; supervision, O.A.S. and T.E.L.D.; project administration, T.E.L.D.; funding acquisition, O.A.S. and T.E.L.D. All authors have read and agreed to the published version of the manuscript.

Funding: These researches on the hydrogel formation, the drug release and anticancer activity of hydrogels was funded by RUSSIAN SCIENCE FOUNDATION (grant number 19-75-10043). T.E.L.D. acknowledges THE BRITISH COUNCIL for their support in the framework of the Researcher Links Russia grant "Patient-tailored biomaterials for tissue regeneration, combating microbial contamination and drug delivery".

Institutional Review Board Statement: Not applicable.

Informed Consent Statement: Not applicable.

Data Availability Statement: The data that support the findings of this study are contained within the article.

Acknowledgments: The authors thank Patrick Ricquier (Omnichem NV, Belgium) for providing the tannic acids.

Conflicts of Interest: The authors declare no conflict of interest. The funders had no role in the design of the study; in the collection, analyses, or interpretation of data; in the writing of the manuscript, or in the decision to publish the results.

Abbreviations

FTIR	Fourier transform infrared
H-bond	Hydrogen bond
MI	Mass increase
PBS	Phosphate buffered saline
TA	Tannic acid
WPI	Whey protein isolate

References

1. Gupta, D.; Kocot, M.; Tryba, A.M.; Serafim, A.; Stancu, I.C.; Jaegermann, Z.; Pamuła, E.; Reilly, G.C.; Douglas, T.E.L. Novel naturally derived whey protein isolate and aragonite biocomposite hydrogels have potential for bone regeneration. *Mater. Des.* **2020**, *188*, 108408. [CrossRef]
2. Norris, K.; Kocot, M.; Tryba, A.M.; Chai, F.; Talari, A.; Ashton, L.; Parakhonskiy, B.V.; Samal, S.K.; Blanchemain, N.; Pamuła, E.; et al. Marine-Inspired Enzymatic Mineralization of Dairy-Derived Whey Protein Isolate (WPI) Hydrogels for Bone Tissue Regeneration. *Mar. Drugs* **2020**, *18*, 294. [CrossRef]
3. Dziadek, M.; Douglas, T.E.L.; Dziadek, K.; Zagrajczuk, B.; Serafim, A.; Stancu, I.C.; Cholewa-Kowalska, K. Novel whey protein isolate-based highly porous scaffolds modified with therapeutic ion-releasing bioactive glasses. *Mater. Lett.* **2020**, *261*, 127115. [CrossRef]

4. Dziadek, M.; Kudlackova, R.; Zima, A.; Slosarczyk, A.; Ziabka, M.; Jelen, P.; Shkarina, S.; Cecilia, A.; Zuber, M.; Baumbach, T.; et al. Novel multicomponent organic–inorganic WPI/gelatin/CaP hydrogel composites for bone tissue engineering. *J. Biomed. Mater. Res. Part A* **2019**, *107*, 2479–2491. [CrossRef]
5. Lorenzen, P.C.; Schrader, K. A comparative study of the gelation properties of whey protein concentrate and whey protein isolate. *Lait* **2006**, *86*, 259–271. [CrossRef]
6. Douglas, T.E.L.; Vandrovcová, M.; Kročilová, N.; Keppler, J.K.; Zárubová, J.; Skirtach, A.G.; Bačáková, L. Application of whey protein isolate in bone regeneration: Effects on growth and osteogenic differentiation of bone-forming cells. *J. Dairy Sci.* **2018**, *101*, 28–36. [CrossRef] [PubMed]
7. Ozel, B.; Cikrikci, S.; Aydin, O.; Oztop, M.H. Polysaccharide blended whey protein isolate-(WPI) hydrogels: A physicochemical and controlled release study. *Food Hydrocoll.* **2017**, *71*, 35–46. [CrossRef]
8. Andoyo, R.; Lestari, V.D.; Mardawati, E.; Nurhadi, B. Fractal Dimension Analysis of Texture Formation of Whey Protein-Based Foods. *Int. J. Food Sci.* **2018**, *2018*. [CrossRef]
9. Chatterjee, S.; Chi-leung HUI, P. Review of Stimuli-Responsive Polymers in Drug Delivery and Textile Application. *Molecules* **2019**, *24*, 2547. [CrossRef] [PubMed]
10. Jourdes, M.; Pouységu, L.; Deffieux, D.; Teissedre, P.L.; Quideau, S. Hydrolyzable tannins: Gallotannins and ellagitannins. In *Natural Products: Phytochemistry, Botany and Metabolism of Alkaloids, Phenolics and Terpenes*; Springer: Berlin/Heidelberg, Germany, 2013; pp. 1975–2010. ISBN 9783642221446.
11. Ky, I.; Le Floch, A.; Zeng, L.; Pechamat, L.; Jourdes, M.; Teissedre, P.L. Tannins. In *Encyclopedia of Food and Health*; Elsevier: Amsterdam, The Netherlands, 2015; pp. 247–255. ISBN 9780123849533.
12. Zaborniak, I.; Chmielarz, P.; Wolski, K.; Grzes´, G.; Isse, A.A.; Gennaro, A.; Zapotoczny, S.; Sobkowiak, A. Tannic Acid-Inspired Star-Like Macromolecules via Temporally Controlled Multi-Step Potential Electrolysis. *Macromol. Chem. Phys.* **2019**, *220*, 1900073. [CrossRef]
13. Isenburg, J.C.; Karamchandani, N.V.; Simionescu, D.T.; Vyavahare, N.R. Structural requirements for stabilization of vascular elastin by polyphenolic tannins. *Biomaterials* **2006**, *27*, 3645–3651. [CrossRef] [PubMed]
14. Pranantyo, D.; Xu, L.Q.; Neoh, K.G.; Kang, E.T.; Ng, Y.X.; Teo, S.L.M. Tea Stains-Inspired Initiator Primer for Surface Grafting of Antifouling and Antimicrobial Polymer Brush Coatings. *Biomacromolecules* **2015**, *16*, 723–732. [CrossRef]
15. Chai, Y.; Lee, H.J.; Shaik, A.A.; Nkhata, K.; Xing, C.; Zhang, J.; Jeong, S.J.; Kim, S.H.; Lü, J. Penta-O-galloyl-β-D-glucose induces G1arrest and DNA replicative S-phase arrest independently of P21 cyclin-dependent kinase inhibitor 1A, P27 cyclin-dependent kinase inhibitor 1B and P53 in human breast cancer cells and is orally active against triple-negative xenograft growth. *Breast Cancer Res.* **2010**, *12*. [CrossRef]
16. He, J.; Dong, Y.; Liu, X.; Wan, Y.; Gu, T.; Zhou, X.; Liu, M. Comparison of Chemical Compositions, Antioxidant, and Anti-Photoaging Activities of Paeonia suffruticosa Flowers at Different Flowering Stages. *Antioxidants* **2019**, *8*, 345. [CrossRef]
17. Mendonca, P.; Taka, E.; Soliman, K.F.A. Proteomic analysis of the effect of the polyphenol pentagalloyl glucose on proteins involved in neurodegenerative diseases in activated BV-2 microglial cells. *Mol. Med. Rep.* **2019**, *20*, 1736–1746. [CrossRef] [PubMed]
18. Bridgeman, C.J.; Nguyen, T.-U.; Kishore, V. Anticancer efficacy of tannic acid is dependent on the stiffness of the underlying matrix. *J. Biomater. Sci. Polym. Ed.* **2018**, *29*, 412–427. [CrossRef] [PubMed]
19. Boyle, W.S.; Chen, W.; Rodriguez, A.; Linn, S.; Tolar, J.; Lozano, K.; Reineke, T.M. Ternary Composite Nanofibers Containing Chondroitin Sulfate Scavenge Inflammatory Chemokines from Solution and Prohibit Squamous Cell Carcinoma Migration. *ACS Appl. Bio. Mater.* **2019**, *2*, 619–624. [CrossRef]
20. Ge, W.; Cao, S.; Shen, F.; Wang, Y.; Ren, J.; Wang, X. Rapid self-healing, stretchable, moldable, antioxidant and antibacterial tannic acid-cellulose nanofibril composite hydrogels. *Carbohydr. Polym.* **2019**, *224*, 115147. [CrossRef]
21. Seczyk, L.; Swieca, M.; Kapusta, I.; Gawlik-Dziki, U. Protein–phenolic interactions as a factor affecting the physicochemical properties of white bean proteins. *Molecules* **2019**, *24*, 408. [CrossRef]
22. Douglas, T.E.L.; Keppler, J.K.; Vandrovcová, M.; Plencner, M.; Beranová, J.; Feuereisen, M.; Parakhonskiy, B.V.; Svenskaya, Y.; Atkin, V.; Ivanova, A.; et al. Enhancement of Biomimetic Enzymatic Mineralization of Gellan Gum Polysaccharide Hydrogels by Plant-Derived Gallotannins. *Int. J. Mol. Sci.* **2020**, *21*, 2315. [CrossRef]
23. Carson, M.; Keppler, J.K.; Brackman, G.; Dawood, D.; Vandrovcova, M.; Fawzy El-Sayed, K.; Coenye, T.; Schwarz, K.; Clarke, S.A.; Skirtach, A.G.; et al. Whey Protein Complexes with Green Tea Polyphenols: Antimicrobial, Osteoblast-Stimulatory, and Antioxidant Activities. *Cells Tissues Organs* **2018**, *206*, 106–118. [CrossRef]
24. Bray, H.G.; Thorpe, W.V. Analysis of phenolic compounds of interest in metabolism. *Methods Biochem. Anal.* **1954**, *1*, 27–52. [CrossRef]
25. Back, S.A.; Khan, R.; Gan, X.; Rosenberg, P.A.; Volpe, J.J. A new Alamar Blue viability assay to rapidly quantify oligodendrocyte death. *J. Neurosci. Methods* **1999**, *91*, 47–54. [CrossRef]
26. In, J.; Lee, S. Statistical data presentation. *Korean J. Anesthesiol.* **2017**, *70*, 267–276. [CrossRef] [PubMed]
27. Ngobili, T.A.; Shah, H.; Park, J.P.; Kwist, K.W.; Inskeep, B.; Burg, K.J.L.; Booth, B.W. Remodeling of tannic acid crosslinked collagen type I induces apoptosis in ER+ breast cancer cells. *Anticancer Res.* **2015**, *35*, 1285–1290.
28. Karakurt, S.; Adali, O. Tannic Acid Inhibits Proliferation, Migration, Invasion of Prostate Cancer and Modulates Drug Metabolizing and Antioxidant Enzymes. *Anticancer. Agents Med. Chem.* **2016**, *16*, 781–789. [CrossRef]

29. Wang, C.-C.; Chen, H.-F.; Wu, J.-Y.; Chen, L.-G. Stability of Principal Hydrolysable Tannins from Trapa taiwanensis Hulls. *Molecules* **2019**, *24*, 365. [CrossRef]
30. Betz, M.; Hörmansperger, J.; Fuchs, T.; Kulozik, U. Swelling behaviour, charge and mesh size of thermal protein hydrogels as influenced by pH during gelation. *Soft Matter.* **2012**, *8*, 2477–2485. [CrossRef]
31. Jia, Z.; Zheng, M.; Tao, F.; Chen, W.; Huang, G.; Jiang, J. Effect of covalent modification by (-)-epigallocatechin-3-gallate on physicochemical and functional properties of whey protein isolate. *LWT Food Sci. Technol.* **2016**, *66*, 305–310. [CrossRef]
32. Jackson, M.; Mantsch, H.H. The use and misuse of FTIR spectroscopy in the determination of protein structure. *Crit. Rev. Biochem. Mol. Biol.* **1995**, *30*, 95–120. [CrossRef] [PubMed]
33. Ferraro, V.; Madureira, A.R.; Sarmento, B.; Gomes, A.; Pintado, M.E. Study of the interactions between rosmarinic acid and bovine milk whey protein α-Lactalbumin, β-Lactoglobulin and Lactoferrin. *Food Res. Int.* **2015**, *77*, 450–459. [CrossRef]
34. Wang, C.; Zhou, X.; Wang, H.; Sun, X.; Guo, M. Interactions between β-Lactoglobulin and 3,3′-Diindolylmethane in Model System. *Molecules* **2019**, *24*, 2151. [CrossRef]
35. Barros, W. Solvent self-diffusion dependence on the swelling degree of a hydrogel. *Phys. Rev. E* **2019**, *99*, 052501. [CrossRef]
36. Kang, G.D.; Cheon, S.H.; Song, S.C. Controlled release of doxorubicin from thermosensitive poly(organophosphazene) hydrogels. *Int. J. Pharm.* **2006**, *319*, 29–36. [CrossRef]
37. Barros, J.; Ferraz, M.P.; Azeredo, J.; Fernandes, M.H.; Gomes, P.S.; Monteiro, F.J. Alginate-nanohydroxyapatite hydrogel system: Optimizing the formulation for enhanced bone regeneration. *Mater. Sci. Eng. C* **2019**, *105*, 109985. [CrossRef] [PubMed]
38. Ozdal, T.; Capanoglu, E.; Altay, F. A review on protein-phenolic interactions and associated changes. *Food Res. Int.* **2013**, *51*, 954–970. [CrossRef]
39. Le Bourvellec, C.; Renard, C.M.G.C. Interactions between polyphenols and macromolecules: Quantification methods and mechanisms. *Crit. Rev. Food Sci. Nutr.* **2012**, *52*, 213–248. [CrossRef] [PubMed]
40. Gunasekaran, S.; Ko, S.; Xiao, L. Use of whey proteins for encapsulation and controlled delivery applications. *J. Food Eng.* **2007**, *83*, 31–40. [CrossRef]
41. Jiang, J.; Zhang, Z.; Zhao, J.; Liu, Y. The effect of non-covalent interaction of chlorogenic acid with whey protein and casein on physicochemical and radical-scavenging activity of in vitro protein digests. *Food Chem.* **2018**, *268*, 334–341. [CrossRef] [PubMed]
42. Damaghi, M.; Wojtkowiak, J.W.; Gillies, R.J. pH sensing and regulation in cancer. *Front. Physiol.* **2013**, *4*, 370. [CrossRef]
43. Kwon, H.Y.; Kim, J.H.; Kim, B.; Srivastava, S.K.; Kim, S.H. Regulation of SIRT1/AMPK axis is critically involved in gallotannin-induced senescence and impaired autophagy leading to cell death in hepatocellular carcinoma cells. *Arch. Toxicol.* **2018**, *92*, 241–257. [CrossRef] [PubMed]
44. Park, E.; Kwon, H.Y.; Jung, J.H.; Jung, D.B.; Jeong, A.; Cheon, J.; Kim, B.; Kim, S.H. Inhibition of Myeloid Cell Leukemia 1 and Activation of Caspases Are Critically Involved in Gallotannin-induced Apoptosis in Prostate Cancer Cells. *Phyther. Res.* **2015**, *29*, 1225–1236. [CrossRef] [PubMed]

materials

MDPI

Article

Evaluation of Biodegradable PVA-Based 3D Printed Carriers during Dissolution

Bálint Basa, Géza Jakab, Nikolett Kállai-Szabó, Bence Borbás, Viktor Fülöp, Emese Balogh and István Antal *

Department of Pharmaceutics, Semmelweis University, Hőgyes E. Street 7-9, 1092 Budapest, Hungary; basa.balint@pharma.semmelweis-univ.hu (B.B.); jakab.geza@pharma.semmelweis-univ.hu (G.J.); kallai.nikolett@pharma.semmelweis-univ.hu (N.K.-S.); borbas.bence@stud.semmelweis-univ.hu (B.B.); fulop.viktor@pharma.semmelweis-univ.hu (V.F.); balogh.emese@pharma.semmelweis-univ.hu (E.B.)

* Correspondence: antal.istvan@pharma.semmelweis-univ.hu; Tel.: +36-1-217-0914 (ext. 53016); Fax: +36-1-217-0914

Abstract: The presence of additive manufacturing, especially 3D printing, has the potential to revolutionize pharmaceutical manufacturing owing to the distinctive capabilities of personalized pharmaceutical manufacturing. This study's aim was to examine the behavior of commonly used polyvinyl alcohol (PVA) under in vitro dissolution conditions. Polylactic acid (PLA) was also used as a comparator. The carriers were designed and fabricated using computer-aided design (CAD). After printing the containers, the behavior of PVA under in vitro simulated biorelevant conditions was monitored by gravimetry and dynamic light scattering (DLS) methods. The results show that in all the dissolution media PVA carriers were dissolved; the particle size was under 300 nm. However, the dissolution rate was different in various dissolution media. In addition to studying the PVA, as drug delivery carriers, the kinetics of drug release were investigated. These dissolution test results accompanied with UV spectrophotometry tracking indirectly determine the possibilities for modifying the output of quality by computer design.

Keywords: 3D printing; fused deposition modelling (FDM); computer aided design (CAD); erosion test; dissolution study; dynamic light scattering (DLS)

Citation: Basa, B.; Jakab, G.; Kállai-Szabó, N.; Borbás, B.; Fülöp, V.; Balogh, E.; Antal, I. Evaluation of Biodegradable PVA-Based 3D Printed Carriers during Dissolution. *Materials* **2021**, *14*, 1350. https://doi.org/10.3390/ma14061350

Academic Editor: Iza Radecka

Received: 29 January 2021
Accepted: 8 March 2021
Published: 11 March 2021

1. Introduction

Among the challenges of pharmaceutical technology and drug development, the desire to produce the perfect treatment fit for the individuals via the construction of the drug delivery system is inevitable. The aspect of producing personalized medicine with optimal pharmacokinetics and physicochemical properties engineered strictly to the patient's needs is gaining more and more attention. 3D printing can change the ways of traditional drug production. The precedent of Spritam®, the first 3D printed pharmaceutical product, shows the enormous potential which hides in so-called Additive Manufacturing (AM) [1]. During this process, the number of unit operations is minimalized [2], and the opportunity to fabricate every single prototype shaped according to the individuals' profile with only minimal human intervention can be the cause of the increased research activity in this field [3]. An additional benefit of this type of manufacturing is the capability of producing customized ways of medication for patients suffering from organ dysfunctions, avoiding the slightest chance of reaching toxic doses in their body. Moreover, preferred patient groups are pediatrics [4] and geriatrics [5] where therapeutic doses perform great variance [6]. Further fields of interest can be the production of orphan drugs due to the low amount of produced medication. With the utilization of 3D printing, these single batches can be microfabricated without retooling all the manufacturing devices [7]. However, revolutionizing pharmaceutical manufacturing also requires a new regulatory attitude [8].

A vast number of methods are available beyond 3D Printing, and few of them which can be employed for tailored pharmaceutical manufacturing [9]. The most widely investigated type of free form fabrication is extrusion printing, in which the technique can

be divided by the step of melting the used materials or not. The Pressure Assisted Microsyringe System (PAM) utilizes the components without melting them [10], while Fused Deposition Modeling (FDM) uses the melted excipients to create the layer-by-layer structure of the 3D object [9]. The mixture of active pharmaceutical ingredients (API), polymers, and other excipients gives a great opportunity to modify the viscosity of the preprinted materials, and therefore there is no need for melting the semi-solid substrates [11]. Via the formulation of the containers, several modified releasing strategies can be applied in the same printlet. The idea of combining osmotic release items into a diffusible containing shell gives a great opportunity to tailor the released doses according to the patient's condition [12]. Moreover, the idea of producing "polypills" containing at least three or more different APIs with different release profiles also seems to be reachable with this technology [13]. In the case of harmonizing these strategies, a whole new dimension of pharmaceutical engineering and manufacturing can be established [2]. Another approach of this layering method is melting the thermoplastic polymers just above their melting temperature, then the melted excipients adhere to the heatable printing bed [14]. Due to the adaptability of the heat of the printing nozzle, the resolution of the printing is much better than in the instance of PAM. The pre-designed modifications inside the CAD file are easier to execute because of the better printing. The great variability of printable filaments and the low cost of this type of manufacturing generated an enormous breakthrough in the field of pharmaceutical manufacturing [15]. Among the most critical printing parameters, the infill and its patterns [16] and the height of the printed layers [17] can be an outstanding opportunity to modify the release kinetics of the microfabricated drugs [18]. In the development of patient-friendly drug delivery, designing and producing various geometries with a standard quality in order to maintain different kinetics is an important objective [19]. FDM printing gives the chance to fabricate unique designs for each object, and these delivery systems can be tailored to the individual's preferences [20]. The FDM extrusion-based technology includes a heating step in which the metal extruder can reach high processing temperature, excluding the possibility of printing thermolabile API filled filaments [21]. In order to formulate dosage forms suited for heat-sensitive APIs, novel nanocomposites have been developed lately [22]. Thermostable APIs can be impregnated onto the surface of the filament, which allows a minimal drug loading percentage [23,24]. The other and widely used method is hot-melt extrusion, where the parallelly co-rotating extruders make the homogenous drug-loaded filaments ready for printing [25]. In most studies, this preparation step was the basis of fabricating tablets and capsules having different geometries containing variant drugs and doses [26–28].

Beside producing drug-loaded filaments, another way to place API into the delivery system is printing separate capsule or carrier parts then filled and assembled in the post-printing phase [29–31]. There was only one previous formulation which aimed at printing a capsule which can be filled with liquid or solid API and excipients mid-printing [32]. Since, in case of this study, the basis of the formulation strategy is a thin-walled carrier, the buckling behavior of the printed structures should be monitored in order to ensure the desired quality [33].

Several types were previously microfabricated: immediate-release tablets [34], fast-disintegrating tablets and orodispersible films [35], floating drug delivery systems [27,36], pulsatile drug release tablets [30], biphasic and multi-active solid dosage forms, and zero-order release tablets [37]. Overcoming the difficulties of on-demand manufacturing of personalized carriers can lead to the spread of the clinical application of pharmaceutical additive manufacturing [38]. The reproducibility of dose dispensing and carrier filling is promising for the future [39].

Polyvinyl alcohol (PVA) is a non-toxic, hydrophilic, synthetic, biodegradable polymer produced via the hydrolysis of vinyl acetate [40], which is the most widespread supporting material in the field of fused deposition modeling. The variants of PVA are usually chosen as supporting structure due to its good solubility in water. The spread of biodegradable excipients in the industrial production not only decreases the ecological footprint [41] but

is also an adequate step towards a sustainable, zero-waste manufacturing [42]. Polyvinyl alcohol is used primarily in topical pharmaceutical and ophthalmic formulations [43]. It has also been used as an emulsifier in the formulation of drug loaded micro sponges [44]. In solid dosage forms PVA is used in coating formulations for tablets as a film forming polymer [45]. In this study our aim was to characterize the erosion of water-soluble PVA-based 3D printed systems with particle size analysis of colloidal PVA particles which appeared during in vitro mimicked dissolution conditions. The effect of pH, and the presence of bile salts were also simulated. An additional objective was to evaluate the effect of orifice numbers on the riboflavin release as a function of time. The optimal setting of this adjustment through CAD design ensures a perfect dose release which is inevitable for personalized therapy. The results of these investigations are intended to promote the spread of the 3D printed production of fillable water-soluble shells. With the opportunity of mixing different API between different layers of the carrier, the individualized medication can gain more emphasis.

2. Materials and Methods

Two commercially available biodegradable polymers were used as printing filament: the water-soluble polyvinyl alcohol (PVA) fiber (Orbi-Tech advanced, Leichlingen, Germany) and the water-insoluble polylactic acid (PLA) fiber (bq Easy Go, Madrid, Spain). The PVA filament has a diameter of 1.75 mm and a melting point of 183 °C, density: 1.13 g/cm^3. According to the manufacturer's specification, the orange PLA fiber had a diameter of 1.75 mm and a density of 1.24 g/cm^3 (ASTM D792), while the melting point temperature is between 145 and 160 °C. As model API riboflavin (Hungaropharma, Budapest, Hungary) was used. Polyethylene glycol 300 (Sigma Aldrich, St. Louis, MO, USA) was applied as the dispersing agent of the API containing liquid filled into the 3D printed carriers.

2.1. Design

Autodesk Fusion 360 (Autodesk Inc., San Rafael, CA, USA) was used during the planning phase of the experiment which exported the prepared structure into a stereolithography file. Further settings should be applied during the slicing. This is an algorithmical step in which the slicing program Ultimaker Cura (Ultimaker, Geldermalsen, Holland) divides the designed object into several, well defined horizontal slices. The exported g-code file includes not only the coordinates the extruder is going to follow but all the other printing parameters which can be set, e.g., printing temperature, bed temperature, cooling fan speed, printing resolution, and the infill percentage.

The PVA and PLA-based carriers were designed as a 9.75 mm high by 9.6 mm in diameter. The structure of the wall was built by concentric movements making 1-mm-thick sides to the printed object. Each carrier was designed to have a hollow structure with approximately 0.4 mL reservoir volume. During the examination of the effects of holes, 1-mm-diameter orifices were designed into the cylinder mantle and top (Figure 1), equally divided around the circumference of the prototype. There was a version of carrier without orifices in order to investigate only the release-modifying effect of the wall. Carriers were also made of PVA and PLA containing 2 or more orifices (Figure 2). The distance between the orifices is the circumference of the cover circle divided by the number of holes. The printer process parameters were set as the following: print speed, 20 mm/s; travel speed, 120 mm/s. The layer parameters were set as a 0.16 mm layer height with a 0.2 mm layer thickness. The printing temperature was 200 °C, accompanied by a 50 °C bed temperature in order to ensure the perfect bonding to the plate. The infill percentage was set to 100%, with maximum cooling fan performance (5000 rpm).

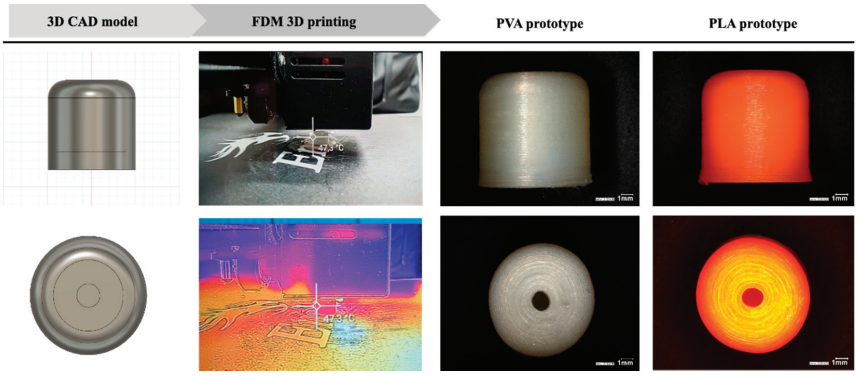

Figure 1. Printlet preparation process and digital microscopic images of polyvinyl alcohol (PVA-) and polylactic acid (PLA)-based prototype with one orifice.

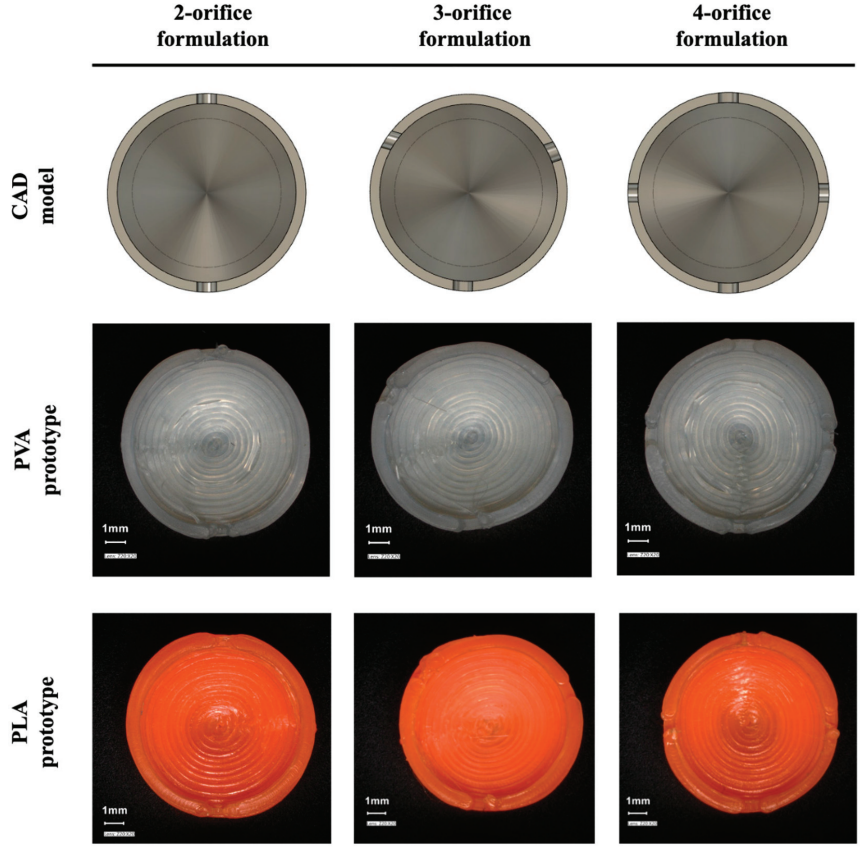

Figure 2. CAD models and digital microscopic images of PVA and PLA-based prototype with multiple orifices.

2.2. FDM Printing

The applied 3D printer was Creality Ender 3 (Creality 3D Technology Co., Shenzhen, China), with an MK-10 hot-end with a 0.4-mm-diameter nozzle. The heated print platform was customized with 3M blue tape. The temperature during the printing was checked by FLIR with CAT S61 (Caterpillar, Deerfield, IL, USA) The frames were layered on each other with pre-selected points where the temperature was indicated. The visual investigations of the printlets were executed using a Keyence VHX-7000 digital microscope (Keyence International, Mechelen, Belgium).

2.3. Preparation of Riboflavin Containing Liquid Fill

In every instance, 20 mg/g concentration of riboflavin-PEG 300 (polyoxyethylene glycol) dispersions were created manually in 10-g-sized batches. The samples were prepared before filling at room temperature with light-protection. The dispersion was applied into the vehicle using a 5 mL syringe (Chirana T. Injecta, Stará Turá, Slovakia) applied with a 23-gauge syringe needle. The filling was monitored by the comparison of the mass of the empty and the filled prototypes. In the instance of carriers without orifice, the filling process should be executed during the printing. The filament extrusion was stopped at 80% of the progress, and the dispersion was filled with the 5 mL syringe. After the application, the printing was continued, and the container was closed.

2.4. Physical Characterisation of 3D Printed Carriers

The 3D printlets are not yet subject to pharmacopoeial requirements; therefore, for the determination of mass uniformity and friability, the tests were performed as described in Chapter 2.9.5 (uniformity of mass of single-dose preparations) and Chapter 2.9.7 (friability of uncoated tablets) of the 9th European Pharmacopoeia for uncoated tablets, with an analytical balance (n = 20; Sartorius LA 230S, Sartorius AG, Göttingen, Germany) and tablet friability apparatus (Erweka AR, Langen, Germany). The printlets' dimension (n = 20; Mitutoyo Absolute, Mitutoyo Corporation, Kawasaki, Japan,) and mechanical strength (n = 10; Erweka TBH 200 TD type, Erweka AR, Langen, Germany). The average values with standard deviation were recorded at each parameter test.

2.5. PVA-Based Carrier and Drug Release Study

The dissolution tests were performed using a Hanson SR-8 Plus™ Dissolution Test Station (Hanson Research, Los Angeles, CA, USA) with the paddle (USP 30 dissolution apparatus II) method at a rotation speed of 50 rpm, in 37 $\pm$ 0.2 °C medium of 500 mL volume. At predetermined time-points, 5 mL of samples were withdrawn and filtered through 10 μm pore size membrane full-flow filters from the media by Hanson® AutoPlus Multifill collector (Hanson Research, Los Angeles, CA, USA). After every sampling, media replacement was accomplished with 5 mL of fresh buffer solution. The dissolution tests were performed in triplicates in the instance of every samples.

2.5.1. Study of PVA-Based Carrier Erosion

The erosion and dissolution of empty PVA-based carriers were characterized by gravimetry, and to trace the number and particle size of PVA colloidal-sized aggregates dispersed in various dissolution media, the DLS (dynamic light scattering) method was utilized.

To evaluate the effect of ionic strength and surface-active agents on degradability, the erosion studies of the empty carriers were conducted in aqueous media of pure demineralized water, pH = 1.2 HCl, pH = 6.8 phosphate buffer and pH = 6.8 tris-(hydroxymethyl)-aminomethane (TRIS) buffer with or without sodium salt of bile acids (cholic acid and deoxycholic acid sodium salt 1:1 mixture (Sigma-Aldrich, St. Louis, MO, USA). The erosion of the carriers was tracked visually (Olympus Stylus TG-4 digital camera, Olympus Corp., Tokyo, Japan).

The erosion of the PVA-based carriers was tracked visually.

Filtered erosion samples were measured with the instrument Zetasizer Nano ZS™ (Malvern Instruments Ltd., Malvern, UK) for the derived count rate (DCR) and particle size. The Zetasizer® instrument was equipped with a He-Ne laser (wavelength 633 nm, 4.0 mW) and an avalanche photodiode served as a detector at a detection angle of 173° (backscatter mode). Transmittance values for DLS were quantified by Agilent 8453 UV-Visible Spectrophotometer (Agilent Technologies Ltd., Santa Clara, CA, USA) at wavelength 633 nm. Measurement settings: automatic mode, NIBS (none-invasive-back-scattering) 173°, 30 sub runs/measurements; run duration: 10 secs, automatic laser position selected at 4.65 mm from the bottom of the cuvette; attenuation: attenuator 9 was selected automatically. Three measurements with 30 runs were performed for each sample, and the mean ± SD values are reported for all DLS parameters in this article.

The weight of the 3D printed PVA carriers was determined on an analytical balance (Sartorius LA 230S, Sartorius AG, Göttingen, Germany), which will give the initial weight (W_i) during the calculation. The carrier was then placed in the apparatus used in the in vitro dissolution test described above. The test was also performed under the conditions mentioned above. The dissolution medium was pH = 1.2. The printlets were taken out 5, 15, 30, 60, 120, and 240 min later; the dissolution medium was removed by vacuum filtration using a Pyrex™ borosilicate glass filter. The residue was stored in an oven (6030 Heraeus Instruments GmbH, Hanau, Germany) at 70° C for 48 h. Dry printlet mass (W_{dry}) was then determined (Sartorius LA 230S, Sartorius AG, Göttingen, Germany). The weight loss by erosion of carriers was calculated by Equation (1) respectively [46]:

$$weight\ (\%) = \frac{w_{dry}}{w_i} \times 100 \quad (1)$$

W_{dry}—mass of the dried printlet; W_i—initial mass of the printlet.

2.5.2. Riboflavin Release

The riboflavin concentrations of the dissolution samples were measured by UV-spectroscopy (Agilent 8453 UV-Vis spectrophotometer; Agilent Technologies, Waldbronn, Germany) at 267 nm.

Numerous theories and kinetic models describe and applied for the characterization of drug dissolution profile [47]. Since the shape of the investigated curves was different, the Weibull distribution function (1) was used for the characterization of the dissolution profile of the riboflavin loaded PVA or PLA-based 3D printlet [48].

$$M_t = M_\infty \left[1 - e^{-\left(\frac{t-t_0}{\tau_d}\right)^\beta}\right] \quad (2)$$

M_t—the percentage of the dissolved API at time; M_∞—the infinite concentration of the API in percentages; t_0—dissolution lag time; β—curve shape parameter; τ_d—time in minutes when 63.2% of the API has been dissolved.

Where M_t is the percentage of the dissolved active pharmaceutical ingredient at time t, M_∞ is the infinite concentration (%) of the drug, t_0 is the dissolution lag-time, β is the shape parameter of the curve, and the τ_d represents the time (minutes) when 63.2% of the drug has been dissolved.

3. Results and Discussion

There are several formulations printed with polyvinyl alcohol, due to its soluble character [21,23,29,32]. However, there is extended research available in connection with the API–PVA formulations [49]; the erosion of PVA itself has not yet been described.

3.1. The CAD Design and the Tracking of the Printlet

The printing process (Figure 1) was captured by a FLIR thermal camera in order to obtain information about the already printed layers, while the upper ones are printed on

the structure. The pinpoint set onto the carrier indicates that while significant heat comes from the nozzle and the heated bed towards the printlet, the state of the solidified layers is extremely acceptable. The temperature of the printed wall has not reached the 50 °C, and this phenomenon means that the filling of thermolabile API can be accomplished during the process.

3.2. Physical Characterisation of 3D Printed Carrier Systems

To guarantee the reproducibility of the manufacturing quality, the investigation of physical characteristics was executed on the printlets. As there is currently no official description in the pharmacopeia for the study of 3D printed carriers, we performed the study according to the pharmacopoeial description (Ph. Eur. 9.) of uncoated tablets.

The measurement results are shown in Table 1. For uniformity of mass, the standard deviation was minimal, well below the 5% allowed in the pharmacopeia. To check the print settings, it is also important to check the height and diameter of the 3D printed carrier. The measured values were close to the original value of the set parameters. The pharmacopoeia concedes a 1% weight loss for friability when testing uncoated tablets. Compared to this value, both PVA and PLA-based printlets had very low friability values, as shown in the data in Table 1. Besides replicability, these results indicate a good opportunity to produce fillable carriers not just for immediate usage but stock can be also piled from them. Due to the structure of the carriers, the weak point of this CAD design is the last layer of the wall around the hollow and the first layer of the closing top area of the printlet. The joint section of the two different layers ruptures if the hardness tests are executed. However, the lowest value of the hardness test performed was 205 N, while the highest was 350 N for PVA. The standard deviation surpasses the 5% limit; however, with the values oscillating in this territory, the mechanical behavior of the carriers shows no diverse differences.

Table 1. Physical characteristics of 3D printed carriers.

	PVA Carrier	**PLA Carrier**
Weight (g) (n = 20; mean ± SD)	0.42 ± 0.007	0.49 ± 0.004
Height (mm) (n = 20; mean ± SD)	9.75 ± 0.053	9.75 ± 0.036
Diameter (mm) (n = 20; mean ± SD)	9.66 ± 0.298	9.66 ± 0.239
Hardness (N) (n = 10; mean ± SD)	212.63 ± 75.87	300.0 ± 1.00
Friability (%)	0.016	0.024

Digital microscopic images show the one-orifice PVA and PLA-based carrier (Figure 1). It is clear from the images that the layers formed according to the design file during FDM printing processes. The top view shows the designed orifice that plays an important part in the filling and dissolution of the active ingredient. Figure 2 shows the cross-section view of the biodegradable polymer carriers containing multiple drug delivery orifices design for 3D printing and the prepared prototypes.

3.3. Erosion of the PVA Carrier

As earlier mentioned PVA is commonly referred to as a water-soluble excipient, but PVA forms a physical hydrogel in an aqueous medium [50]. Of course, concentration conditions must be taken into account. Dilution of a physical hydrogel with water gives a colloidal solution. During the studies, our aim was to follow the behavior of the printed PVA carrier through the simulated circumstances of the GI tract. The third figure (Figure 3) shows what happens to a PVA-based carrier contacting aqueous medium. The colloidal dissolution/erosion of PVA is a consecutive process. The digital microscope image in the figure shows the wall of a PVA carrier located in a 90-minute release medium (pH = 1.2). Erosion and gel state of PVA can be observed. The solid-state wall is eroded into physical hydrogel state and very small fibers by the medium, forming a gel state before forming the colloidal solution. In the case of water-soluble PVA, the weight of the carrier decreases continuously (black line), while the DCR value determined from the release medium

increases (red line, violet line). It is known in the literature that the increase in DCR is due to an increase in the concentration of the dispersed particles and/or an increase in the size of the dispersed particle [51].

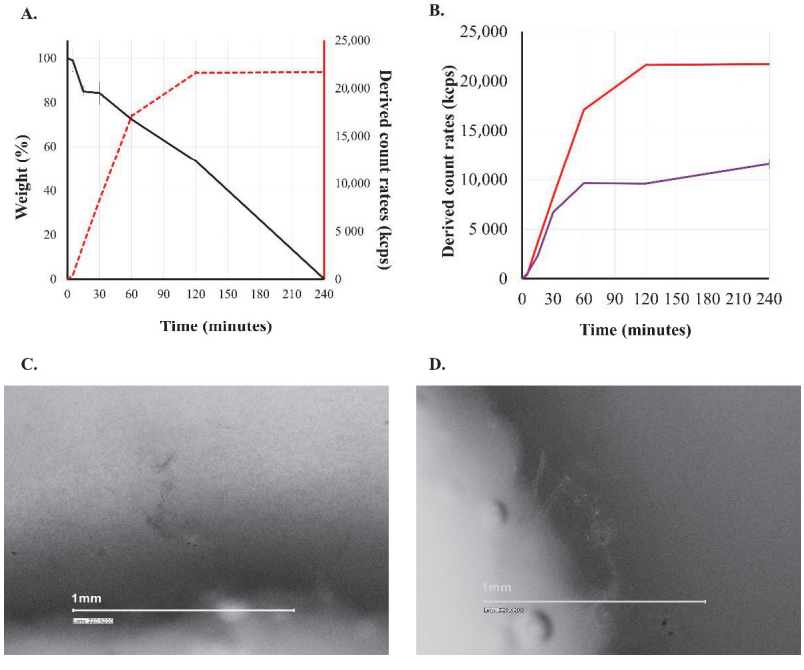

Figure 3. Erosion of PVA-based carrier (**A**): black line—weight loss; red line—pH = 1.2 HCl; (**B**): red line—pH = 1.2 HCl; violet line:—pH = 6.8 phosphate buffer (carrier = PVA; n = 3; mean ± SD). (**C**,**D**): digital images of PVA wall during dissolution (pH = 1.2; time = 90 min).

Since the particle size in the samples was below 300 nm (Figure 4) for the entire period, the decisive process was the increase in the concentration of PVA in the dissolution medium. The colloidal dissolved particles reach the colloid particle size interval and remain in this state during at least 24 h.

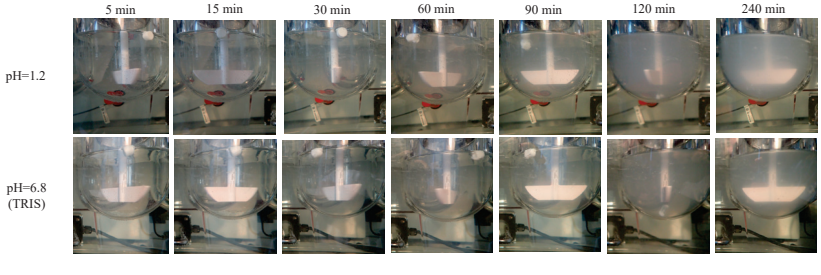

Figure 4. Visual tracking of the PVA-based carrier erosion in different media.

Comparing the derived count rates of each carrier dissolved in different media (Table 2) shows that the highest proportion of the PVA walls are being dissolved during the first 120 min in the case of demineralized water, pH = 1.2 solution. Comparing the derived count rates of each carrier dissolved in different media (Table 2) shows that the highest proportion of the PVA walls are being dissolved during the first 120 min in the

case of demineralized water, pH = 1.2 solution. However, in the TRIS buffer (pH = 6.8), used in order to avoid the PVA incompatibilities with inorganic phosphate [52], the erosion and formation of colloidal solution process were much slower, and the presence of surface active bile salts did not accelerate the progress. The visible tracking of the solid samples also showed that the intact structure of the solid carriers did not disappeare during the first two hours of the study, but as can be seen in the images and in the weight measurement, at 240 min the carrier is completely disintegrated into colloidal particles (Figures 3–5).

Table 2. The percentages of derived count rates *(DCR_t /$DCR_{1440min}$ × 100)* of various dissolution media (carrier = PVA; n = 3; mean ± SD).

Medium	5 min	15 min	30 min	60 min	120 min	1440 min
pH = 1.2	1.83 ± 0.92	15.94 ± 1.26	36.3 ± 1.4	75.15 ± 0.92	94.79 ± 0.66	100 ± 1.18
pH = 6.8 (Phosphate)	4.49 ± 0.46	19.77 ± 0.38	57.83 ± 1.28	83.21 ± 0.42	85.76 ± 1.01	100 ± 1.49
pH = 6.8 (TRIS)	0.55 ± 0.15	2.81 ± 0.4	10.95 ± 2.61	19.33 ± 0.11	36.0 ± 0.43	100 ± 1.01
pH = 6.8 (TRIS) + 10 mm BS	1.0 ± 0.1	3.57 ± 1.56	7.4 ± 1.02	13.8 ± 1.12	25.7 ± 1.54	100 ± 6.9
Demineralized water	2.37 ± 1.0	10.97 ± 0.76	30.01 ± 0.61	50.76 ± 0.8	73.89 ± 0.52	100 ± 0.54

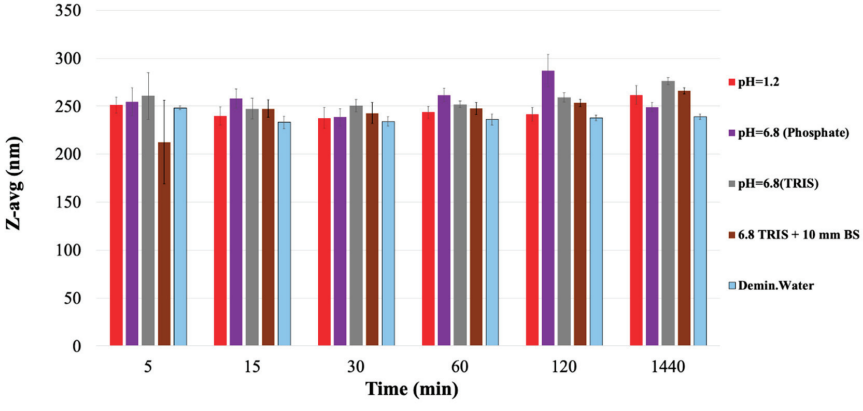

Figure 5. Particle size of dissolution sample (carrier = PVA; n = 3; mean ± SD).

3.4. Riboflavin Release

Figure 6 shows the release of riboflavin loaded PVA and PLA carriers in pH = 1.2 medium. Carriers without drug delivery orifices were prepared from both biodegradable polymers and dissolution studies were performed. In the case of PLA, which is insoluble in water, no drug release was expected, while in the case of PVA, after a short time a practically linear release of riboflavin was observed. If an orifice for drug release was formed on the support, the drug delivery profile was completely changed, as shown in Figure 6. There were 1, 2, 3, or 4 orifices in the 3D printed carriers. The location and the number of the pores were customized in the CAD design, so the indirect effect of the CAD modifications could have been inspected. The PLA is water-insoluble, so erosion of the body does not affect drug release. This case is clearly controllable by the number of carrier orifices, both the total amount of liberated riboflavin and the rate of drug release.

The results of the model-dependent evaluation of the dissolution profiles are shown in the third table. The correlations during the fits are between 0.9925 and 0.9999, so they are considered adequate. The kinetic evaluation of the dissolution profiles (Table 3) of riboflavin loaded PLA-based carrier system also show that increasing the number of orifices in the carrier accelerated the dissolution and also increased the maximum amount of drug released, i.e., the infinite value of M increased.

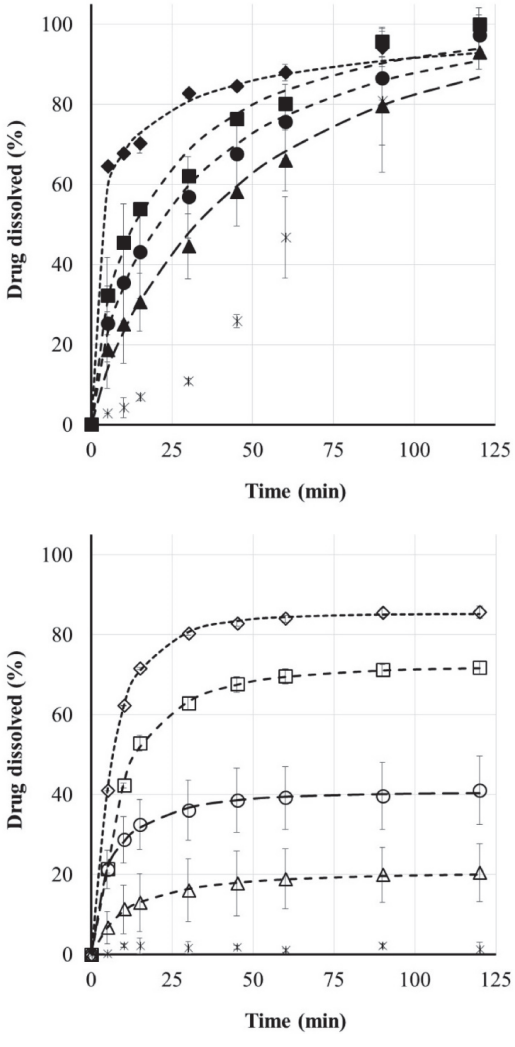

Figure 6. Drug release profile of riboflavin loaded PLA and PVA carriers printed containing various number of orifices (zero—cross; one—triangle; two—circle; three—square; four—diamond; n = 3; mean ± SD) with fitted Weibull (dotted lines).

In the instance of the PVA carrier, not only do the orifices play an important role in drug release, but also erosion and deformation of the printed object. This is demonstrated by the fact that the dissolution profile of drug loaded PVA-based systems differs from the PLA-based system. Erosion of PVA is slower in time than the dissolution of riboflavin (Biopharmaceutics Classification System I), so here the PVA carrier can slow drug release. In contrast to the drug loaded PLA carrier, the presence of only one orifice in this system meant almost 100% drug release, since, as our previous studies show, the skeleton was completely dissolved in the first hours of dissolution. As the number of orifices increased, as expected, the τ_d value decreased. It is also important to note that the maximum amount of drug released in the case of PLA printlets is obtained in a shorter time, which is also shown by the low tau values according to the Weibull model; however, due to the rigid, water-insoluble wall, drug occlusion occurs. In the case of PVA carriers, the maximum

amount of active ingredient available is higher; there is no such occlusion, but the value of tau is higher compared to PLA, which is probably because the wall material forms a gel not only towards the release medium but also towards the cavity.

Table 3. Kinetic parameters of dissolution estimated according to Weibull distribution function (pH = 1.2).

Filament Base	**PLA**				**PVA**			
Number of orifices	1	2	3	4	1	2	3	4
M_∞ (%)	20.46	40.52	72.15	85.28	100.00	100.00	99.92	100.00
t_0 (min)	2.42	0.11	3.71	2.43	0.00	0.00	0.00	0.00
τ_d (min)	12.17	7.54	7.53	5.00	50.77	34.48	23.96	6.90
β	0.59	0.62	0.60	0.63	0.82	0.70	0.64	0.34
r	0.9991	0.9992	0.9999	0.9999	0.9947	0.9960	0.9925	0.9950

4. Conclusions

3D printing is going to change the ways of conventional drug manufacturing, and the FDM method enables the researchers to produce high quality tailored dosage forms for each patient according to their individual needs.

The results demonstrate that dissolution of tested PVA-based 3D printed placebo carriers can be characterized with the appearance of colloidal particles under 300 nm. According to the gravimetry and derived count rate data of the dynamic light scattering method, due to the erosion in the dissolution media the carrier dissolved into colloid state. The most commonly used supporting material can be upgraded into an important excipient filament used in personalized therapy. Due to the characteristics of the polymer, the phenomenon of "ghost tablets" can be abolished because the PVA-based dosage forms biodegrade in the patient's body in hours. The CAD design ensures the opportunity to add drug-releasing holes into the surface of the carrier. Utilizing this effect, extremely precise individualized treatment can be pharmaceutically engineered, and 3D printed to any patients regarding their needs. With this novel method, standardized drug release can be programmed into the CAD and gcode files of the carriers. The easy modification opportunities ensure extremely wide range of personalized medication. The following experiments would focus on the wider understanding of the behavior of the PVA and other water-soluble filaments.

Author Contributions: Conceptualization, B.B. (Bálint Basa) and I.A.; data curation, B.B. (Bálint Basa); formal analysis, N.K.-S. and V.F.; investigation, B.B. (Bálint Basa), G.J. and B.B. (Bence Borbás); methodology, B.B. (Bálint Basa), G.J., V.F. and E.B.; project administration, I.A.; resources, E.B.; software, B.B. (Bálint Basa); supervision, I.A.; visualization, N.K.-S.; writing—original draft, B.B. (Bálint Basa) and N.K.-S.; writing—review and editing, B.B. (Bálint Basa), N.K.-S. and I.A. All authors have read and agreed to the published version of the manuscript.

Funding: This research received no external funding.

Institutional Review Board Statement: Not applicable.

Informed Consent Statement: Not applicable.

Conflicts of Interest: The authors declare no conflict of interest.

References

1. Center for Drug Evaluation and Research (CDER). *Approval Package for SPRITAM*; CDER: Rockville, MD, USA, 2015.
2. Alhnan, M.A.; Okwuosa, T.C.; Sadia, M.; Wan, K.-W.; Ahmed, W.; Arafat, B. Emergence of 3D Printed Dosage Forms: Opportunities and Challenges. *Pharm. Res.* **2016**, *33*, 1817–1832. [CrossRef] [PubMed]
3. Prasad, L.K.; Smyth, H. 3D Printing technologies for drug delivery: A review. *Drug Dev. Ind. Pharm.* **2016**, *42*, 1019–1031. [CrossRef] [PubMed]
4. Preis, M.; Öblom, H. 3D-Printed Drugs for Children—Are We Ready Yet? *AAPS PharmSciTech* **2017**, *18*, 303–308. [CrossRef]
5. Korte, C.; Quodbach, J. 3D-Printed Network Structures as Controlled-Release Drug Delivery Systems: Dose Adjustment, API Release Analysis and Prediction. *AAPS PharmSciTech* **2018**, *19*, 3333–3342. [CrossRef]

6. Jamróz, W.; Szafraniec, J.; Kurek, M.; Jachowicz, R. 3D Printing in Pharmaceutical and Medical Applications—Recent Achievements and Challenges. *Pharm. Res.* **2018**, *35*, 1–22. [CrossRef]
7. Mechanics, A.; Devices, O.; di Prima, M. *Technical Considerations for Additive Manufactured Medical Devices. Guidance for Industry and Food and Drug Administration Staff*; FDA: Rockville, MD, USA, 2017.
8. FDA; CDER. *Advancement of Emerging Technology Applications for Pharmaceutical Innovation and Modernization Guidance for Industry*; CDER: Rockville, MD, USA, 2017.
9. Konta, A.A.; García-Piña, M.; Serrano, D.R. Personalised 3D printed medicines: Which techniques and polymers are more successful? *Bioengineering* **2017**, *4*, 79. [CrossRef] [PubMed]
10. AlGahtani, M.S.; Mohammed, A.A.; Ahmad, J.; Saleh, E. Development of a 3D Printed Coating Shell to Control the Drug Release of Encapsulated Immediate-Release Tablets. *Polymers* **2020**, *12*, 1395. [CrossRef] [PubMed]
11. Rattanakit, P.; Moulton, S.E.; Santiago, K.S.; Liawruangrath, S.; Wallace, G.G. Extrusion printed polymer structures: A facile and versatile approach to tailored drug delivery platforms. *Int. J. Pharm.* **2012**, *422*, 254–263. [CrossRef]
12. Khaled, S.A.; Burley, J.C.; Alexander, M.R.; Yang, J.; Roberts, C.J. 3D printing of tablets containing multiple drugs with defined release profiles. *Int. J. Pharm.* **2015**, *494*, 643–650. [CrossRef]
13. Khaled, S.A.; Burley, J.C.; Alexander, M.R.; Yang, J.; Roberts, C.J. 3D printing of five-in-one dose combination polypill with defined immediate and sustained release profiles. *J. Control. Release* **2015**, *217*, 308–314. [CrossRef]
14. McMains, S. *Layered Manufacturing Technologies*; ACM: New York, NY, USA, 2005; Volume 48.
15. Wong, K.V.; Hernandez, A. A Review of Additive Manufacturing. *ISRN Mech. Eng.* **2012**, *2012*, 1–10. [CrossRef]
16. Goyanes, A.; Buanz, A.B.M.; Basit, A.W.; Gaisford, S. Fused-filament 3D printing (3DP) for fabrication of tablets. *Int. J. Pharm.* **2014**, *476*, 88–92. [CrossRef] [PubMed]
17. Dezaki, M.L.; Ariffin, M.K.A.M. The Effects of Combined Infill Patterns on Mechanical Properties in FDM Process. *Polymers* **2020**, *12*, 2792. [CrossRef]
18. Fina, F.; Goyanes, A.; Rowland, M.; Gaisford, S.; Basit, A.W. 3D Printing of Tunable Zero-Order Release Printlets. *Polymers* **2020**, *12*, 1769. [CrossRef]
19. Alhijjaj, M.; Nasereddin, J.; Belton, P.; Qi, S. Impact of Processing Parameters on the Quality of Pharmaceutical Solid Dosage Forms Produced by Fused Deposition Modeling (FDM). *Pharmaceutics* **2019**, *11*, 633. [CrossRef] [PubMed]
20. Goyanes, A.; Martinez, P.R.; Buanz, A.; Basit, A.W.; Gaisford, S. Effect of geometry on drug release from 3D printed tablets. *Int. J. Pharm.* **2015**, *494*, 657–663. [CrossRef] [PubMed]
21. Goyanes, A.; Buanz, A.B.; Hatton, G.B.; Gaisford, S.; Basit, A.W. 3D printing of modified-release aminosalicylate (4-ASA and 5-ASA) tablets. *Eur. J. Pharm. Biopharm.* **2015**, *89*, 157–162. [CrossRef] [PubMed]
22. Chou, P.-Y.; Chou, Y.-C.; Lai, Y.-H.; Lin, Y.-T.; Lu, C.-J.; Liu, S.-J. Fabrication of Drug-Eluting Nano-Hydroxylapatite Filled Polycaprolactone Nanocomposites Using Solution-Extrusion 3D Printing Technique. *Polymers* **2021**, *13*, 318. [CrossRef] [PubMed]
23. Skowyra, J.; Pietrzak, K.; Alhnan, M.A. Fabrication of extended-release patient-tailored prednisolone tablets via fused deposition modelling (FDM) 3D printing. *Eur. J. Pharm. Sci.* **2015**, *68*, 11–17. [CrossRef] [PubMed]
24. Beck, R.C.R.; Chaves, P.; Goyanes, A.; Vukosavljevic, B.; Buanz, A.; Windbergs, M.; Basit, A.; Gaisford, S. 3D printed tablets loaded with polymeric nanocapsules: An innovative approach to produce customized drug delivery systems. *Int. J. Pharm.* **2017**, *528*, 268–279. [CrossRef] [PubMed]
25. Pietrzak, K.; Isreb, A.; Alhnan, M.A. A flexible-dose dispenser for immediate and extended release 3D printed tablets. *Eur. J. Pharm. Biopharm.* **2015**, *96*, 380–387. [CrossRef]
26. Arafat, B.; Qinna, N.; Cieszynska, M.; Forbes, R.T.; Alhnan, M.A. Tailored on demand anti-coagulant dosing: An in vitro and in vivo evaluation of 3D printed purpose-designed oral dosage forms. *Eur. J. Pharm. Biopharm.* **2018**, *128*, 282–289. [CrossRef]
27. Chai, X.; Chai, H.; Wang, X.; Yang, J.; Li, J.; Zhao, Y.; Cai, W.; Tao, T.; Xiang, X. Fused Deposition Modeling (FDM) 3D Printed Tablets for Intragastric Floating Delivery of Domperidone. *Sci. Rep.* **2017**, *7*, 1–9. [CrossRef]
28. Melocchi, A.; Parietti, F.; Maroni, A.; Foppoli, A.; Gazzaniga, A.; Zema, L. Hot-melt extruded filaments based on pharmaceutical grade polymers for 3D printing by fused deposition modeling. *Int. J. Pharm.* **2016**, *509*, 255–263. [CrossRef]
29. Maroni, A.; Melocchi, A.; Parietti, F.; Foppoli, A.; Zema, L.; Gazzaniga, A. 3D printed multi-compartment capsular devices for two-pulse oral drug delivery. *J. Control. Release* **2017**, *268*, 10–18. [CrossRef] [PubMed]
30. Melocchi, A.; Parietti, F.; Loreti, G.; Maroni, A.; Gazzaniga, A.; Zema, L. 3D printing by fused deposition modeling (FDM) of a swellable/erodible capsular device for oral pulsatile release of drugs. *J. Drug Deliv. Sci. Technol.* **2015**, *30*, 360–367. [CrossRef]
31. Melocchi, A.; Parietti, F.; Maccagnan, S.; Ortenzi, M.A.; Antenucci, S.; Briatico-Vangosa, F.; Maroni, A.; Gazzaniga, A.; Zema, L. Industrial Development of a 3D-Printed Nutraceutical Delivery Platform in the Form of a Multicompartment HPC Capsule. *AAPS PharmSciTech* **2018**, *19*, 3343–3354. [CrossRef]
32. Smith, D.; Kapoor, Y.; Hermans, A.; Nofsinger, R.; Kesisoglou, F.; Gustafson, T.P.; Procopio, A. 3D printed capsules for quantitative regional absorption studies in the GI tract. *Int. J. Pharm.* **2018**, *550*, 418–428. [CrossRef]
33. Khezri, M.; Rasmussen, K. An energy-based approach to buckling modal decomposition of thin-walled members with arbitrary cross sections, Part 1: Derivation. *Thin Walled Struct.* **2019**, *138*, 496–517. [CrossRef]
34. Okwuosa, T.C.; Stefaniak, D.; Arafat, B.; Isreb, A.; Wan, K.-W.; Alhnan, M.A. A Lower Temperature FDM 3D Printing for the Manufacture of Patient-Specific Immediate Release Tablets. *Pharm. Res.* **2016**, *33*, 2704–2712. [CrossRef]

35. Jamróz, W.; Kurek, M.; Łyszczarz, E.; Szafraniec, J.; Knapik-Kowalczuk, J.; Syrek, K.; Paluch, M.; Jachowicz, R. 3D printed orodispersible films with Aripiprazole. *Int. J. Pharm.* **2017**, *533*, 413–420. [CrossRef] [PubMed]
36. Li, Q.; Guan, X.; Cui, M.; Zhu, Z.; Chen, K.; Wen, H.; Jia, D.; Hou, J.; Xu, W.; Yang, X.; et al. Preparation and investigation of novel gastro-floating tablets with 3D extrusion-based printing. *Int. J. Pharm.* **2018**, *535*, 325–332. [CrossRef] [PubMed]
37. Khatri, P.; Shah, M.K.; Vora, N. Formulation strategies for solid oral dosage form using 3D printing technology: A minireview. *J. Drug Deliv. Sci. Technol.* **2018**, *46*, 148–155. [CrossRef]
38. Araújo, M.R.P.; Sa-Barreto, L.L.; Gratieri, T.; Gelfuso, G.M.; Cunha-Filho, M. The Digital Pharmacies Era: How 3D Printing Technology Using Fused Deposition Modeling Can Become a Reality. *Pharmaceutics* **2019**, *11*, 128. [CrossRef] [PubMed]
39. Okwuosa, T.C.; Soares, C.; Gollwitzer, V.; Habashy, R.; Timmins, P.; Alhnan, M.A. On demand manufacturing of patient-specific liquid capsules via co-ordinated 3D printing and liquid dispensing. *Eur. J. Pharm. Sci.* **2018**, *118*, 134–143. [CrossRef]
40. Solaro, R.; Corti, A.; Chiellini, E. Biodegradation of poly(vinyl alcohol) with different molecular weights and degree of hydrolysis. *Polym. Adv. Technol.* **2000**, *11*, 873–878. [CrossRef]
41. Rai, P.; Mehrotra, S.; Priya, S.; Gnansounou, E.; Sharma, S.K. Recent advances in the sustainable design and applications of biodegradable polymers. *Bioresour. Technol.* **2021**, *325*, 124739. [CrossRef]
42. Khosravani, M.R.; Reinicke, T. On the environmental impacts of 3D printing technology. *Appl. Mater. Today* **2020**, *20*, 100689. [CrossRef]
43. Krishna, N.; Brow, F. Polyvinyl alcohol as an ophthalmic vehicle. Effect on regeneration of corneal epithelium. *Am. J. Ophthalmol.* **1964**, *57*, 99–106. [CrossRef]
44. Ivanova, N.A.; Trapani, A.; Di Franco, C.; Mandracchia, D.; Trapani, G.; Franchini, C.; Corbo, F.; Tripodo, G.; Kolev, I.N.; Stoyanov, G.S.; et al. In vitro and ex vivo studies on diltiazem hydrochloride-loaded microsponges in rectal gels for chronic anal fissures treatment. *Int. J. Pharm.* **2019**, *557*, 53–65. [CrossRef]
45. Debevec, V.; Ljubin, T.S.; Jeraj, Ž; Peterka, T.R.; Bratuž, B.; Gašperlin, D.; Srčič, S.; Horvat, M. Step-wise approach to developing a scale-independent design space for functional tablet coating process. *Drug Dev. Ind. Pharm.* **2020**, *46*, 566–575. [CrossRef] [PubMed]
46. Yang, Y.; Huang, Z.; Zhang, X.; Li, J.; Huang, Y.; Chen, W.; Pan, X.; Wu, C. Development of Paroxetine Hydrochloride Single Layer Controlled-Release Tablets Based on 32 Factorial Design. *Pharmaceutics* **2018**, *10*, 243. [CrossRef] [PubMed]
47. Samaha, D.; Shehayeb, R.; Kyriacos, S. Modeling and Comparison of Dissolution Profiles of Diltiazem Modified-Release Formulations. *Dissolution Technol.* **2009**, *16*, 41–46. [CrossRef]
48. Kállai, N.; Luhn, O.; Dredán, J.; Kovács, K.; Lengyel, M.; Antal, I. Evaluation of drug release from coated pellets based on isomalt, sugar, and microcrystalline cellulose inert cores. *AAPS PharmSciTech* **2010**, *11*, 383–391. [CrossRef] [PubMed]
49. Arany, P.; Róka, E.; Mollet, L.; Coleman, A.W.; Perret, F.; Kim, B.; Kovács, R.; Kazsoki, A.; Zelkó, R.; Gesztelyi, R.; et al. Fused deposition modeling 3D printing: Test platforms for evaluating post-fabrication chemical modifications and in-vitro biological properties. *Pharmaceutics* **2019**, *11*, 277. [CrossRef] [PubMed]
50. Toyoda, N.; Yamamoto, T.; Arakawa, K.; Teshima, A. Preparation of PVA/Polymer Colloid nanocomposite Hydrogel Using PS-PNVA Particles. *Chem. Lett.* **2019**, *48*, 378–381. [CrossRef]
51. Bastiat, G.; Pritz, C.O.; Roider, C.; Fouchet, F.; Lignières, E.; Jesacher, A.; Glueckert, R.; Ritsch-Marte, M.; Schrott-Fischer, A.; Saulnier, P.; et al. A new tool to ensure the fluorescent dye labeling stability of nanocarriers: A real challenge for fluorescence imaging. *J. Control. Release* **2013**, *170*, 334–342. [CrossRef]
52. Sheskey, P.J.; Cook, W.G.; Cable, C.G. (Eds.) *Handbook of Pharmaceutical Excipients*, 8th ed.; Pharmaceutical Press: London, UK, 2017.

materials

MDPI

Article

Cell-Mediated Immunoreactivity of Poly(2-isopropenyl-2-oxazoline) as Promising Formulation for Immunomodulation

Ema Paulovičová [1], Zuzana Kroneková [2], Lucia Paulovičová [1], Monika Majerčíková [2] and Juraj Kronek [2,*]

[1] Immunol & Cell Culture Laboratories, Department Immunochemistry of Glycoconjugates, Center of Glycomics, Institute of Chemistry, Slovak Academy of Sciences, Dúbravská cesta 9, 845 38 Bratislava, Slovakia; ema.paulovicova@savba.sk (E.P.); lucia.paulovicova@savba.sk (L.P.)

[2] Department for Biomaterials Research, Polymer Institute, Slovak Academy of Sciences, Dúbravská cesta 9, 845 41 Bratislava, Slovakia; zuzana.kronekova@savba.sk (Z.K.); upolmoma@savba.sk (M.M.)

* Correspondence: Juraj.kronek@savba.sk; Tel.: +421-2-3229-4366

Abstract: Poly(2-isopropenyl-2-oxazoline) (PIPOx) represents a functional polymer with high potential for drug delivery, tissue engineering, and immunomodulation. The immunomodulatory efficiency of the PIPOx formulation has been studied in vitro following splenic cells and RAW 264.7 macrophages exposition. The cell-specific immunomodulative effect on production of Th1, Th2, Th17, and Treg signature cytokines has been demonstrated. The impact on the functionality of PIPOx-sensitized RAW 264.7 macrophages was assessed by cell phagocytosis. Time- and concentration-dependent cell internalization and intracellular organelles colocalization of fluorescently labeled PIPOx has been examined. The in vitro results demonstrated the PIPOx bioavailability and the capability of triggering immune cell responses resulting in the induced production of cell-specific signature interleukins, important prerequisite properties for future potential biomedical applications.

Keywords: poly(2-isopropenyl-2-oxazoline); immunomodulation; cytokines; RAW 264.7; phagocytosis; cell internalization

Citation: Paulovičová, E.; Kroneková, Z.; Paulovičová, L.; Majerčíková, M.; Kronek, J. Cell-Mediated Immunoreactivity of Poly(2-isopropenyl-2-oxazoline) as Promising Formulation for Immunomodulation. *Materials* **2021**, *14*, 1371. https://doi.org/10.3390/ma14061371

Academic Editors: Montserrat Colilla and Yury A. Skorik

Received: 20 December 2020
Accepted: 8 March 2021
Published: 12 March 2021

1. Introduction

Poly(2-alkyl-2-oxazolines) represent biocompatible and non-cytotoxic polymeric materials [1] with a high potential in different biomedical applications such as controlled drug and gene release, tissue engineering, hydrogel technologies, etc. [2–4]. Usually, they are achieved in the cationic ring-opening polymerization (CROP) of 2-alkyl-2-oxazolines leading to polymers with defined structure, predicted molar mass, and narrow dispersity [5,6]. Using different 2-oxazoline monomers, the wide library of hydrophilic, thermosensitive [7,8], hydrophobic, amphiphilic [9], or functional [10] polymers has been prepared. Apart from 2-alkyl-2-oxazolines, 2-alkenyl-2-oxazolines can provide, depending on polymerization conditions, several polymerization reactions leading to polymers with various structures and architectures [11–14].

From this group of monomers, 2-isopropenyl-2-oxazoline represents a monomer with dual orthogonal functionality able to polymerize by CROP of 2-oxazoline unit providing polymers with free double bonds [15,16]. On the other hand, an isopropenyl unit enables the preparation of poly(2-isopropenyl-2-oxazolines) (PIPOx) containing a free 2-oxazoline group in the side chain. Free-radical polymerization belongs to the most common polymerizations of 2-isopropenyl-2-oxazolines leading to polymers with broader dispersity (Đ) and lower control over molar mass and architecture [17,18]. Similarly, polymers with broader dispersity were achieved in the frustrated Lewis-pair polymerization of 2-isopropenyl-2-oxazoline [19]. Better-defined polymers have been achieved using various methods of living or controlled polymerizations. Living polymerizations of 2-isopropenyl-2-oxazoline typically involve living anionic polymerization initiated by

diphenylmethylpotassium/diethylzinc [20] or n-butyllithium [21]. Polymers with low dispersity were also achieved in the rare-earth metal-mediated group transfer polymerization of 2-isopropenyl-2-oxazoline [22]. On the other hand, reversible addition−fragmentation chain transfer polymerization of 2-isopropenyl-2-oxazoline provided PIPOx with molar mass under 3000 g/mol and relatively high dispersity around 1.35 [23]. Moreover, polymerizations proceeded in only 30% of conversions. Recently, Raus at al. for the first time successfully prepared PIPOx through aqueous Cu(0)-mediated atom-transfer radical polymerization of 2-isopropenyl-2-oxazoline in a controlled way initiated and catalyzed by the 2-chloropropionitrile/CuCl($CuCl_2$)/TPMA system [24].

PIPOx containing a free 2-oxazoline ring can be further modified employing a reaction of 2-oxazoline moiety with compounds containing thiol [25] or carboxylic groups [17,18,23,25]. Due to these unique chemical features, PIPOx is currently attractive for different fields of biotechnology and medicine due to possible preparation of thermosensitive polymers [26,27], hydrogels [27–30], or (bio)conjugates with peptides, saccharides, or drugs [31]. Therefore, their rising importance is expected, especially in drug delivery, gene delivery, tissue engineering, or vaccine technology. The basic requirement for the perspective use in biomedical applications is the tolerance of cells to the used polymer materials. Therefore, the assessment of biocompatibility using tissue cultures evaluating acute and system toxicity, examining of the inhibition of cell growth, mutagenicity, carcinogenicity, teratogenicity, and pro-allergenic potential must be included.

Immunomodulative activities of polymeric biomaterials have become the most relevant ones concerning their bioavailability and biocompatibility. Different strategies of triggering the appropriate immune system responses by functional biomaterials and various applications of biomaterials mimicking the physiological extracellular matrix and modifications of cell-mediated immune responses are of interest [32,33]. Spleen-derived cells are represented by a mixture of immune cells including macrophages, monocytes, dendritic cells (DCs), and T-lymphocytes that possess different functions in immune system. Myeloid phagocytes such as macrophages or DCs representing a complex network of cells with protective functionalities are also involved in mechanisms of homoeostasis such as tissue remodeling and wound healing [34]. Macrophages, comparable with Th-lymphocytes, have been divided into main subsets: pro-inflammatory M1-classically activated macrophages and anti-inflammatory M2-alternatively activated macrophages with distinct functional and phenotypical characteristics [35,36]. In general, inflammatory cytokines such as TNF-α and IFN-γ induce the M1 phenotype. On the contrary, anti-inflammatory interleukins such as IL-10, IL-4, and IL-13 induce the M2 phenotype [33]. Macrophages play an important role in orchestrating immune responses to biomaterials used in the construction of implantable devices and drug-delivery systems [37].

It was shown recently that positively charged polymers such as polyethyleneimine and cationic dextran have the potential to modulate macrophages and change their phenotype from tumor growth-promoting M2 macrophages to anti-tumor M1 macrophages [38]. In the last study, we showed that PIPOx is also not cytotoxic to the cells up to 10 mg/mL and significantly stimulates in vitro and ex vivo proliferation of macrophages [18]. We have shown that co-stimulation of non-adherent cells (T-lymphocyte-enriched splenocytes) with PIPOx-stimulated adherent cells (enriched in DCs) leads to their induced proliferation. These results suggest that PIPOx may play a role in various immunomodulatory processes [18].

In this work, we focused on the cell-mediated bioimmunological behavior of PIPOx and its cellular compatibility as promising matrix biomaterial. The sequential adherence of splenocytes and isolated cell populations have been used to ascertain their immunobiological activity following PIPOx exposure. The aim of study suggested the sensitization of population of adherent $CD11c^+$ and $CD14^+$ spleen cells and adherent spleen cells more enriched in $CD11c^+$ antigen-presenting cells with PIPOx and follow up the polarization of immune response towards Th1, Th2, Th17, or Treg evaluated by measuring the production of selected signature cytokines. The cytotoxicity has been determined via phagocytosis

process. Next, the RAW 264.7 macrophage internalization of PIPOx-FITC followed by intracellular localization has been assayed based on colocalization in vesicular structures of the cells resembling organelles of phagocytic and/or endocytic pathway.

2. Materials and Methods

2.1. Material

2-Isopropenyl-2-oxazoline (Sigma-Aldrich, Weinheim, Germany) was distilled in the presence of 2,6-di-tert-butyl-4-methylphenol (Sigma-Aldrich, Weinheim, Germany) under reduced pressure, and stored at −20 °C under argon atmosphere. N,N-Dimethylacetamide (DMAc) (Sigma-Aldrich, Weinheim, Germany) was distilled over phosphorus pentaoxide (Sigma-Aldrich, Weinheim, Germany) under reduced pressure. Fluorescein isothiocyanate (FITC) and dimethylsulfoxide (DMSO) were purchased from Sigma-Aldrich (Weinheim, Germany) and used as received. 4-Aminobutyric acid (ABA) was purchased from Fluka (Buchs, Germany) and used as received.

2.2. Synthesis of Polymers

PIPOx was synthesized by a free-radical polymerization in bulk initiated by azobisisobutyronitrile (AIBN) as described elsewhere [18]. Molar mass of PIPOx was equal to 21,000 g/mol and Đ = 1.85. For ^{1}H nuclear magnetic resonance (NMR) and Fourier-transform infrared spectroscopy (FTIR) spectra of PIPOx see Figures S1 and S2 in Supplementary Material.

PIPOx labeled with FITC (PIPOx-FITC) was prepared from PIPOx by two-step synthesis. In the first step, PIPOx (0.22 g, 0.001 mol of structural units) and ABA (0.020 g, 0.0002 mol) were dissolved in dry DMAc (1 mL) and heated at 120 °C for 6 h under argon. Reaction mixture was cooled, diluted with 5 mL of water, dialyzed towards deionized water (dialysis membrane Spectra/Por 6, Molecular weight cut-off (MWCO) 3.5 kDa, Spectrum Laboratories, Rancho Dominguez, CA, USA) for 4 × 1.5 h, and freeze-dried. Yield of reaction was 95% of PIPOx containing ABA (PIPOx-ABA). The chemical structure was determined from FTIR and NMR (Figures S3 and S2 in Supplementary Material). Prepared intermediate was functionalized with FITC using a standard protocol for labeling proteins. Briefly, 23 mg of PIPOx-ABA was dissolved in 0.1 M bicarbonate buffer (10 mL, pH = 9) and 1.6 mL of FITC in DMSO (1 mg/mL) was dropwise added for 5 min. Reaction mixture was held in 2–8 °C for 8 h under argon and product was purified using dialysis toward distilled water (dialysis membrane Spectra/Por 6, MWCO 3.5 kDa, Spectrum Laboratories, Rancho Dominguez, CA, USA). Yield: ~100%. The chemical structure was evaluated using ^{1}H NMR and FTIR (Figures S4 and S2 in Supplementary Material), and degree of addition was calculated from UV/Vis absorption spectroscopy (Figure S5 in Supplementary Material).

2.3. Analytical Methods

The ^{1}H and ^{13}C NMR spectra for all polymers were conducted in $CDCl_3$ and DMSO-d_6 at room temperature using a Varian VXR-400 (Wilmington, DE, USA). In all measurements, tetramethylsilane was used as an internal standard. ATR-FTIR spectra of polymers were conducted by NICOLET 8700 (Thermo Scientific, Madison, WI, USA) using a Ge crystal with 64 scans and in resolution of 4 cm^{-1}.

The molar mass and dispersity of PIPOx was recorded using size exclusion chromatography (SEC) as described elsewhere [18].

The UV/VIS spectra were recorded using Shimadzu 1650 PC (Shimadzu, Kyoto, Japan) in methanol at the concentration of 0.1 mg/mL for labeled polymers in the range of 210 to 600 nm in the resolution of 0.2 nm. The emission spectra were recorded on a Shimadzu RF-5301 (Shimadzu, Kyoto, Japan) in methanol using concentration ranged from 0.01 to 0.1 mg/mL with excitation wavelength of 495 nm.

2.4. Preparation of Splenocytes

Balb/c mice (female, 8–12 weeks old, breeding facility VELAZ, Prague, Czech Republic) were used for extirpation of spleens and isolation of splenocytes. The experiments were performed according to GLP and OECD guidelines, based on the ethical guidelines of the Research Base of Slovak Medical University, Institute of Preventive and Clinical Medicine (Bratislava, Slovakia), the approval No. Ro 2939/09-221 of State veterinary and food administration of the Slovak Republic. Spleens were aseptically removed and were poured into the ice-cold saline (1 mL per spleen). Splenocytes were isolated by homogenization of splenic tissue with the plunger end of the syringe. The splenocytes suspension was filtered (50µm-mesh filter (CellTrics disposable filter; Partec, Görlitz, Germany) and centrifuged at 800× *g* for 10 min at 4 °C. The splenocytes were resuspended in 5 mL of ACK lysis buffer (0.15 M NH_4Cl, 1 M K_2CO_3, and 0.01 M EDTA, pH 7.2) and the lysis of erythrocytes was completed at room temperature for 5 min. Afterwards, cells were washed twice with saline and resuspended in complete RPMI-1640 medium (Lonza, Basel, Switzerland) supplemented with 10 % of fetal bovine serum, penicillin (100 U/mL) and streptomycin sulphate (100 mg/mL) (Gibco, NY, USA). Following assessment of splenocyte viability by Trypan blue staining method, the density of cells has been adjusted to 1×10^6 cells/mL.

2.5. Stimulation

Isolated and collected splenocytes were seeded (4×10^5 cells per well) into 24 well culture plates (Nunc, Roskilde, Denmark) and stimulated in vitro with Concanavalin A (Con A), final concentration of 10 µg/mL (Sigma, Stockholm, Sweden) and PIPOx (final concentration of 5 mg/mL) for 24 h in a 37 °C incubator (5% CO_2, humidified atmosphere). Following the exposition, the culture media were stored at −20 °C for determination of interleukins and growth factors.

Isolated splenocytes in complete RPMI-1640 (1×10^6 cells per ml) were seeded into 6-well culture plates (Nunc, Denmark). Afterwards, the cells were incubated for 1 h at 37 °C (humidified incubator, 5% CO_2). Following this 1st incubation period, non-adherent cells were taken away and seeded into new 6-well culture plates. The adherent cells from the 1st incubation period were washed 3 times to take out all non-adherent cells and were adjusted with 500 µL of fresh complete RPMI-1640 medium. The first isolated non-adherent cells were allowed to adhere overnight in the complete RPMI-1640 medium at 37 °C, 5% CO_2 in humidified incubator. Following this 2nd adherence period splenocytes depleted of adherent cells were collected and the adherent cells after 2nd adherence period were washed 3 times to eliminate any non-adherent cells.

The adherent cells (following the 1st and the 2nd incubation period) were harvested. Adherent cells obtained in this fashion after the 1st and the 2nd adherence period together with non-adherent cells were subjected to the immunocytometric analysis (FC500, Beckman Coulter, Fullerton, CA, USA) using Anti-Mouse CD3-FITC (clone KT3, Rat IgG2a), Anti-Mouse CD4-PE (clone YTS, Rat IgG2b), Anti-Mouse CD8α-PE (clone KT15, Rat IgG2a), Anti-Mouse CD11c-FITC (clone N418, Armenian Hamster IgG) (Antigenix America Inc., Melville, NY, USA), Anti-Mouse CD14-PE (clone rmC5-3 (RUO), Rat LOU/M IgG1, κ, BD Pharmingen). Phenotyping analysis of adherent cells after the 1st adherence period revealed enrichments in DCs and monocytes/macrophages with reduced proportion of lymphocytes (Table 1). Adherent cells obtained after the 2nd adherence period were more enriched in DCs with fewer monocytes/macrophages in comparison with enrichment after the 1st adherence period, as resulted from the immunocytometric assay of $CD11c^+$ and $CD14^+$ immunocytes.

The adherent and non-adherent cells from sequential adherent phases underwent in vitro stimulation with Con A and PIPOx in the same way as previous stimulation of splenocytes was conducted. Co-stimulation of adherent cells (1×10^6 cells/mL, adherent cells after the 1st and the 2nd adherence period, unstimulated or stimulated with Con A and PIPOx) with non-adherent splenocytes (1×10^6 cells/mL) was carried out by co-

cultivation in fresh complete RPMI-1640 medium for 4 days (37 °C humidified incubator, 5% CO_2 atmosphere).

Table 1. Characterization of cell populations enriched by a sequential adherence method. Differentiation markers of cell populations: $CD3^+$-T-cells, $CD4^+$-helper T-cells (Th), $CD8^+$-cytotoxic T-lymphocytes (CTLs), $CD11c^+$-DCs, monocytes, granulocytes, $CD14^+$-macrophages, monocytes.

Cell Population	$CD3^+$ (%)	$CD4^+$ (%)	$CD8^+$ (%)	$CD11c^+$ (%)	$CD14^+$ (%)
Splenocytes	30.8 ± 2.2	22.3 ± 1.8	11.8 ± 2.6	8.1 ± 1.7	5.3 ± 1.3
1st adherence period	16.9 ± 3.1	15.7 ± 2.2	7.0 ± 1.3	23.3 ± 2.3	10.0 ± 3.1
2nd adherence period	14.1 ± 2.9	14.7 ± 3.1	6.5 ± 1.2	35.4 ± 3.4	9.1 ± 2.5
non-adherent cells	33.2 ± 2.1	28.3 ± 3.1	12.4 ± 2.3	5.3 ± 1.2	3.3 ± 0.3

2.6. Cytokine Secretion Assay, Immunocytometry, and ELISA

As previously described, washed and lysed splenocytes were adjusted by growth medium approximately to 4 × 10^7 cell/mL and 400 µL aliquots were stimulated with PIPOx (concentration of 5 mg/mL) and plated in 24-well tissue culture plates (Nunc, Denmark). Polyclonal cell stimulation with mitogen Con A (10 µg/mL) was included into experiment as a positive control. 24-well tissue culture plates were allowed at 37 °C, 5% CO_2 incubator for 24 h. Afterwards, the cell suspension was centrifuged at 800× *g* for 10 min at 4 °C and the cell pellet was resuspended in cold PBS pH 7.2 containing 0.5% bovine serum albumin and 2mM EDTA. The IL-10, IL-4, IFN-γ and IL-17 secretion assays were processed according to manufacturer's recommendation (MACS Cytokine Secretion Assay, Miltenyi Biotec, GmbH, Bergisch Gladbach, Germany). Counterstaining of $CD4^+$ T-cells was performed by using rat anti-mouse CD4 FITC conjugate (Antigenix America). 10,000 viable cells were acquired by immunoflowcytometry using a Beckman Coulter FC 500 flow cytometer (Beckman Coulter Inc., Fullerton, CA, USA) equipped with a 488 nm argon laser and a 637 nm HeNe collinear laser, and controlled by CXP software [39]. A lymphocyte gate based on forward scatter vs. side scatter dot plot discrimination and settings was activated prior to further gating to exclude debris. The samples were assayed twice. The values are expressed as percentage of cytokine positive cells among $CD4^+$ cells ± SD. Quantitative detection of mouse IL-4, IL-10, IL-17 and IFN-γ cytokines in cell culture media supernatants following PIPOx and Con A specific stimulation of isolated splenocytes (see Section 2.5) was conducted by enzyme-linked immunosorbent assay Mouse Instant ELISA (Thermofisher Scientific, Waltham, MA, USA) according to manufacturer's recommendations. All samples were measured twice. The data are expressed as average ± SD.

2.7. Phagocytosis

Determination of cell phagocytosis, based on the ingestion of FITC-labeled *C. albicans* cells, was assayed under controlled conditions, following incubation with fluorescein isothiocyanate (FITC)-labeled *C. albicans* and RAW 264.7 macrophages for 30 min at 37 °C. Following treatment, the reaction was stopped by ice cooling the samples. The total amount of phagocyting cells, i.e., cells ingested at least one *C. albicans* cell was determined by immunocytometric assay, using a Beckman Coulter FC 500 flow cytometer (Beckman Coulter Inc., Fullerton, CA, USA).

2.8. Cell Uptake and Cell Tracking of PIPOx-FITC by Fluorescence Quenching Cytofluorometric Assay

The uptake and intracellular tracking of PIPOx-FITC by RAW 264.7 cells was performed at 37 °C, for time period from 1–24 h, with 0.05, 0.1 and 0.5 mg/mL of PIPOx-FITC. The extracellular fluorescein isothiocyanate fluorescence of PIPOx-FITC has been quenched using 0.4% Trypan blue dye (Sigma-Aldrich, St. Louis, MO, USA). Trypan blue treated RAW 264.7 cells following exposure to PIPOx-FITC were assayed after 30 min incubation in dark by using immunocytometric evaluation. The amounts of adherent extracellular

and ingested intracellular PIPOx-FITC were distinguished and determined based on the difference between resulting total number of phagocyting cells and number of phagocyting cells following fluorescence quenching (Trypan blue assay).

2.9. Colocalization of PIPOx-FITC in Macrophages

The distribution fluorescently labeled PIPOx-FITC and its colocalization with specific organelles in RAW 264.7 macrophages was assessed by Confocal laser scanning microscope (CLSM) LSM510 META on an Axiovert 200 and 40×/1.2W C-Apochromat objective (Zeiss, Jena, Germany). The optical setup for FITC fluorescence was excitation with 488 nm laser line, and a 500–550 nm long-pass emission filter; for Mito-Tracker-Orange (Zeiss, Jena, Germany) a 543 nm laser line and a 565–615 nm long-pass emission filter, and for LysoTracker-deep red fluorescence. a 633 nm laser line and a 650–710 nm long-pass emission filter. Concentration of PIPOx-FITC for colocalization study was 1 mg/mL in full growth medium. Living cells were treated for 20 h with PIPOx–FITC, then rinsed with PBS and incubated for 10 min with MitoTracker or LysoTracker (both Molecular Probes, Eugene, OR, USA) at concentration of 75×10^{-9} mol/dm^3. Cells were washed with PBS before imaging. A region of interest (ROI) analysis was performed using ZEN software (Zeiss) [40] The results are presented as the average of correlation coefficients from six different cells for each Tracker dye.

2.10. Statistical Analysis

The immunobiological results were expressed as mean values ± SD. Data were tested for normality by Shapiro–Wilk test at the 0.05 level of significance. Statistics was performed by one-way ANOVA and post hoc Bonferroni test. Results were considered significant when differences equaled or exceeded the 95% confidence level ($p < 0.05$). Statistics was completed by ORIGIN 2018 software (OriginLab Corporation, Northampton, MA, USA). Pearson's correlation coefficient has been applied to compare the strength of the relationship between variables.

3. Results

3.1. Synthesis and Labeling of PIPOx

PIPOx represents a functional polymer with strong potential for different biomedical applications. We showed previously that PIPOx is non-cytotoxic up to a concentration of 10 mg/mL for fibroblasts and macrophages cell lines. For immunomodulation studies, we used splenocytes isolated from Balb/c mice [18]. This paper is a continuation of the work on immunomodulation properties studied on the splenocytes and mouse macrophages [18]. For better comparison, we used for all experiments the same batch of PIPOx as in the previous study. PIPOx was synthesized by the free-radical polymerization using AIBN as an initiator in bulk at 60 °C for 8 h. This type of polymerization provided PIPOx with broader dispersity (Đ = 1.85) and molar mass of 21,000 g/mol. Chemical structure of PIPOx was confirmed by NMR and FTIR (see Figures S1 and S2 in Supplementary Material).

Fluorescently labeled PIPOx containing FITC was prepared by two-step modification (Figure 1). The first step included thermally induced reaction of PIPOx with 4-aminobuttyric acid in DMAc at 120 °C for 6 h. The chemical structure was estimated by ^{1}H NMR and FTIR (see Figures S3 and S2 in Supplementary Material). Second step comprised addition of FITC on amino groups of PIPOx-ABA according to standard procedure described in Experimental part. Similarly, the real content of fluorescein moieties in PIPOx-FITC was calculated from UV/Vis absorbance and found close to feeding ratio of 1 mol.% (Figure S5 in Supplementary Material). Fluorescence ability of PIPOx-FITC was studied by emission measurements in methanol in different concentrations ranged from 0.01 to 0.1 mg/mL (Figure 2). It can be seen from spectra that emission maximum was for all concentration same and equal to 520 nm. PIPOx-FITC was used for cell internalization and organelles tracking in macrophage cell lines.

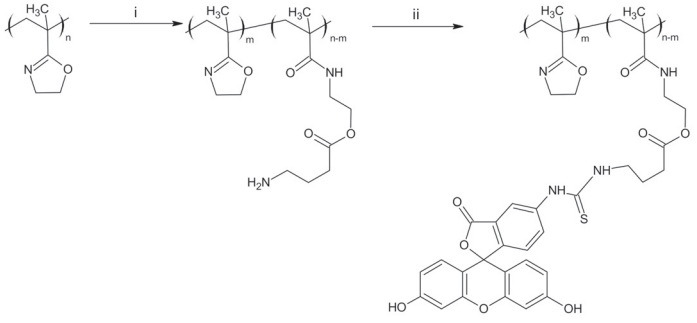

Figure 1. Two-step synthesis of PIPOx labeled with fluorescein (PIPOx-FITC) comprising of the introduction of amino moiety and reaction with fluorescein isothiocyanate (FITC). (i) ABA, DMAc, 120 °C, 6 h, (ii) FITC, 0.1 M bicarbonate buffer, 2–8 °C, 8 h.

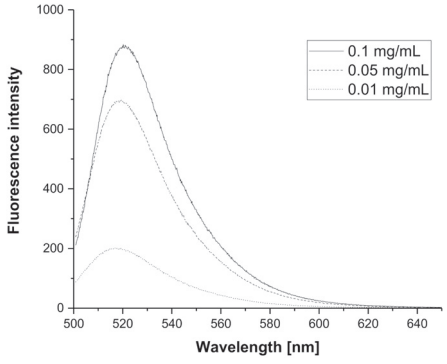

Figure 2. Emission spectra of PIPOx-FITC measured in methanol in three concentrations (0.1 mg/mL, 0.05 mg/mL and 0.01 mg/mL).

3.2. Immunomodulation Properties

Immunological behavior of spleen-derived immunocompetent cells and RAW 264.7 cells exposed to PIPOx has been followed up according to inductive release of signature Th1 (IFN-γ), Th2 (IL-4), Th17 (IL-17) and Treg (IL-10) cytokines and effectivity of phagocytic activity.

The isolated spleen cells were divided into the cell populations using the sequential adherence technique and 4 different groups enriched with distinct types of immunocytes were obtained as described in Table 1. Subsequently, these cell populations were used for stimulation and co-stimulation experiments (Figures 3–5).

Cytokine profile analysis of culture media after splenocytes stimulated with PIPOx reveal statistically significant increase of IL-10 production, even higher compared to Con A stimulation. Increase of IFN-γ, IL-17 and IL-4 production was not induced by PIPOx stimulation of complete splenocytes (Figure 3). PIPOx stimulation of adherent spleen cells obtained after the 1st adherence period, enriched in $CD11c^+$ and $CD14^+$ antigen-presenting cells (APCs), induced significantly enhanced production of IFN-γ (72 times higher compared to unstimulated control and 4.4 times higher than Con A) and increase in production of IL-17 (2.4 times higher compared to unstimulated control but 20 times lower than Con A). The cell-release of IL-4 and IL-10 was not affected. Obtained results indicate direction of the immune response polarization towards Th1/Th17 over Th2 and Treg immune responses (Figure 3). Adherent spleen cells following the 2nd adherence period, more enriched in $CD11c^+$ APCs, upon stimulation with PIPOx produced statistically

significantly higher amount of IL-10 (1.8 times higher in comparison with unstimulated control although 1.3 times lower than Con A) indicating Treg polarization of immune response (Figure 3).

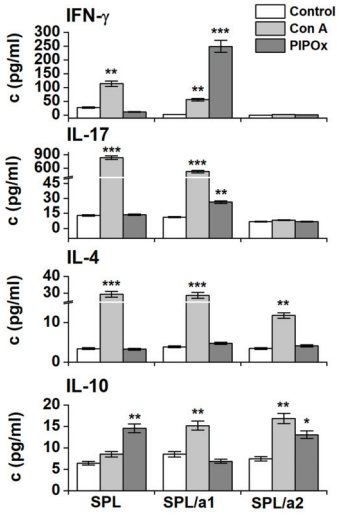

Figure 3. Production of cytokines after in vitro stimulation. Concentrations of IFN-γ, IL-17, IL-4 and IL-10 in media after stimulation of splenocytes and adherent spleen cells after the 1st (SPL/a1) and the 2nd (SPL/a2) adherence period. Response to stimulation with Con A (10 μg/mL) and PIPOx (5 mg/mL). As a negative control, media of unstimulated cells were used. All data are shown as mean ± SD and statistical significance of differences between Con A or PIPOx-stimulated cells and unstimulated cells are expressed: ***—$p < 0.001$, **—$0.001 < p < 0.01$, *—$0.01 < p < 0.05$. Tests were performed in triplicate.

Adherent spleen cells, enriched in APCs, were pulsed with PIPOx or Con A and co-cultured with non-adherent splenocytes (increased proportion of T-lymphocytes). Culture media after co-cultivation were used for cytokines analysis (Figure 4). PIPOx induced statistically significant increase of IFN-γ production (14.9 times higher than unstimulated APCs, but 8 times lower compared to Con A), IL-17 production (5.7 times higher in comparison with unstimulated APCs although 42.8 times lower compared to Con A), IL-10 production (5.0 times higher than unstimulated APCs and 2.1 times lower compared to Con A) and slight statistically non-significant increase of IL-4 production (1.8 times higher than unstimulated APCs and 79.1 times lower compared to Con A) in cultures containing pulsed adherent spleen cells population following the 1st adherence period (Figure 4). Adherent spleen cells after the 2nd adherence period pulsed with PIPOx did not induced significant increase of cytokines production after co-cultivation with splenic non-adherent cells (Figure 4).

Splenocytes stimulated with PIPOx were analyzed for production of Th1, Th2, Th17 and Treg signature cytokines via flow cytometry (Figure 5). PIPOx exposition induced increase of $CD4^+$ producing cells for all monitored cytokines. Results reveal higher percentage of IFN-γ (1.43 times higher than control) and IL-10 (1.92 times higher than control) producing $CD4^+$ T-lymphocytes compared to $CD4^+IL\text{-}4^+$ (1.85 times higher than control) and $CD4^+IL\text{-}17^+$ (2.33 times higher than control) cells (Figure 5). Induction of cytokine producing cells upon stimulation with PIPOx was for IFN-γ, IL-10, and IL-4 lesser than Con A stimulation, except 1.74 times higher proportion of IL-17 producing $CD4^+$ cells induced by PIPOx in comparison with Con A stimulation.

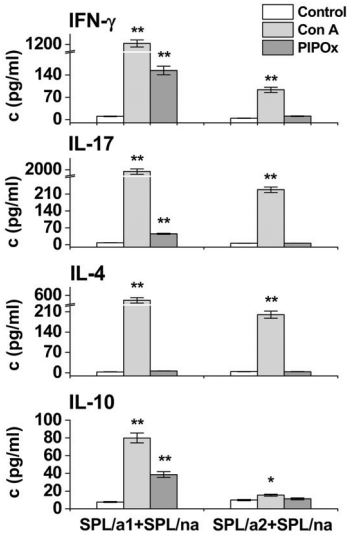

Figure 4. Production of cytokines after in vitro co-stimulation. Concentration of IFN-γ, IL-17, IL-4 and IL-10 in media after co-stimulation of non-adherent spleen cells with stimulated adherent spleen cells obtained after the 1st (SPL/a1) and the 2nd (SPL/a2) adherence period. Response to stimulation with Con A (10 μg/mL) and PIPOx (5 mg/mL). As a negative control, media of unstimulated cells were used. Tests were carried out in triplicate. The experimental data are expressed as geometric means of three replicates ± SD. Levels of significance: ** $0.001 < p < 0.01$, * $0.01 < p < 0.05$. Differences were considered significant at $0.01 < p < 0.05$.

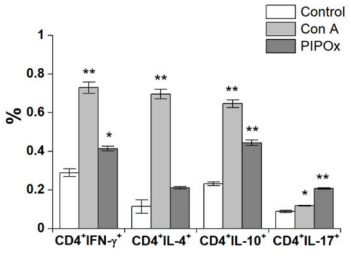

Figure 5. Flow-cytometric analysis of cytokine producing $CD4^+$ lymphocytes. Distribution of IFN-γ, IL-4, IL-10 and IL-17 producing $CD4^+$ cells within spleen cells stimulated with Con A (10 μg/mL) and PIPOx (5 mg/mL). Tests were done in triplicate. The experimental data are expressed as geometric means of three replicates ± SD. Levels of significance: ** $0.001 < p < 0.01$, * $0.01 < p < 0.05$. Differences were considered significant at $0.01 < p < 0.05$.

PIPOx stimulation of adherent $CD11c^+$ and $CD14^+$ spleen cells induced significantly enhanced production of IFN-γ and increased production of IL-17 thus indicating polarization of immune response towards Th1 (IFN-γ, $p < 0.001$) and Th17 (IL-17, $p < 0.01$) over Th2(IL-4, ns) and Treg(IL-10, ns) immune responses. Adherent spleen cells more enriched in $CD11c^+$ APCs produced significantly higher amount of IL-10 indicating Treg polarization of immune response.

Flow-cytometric analysis of cytokine producing $CD4^+$ lymphocytes reveal higher proportion of IFN-γ and IL-10 producing $CD4^+$ T-lymphocytes compared to $CD4^+IL\text{-}4^+$ and $CD4^+IL\text{-}17^+$ cells. Evidently, according to the PIPOx induced production of Th1, Th2, Th17and Treg signature cytokines, pro-inflammatory Th1 (IFN-γ, $p < 0.001$) and

Th17 (IL-17, $p < 0.01$) immune responses are more profound in exposed adherent $CD11c^+$ and $CD14^+$ spleen cells, the adherent spleen cells with higher expression $CD11c^+$ exert anti-inflammatory Treg (IL-10, $p < 0.05$) polarized response.

The immunocytometric analysis of RAW 264.7 macrophages exposed to different concentration of PIPOx revealed no significant impact on effective phagocytosis of *C. albicans*–FITC complex (Figure 6). Thus, the phagocytic capacity and functional effectivity of RAW 264.7 macrophages remained upon treatment with PIPOx without any significant impacts.

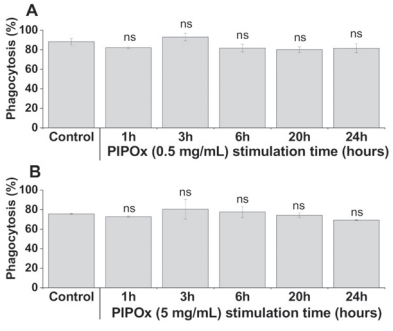

Figure 6. RAW 264.7 macrophage phagocytosis of *C. albicans*–FITC (%) following treatment with PIPOx analyzed by flow cytometry. The phagocytosis of FITC-labeled *C. albicans* cells by RAW 264.7 macrophages was analyzed by pre-treatment of cells for 1, 3, 6, 20, and 24 h with 0.5 mg/mL (**A**), and 5 mg/mL (**B**) of PIPOx and subsequent phagocytosis test analyzed using flow cytometry. Control represents untreated cells (Control). All data are expressed as Mean ± SD. Tests were carried out in triplicate. The one-way ANOVA and post hoc Bonferroni's tests was used to determine statistical significance of differences between untreated and stimulated cells and is expressed as ns—$p > 0.05$.

3.3. Cell Internalization and Organelles Tracking Study

The time and concentration-dependent PIPOx cell-processing (Figure 7) revealed sequential highly concentration-dependent intracellular accumulation of PIPOx. The highest intracellular accumulation of PIPOx for concentration 0.05 mg/mL was observed after 3 h exposition (68.9 times higher compared to the control), for concentration 0.1 mg/mL after 6 h treatment (120.9 times higher compared to the control) and for concentration 0.5 mg/mL after 3 h treatment (271.2 times higher compared to the control). The maximal PIPOx internalization, observed for the highest concentration (0.5 mg/mL), markedly exceeded (3.94-fold) the internalization of the lowest PIPOx concentration (0.05 mg/mL).

Using the flow cytometry, we have clearly demonstrated the uptake of PIPOx into the macrophages. Furthermore, the localization of PIPOx within the macrophage cell was performed using the organelle tracking dyes and fluorescently labeled PIPOx-FITC. The PIPOx-FITC treatment and staining with organelle tracking dyes was followed by ROI analysis according to Pearson and colocalization was expressed by correlation coefficient (R). Colocalization of PIPOx-FITC with organelle is considered when $R > 0.5$. PIPOx-FITC is localized within the macrophage in vesicular particles as seen on CLSM images (Figure 8). Based on ROI analysis, these vesicles containing PIPOx-FITC do not co-localize with mitochondrial network as $R = 0.3 \pm 0.1$ (Figure 8A,C). Partial colocalization of PIPOx-FITC containing vesicles with lysosomes stained with Lyso Tracker (Figure 8B,D) with $R = 0.5 \pm 0.16$ is observed. There are many vesicles containing PIPOx that do not co-localize with lysosomes.

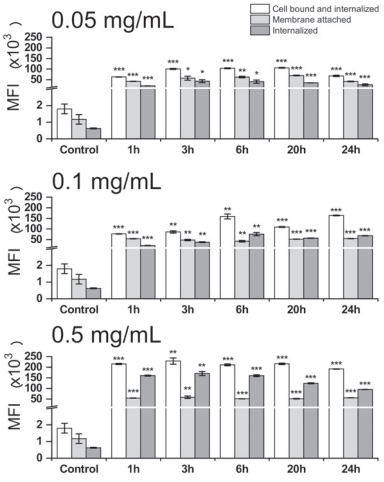

Figure 7. Flow-cytometric analysis of time kinetics and concentration-dependent PIPOx-FITC processing by RAW 264.7 macrophages. The PIPOx-FITC cell bound and internalized by RAW 264.7 macrophages was analyzed by exposition of cells for 1, 3, 6, 20, and 24 h with 0.05 mg/mL, 0.1 mg/mL and 0.5 mg/mL or FITC-labeled PIPOx using flow cytometry. The internalized PIPOx-FITC was analyzed after Trypan blue quenching. The amount of membrane attached PIPOx-FITC is expressed as a difference between the cells with cell bound and internalized PIPOx-FITC and Trypan blue quenched cell population (internalized PIPOx-FITC). Cell bound and internalized, membrane attached and internalized PIPOx-FITC were expressed as mean fluorescence intensities (MFI) of 10,000 analyzed cells. All data are shown as Mean ± SD. Tests were done in triplicate. The statistical significance of differences between control cells and stimulated cells by means of one-way ANOVA and post hoc Bonferroni's test is presented as: ***—$p < 0.001$, **—$0.001 < p < 0.01$, *—$0.01 < p < 0.05$.

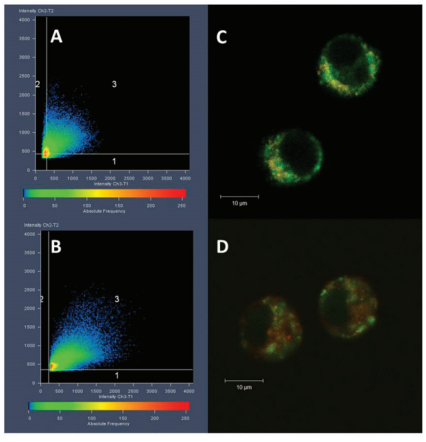

Figure 8. CLSM imaging and ROI analysis of PIPOx-FITC colocalization with organelles. ROI analysis in (**A**) mitochondria, R = 0.3 ± 0.1, and (**B**) lysosomes, R = 0.5 ± 0.16. Merged CLSM images of fluorescently labeled PIPOx-FITC (green) with (**C**) MitoTracker-labeled mitochondria (orange) or (**D**) LysoTracker-labeled lysosomes (red).

4. Discussion

The assessment of the interaction of the biomaterial structure and modulation of the host immune response represents one of most important strategies for effective in vivo inte-

gration of biomaterial. Moreover, immunomodulation strategies based on biomaterials can significantly improve the outcomes of medical implants and tissue engineering therapies. In general, the immunomodulation of immune responses based on the physicochemical modification of a biomaterial is important for effective biomaterial implementation [32]. The current medical research focuses on immunotherapy [32], development of safe vaccines [41] and combinations of therapies [42,43] to achieve the most effective treatment.

Our previous study revealed the immunomodulative properties of PIPOx based on follow-up of the immunocompetent cell proliferation following specific sensitization of splenic cell fractions [18]. The stimulation of splenocytes with PIPOx induced a significant increase of the proliferation rate. Co-cultivation of non-adherent spleen cells with PIPOx-stimulated adherent spleen cells after the first adherence period did not cause an increase in cell proliferation compared with unstimulated control cells, but after coculturing of non-adherent fraction of splenocytes with PIPOx-stimulated adherent spleen cells from a second adherence period, a significant increase of the proliferation rate was observed [18]. These results indicated that PIPOx exerted different immunomodulative effectivity with an emphasis on the phenotype of stimulation-affected immunocompetent cells. Now, regarding these results of previous observations, we perform analysis of the splenic cell-secreted cytokine profile following stimulation, to ascertain character of specific induced immune response and polarization.

In this study, the myeloid phagocytes represented by adherent $CD11c^+$ and $CD14^+$ spleen cells significantly induced production of IFN-γ and increased production of IL-17 after PIPOx stimulation. Thus, polarization of immune response towards Th1 and Th17 over Th2 and Treg immune responses is indicated. The adherent spleen cells more enriched in $CD11c^+$ APCs produced significantly higher amount of IL-10 indicating Treg polarization of immune response. Evidently, in PIPOx-exposed adherent $CD11c^+$ and $CD14^+$ spleen cells, pro-inflammatory Th1 and Th17 response is more profound, while in the adherent spleen cells with higher expression, $CD11c^+$ anti-inflammatory Treg polarized response is applied.

Generally, the Th1 response correlates with protective immunity, contrary to the Th2 responses, whose signature cytokine is IL-4, down-regulating Th1 immunity. Th17 cells were previously believed to be a subset of Th1 cells. They presumably have a regulatory role supporting the Th1-response and down-regulating the Th2-response. Th17 cells producing IL-17 have a crucial role in inflammatory processes. On the contrary, Treg subsets producing signature cytokine IL-10 exerted anti-inflammatory capacity to limit the pro-inflammatory T-cell responses [44].

DCs as APCs respond to molecular patterns by inducing differentiation of naive T-cells into effector T-helper subpopulations and activation of adaptive immunity and initiated both pro-inflammatory and anti-inflammatory immune responses. Moreover, DCs, by taking up, processing, and presenting foreign antigens to Th cells, have a critical role in connecting innate and adaptive immunities. Inflammatory DCs initiate Th17 and Th2 cell responses, while tolerogenic DCs activate Th1 and Tregs. Evidently, the engagement of $CD11c^+$ $CD14^+$-enriched spleen cells, $CD11c^+$-enriched spleen cells, and $CD3^+$, $CD4^+$, $CD8^+$ cells as a result of PIPOx cell-processing, cell presentation, and immune response polarization (Figures 4 and 5) has been observed.

The results revealed that the phagocytic capacity of RAW 264.7 macrophages remained unchanged upon treatment with PIPOx, without down-regulation of cell engulfment and internalization. Previously published immunobiological effectivity of poly(2-ethyl-2-oxazoline) (PETOx) and selected poly [2-(4-aminophenyl)-2-oxazoline-co-2-ethyl-2-oxazoline] (AEOx) copolymer in lymphoid mouse macrophage P388.D1 (Clone 3124) revealed a similar trend of phagocytosis, without any destructive interference with cell viability and phagocyting capability [1].

The uptake of polymers by cells depends on molecular structure, molar mass and the type of cell [45]. High molar mass of polymers can be a limiting factor in cell internalization and therefore some polymer domains that help polymer cell internalization were

already identified [46]. In our previous work devoted to cytotoxicity study of PIPOx, we have shown that PIPOx is internalized to fibroblast cells by endocytic pathway [18]. In macrophages, which are professional phagocytes, the phagocytic/endocytic activity is expected. Here, we show that internalization of PIPOx into RAW 264.7 macrophages is concentration-dependent and fast, as after 1h only slow increase of cell-internalized PIPOx is shown during 24 h incubation.

The fate of cell-internalized PIPOx was studied in colocalization studies with organelle markers. As shown by CLSM, PIPOx-FITC is not localized in mitochondria and is localized in vesicular structures that only partially co-localize with lysosomes (Figure 8). This is the difference between PIPOx colocalization in macrophages compared to mouse 3T3 fibroblasts where after 24 h PIPOx was mostly localized in lysosomes [18]. These other vesicular structures in macrophages could resemble other organelles of phagocytic or endocytic pathways, such as phagosomes or endosomes, which supports the hypothesis that PIPOx can be taken up and processed by APCs.

Biomaterials can thus act as synthetic adjuvants or DCs activators. Following internalization of the biomaterial vehicles by DCs, the antigens could be released intracellularly and activate MHC class I and II pathways and induce $CD4^+$ and $CD8^+$ T-cell immunity [41]. It was shown that polymers can fulfill not only an indirect role as drug carriers [43], agents solubilizing hydrophobic drugs, materials capable of reducing drug cytotoxicity, etc., but they can also function as therapeutic molecules.

It was already mentioned previously that poly(2-oxazoline)s are biocompatible polymers with increasing interest as biomaterials for drug, gene, protein, and radionuclide delivery [2]. For example, novel delivery platforms based on poly(2-oxazolines) with different molar masses have been reported as promising conjugates with interleukins and growth factors [47,48].

They are, however, relatively new in comparison to other classes of water-soluble polymers already established for such use. Besides intensive study of poly(2-oxazoline)s biological properties, only a limited number of them comprises immunomodulatory activity (mainly our previous studies) [1,49,50]. Although PIPOx is formally a member of the poly(2-oxazoline) family, it is a structurally different polymer with free 2-oxazoline rings in the side chain, compared to previously studied polymers of this class.

It was of high importance to subject PIPOx, as a promising biomedical formulation, for evaluation of immunomodulative effectivity in primary immunocytes and its capability to effectively polarize immune responses, thus to reach the best possible strategy to construct new biocompatible delivery systems. Further research in this area is therefore highly appreciated.

5. Conclusions

We have shown that PIPOx stimulation of different immunocompetent cells accelerates cell-specific immune responses. PIPOx-sensitized adherent $CD11c^+$ and $CD14^+$ spleen cells induced statistically significantly enhanced production of IFN-γ and IL-17, indicating polarization of immune cell response towards Th1/Th17 over Th2 and Treg immune responses. Adherent spleen cell-derived $CD11c^+$-enriched APCs produced statistically significantly higher secretion of IL-10, the signature cytokine of Treg phenotype. The time and concentration-dependent PIPOx-FITC RAW 264.7 cell-processing revealed sequential intracellular accumulation of PIPOx. The complex phagocytosis of RAW 264.7 macrophages following PIPOx exposure did not exert significant down-regulation of engulfment and internalization throughout effective cell phagocytosis. Using the colocalization of fluorescently labeled PIPOx and organelle tracking dyes, it was shown that PIPOx after internalization to cell occurs in lysosomes and other vesicular structures of endocytic pathway. The results of this study suggest PIPOx as a biocompatible polymer enhancing protective Th1/Th17 immunity over the Treg immune responses.

Supplementary Materials: The following are available online at https://www.mdpi.com/1996-1944/14/6/1371/s1, Figure S1: ^{1}H NMR spectrum of PIPOx measured in $CDCl_3$. Figure S2: ATR-FTIR spectrum of PIPOx, PIPOx-ABA, and PIPOx-FITC. Figure S3: ^{1}H NMR spectrum of PIPOx-ABA measured in $CDCl_3$. Figure S4: ^{1}H NMR spectrum of PIPOx-FITC measured in DMSO-d_6. Figure S5. UV/Vis measurements of fluorescein isothiocyanate and PIPOx-FITC. (a) UV/Vis spectra of fluorescein isothiocyanate measured in methanol in the concentration range from 5×10^{-6} mol dm^{-3} to 10^{-4} mol dm^{-3}. (b) Calibration curves of fluorescein isothiocyanate at 278 and 452 nm. (c) UV/Vis spectra of PIPOx-FITC measured in methanol in the concentrations of 0.5 and 1 mg/mL. Concentration of fluorescein unit in PIPOx-FITC calculated from calibration curve was equal to 1 mol.%.

Author Contributions: Conceptualization: E.P., J.K. and Z.K.; Funding acquisition: J.K., Z.K. and E.P.; Synthesis and material preparation: M.M. and J.K.; Bioimmunological experiments: E.P. and L.P., Colocalization experiments: Z.K.; Writing—original draft preparation: E.P., L.P., J.K. and Z.K.; Writing—review and editing: E.P., Z.K. and J.K. All authors have read and agreed to the published version of the manuscript.

Funding: This work was supported by the Slovak Grant Agency VEGA in the project 2/0124/18 and Slovak Research and Development Agency in the project APVV 19-0487. This study was performed during the implementation of the project Building-up Centre for advanced materials application of the Slovak Academy of Sciences, ITMS project code 313021T081 supported by Research & Innovation Operational Program funded by the ERDF.

Institutional Review Board Statement: The study was conducted according to the guidelines of the Declaration of Helsinki, and approved by Ethics Committee of Research Base of Slovak Medical University, Institute of Preventive and Clinical Medicine and State veterinary and Food Administration of the Slovak Republic (protocol code 2939/09-221, 30.12.2009).

Informed Consent Statement: Not applicable.

Data Availability Statement: The data presented in this study are available in Supplementary Materials.

Conflicts of Interest: The authors declare no conflict of interest.

References

1. Kronek, J.; Kroneková, Z.; Lustoň, J.; Paulovičová, E.; Paulovičová, L.; Mendrek, B. In vitro bio-immunological and cytotoxicity studies of poly(2-oxazolines). *J. Mater. Sci. Mater. Med.* **2011**, *22*, 1725–1734. [CrossRef] [PubMed]
2. Lorson, T.; Lübtow, M.M.; Wegener, E.; Haider, M.S.; Borova, S.; Nahm, D.; Jordan, R.; Sokolski-Papkov, M.; Kabanov, A.V.; Luxenhofer, R. Poly(2-oxazoline)s based biomaterials: A comprehensive and critical update. *Biomaterials* **2018**, *178*, 204–280. [CrossRef]
3. Sedláček, O.; Monnery, B.D.; Filippov, S.K.; Hoogenboom, R.; Hrubý, M. Poly(2-oxazoline)s—Are they more advantageous for biomedical applications than other polymers? *Macromol. Rapid Commun.* **2012**, *33*, 1648–1662. [CrossRef]
4. Adams, N.; Schubert, U.S. Poly(2-oxazolines) in biological and biomedical application contexts. *Adv. Drug Deliv. Rev.* **2007**, *59*, 1504–1520. [CrossRef]
5. Verbraeken, B.; Monnery, B.D.; Lava, K.; Hoogenboom, R. The chemistry of poly(2-oxazoline)s. *Eur. Polym. J.* **2017**, *88*, 451–469. [CrossRef]
6. Aoi, K.; Okada, M. Polymerization of oxazolines. *Prog. Polym. Sci.* **1996**, *21*, 151–208. [CrossRef]
7. Weber, C.; Hoogenboom, R.; Schubert, U.S. Temperature responsive bio-compatible polymers based on poly (ethylene oxide) and poly (2-oxazoline)s. *Prog. Polym. Sci.* **2012**, *37*, 686–714. [CrossRef]
8. Hoogenboom, R.; Schlaad, H. Thermoresponsive poly(2-oxazoline)s, polypeptoids, and polypeptides. *Polym. Chem.* **2017**, *8*, 24–40. [CrossRef]
9. Datta, S.; Jutková, A.; Šrámková, P.; Lenkavská, L.; Huntošová, V.; Chorvát, D.; Miškovský, P.; Jancura, D.; Kronek, J. Unravelling the Excellent Chemical Stability and Bioavailability of Solvent Responsive Curcumin-Loaded 2-Ethyl-2-oxazoline-grad-2-(4-dodecyloxyphenyl)-2-oxazoline Copolymer Nanoparticles for Drug Delivery. *Biomacromolecules* **2018**, *19*, 2459–2471. [CrossRef] [PubMed]
10. Lava, K.; Verbraeken, B.; Hoogenboom, R. Poly(2-oxazoline)s and click chemistry: A versatile toolbox toward multi-functional polymers. *Eur. Polym. J.* **2015**, *65*, 98–111. [CrossRef]
11. Miyamoto, M.; Sano, Y. Reactivity of N-alkylated cyclic iminoether salts having vinyl groups, 2) Polymerization and copolymerization of 2-isopropenyl-3-methyl-2-oxazolinium salts. *Makromol. Chem.* **1986**, *187*, 1807–18017. [CrossRef]
12. Miyamoto, M.; Sano, Y.; Kimura, Y.; Saegusa, T. "Spontaneous" vinyl polymerization of 2-vinyl-2-oxazolines. *Macromolecules* **1985**, *18*, 1641–1648. [CrossRef]

13. Kagiya, T.; Matsuda, T.; Zushi, K. Radical Copolymerization of 2-lsopropenyl-2-oxazoline with Styrene in the Presence of Lewis Acids. *J. Macromol. Sci. Chem.* **1972**, *6*, 1349–1372. [CrossRef]
14. Palem, R.R.; Ganesh, S.D.; Saha, N.; Kronek, J.; Saha, P. 'Green' synthesis of silver polymer Nanocomposites of poly(2-isopropenyl-2-oxazoline-co-N vinylpyrrolidone) and its catalytic activity. *J. Polym. Res.* **2018**, *25*, 152. [CrossRef]
15. Kagiya, T.; Matsuda, T. Selective Polymerization of 2-Isopropenyl-2-oxazoline and Cross-linking Reaction of the Polymers. *Polym. J.* **1972**, *3*, 307–314. [CrossRef]
16. Yilmaz, G.; Uzunova, V.; Hartweg, M.; Beyer, V.; Napier, R.; Becer, C.R. The effect of linker length on ConA and DC-SIGN binding of S-glucosyl functionalized poly(2-oxazoline)s. *Polym. Chem.* **2018**, *9*, 611–618. [CrossRef]
17. Kagiya, T.; Matsuda, T.; Nakato, M.; Hirata, R. Polymerization of 2-Oxazolines. IV. The Structure and the Reactivity of 2-Substituted-2-oxazolines and Oxazolinium Perchlorates. *J. Macromol. Sci. Chem.* **1972**, *6*, 1631–1652. [CrossRef]
18. Kroneková, Z.; Mikulec, M.; Petrenčíková, N.; Paulovičová, E.; Paulovičová, L.; Jančinová, V.; Nosál', R.; Reddy, P.S.; Shimoga, G.D.; Chorvát, D.; et al. Ex Vivo and In Vitro Studies on the Cytotoxicity and Immunomodulative Properties of Poly(2-isopropenyl-2-oxazoline) as a New Type of Biomedical Polymer. *Macromol. Biosci.* **2016**, *16*, 1200–1211. [CrossRef] [PubMed]
19. He, J.; Zhang, Y.; Chen, E.Y.X. Synthesis of Pyridine- and 2-Oxazoline-Functionalized Vinyl Polymers by Alane-Based Frustrated Lewis Pairs. *Synlett* **2014**, *25*, 1534–1538.
20. Feng, H.; Changez, M.; Hong, K.; Mays, J.W.; Kang, N.G. 2-Isopropenyl-2-oxazoline: Well-Defined Homopolymers and Block Copolymers via Living Anionic Polymerization. *Macromolecules* **2017**, *50*, 54–62. [CrossRef]
21. Tomalia, D.A.; Thill, B.P.; Fazio, M.J. Ionic Oligomerization and Polymerization of 2-Alkenyl-2-oxazolines. *Polym. J.* **1980**, *12*, 661–675. [CrossRef]
22. Zhang, N.; Salzinger, S.; Soller, B.S.; Rieger, B. Rare Earth Metal-Mediated Group-Transfer Polymerization: From Defined Polymer Microstructures to High-Precision Nano-Scaled Objects. *J. Am. Chem. Soc.* **2013**, *135*, 8810–8813. [CrossRef] [PubMed]
23. Weber, C.; Neuwirth, T.; Kempe, K.; Ozkahraman, B.; Tamahkar, E.; Mert, H.; Becer, C.R.; Schubert, U.S. 2-Isopropenyl-2-oxazoline: A versatile monomer for functionalization of polymers obtained via RAFT. *Macromolecules* **2012**, *45*, 20–27. [CrossRef]
24. Raus, V.; Hološ, A.; Kronek, J.; Mosnáček, J. Well-Defined Linear and Grafted Poly(2-isopropenyl-2-oxazoline)s Prepared via Copper-Mediated Reversible-Deactivation Radical Polymerization Methods. *Macromolecules* **2020**, *53*, 2077–2087. [CrossRef]
25. Nishikubo, T.; Kameyama, A.; Tokai, H. Synthesis of Polymers in Aqueous Solutions. Selective Addition Reaction of Poly(2isopropenyl-2-oxazoline) with Thiols and Carboxylic Acids in Aqueous Solutions. *Polym. J.* **1996**, *28*, 134–138. [CrossRef]
26. Jerca, F.A.; Jerca, V.V.; Anghelache, A.M.; Vuluga, D.M.; Hoogenboom, R. Poly(2-isopropenyl-2-oxazoline) as a versatile platform towards thermoresponsive copolymers. *Polym. Chem.* **2018**, *9*, 3473–3478. [CrossRef]
27. Kronek, J.; Šrámková, P.; Kroneková, Z.; Zahoranová, A.; Petrenčíková, N.; Kleinová, A.; Mrlík, M.; Mosnáček, J. Functional polymers based on unsaturated 2-oxazolines: From thermosensitive polymers to hydrogels. *Abstr. Pap. Am. Chem. Soc.* **2016**, *252*, 2.
28. Xu, X.; Jerca, F.A.; Jerca, V.V.; Hoogenboom, R. Covalent Poly(2-Isopropenyl-2-Oxazoline) Hydrogels with Ultrahigh Mechanical Strength and Toughness through Secondary Terpyridine Metal-Coordination Crosslinks. *Adv. Funct. Mater.* **2019**, *29*, 1904886. [CrossRef]
29. Jerca, F.A.; Anghelache, A.M.; Ghibu, E.; Cecoltan, S.; Stancu, I.C.; Trusca, R.; Vasile, E.; Teodorescu, M.; Vuluga, D.M.; Hoogenboom, R.; et al. Poly(2-isopropenyl-2-oxazoline) Hydrogels for Biomedical Applications. *Chem. Mater.* **2018**, *30*, 7938–7949. [CrossRef]
30. Xu, X.; Jerca, F.A.; Van Hecke, K.; Jerca, V.A.; Hoogenboom, R. High compression strength single network hydrogels with pillar[5]arene junction points. *Mater. Horiz.* **2020**, *7*, 566–573. [CrossRef]
31. Leiske, M.N.; Mahmoud, A.M.; Warne, N.M.; Goos, J.A.C.M.; Pascual, S.; Montembault, V.; Fontaine, L.; Davis, T.P.; Whittaker, M.R.; Kempe, K. Poly(2-isopropenyl-2-oxazoline)—A structural analogue to poly(vinyl azlactone) with Orthogonal Reactivity. *Polym. Chem.* **2020**, *11*, 5681–5692. [CrossRef]
32. Vishwakarma, A.; Bhise, N.S.; Evangelista, M.B.; Rouwkema, J.; Dokmeci, M.R.; Ghaemmaghami, A.M.; Vrana, N.E.; Khademhosseini, A. Engineering Immunomodulatory Biomaterials To Tune the Inflammatory Response. *Trends Biotechnol.* **2016**, *34*, 470–482. [CrossRef] [PubMed]
33. Mallapragada, S.K.; Narasimhan, B. Immunomodulatory biomaterials. *Int. J. Pharm.* **2008**, *364*, 265–271. [CrossRef]
34. Katholnig, K.; Linke, M.; Pham, H.; Hengstschläger, M.; Weichhart, T. Immune responses of macrophages and dendritic cells regulated by mTOR signaling. *Biochem. Soc. Trans.* **2013**, *41*, 927–933. [CrossRef] [PubMed]
35. Gordon, S. The macrophage: Past, present and future. *Eur. J. Immunol.* **2007**, *37*, S9–S17. [CrossRef]
36. Price, J.V.; Vance, R.E. The macrophage paradox. *Immunity* **2014**, *41*, 685–693. [CrossRef]
37. Rostama, H.M.; Singh, S.; Salazar, F.; Magennis, P.; Hook, A.; Singhb, T.; Vrana, N.E.; Alexander, M.R.; Ghaemmaghami, A.M. The impact of surface chemistry modification on macrophage polarization. *Immunobiology* **2016**, *221*, 1237–1246. [CrossRef] [PubMed]
38. Huang, Z.; Yang, Y.; Jiang, Y.; Shao, J.; Sun, X.; Chen, J.; Dong, L.; Zhang, J. Anti-tumor immune responses of tumor-associated macrophages via toll-like receptor 4 triggered by cationic polymers. *Biomaterials* **2013**, *34*, 746–755. [CrossRef]
39. *CXP Software*, Flow Cytometry Software; Beckman Coulter Inc.: Fullerton, CA, USA.
40. *ZEN software*, Digital Microscope Software; Zeiss: Jena, Germany, 2014.
41. Reddy, S.T.; Swartz, M.A.; Hubbell, J.A. Targeting dendritic cells with biomaterials: Developing the next generation of vaccines. *Trends Immunol.* **2006**, *27*, 573–579. [CrossRef] [PubMed]

42. Savitsky, K.; Yu, X. Combined strategies for tumor immunotherapy with nanoparticles. *Clin. Transl. Oncol.* **2019**, *21*, 1441–1449. [CrossRef] [PubMed]
43. Yu, N.; Li, X.; Wen, M.; Geng, P.; Ren, X.; Wang, Z.; Chen, Z. Doxorubicin-Loaded Bi-PEG Nanoparticles as Novel Chemo-Photothermal Nanoagents for Efficiently Killing Cancer Cells. *J. Nanosci. Nanotechnol.* **2020**, *20*, 2032–2039. [CrossRef] [PubMed]
44. Liu, K.J. Dendritic cell, toll-like receptor, and the immune system. *J. Cancer Mol.* **2006**, *2*, 213–215.
45. Gündel, D.; Allmeroth, M.; Reime, S.; Zentel, R.; Thews, O. Endocytotic uptake of HPMA-based polymers by different cancer cells: Impact of extracellular acidosis and hypoxia. *Int. J. Nanomed.* **2017**, *12*, 5571–5584. [CrossRef] [PubMed]
46. Kolonko, E.M.; Kiessling, L.L. A Polymeric Domain That Promotes Cellular Internalization. *J. Am. Chem. Soc.* **2008**, *130*, 5626–5627. [CrossRef] [PubMed]
47. Alconcel, S.N.S.; Baas, A.S.; Maynard, H.D. FDA-approved poly(ethylene glycol)–protein conjugate drugs. *Polym.Chem.* **2011**, *2*, 1442–1448. [CrossRef]
48. Mero, A.; Fang, Z.; Pasut, G.; Veronese, F.M.; Viegas, T.X. Selective conjugation of poly(2-ethyl 2-oxazoline) to granulocyte colony stimulating factor. *J. Control. Release* **2012**, *159*, 353–361. [CrossRef]
49. Kronek, J.; Lustoň, J.; Kroneková, Z.; Paulovičová, E.; Farkaš, P.; Petrenčíková, N.; Paulovičová, L.; Janigová, I. Synthesis and bioimmunological efficiency of poly(2-oxazolines) containing a free amino group. *J. Mater. Sci.: Mater. Med.* **2010**, *21*, 879–886. [CrossRef] [PubMed]
50. Kronek, J.; Paulovičová, E.; Kroneková, Z.; Paulovičová, L.; Lustoň, J. Immunomodulatory efficiency of poly(2-oxazolines). *J. Mater. Sci. Mater. Med.* **2012**, *23*, 1457–1464. [CrossRef] [PubMed]

materials

MDPI

Article

The Mould War: Developing an Armamentarium against Fungal Pathogens Utilising Thymoquinone, Ocimene, and Miramistin within Bacterial Cellulose Matrices

Sam Swingler [1,2,*], Abhishek Gupta [2,3], Hazel Gibson [1,2], Wayne Heaselgrave [2,4], Marek Kowalczuk [5], Grazyna Adamus [5] and Iza Radecka [1,2,*]

1 Wolverhampton School of Sciences, Faculty of Science and Engineering, University of Wolverhampton, Wulfruna Street, Wolverhampton WV1 1LY, UK; h.gibson@wlv.ac.uk
2 Research Institute in Healthcare Science, Faculty of Science and Engineering, University of Wolverhampton, Wulfruna Street, Wolverhampton WV1 1LY, UK; a.gupta@wlv.ac.uk (A.G.); w.heaselgrave@wlv.ac.uk (W.H.)
3 Institute of Health, Faculty of Education, Health and Wellbeing, University of Wolverhampton, Jerome K Jerome Building, Gorway Road, Walsall Campus, Walsall WS1 3BD, UK
4 Department of Biomedical Science, University of Wolverhampton, MA Building, Wulfruna Street, Wolverhampton WV1 1LY, UK
5 Centre of Polymer and Carbon Materials, Polish Academy of Sciences, M. Curie-Sklodowskiej 34, 41-819 Zabrze, Poland; marek.kowalczuk@cmpw-pan.edu.pl (M.K.); gadamus@cmpw-pan.edu.pl (G.A.)
* Correspondence: s.swingler@wlv.ac.uk (S.S.); i.radecka@wlv.ac.uk (I.R.)

Abstract: An increase in antifungal resistance has seen a surge in fungal wound infections in patients who are immunocompromised resulting from chemotherapy, disease, and burns. Human pathogenic fungi are increasingly becoming resistant to a sparse repertoire of existing antifungal drugs, which has given rise to the need to develop novel treatments for potentially lethal infections. Bacterial cellulose (BC) produced by *Gluconacetobacter xylinus* has been shown to possess many properties that make it innately useful as a next-generation biopolymer to be utilised as a wound dressing. The current study demonstrates the creation of a pharmacologically active wound dressing by loading antifungal agents into a biopolymer hydrogel to produce a novel wound dressing. Amphotericin B is known to be highly hepatotoxic, which reduces its appeal as an antifungal drug, especially in patients who are immunocompromised. This, coupled with an increase in antifungal resistance, has seen a surge in fungal wound infections in patients who are immunodeficient due to chemotherapy, disease, or injury. Antifungal activity was conducted via Clinical & Laboratory Standards Institute (CLSI) M27, M38, M44, and M51 against *Candida auris*, *Candida albicans*, *Aspergillus fumigatus*, and *Aspergillus niger*. This study showed that thymoquinone has a comparable antifungal activity to amphotericin B with mean zones of inhibition of 21.425 ± 0.925 mm and 22.53 ± 0.969 mm, respectively. However, the mean survival rate of HEp-2 cells when treated with 50 mg/L amphotericin B was 29.25 ± 0.854% compared to 71.25 ± 1.797% when treated with 50 mg/L thymoquinone. Following cytotoxicity assays against HEp-2 cells, thymoquinone showed a 71.25 ± 3.594% cell survival, whereas amphotericin B had a mean cell survival rate of 29.25 ± 1.708%. The purpose of this study was to compare the efficacy of thymoquinone, ocimene, and miramistin against amphotericin B in the application of novel antifungal dressings.

Keywords: antifungal; thymoquinone; ocimene; miramistin amphotericin b; bacterial cellulose; wound dressing

Citation: Swingler, S.; Gupta, A.; Gibson, H.; Heaselgrave, W.; Kowalczuk, M.; Adamus, G.; Radecka, I. The Mould War: Developing an Armamentarium against Fungal Pathogens Utilising Thymoquinone, Ocimene, and Miramistin within Bacterial Cellulose Matrices. *Materials* **2021**, *14*, 2654. https://doi.org/10.3390/ma14102654

Academic Editor: John T. Kiwi

Received: 1 April 2021
Accepted: 15 May 2021
Published: 18 May 2021

1. Introduction

Wounds from various sources that have been in a prolonged state of irritation and rubor, with a high degree of exudate, are decidedly prone to becoming infected by various opportunistic and commensal organisms. The typical approach in treating these wounds is to reduce infection and increase more favourable conditions at the wound site for

healing, thus encouraging a more suitable environment for successful re-epithelisation and angiogenesis [1,2].

Immunodeficiency arising from burn injuries poses a genuine and present threat to the successful healing of patients. The central difficulty in burn patients is the burn wound itself. Although the body as a whole reacts to a burn dependent on severity, thickness, and coverage, those with thermal injuries that are extensive typify a whole-body reaction. As a result of this reaction, the inflammation arising from the injury mandates that the wound is protected from infection and that there is a timely closure of the exposed areas. Burn wound infections and mortality rates are drastically decreased with the application of topical treatments such as silver sulfadiazine and mafenide acetate by nearly 50% [3,4].

Antifungal resistance is an ever-growing issue within the healthcare sector, seeing over 1.5 million people die annually from fungal infections [5,6]. Immunocompromised patients make up the bulk of these deaths, and with classical antifungal drugs such as the azoles becoming less effective in the treatment of infections as a result of decreased efficacy, this figure is most likely going to increase.

A dramatic increase in fungal infections in recent years is associated with several factors such as prolonged dosage of broad-spectrum antibiotics, immunosuppressive therapy, extended stays in hospitals, burns, and recently undergone surgery as well as malignancy [7,8].

Candida species are polymorphic yeasts that can exist in various morphological forms that facilitate survival under extreme microenvironments by forming biofilms or invading and destructing target tissues, primarily in the pseudo-hyphae and true hyphae morphological state [9]. Unlike other pathogenic organisms, morphogenic plasticity helps *Candida* species evade host immune responses and confers differential responses towards antifungal agents [10]. Being eukaryotic organisms, fungal specific drug targets are very few and thus, limited numbers of antifungal agents such as azoles, polyenes, allylamines, and echinocandins, et cetera are available on the market [11].

Thymoquinone (Figure 1A) and ocimene (Figure 1B) are the major constituents of *Nigella sativa* and *Azadirachta indica*, respectively. It has been shown that both of these compounds possess various pharmacological qualities, which include antibacterial, antiparasitic, anti-inflammatory, anti-viral, and antifungal properties [12–14]. They have also been shown to provide a level of protection against nephrotoxicity [15]. Miramistin (benzyl dimethyl [3-(myristoilamino) propyl] ammonium chloride monohydrate) (Figure 1C) is a topical antiseptic that was developed in the Soviet Union during the Cold War within the framework of the 'Space Biotechnology Program' [16].

Amphotericin B (Figure 1D) is the principal antifungal polyene agent with a broad-spectrum activity used to treat burn patients. The mode of the action revolves around the drug destabilising ergosterol within the cell wall of the fungi, thus causing rapid ion leakage culminating in cellular death [17]. The administration of amphotericin B ranges from 0.6 to 1 mg/kg/day and poses significant intolerance in burn patients who exhibit side effects such as hypoxia, hypertension, fevers, and more significantly, nephrotoxicity—although the introduction of liposomal formulations has eased this side effect [18]. This side effect limits the overall effectiveness of intravenously administering amphotericin B as tubular wasting is significantly reduced. Therefore, a method for delivering this drug to patients' burn site is greatly needed [19]. The topical administration of amphotericin B to burn patients' wounds would allow for rapid, localised control and prevention of fungal pathogens becoming disseminated, consequently minimising the risk of fungal infections becoming deep-rooted, which drastically increases the risk of death.

Although the overall mechanism of the antifungal actions of both thymoquinone and ocimene is not fully understood, it is well documented that both thymoquinone and ocimene are sources of reactive oxygen species (ROS), leading to oxidative stress, which could play a significant role in the fungicidal properties [20,21]. However, the antifungal activity of miramistin is poorly documented (Figure 2).

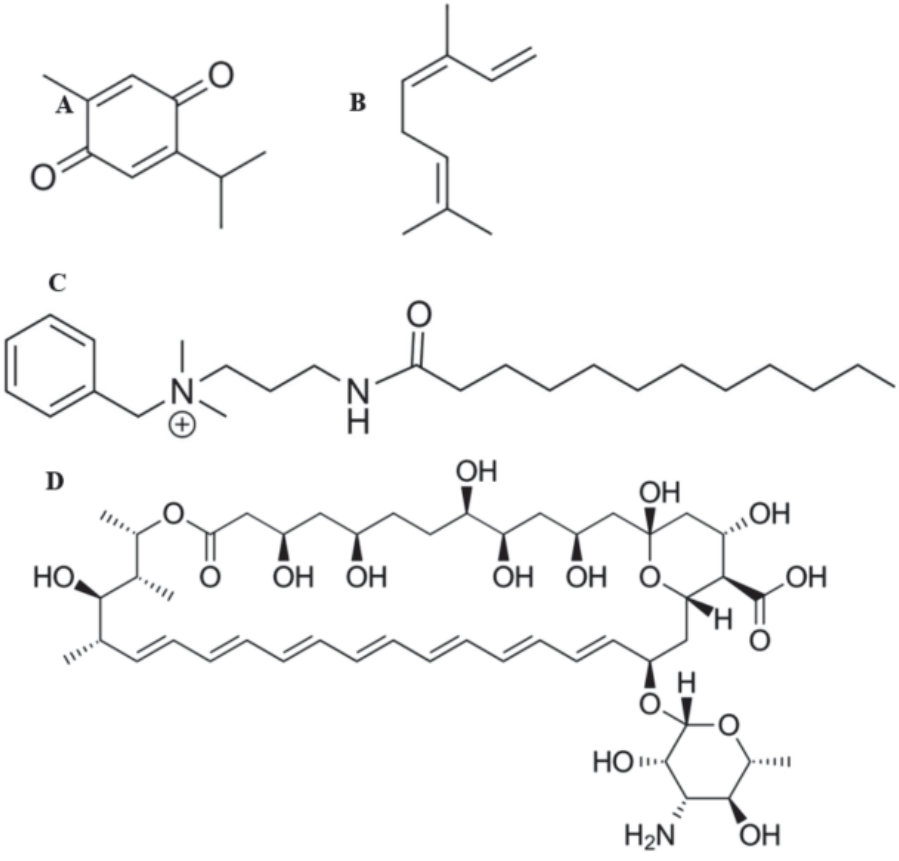

Figure 1. Chemical structures of thymoquinone (**A**), ocimene (**B**), miramistin (**C**), and amphotericin B (**D**).

The two most prevalent fungal genera responsible for burn wound infections are *Candida* and *Aspergillus* species. In the present study, *C. albicans*, *C. auris*, *A. fumigatus*, and *A. niger* are being investigated providing representative pathogenic organisms of both non-dermatophyte fungi and yeasts. *Candida* species are responsible for approximately 80% of nosocomial yeast infections, of which 4–11% of burn patients are diagnosed with invasive candidemia, which results in a 30–58% mortality rate [22]. However, *Aspergillus* species account for 0.3–7% of fungal wound infections in burn patients, resulting in invasive aspergillosis. Nevertheless, the highly angio-invasive nature of aspergillosis results in a 50–78% mortality rate [23–25].

Established dressings such as gauze and tulle form a barrier between the wound site and the external environment that keeps the wound site dry. However, they are unable to impart any anti-microbial activity directly or influence the wound-healing process [26]. Conversely, moist wound dressings such as bacterial cellulose dressings act as a barrier to infection and also maintain moisture levels around the wound. One advantage of these dressings is that they are easily removed from the wound site, thus avoiding further trauma during dressing changes. These dressings also respond to variations in moisture levels, thereby facilitating re-epithelialisation of the wound site [27]. In addition to absorbing and retaining excess wound exudate, hydrocolloid dressings also provide a cooling, soothing effect, which also reduces rubor and the sensation of pain [28].

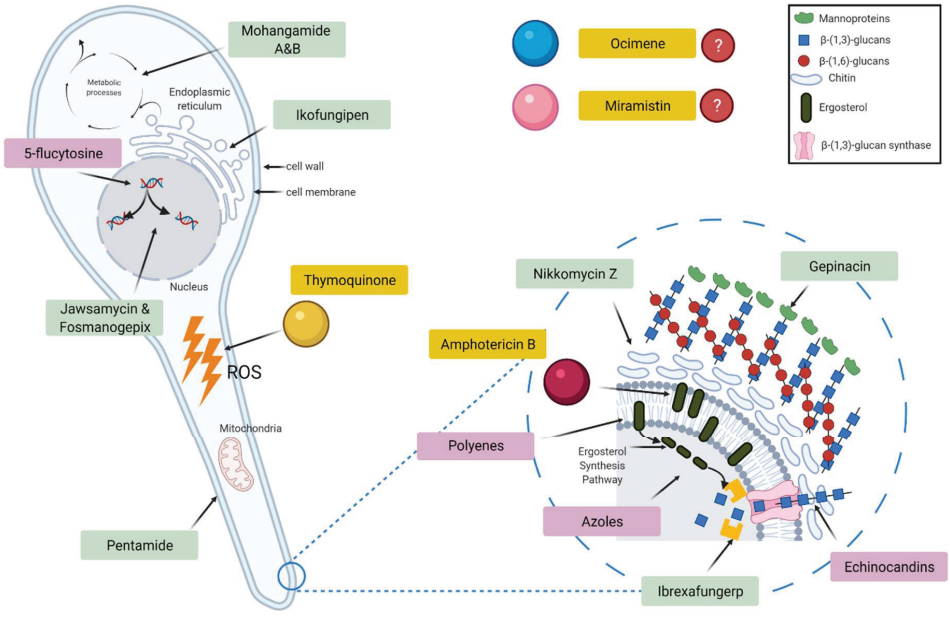

Figure 2. Schematic diagram showing the target sites of currently used antifungal drugs (pink), pipeline antifungals (green), and the test drugs used in this study (yellow).

Bacterial cellulose (BC) can be used as part of a biocompatible system; it is non-pyrogenic and hydrophilic, which make it innately suitable for wound treatment applications [29]. In addition, BC also contours superbly to the undulating surface of the skin, providing a uniform covering even in areas that are usually difficult to dress, such as the groin and neck. BC also provides protection to healing wounds due to the thickness of the dressing, which reduces further injury from further trauma. This protection further aids in the promotion of angiogenesis and rapid wound healing [30,31].

Bacterial cellulose is biosynthesised through the conjugation of linear homopolysaccharides and β-D-glucose units which are linked by 1,4-β-glycosidic linkages [1]. Once the exopolysaccharides have formed, they then randomly become organised into chains consisting of 10 to 15 individual chains of cellulose, resulting in cellulose nanofibers. These single chains of nanofibers become further entangled to form microfibrils, which are up to 100 times smaller than commercially available vegetal analogues [32–34].

Then, the synthesised cellulose microfibrils form ribbon bundles, which are 3–4 nm thick and 70–80 nm wide, which are what form the cellulose pellicle. This is achieved through inter and extra-chemical bonding, primarily hydrogen bonding between hydroxyl groups within between the cellulose fibres [35].

Due to the high levels of hydrogen bonding between the cellulose fibres, pores are formed within the cellulose, which possess an overall negative ionic charge resulting from hydroxyl groups and permit additional compounds to be embedded. This intrinsic physical property of cellulose allows for an increased level of influence over the bioactivity of the material as additional compounds, providing there is some level of positive ionic charge owing to the negative ions charge in the bacterial cellulose arising from the hydroxyl groups, such as antifungal agents, which can be easily incorporated [36].

As bacterial cellulose is a biopolymer, there are naturally varying degrees of pore size and distribution. These pores can be further influenced by the method of fermentation itself, whether it be static or agitated. Previous research conducted by Revin et al. (2019) showed that under agitated conditions, the bacterial cellulose forms spheres with a pore

size of 165–330 μm, while under static conditions, the cellulose formed as a pellicle with an average pore size of 4 nm to 1000 μm in diameter [37,38].

The overall distribution and size of the pores within the bacterial cellulose pellicle greatly impacts both the physical and mechanical properties of the biomaterial, in that larger pores introduce greater voids resulting in a less dense material. Subsequently, these larger pores allow for larger molecules or substances to be loaded more easily as a result of increased porosity. However, the drawback with larger pores is that the overall mechanical strength of the material is negatively impacted [39]. In the lyophilised form, bacterial cellulose has an elongation at break of approximately 5% and a typical tensile strength of 340 mPa, a Young's modulus of 12 GPa, and a maximum strain order of 4%. However, wet bacterial cellulose has a maximum strain order of 20%, tensile strength of 400 mPa, and Young's modulus of 130–145 GPa, indicating that wet bacterial cellulose has a greater level of elasticity [40–42].

Due to bacterial cellulose only comprising approximately 1% of the overall pellicle weight, with water (approximately 99%) comprising the remainder, it was also deduced that this material also has a significantly higher swelling ratio compared to commercially available cellulose [42]. It was further shown that the biomaterial is capable of regulating moisture content, which is ideal for applications in heavily exuding wounds [43]. This water-holding capacity of bacterial cellulose has been found to be 50 to 100 times its dry weight and is directly related to the overall surface area and distribution of pores within the material.

Another pertinent difference between commercially available cellulose derived from plants is that in bacterial cellulose, the crystallinity ratio is much higher (85–90%) in comparison to its commercial counterpart (60–65%). Moreover, in bacterial cellulose, there are no additional by-products that need to be removed, such as lignin and hemicellulose, allowing for a more streamlined and efficient production process [39].

All of these properties of bacterial cellulose have led to the successful commercialisation of bacterial cellulose hydrogels (e.g., Dermafill® and Biofill®) for the treatment of burns, chronic ulcers, skin lesions, and periodontal disease [1]. Even though bacterial cellulose is not inherently antimicrobial itself, the unique 3D fibrillar network is highly porous and amenable to high loading with a controlled release of a range of antimicrobial agents, which can be delivered directly to the wound site [35,36].

The aim of this study was to evaluate the antifungal potential of biofunctionalised BC loaded with either thymoquinone, ocimene, and miramistin in comparison to the action of amphotericin B loaded in BC to determine whether alternative anti-fungal options can be used in the prevention and treatment of fungal wound infections.

2. Materials and Methods

2.1. Media and Reagents

Thymoquinone, ocimene, and amphotericin B, foetal bovine serum, glutamine, and antibiotics (penicillin G, 60 mg/L; streptomycin, 100 mg/L; standard amphotericin B, 50 μL/L) were purchased from Sigma-Aldrich (Irvine, UK). Miramistin was purchased from Carbosynth Ltd. (Compton, UK). Dimethyl sulfoxide (DMSO) reagent grade, sodium hydroxide, disodium phosphate, and citric acid were purchased from Sigma-Aldrich (Irvine, UK). Dextrose, bacteriological peptone, yeast extract, agar number 2, Sabouraud dextrose agar (SDA), malt extract agar (MEA), Hestrin and Schramm agar (HSA), Hestrin and Schramm media (HS), and Ringer's solution were purchased from Lab M (Bury, UK). RPMI-1640 (Roswell Park Memorial Institute) was purchased from Fisher Scientific (Cramlington, UK). All media and reagents were prepared according to the manufacturer's instructions.

2.2. Microorganisms

Gluconacetobacter xylinus ATCC® 23770, Candida albicans ATCC® 10,231 and Aspergillus niger ATCC® 16,888 were obtained from the LGC Standards Ltd. (Middlesex,

UK). Aspergillus fumigatus NCPF 2140 and Candida auris NCPF 8971 were obtained from Public Health England, Porton Down, UK. All organisms were obtained in lyophilised form and maintained at −20 °C before use. C. albicans, C. auris, A. fumigatus, and A. niger were revived on sterile SDA made to manufacturers' specification, sterilised by autoclaving before use and incubated at 30 °C for 24 h to obtain maximum growth. G. xylinus was revived on sterile HSA at 37 °C for five days. Overnight cultures of G. xylinus were grown under agitation in HS broth medium at 37 °C for 24 h from stock plates to ensure the bacterial cells are well dispersed within the media, rather than conglomerating into a single bacterial pellicle.

2.3. Cell Culture

Human epithelial type 2 (HEp-2) cell lines were obtained from the American Type Culture Collection (ATCC® CCL23™). The cells were cultured in RPMI-1640 containing 10% foetal bovine serum, 2 mM glutamine, and antibiotics (penicillin G, 60 mg/L; streptomycin, 100 mg/L; amphotericin B, 50 mg/L) under a humid atmosphere (37 °C, 5% CO_2) for 96 h until confluent. Media were replaced every three days. The cells were washed with phosphate-buffered saline and passaged twice before use, again, once confluent.

2.4. Fungal Starter Cultures

Overnight cultures of fungi were prepared by using stock SDA plates to inoculate RPMI-1640 without bicarbonate, supplemented with 3-(N-morpholino)propane sulfonic acid (MOPS), 2% (*w*/*v*) glucose, and pH adjusted to 7 with 10 M NaOH. Then, the stocks were incubated statically at 30 °C for 24 h. C. albicans and C. auris pseudo-hyphae were produced using conditions published previously [44]. Briefly, overnight cultures of Candida species were collected by centrifugation at 1500 G for 15 min at 4 °C, washed twice with 0.15 M NaCl, resuspended in 0.15 M NaCl, and incubated at room temperature for 24 h to induce starvation. After 24 h of starvation, cells were inoculated into RPMI 1640 at a final concentration of 1×10^6 cells/mL and incubated at 37 °C with shaking for 6 h.

2.5. Production and Purification of Bacterial Cellulose

BC production was carried out following the protocol reported in our previous paper [36]. Briefly, starter cultures of *G. xylinus* were used to inoculate HS media and incubated statically for 14 days at 37 °C. Following the incubation period, bacterial cellulose (BC) pellicles that formed as a raft on the surface of the HS media were aseptically harvested. The unpurified BC was initially heated to 100 °C in distilled water, which was followed by the addition of 2% (*w*/*v*) sodium hydroxide and reheating to 100 °C in fresh distilled water for a further hour or until the BC became fully transparent. Then, each pellicle was frozen at −20 °C before lyophilisation.

2.6. Preparation of Working Solutions and Loading of Antifungal Agents

Stock solutions, working solutions, and dilution series' were conducted according to ISO 16256:2012(en) [45]. Briefly, 12,800 mg/L thymoquinone, ocimene, or miramistin and 3200 mg/L amphotericin B were made by dissolving each compound in DMSO. A dilution series following Tables 1 and 2 were conducted to obtain working solutions at 200-fold the final concentration. Then, a 1:100 dilution was conducted to produce drug concentrations at twice the final concentration. The final concentration of amphotericin B ranged from 0.03 to 16 mg/L, and thymoquinone, ocimene, and miramistin ranged from 0.125 to 64 mg/L. Clean lyophilised BC pellicles were aseptically cut into 4 mm (used in cytotoxicity assays to fit 96-well plates) and 8 mm disks using a biopsy punch, which was then submerged in the varying concentrations of either thymoquinone, ocimene, miramistin, or amphotericin B and were placed on an orbital shaker (150 rpm) for 24 h in the dark at room temperature. Confirmation of loading was achieved through FTIR analysis

Table 1. Scheme for preparing amphotericin B in DMSO with a final concentration of 0.06 to 16 mg/L.

Step	Concentration (mg/L)	Source	Volume of Antifungal (µL)	Volume of Solvent (µL)	Intermediate Concentration (mg/L)	Concentration (mg/L) after 1:100 Dilution with Double Strength RPMI 2% (*w*/*v*)
1	3200	Stock	200	0	3200	32
2	3200	Stock	100	100	1600	16
3	3200	Stock	50	150	800	8
4	3200	Stock	50	350	400	4
5	400	Step 4	100	100	200	2
6	400	Step 4	50	150	10	1
7	400	Step 4	50	350	50	0.5
8	50	Step 7	100	100	25	0.25
9	50	Step 7	50	150	12.5	0.125
10	50	Step 7	25	175	6.25	0.06

Table 2. Scheme for preparing thymoquinone, ocimene, and miramistin in DMSO 0.26 to 64 mg/L.

Step	Concentration (mg/L)	Source	Volume of Antifungal (µL)	Volume of Solvent (µL)	Intermediate Concentration (mg/L)	Concentration (mg/L) after 1:100 Dilution with Double Strength RPMI 2% (*w*/*v*)
1	12,800	Stock	200	0	12,800	128
2	12,800	Stock	100	100	6400	64
3	12,800	Stock	50	150	3200	32
4	12,800	Stock	50	350	1600	16
5	1600	Step 4	100	100	800	8
6	1600	Step 4	50	150	400	4
7	1600	Step 4	50	350	200	2
8	200	Step 7	100	100	100	1
9	200	Step 7	50	150	50	0.5
10	200	Step 7	25	175	25	0.26

2.7. Minimum Inhibition Concentration (MIC)

The MIC_{90} (where the antifungal drug inhibits the growth of 90% of the organism) of thymoquinone, ocimene, miramistin, and amphotericin B was determined for all fungal strains using a standardised methods: CLSI M27 and M38 [46,47]. Briefly, RPMI without bicarbonate was supplemented with 3-(N-morpholino)propanesulfonic acid (MOPS), 2% (*w*/*v*) glucose and pH adjusted to 7 with 10 M NaOH. All fungal strains were grown on SDA, and suspensions were made in the RPMI-1640 to 0.5 McFarland standard at 530 nm, approximately 5×10^6 CFU/mL. The microtiter plates were incubated for 24 h at 35 °C, and the OD570 was measured with a microtiter plate reader (SPECTROstar® Nano, BMG Labtech, Ortenberg, Germany). All experiments were repeated in triplicate.

2.8. Minimum Fungicidal Concentration (MFC)

The MFC for all four antifungal compounds was determined by transferring 100 µL from all clear wells obtained during MIC assays (lack of turbidity is indicative of little impediment to growth) onto SDA plates and incubated overnight at 35 °C.

2.9. Quantification of Loaded Compound in BC

Lyophilised unloaded BC was aseptically cut into 8 mm disks and weighed. Then, the disks were individually placed into 1 mL aliquots of 50 mg/L (*w*/*v*) solutions of either thymoquinone, ocimene, miramistin, or amphotericin B for 24 h at room temperature under agitation (100 RPM). The concentration of 50 mg/L was chosen for all compounds, as it is twice the concentration of the highest MIC/MFC value and in accordance with standardised operating protocols [46,47]. After loading, the samples of BC were removed from the solutions and were again lyophilised by freezing at −20 °C for 24 h and lyophilised for a further 72 h and weighed again. All experiments were conducted ten times.

2.10. Zone of Inhibition (ZOI)

Disk diffusion assays were conducted using a modified Kirby–Bauer procedure [48] following internationally recognised standardised techniques in CLSI M44 and M51 protocols [49,50]. Briefly, Mueller–Hinton (2% (*w/v*) glucose) agar plates were flooded with overnight broth cultures (0.5 McFarland) of either *C. auris*, *C. albicans*, *A. fumigatus*, or *A. niger*. Control plates of Mueller–Hinton (2% glucose) agar flooded with filter sterile RPMI-1640. Once the plates were inoculated, four 8 mm BC disks which were loaded with varying concentrations of the antifungal drug, were placed onto the surface of the seeded plates in triplicate and were incubated for 24 h at 35 °C. Pure BC discs loaded with water were used as controls. After incubation, the diameter of the clear zone (ZOI), including the diameter of the 8 mm disk, was measured and statistically analysed using one-way ANOVA post hoc Tukey ($p < 0.05$) (GraphPad Prism V. 9.0.1(151), GraphPad Software, San Diego, CA, USA).

2.11. Cytotoxicity

The assay detects the reduction of MTT (3-(4,5-dimethylthiazolyl)-2,5-diphenyl-tetrazolium bromide) by mitochondrial dehydrogenase within the fungi to form blue formazan, which indicates that the mitochondria are functioning normally, and hence the measurement of cell viability. Briefly, 25 cells/µL HEp-2 in RPMI-1640 were added to each well in a 96-well plate and incubated for 24 h. After incubation, the cells were washed twice with phosphate-buffered saline (PBS), and fresh RPMI-1640 was added. Bacterial cellulose 4 mm disks, which had been loaded with 50 mg/L solutions of thymoquinone, ocimene, or miramistin, were then added and incubated for a further 24 h in triplicate ($n = 4$). Following incubation, MTT (0.5 mg/mL PBS) was added to each well and incubated at 37 °C for 3 h. The solubilisation of formazan crystals was achieved by mixing DMSO (100 µL/well), which was gently agitated for 10 min, and the absorbance was read at 570 nm using a microplate scanning spectrophotometer (SPECTROstar® Nano, BMG Labtech). The following formula calculated toxicity level:

$$Cytotoxicity\ \% = 1 - \frac{mean\ abs\ of\ antifungal}{mean\ abs\ of\ negative} \times 100 Viability\ \% = 100 - cytotoxicity\ \% \quad (1)$$

To reduce test error level, MTT was added to wells without cells, and along with other wells, absorbance level was read and ultimately subtracted from the whole absorbance.

2.12. Scanning Electron Microscopy (SEM)

Bacterial cellulose was lyophilised for 24 h (Christ b 1,8-LSC plus, Martin Christ GmbH, Osterode am Harz, Germany) and then gold-coated (EM-Scope SC500). SEM analysis was undertaken on a Zeiss Evo 50 EP, SEM (Carl Zeiss AG, Oberkochen, Germany). The SEM was set to a 10 kV acceleration beam at 100 µA. The probe ampere was set at 36 pA, and the data were analysed on INCA software (version 7.2, ETAS, Stuttgart, Germany).

2.13. Fourier Transform Infrared Spectroscopy

Purified BC and BC loaded with the respective antifungal drugs were cut into 8 mm disks and again lyophilised and then analysed using a Bruker ATR FTRI spectroscope after running background scans (Bruker, Billerica, MA, USA). Each loaded BC sample was analysed in triplicate for each respective drug and was scanned 12 times at 400–4000 cm^{-1} at room temperature.

2.14. Statistical Analysis

All experiments in this project were conducted in triplicate, and all data presented are means± standard deviation (SD). Data recorded during all experiments were analysed statistically by one-way ANOVA post hoc Tukey (GraphPad Prism V. 9.0.1(151), GraphPad Software, San Diego, CA, USA) with ($p < 0.05$) for ZOI, MIC and MFC. p values for cytotoxicity studies were ($p < 0.01$).

3. Results and Discussion

The discovery of multi drug-resistant fungal pathogens increases the risk of medical complications whilst simultaneously limiting therapeutic options. The presented work is focused on the design and development of novel antifungal hydrogels for improvement of therapeutic efficacy of antifungal drugs such as thymoquinone, ocimene, and miramistin and compared to conventional drugs such as amphotericin B.

3.1. Preparation of BC Hydrogels and Characterisation

The successful biosynthesis of bacterial cellulose is shown in Figure 3. The BC pellicles were harvested from the top of the growth media (A) and are opaque in colour (B), following purification by boiling in water and 2% (*w/v*) sodium hydroxide and again in water (C), then, the pellicles were removed and have become transparent after the purification process (D) as all remanence of growth media and *G. xylinus* cells were removed.

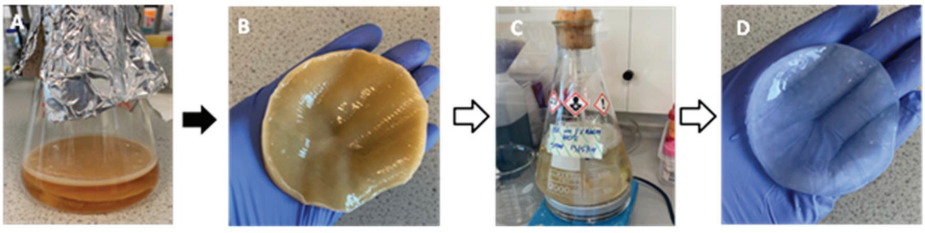

Figure 3. Biosynthesis of bacterial cellulose in Hestrin and Schramm medium, including pre- and post-purification. (**A**) static biosynthesis of BC which can be seen floating on top of the medium, (**B**) unpurified BC post harvest, (**C**) purification of BC in 2% (*w/v*) sodium hydroxide and, (**D**) purified BC.

After biosynthesis, both unpurified and purified BC were lyophilised for 96 h and analysed using a scanning electron microscope. Figure 4A shows an unpurified sample of BC, which has been false coloured to highlight the closed matrix as it is laden with growth media and biomass, the bacteria, *G. xylinus*, can be seen highlighted in blue. Figure 4B shows an SEM micrograph of purified BC, and the nanofibrous matrix is now visible (blue) with typical voids (purple) also present.

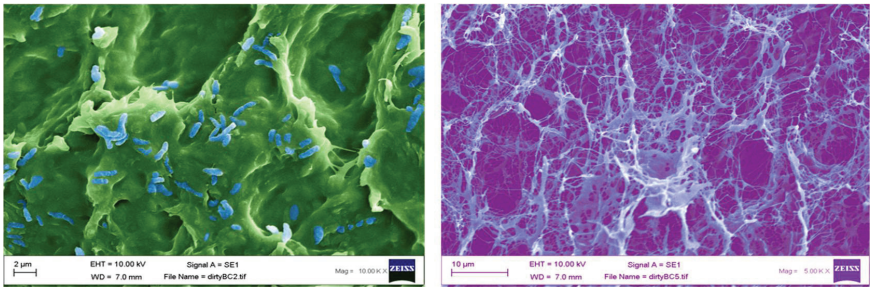

Figure 4. False coloured scanning electron micrographs of (**A**) unpurified (*G. xylinus* coloured blue), and (**B**) purified bacterial cellulose (cellulose nanofibres highlighted in light blue).

Once the bacterial cellulose was purified and lyophilised, SEM analysis was undertaken to confirm the pore size. Our results are concordant with previously published data [51], which show an average pore size of 117.9 nm to 3.4 µm (Figure 5A,B).

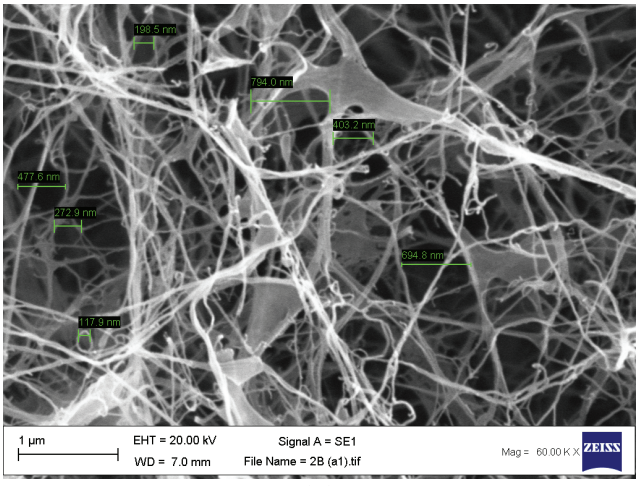

(**A**)

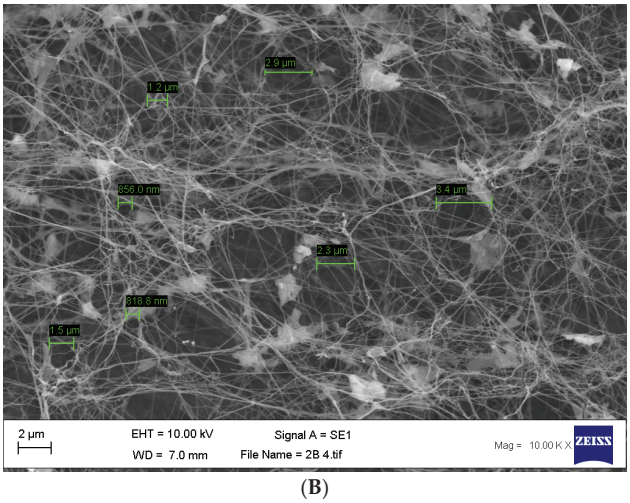

(**B**)

Figure 5. (**A**,**B**) Scanning electron micrographs of purified bacterial cellulose highlighting the size of the pores found within the matrix with an average range of 117.9 nm to 3.4 µm. n = 14, error bar 1 µm.

Following the characterisation of the purified BC via SEM, the lyophilised BC was aseptically cut using biopsy punches into 4 mm disks to be used in cytotoxicity assays and 8 mm disks used in disk diffusion assays. After this, the BC disks were placed into solutions of amphotericin b, thymoquinone, ocimene, or miramistin and were agitated overnight to ensure maximum loading of the antifungal agent. To confirm the successful loading, FTIR was performed on each of the samples (Figure 6A–F).

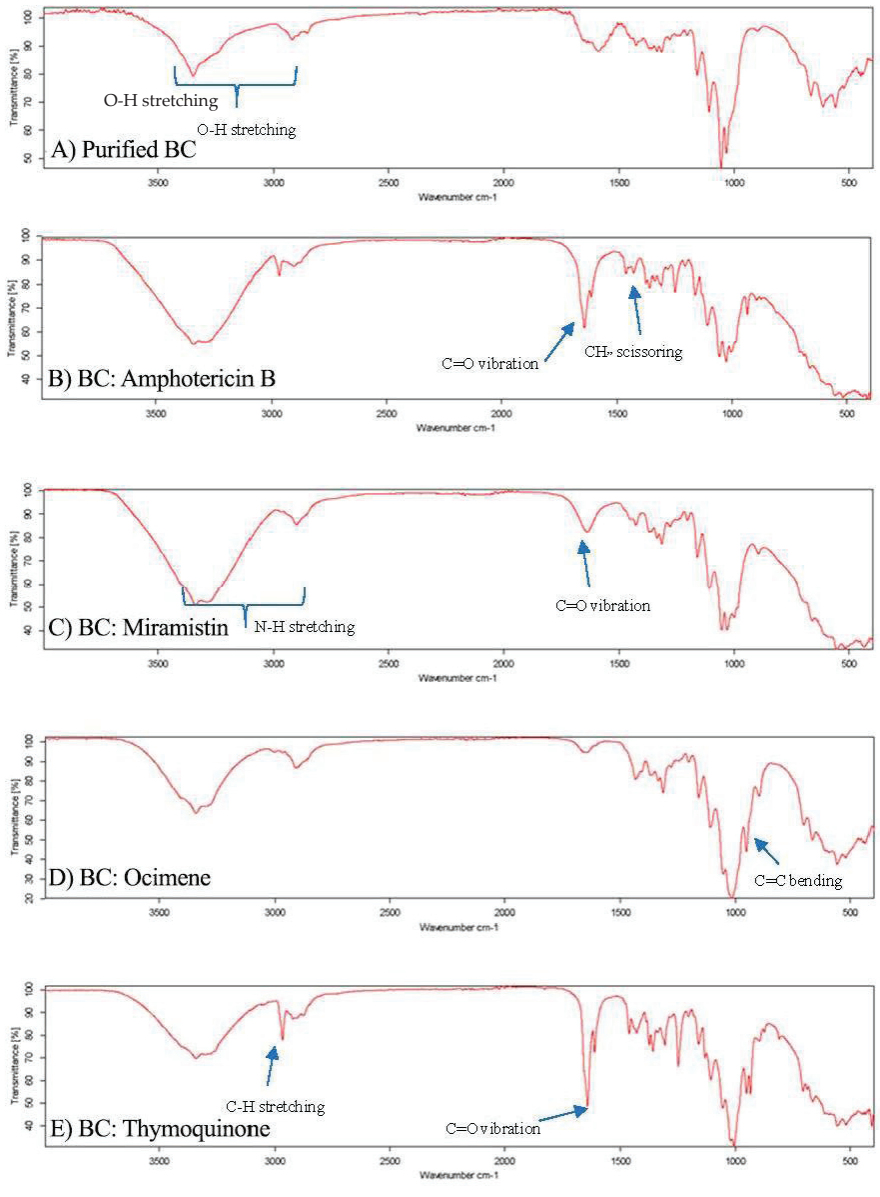

Figure 6. FTIR spectrographs of (**A**) purified BC, (**B**) BC: Amphotericin B, (**C**) BC: Miramistin, (**D**) BC: Ocimene, and (**E**) BC: Thymoquinone. (n = 3, 16 scans).

Each sample displayed characteristic O-H stretching between 2500 and 3300 cm^{-1} due to hydroxyl groups found in the bacterial cellulose matrix (Figure 6A). It is worth noting that all samples analysed displayed similar characteristic wavelengths to pure cellulose of 3330, 2894, 1614, 1370, 1159, and 1056 cm^{-1}, as seen in research previously conducted [52]; however, subtle additions to these wavelength peaks in the fingerprint region were used to confirm the presence of the antifungal agents in the respective samples.

The FTIR spectrum for BC: amphotericin B (Figure 6B) shows three principal vibrations of the amphotericin B molecule: the band with a maximum at 1730 cm^{-1}, which can be assigned to the vibration of C=O in the –COOH group, the CH_2 scissoring vibrations (the band centred at 1460 cm^{-1}), and the C=C stretching vibration, which is represented by peaks between 1486 and 1631 cm^{-1}. Additionally, the peaks in the region of 3300–3400 cm^{-1} indicate stretching vibrations of the O–H group and the N–H stretching in concordance with previous research [53]. The appearance of peaks between 3400 and 3300 cm^{-1} in the FTIR spectra, Figure 5B, can be also attributed as a band of OH groups of BC involved in forming hydrogen bonds with the antifungal agent, indicating an interaction between BC and amphotericin B.

The FTIR spectrum for BC: miramistin (Figure 6C) shows two principal vibrations of the miramistin molecule: the signals from the amide group (NH–CO) were observed in the range of 3400–3200 cm^{-1} and C=O in the range 1650–1700 cm^{-1}. In addition, peaks seen at 1650–1580 cm^{-1} suggest bending in N-H groups and stretching vibrations of C=C in the phenolic ring [54]. Moreover, the broad band seen between 3400 and 3300 cm^{-1} in Figure 6C, can also indicate on the formation of the hydrogen bonding between functional amide groups NHCO of miramistin and BC.

A strong peak observed at 3000–2900 cm^{-1} in Figure 6D corresponds to C–H stretching in the alkyne of ocimene. Peaks at 1605 cm^{-1} and 1640 cm^{-1} suggest C=C bonding. However, the confirmation of successful loading of ocimene was achieved by identifying a sharp peak at 892 cm^{-1} which corresponds to C=C bending in the vinylidene group, which is similar to other research [55].

The results of FTIR spectra for thymoquinone-loaded BC (Figure 6E) have assigned the existence of a variety of sharp, strong, and weak peaks as well as crucial functional groups that correspond to C=O, C-H, $–CH_2$, $–CH_3$, C=C, and C–O, suggesting the successful loading of thymoquinone within the BC sample. The intense band present at 2967 cm^{-1} corresponds to the C-H stretching of aliphatic groups, while the band observed at a higher wavenumber ≈3040 cm^{-1} was assigned to the stretching observed in the vinylic C–H in the C=C–H groups, which had previously been reported [56]. Additionally, the characteristic strong band of the carbonyl groups of a cyclohexadiene ring is observed at the wavenumber ≈1650 cm^{-1}. As a result of FTIR analysis, we can confirm that the bacterial cellulose was successfully loaded with each antifungal drug, respectively.

3.2. Antifungal Studies

After successfully loading the drug compounds, we proceeded to conduct MIC_{90} and MFC studies to determine the optimum concentration to apply in disk diffusion and cytotoxicity assays. All MIC_{90} results (Table 3) obtained in this study are consistent with published MIC_{90} breakpoints where available in CLSI M60 and M61 standardised protocols [57,58]. This suggests that the test compounds have similar antifungal properties to amphotericin B, but on average, they are 69% less cytotoxic while maintaining similar antifungal profiles. This could prove beneficial in treating resistant and difficult to treat fungal infections, as compounds such as thymoquinone or ocimene, which appear to have similar antifungal profiles to amphotericin B, could be given without the harsh side effects that are often observed when administering amphotericin B.

Table 3. MIC and MFC of antifungal agents against fungal isolates.

Fungi	Amphotericin B		Thymoquinone		Ocimene		Miramistin	
	MIC_{90} (mg/L)	MFC (mg/L)	MIC_{90} (mg/L))	MFC (mg/L)	MIC_{90} (mg/L)	MFC (mg/L)	MIC_{90} (mg/L)	MFC (mg/L)
A. fumigatus	0.06–1	0.07–1	1.3–2	1.5–2	0.7–1	1.6–2	21	27
A. niger	0.06–1	0.09–1	0.9–2	1–2	0.4–0.9	1–2	18-20	25
C. albicans	0.03	0.06–1	4.9–5.2	6.2–7	0.3–0.9	0.3–0.9	1.3–3	2.6–4
C. auris	0.05	0.08–1	7.9–8.2	8.4–9.7	1.2–1.9	2–2.5	1.4–2.8	3–5

In previous research by Abdel et al. (2013), they demonstrated that topical thymoquinone cream could be used safely against vaginal candidiasis in mice at concentrations of 10% (*w/v*) [59], which is twice the concentration used in this present study (Table 3).

The mean zones of inhibition for each compound at 50 mg/L, which is twice the concentration required as advised by CLSI for all fungi, are shown in Figure 7, and examples of these zones are shown in Figure 8. The disk diffusion assay for antifungal activity indicated that thymoquinone-loaded BC has comparable inhibitory effects against all four genera of fungi to amphotericin B with no significant difference ($p > 0.05$). However, ocimene and miramistin-loaded BC compared to amphotericin B against both *Candida* and *Aspergillus* species showed a significant difference ($p < 0.05$) in activity. Amphotericin B had a mean ZOI against all four genera of fungi of 22.53 ± 0.969 mm, while thymoquinone similarly had a mean ZOI of 21.425 ± 0.925 mm. However, the mean ZOI for ocimene and miramistin were 12.475 ± 1.536 mm and 11.875 ± 1.682 mm, respectively, as seen in Figure 8A–D.

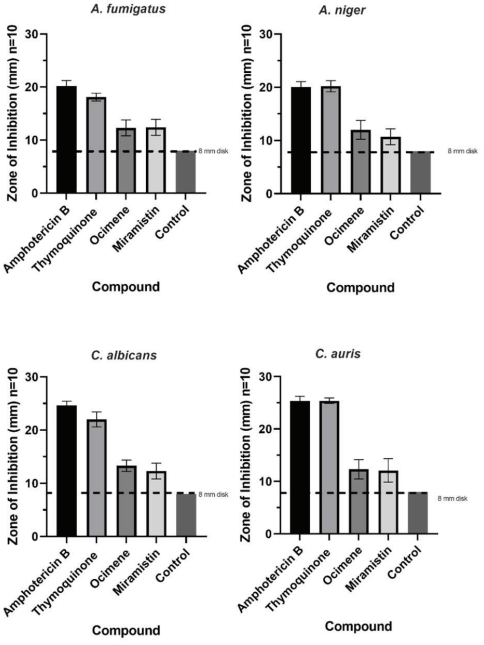

Figure 7. Mean zone of inhibition graphs for all four antifungal agents at a concentration of 50 mg/L loaded into 8 mm disks of purified BC tested against *A. fumigatus*, *A. niger*, *C. albicans*, and *C. auris*. Disks of pure BC were used as controls. Each test was conducted in triplicate 10 times ($p \leq 0.05$, $n = 10$, error bars = SD).

Quantification of the drugs entrapped throughout the bacterial cellulose matrices were achieved by comparing the difference in weight of lyophilised unloaded BC to lyophilised loaded BC (Table 4). The difference in weight is directly proportional to the available free compound within the solution at a concentration of 50 mg/L (twice the required concentration to maintain consistency between compound concentrations), along with the ability for the BC to absorb up to 99% its weight in liquid, thus absorbing up to 99% of solubilised compounds available. Table 4 shows that all compounds were successfully loaded and retained within the BC matrix up to 78.95 ± 17.5%. Similarly processed disks were subsequently used in MTT assays to confirm any cytotoxic effects they may exert on HEp-2 cells.

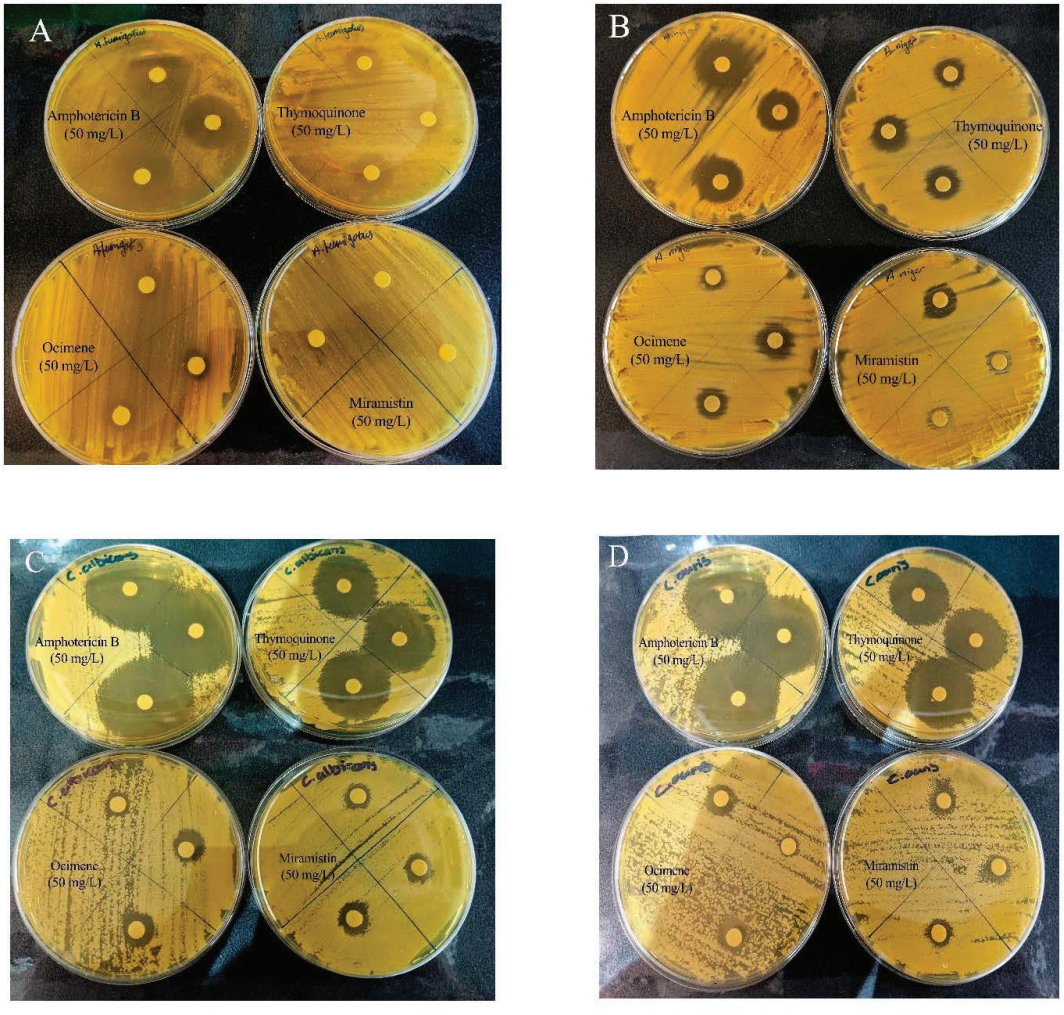

Figure 8. Representative disk diffusion assay plates showing the ZOI of bacterial cellulose disks loaded with amphotericin B, thymoquinone, ocimene, and miramistin against (**A**) *A. fumigatus*, (**B**) *A. niger*, (**C**) *C. albicans*, and (**D**) *C. auris* ($n = 3$).

Table 4. Quantification of antifungal compounds loaded within lyophilised 8 mm disks of bacterial cellulose ($n = 10$, ±SD).

Drug	Unloaded BC (mg)	Loaded BC (mg)	Average Compound Loaded (µg)
Thymoquinone	1.6375 ± 0.364	1.678 ± 0.357	42.0 ± 8
Ocimene	1.5500 ± 0.208	1.588 ± 0.207	37.4 ± 9
Miramistin	1.5750 ± 0.175	1.615 ± 0.183	46.0 ± 8
Amphotericin B	1.7000 ± 0.221	1.733 ± 0.220	32.5 ± 10
Control	1.6200 ± 0.125	1.627 ± 0.120	7.00 ± 2

The results from our study for amphotericin B and thymoquinone against both *Candida* species are similar to previous studies conducted; however, in these studies, the drugs were modified to be either liposomal or nanoparticulate, which may have impacted

the overall MIC/MFC concentrations [60–62]. However, it should be noted that in the mentioned research, only Randhawa et al. (2015) [61] conducted their studies using internationally recognised protocols; therefore, the studies conducted by Khan et al. (2018) and Cavaleiro et al. (2015) [62,63] would benefit from being repeated using appropriate standardised protocols. Additionally, the results obtained for the antifungal activity of thymoquinone against all four genera of fungi in our study are similar to results published by Khader et al. (2009) [64]. They also showed that the MIC/MFC for yeasts ranged from 1.25 to 0.08 µg/mL and for non-dermatophyte fungi $\geq 10^{-5}$ µg/mL [64]. Their results may be slightly lower than our MIC/MFC data, as the study mentioned above used clinical isolates, which could show reduced resistance to the compounds.

The results show evidence that bacterial cellulose loaded with thymoquinone, ocimene, or miramistin display antifungal activity against different species of *Candida* and *Aspergillus*. This is especially poignant as both *Candida* species and *Aspergillus* species can develop resistance to commonly used antifungal drugs [5].

3.3. Cytotoxicity Studies

Once minimum fungicidal concentrations were determined, we proceeded to conduct cytotoxicity studies with concentrations of each respective drug ranging from 80 to 10 mg/L encompassing all values (Figure 9A–E) to find the most potent concentration while maintaining an acceptable level of toxicity toward HEp-2 cells. It is also shown through the cytotoxicity assays that all three test compounds have significantly lower ($p < 0.01$) cytotoxic effects against HEp-2 cells in comparison to amphotericin B; cell viability for 50 mg/L solutions of amphotericin B was 29.25 ± 1.708%, whereas for thymoquinone, ocimene, and miramistin, it was 71.25 ± 3.594%, 65.5 ± 4.435%, and 42.5 ± 8.266%, respectively.

As a result of MIC/MFC assays, it was determined that a concentration of 50 mg/L (*w/v*) would be used in disk diffusion assays owing to an average cell viability rate of Hep-2 cells of 40% to 60% and because standard operating protocols advise using twice the drug concentration of the highest MIC. It is also worth noting that Figure 9E compiles cell viability rates for all drugs at a concentration of 50 mg/L (*w/v*); a significant difference ($p < 0.05$) can be seen in the survivability of HEp-2 cells when treated with thymoquinone, ocimene, and miramistin in comparison to amphotericin B, which showed a mean cell survival rate of 29.25 ± 0.854%. In contrast, thymoquinone at a concentration of 50 mg/L (*w/v*) showed a mean survival rate of 71.25 ± 1.797%. As shown by the 8 mm BC disk compound quantification assay, we can anticipate that up to 78.95 ± 17.5% of the free compound in solution will also be absorbed by the 4 mm BC disks used for the cytotoxicity assay. These data are supported by Khader et al. (2009), who concluded that ≥20 uM concentration of thymoquinone in vitro caused 6.37 ± 0.75% necrosis in hepatocytes [64]. The in vitro toxicity of miramistin was also supported by Osmanov et al. (2020) [65], who concluded that there were no cytotoxic effects seen at a concentration of 1000 mg/L against McCoy mammalian cell lines. Subsequent confocal microscopy of the HEp-2 cells after being exposed to the antifungal agents for 24 h can be seen in Figure 10A–E. The typical morphology (triangular) of HEp-2 cells can be observed in Figure 10E (control) with all previous images (Figure 10A–D) showing treated cells.

Figure 10A shows cells treated with amphotericin B, and as expected, they became detached from the base of the well and died, as evidenced by the circular appearance rather than being triangular in nature. Figure 9B–D show HEp-2 cells treated with thymoquinone, miramistin, and ocimene, respectively, and both show a positive correlation to the survivability data in Figure 9A–E. The vast majority of cells have retained their triangular appearance and have remained attached to the well's base, suggesting cellular survival, which is in accordance with Uribe et al. (2013), who described the cytotoxic effects of amphotericin B in myofibroblast cell lines [66].

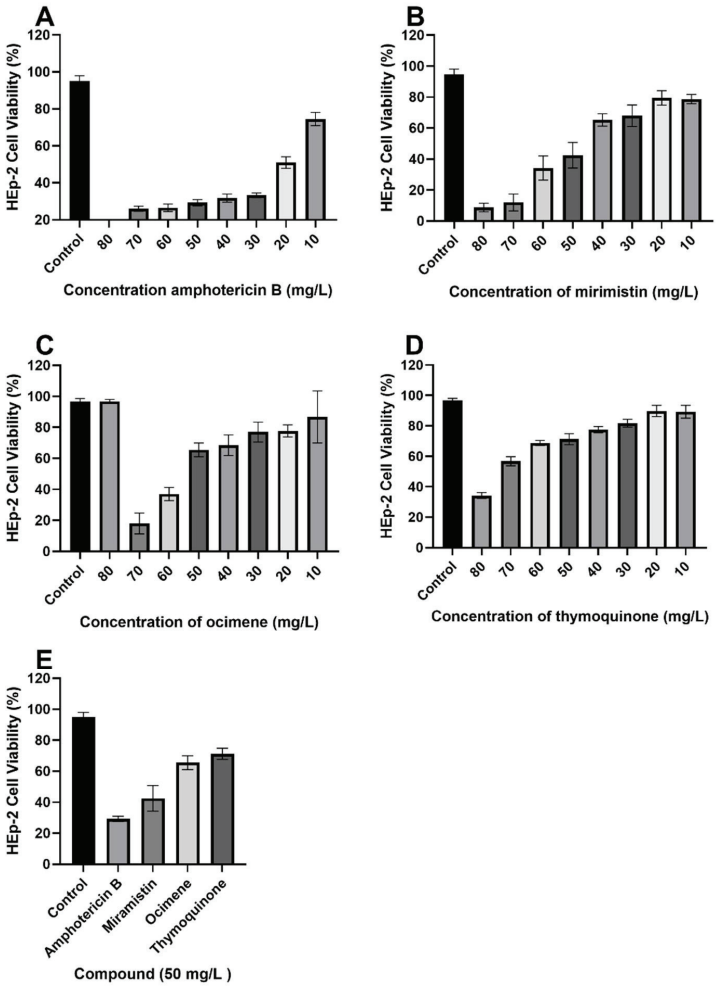

Figure 9. MTT cytotoxicity assay with varying concentrations of each respective drug, (**A**) amphotericin B, (**B**) miramistin, (**C**) ocimene, and (**D**) thymoquinone, against HEp-2 cells, (**E**) condenses data of 50 mg/L drug concentration from each graph (**A**–**D**) for ease of comparison. All tests were carried out in triplicate. Control was DMSO and RPMI-1640 (50:50) ($p \leq 0.01$, $n = 10$, error bars = SD).

Additionally, it would be interesting to investigate the antifungal agents in vivo against animal models, which would elucidate the antifungal agents' real potential as the hemocompatibility, along with biocompatibility of the overall biofunctionalised material system, could be collated. Moreover, future studies could be performed using clinical isolates to reduce the risk of selection bias. Secondly, further investigation into the mechanism of action of miramistin, ocimene, and thymoquinone would allow for a greater understanding of how these drugs exert their antifungal properties. Researchers have reported that thymoquinone and ocimene potentiate the mode of action of antibiotic compounds; however, research toward ocimene in this area is still lacking [67–69]. Nevertheless, as the studies conducted by Goyal et al. (2017), Liu et al. (2019), and Sarah et al. (2019) [67–69] were outside the remit of internationally recognised protocols, their results should be reconfirmed utilising appropriate standard protocols such as those produced by CLSI. Still,

the test compound results for the antifungal potential in our study show promise and merit further investigation.

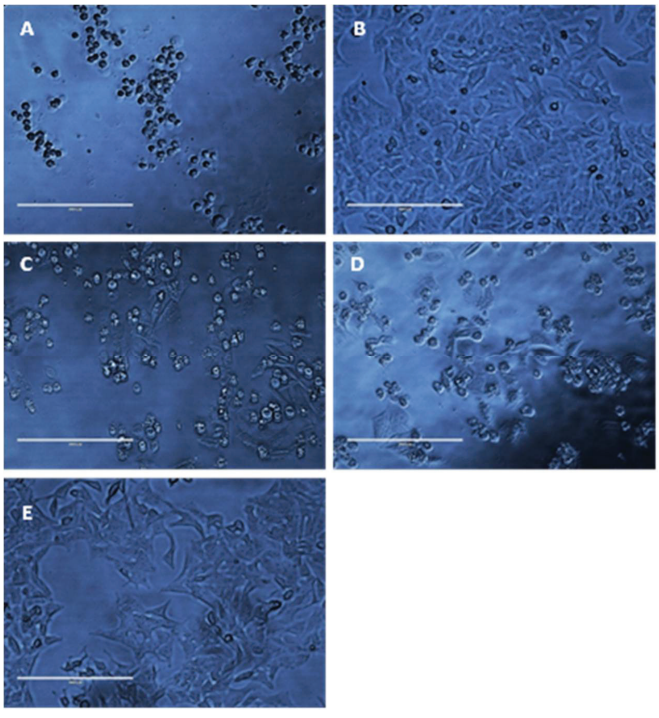

Figure 10. Representative photomicrographs of HEp-2 cells (40× magnification) after exposure to 50 mg/L amphotericin B (**A**), thymoquinone (**B**), miramistin (**C**), ocimene (**D**), and control (**E**) for 24 h. Control (**E**) was cultured without any addition of antifungal agents for 24 h in RPMI-40 (scale bar = 200 μm).

4. Conclusions and Future Prospects

The development of novel antifungal treatment options is an ever-pressing issue as the rise in the incidence of wound infections among both civil and military traumatic injuries, along with burns, trauma, and ulcers, are becoming more frequent. These injuries and subsequent infections by fungal pathogens are linked with increased mortality, risk of limb loss, prolonged stays in hospital, failure of the treatment regimen, and further systemic infection. As shown in this study, thymoquinone, ocimene, or miramistin-loaded bacterial cellulose wound dressings are promising antifungal hydrogels that could address the aforementioned issues. As shown through the MFC and cytotoxicity assays, these materials could be potentially used in the groups mentioned above owing to the high level of antifungal activity and low cytotoxic effects when compared to conventional antifungal drugs that could exasperate pre-existing conditions, namely amphotericin B [70].

The results of this study indicate that the implementation of thymoquinone, ocimene, or miramistin hydrogel wound dressings may depreciate the need to use other systemic antifungal compounds in the treatment of superficial and deep tissue wounds, which is also in line with currently antimicrobial stewardship agendas and has been developed to specifically target and reduce the incidence of antimicrobial resistance [71]. Prolonged states of trauma are usually associated with inappropriate therapy, which is well documented in being a causative factor toward the development of antimicrobial resistance [72,73]. The issue of antifungal resistance and the need to develop newer and more efficacious products

was highlighted by The World Health Organisation in 2020 during the first meeting of the WHO antifungal expert group tasked with identifying priority fungal pathogens and subsequent treatment options [6].

Through this study, the preliminary antifungal properties of thymoquinone, ocimene and miramistin have been conducted against four commonly encountered fungi, which are causative agents in wound infections. The agents have been shown through internationally recognised disk diffusion and broth dilution assay protocols to possess a similar antifungal profile compared to amphotericin B. However, the marked difference is found within our agents' cytotoxicity profiles, which are significantly lower ($p < 0.01$) than that of amphotericin B.

Future perspectives of this study will focus on the loading capabilities of bacterial cellulose and combinations of potential antifungal agents to increase the bioactivity to a broader spectrum of organisms. Additionally, as the water-holding capability of the material is so high, this introduces issues of adherence of the wound dressing to the skin. Further investigations are required to develop a method by which the biomaterial can be modified to become adherent, possibly taking advantage of the ionic pores (Figure 5) within the cellulose matrices. Additionally, further investigations into the time release of each compound from BC will be conducted with appropriate time kill studies to determine how long these materials remain bioactive.

Following SEM characterisation of purified BC, it is clear that the pore sizes found within the matrices are generally uniform in size, around 117.9 nm to 3.4 µm, which is in concordance with existing research [38]. It is also postulated that there are two forms of pore that can be seen. The main pores, which are easily observed, fall within the mentioned dimensions; however, there are also indications that there are more superficial pores that are much larger in the region of 200 µm in diameter. This development in identifying various sizes and conformations of pores would allow future developments to be pursued in the area of incorporating additional compounds with a much larger structure, such as bioactivated zeolites loaded with antimicrobial metal ions. Table 3 highlights the efficacy of bacterial cellulose to absorb a large amount of free compound within a solution, showing up to 78.95 $\pm$ 17.5% successful loading and retainment throughout the entire material via physical absorption. This is agreeable to published data for the swelling ratio of bacterial cellulose [36].

The data collected during this study have highlighted the efficacy and high in vitro tolerability of our agents in use as an antifungal and would benefit greatly from further investigation. As we have highlighted in this study, the importance of utilising naturally occurring products is paramount in fighting the burdening issue of antifungal resistance [74,75]. It is clear that pharmaceutical agents such as amphotericin B are usually accompanied by severe side effects that make their use intolerable to individuals while having low efficacy to their target organism [76,77]. To the best of our knowledge, we are the first to successfully load thymoquinone into bacterial cellulose hydrogels, thus producing a novel wound dressing. We have also determined that thymoquinone and amphotericin B have similar antifungal potencies; however, the thymoquinone's overall cytotoxicity is significantly lower ($p < 0.01$).

Author Contributions: S.S. writing original draft; I.R. and S.S. were the main persons involved in the planning of experiments and interpretation of the data; G.A. was involved in FTIR interpretation, I.R., S.S., H.G., A.G., W.H., M.K. and G.A. editing and assisting with the preparation of the manuscript. All authors have read and agreed to the published version of the manuscript.

Funding: Partial financial support from the European Regional Development Fund Project EnTRESS No. 01R16P00718.

Institutional Review Board Statement: Not applicable.

Informed Consent Statement: Not applicable.

Data Availability Statement: The data presented in this study are openly available.

Acknowledgments: The authors would like to thank Biorender.com (2021) for their paid subscription in creating a graphical abstract and Figure 2. We would like to thank Keith R. Jones form the University of Wolverhampton, UK for his help with scanning electron microscopy images. The authors would also like to thank Enas Al-Ani (University of Wolverhampton, Wolverhampton, UK) for her very kind assistance and work with producing confocal images of Hep-2 cells in this study.

Conflicts of Interest: The authors declare no conflict of interest.

References

1. Swingler, S.; Gupta, A.; Gibson, H.; Kowalczuk, M.; Heaselgrave, W.; Radecka, I. Recent Advances and Applications of Bacterial Cellulose in Biomedicine. *Polymers* **2021**, *13*, 412. [CrossRef]
2. Gupta, A.; Briffa, S.M.; Swingler, S.; Gibson, H.; Kannappan, V.; Adamus, G.; Kowalczuk, M.M.; Martin, C.; Radecka, I. Synthesis of Silver Nanoparticles Using Curcumin-Cyclodextrins Loaded into Bacterial Cellulose-Based Hydrogels for Wound Dressing Applications. *Biomacromolecules* **2020**, *21*, 1802–1811. [CrossRef]
3. Farrington, M.; Sharma, S.K. Chapter 14—Chemotherapy of bacterial infections. In *Clinical Pharmacology*, 11th ed.; Bennett, P.N., Brown, M.J., Sharma, P., Eds.; Churchill Livingstone: London, UK, 1996; pp. 191–212.
4. Maurel, V.; Denis, B.; Camby, M.; Jeanne, M.; Cornesse, A.; Glavnik, B.; Alanio, A.; Rousseau, A.-F.; Lefloch, R.; Lagrange-Xelot, M.; et al. Outcome and characteristics of invasive fungal infections in critically ill burn patients: A multicenter retrospective study. *Mycoses* **2020**, *63*, 535–542. [CrossRef]
5. Janbon, G.; Quintin, J.; Lanternier, F.; D'Enfert, C. Studying fungal pathogens of humans and fungal infections: Fungal diversity and diversity of approaches. *Microbes Infect.* **2019**, *21*, 237–245. [CrossRef] [PubMed]
6. World Health Organization. *First Meeting of the WHO Antifungal Expert Group on Identifying Priority Fungal Pathogens: Meeting Report*; World Health Organization: Geneva, Switzerland, 2020.
7. Enoch, D.A.; Yang, H.; Aliyu, S.H.; Micallef, C. The Changing Epidemiology of Invasive Fungal Infections. In *Methods in Molecular Biology*; Springer: Berlin, Germany, 2017; Volume 1508, pp. 17–65.
8. Jenks, J.D.; Cornely, O.A.; Chen, S.C.-A.; Thompson, G.R.; Hoenigl, M. Breakthrough invasive fungal infections: Who is at risk? *Mycoses* **2020**, *63*, 1021–1032. [CrossRef] [PubMed]
9. Paul, S.; Dadwal, R.; Singh, S.; Shaw, D.; Chakrabarti, A.; Rudramurthy, S.M.; Ghosh, A.K. Rapid detection of ERG11 polymorphism associated azole resistance in Candida tropicalis. *PLoS ONE* **2021**, *16*, e0245160. [CrossRef]
10. Mba, I.E.; Nweze, E.I. Mechanism of Candida pathogenesis: Revisiting the vital drivers. *Eur. J. Clin. Microbiol. Infect. Dis.* **2020**, *39*, 1797–1819. [CrossRef] [PubMed]
11. Khan, M.A. Antimicrobial Action of Thymoquinone. In *Molecular and Therapeutic actions of Thymoquinone*; Metzler, J.B., Ed.; Springer: Berlin, Germany, 2018; pp. 57–64.
12. Russo, E.B.; Marcu, J. Cannabis Pharmacology: The Usual Suspects and a Few Promising Leads. *DNA Topoisomerases Biochem. Mol. Biol.* **2017**, *80*, 67–134. [CrossRef]
13. Devi, M.A.; Sahoo, D.; Singh, T.B.; Rajashekar, Y. Antifungal activity and volatile organic compounds analysis of essential oils from Cymbopogon species using solid-phase microextraction-gas chromatography-mass spectrometry. *J. Agric. Food Res.* **2021**, *3*, 100110. [CrossRef]
14. Al-Thobity, A.M.; Al-Khalifa, K.S.; Gad, M.M.; Al-Hariri, M.; Ali, A.A.; Alnassar, T. In Vitro Evaluation of the Inhibitory Activity of Thymoquinone in Combatting Candida albicans in Denture Stomatitis Prevention. *Int. J. Environ. Res. Public Health* **2017**, *14*, 743. [CrossRef]
15. Shaterzadeh-Yazdi, H.; Noorbakhsh, M.-F.; Samarghandian, S.; Farkhondeh, T. An Overview on Renoprotective Effects of Thymoquinone. *Kidney Dis.* **2018**, *4*, 74–82. [CrossRef] [PubMed]
16. Osmanov, A.; Wise, A.; Denning, D.W. In vitro and in vivo efficacy of miramistin against drug-resistant fungi. *J. Med. Microbiol.* **2019**, *68*, 1047–1052. [CrossRef] [PubMed]
17. Cavassin, F.B.; Baú-Carneiro, J.L.; Vilas-Boas, R.R.; Queiroz-Telles, F. Sixty years of Amphotericin B: An Over-view of the Main Antifungal Agent Used to Treat Invasive Fungal Infections. *Infect. Dis.* **2021**, *10*, 115–147.
18. Laurent, A.; Pantet, O.; Laurent, L.; Hirt-Burri, N.; de Buys Roessingh, A.; Raffoul, W.; Laurent, P.; Monod, M.; Applegate, L. Potency and stability of liposomal Amphotericin B formulated for topical management of Aspergillus species. infections in burn patients. *Burns Open* **2019**, *4*, 110–116. [CrossRef]
19. Wasan, K.M. Development of an Oral Amphotericin B Formulation as an Alternative Approach to Parenteral Amphotericin B Administration in the Treatment of Blood-Borne Fungal Infections. *Curr. Pharm. Des.* **2020**, *26*, 1521–1523. [CrossRef]
20. Almshawit, H.; Macreadie, I. Fungicidal effect of thymoquinone involves generation of oxidative stress in Candida glabrata. *Microbiol. Res.* **2017**, *195*, 81–88. [CrossRef]
21. Gintjee, T.J.; Donnelley, M.A.; Thompson, G.R. Aspiring Antifungals: Review of Current Antifungal Pipeline Developments. *J. Fungi* **2020**, *6*, 28. [CrossRef]
22. Zhou, J.; Tan, J.; Gong, Y.; Li, N.; Luo, G. Candidemia in major burn patients and its possible risk factors: A 6-year period retrospective study at a burn ICU. *Burns* **2019**, *45*, 1164–1171. [CrossRef]
23. Que, A.T.; Nguyen, N.M.T.; Do, N.A.; Nguyen, N.-L.; Tran, N.D.; Le, T.A. Infection of burn wound by Aspergillus fumigatus with gross appearance of fungal colonies. *Med. Mycol. Case Rep.* **2019**, *24*, 30–32. [CrossRef]

24. Berger, A.; Ford, B.; Brown-Joel, Z.; Shields, B.; Rosenbach, M.; Wanat, K. Angioinvasive fungal infections impacting the skin. *J. Am. Acad. Dermatol.* **2019**, *80*, 883–898.e2. [CrossRef]
25. Chourasia, S.; Rautji, R.; Radhakrishna, K.; Baghel, J.; Shivakumar, D.; Aziz, N. Disseminated invasive Aspergillosis in a case of fatal antemortem flame burns. *J. Indian Acad. Forensic Med.* **2019**, *41*, 145. [CrossRef]
26. Amphotericin Bekar, R.; Kandasubramanian, B. Advancements in nanofibers for wound dressing: A review. *Eur. Polym. J.* **2019**, *117*, 304–336.
27. Alexis, O.D.P.; Guang, Y.; Guiaro, M.N. New Approach for Skin Repair by Using Bacterial Cellulose Altered with Paraffin and Porous Bacterial Cellulose based Scaffold with Alginate. *J. Anal. Pharm. Res.* **2017**, *5*, 1–6. [CrossRef]
28. Ghomi, E.R.; Khalili, S.; Khorasani, S.N.; Neisiany, R.E.; Ramakrishna, S. Wound dressings: Current advances and future directions. *J. Appl. Polym. Sci.* **2019**, *136*, 47738. [CrossRef]
29. Portela, R.; Leal, C.R.; Almeida, P.L.; Sobral, R.G. Bacterial cellulose: A versatile biopolymer for wound dressing applications. *Microb. Biotechnol.* **2019**, *12*, 586–610. [CrossRef]
30. Ahmed, J.; Gultekinoglu, M.; Edirisinghe, M. Bacterial cellulose micro-nano fibres for wound healing applications. *Biotechnol. Adv.* **2020**, 107549. [CrossRef]
31. Veith, A.P.; Henderson, K.; Spencer, A.; Sligar, A.D.; Baker, A.B. Therapeutic strategies for enhancing angiogenesis in wound healing. *Adv. Drug Deliv. Rev.* **2019**, *146*, 97–125. [CrossRef]
32. Thiruvengadam, V.; Vitta, S. Bacterial cellulose based flexible multifunctional nanocomposite sheets. *Cellul.* **2017**, *24*, 3341–3351. [CrossRef]
33. Prosvirnikov, D.B.; Safin, R.G.; Zakirov, S. Microcrystalline Cellulose Based on Cellulose Containing Raw Material Modified by Steam Explosion Treatment. *Solid State Phenom.* **2018**, *284*, 773–778. [CrossRef]
34. Volova, T.G.; Prudnikova, S.; Sukovatyi, A.G.; Shishatskaya, E.I. Production and properties of bacterial cellulose by the strain Komagataeibacter xylinus B-12068. *Appl. Microbiol. Biotechnol.* **2018**, *102*, 7417–7428. [CrossRef]
35. Gupta, A.; Low, W.; Radecka, I.; Britland, S.; Mohd Amin, M.; Martin, C. Characterisation And In Vitro Antimicrobial Activity Of Biosynthetic Silver-Loaded Bacterial Cellulose Hydrogels. *J Microencapsul.* **2016**, *33*, 725–734. [CrossRef] [PubMed]
36. Gupta, A.; Low, W.-L.; Britland, S.; Radecka, I.; Martin, C. Physicochemical characterisation of biosynthetic bacterial cellulose as a potential wound dressing material. *Br. J. Pharm.* **2017**, *2*, S37–S38.
37. Revin, V.; Pestov, N.; Shchankin, M.; Mishkin, V.; Platonov, V.; Uglanov, D. A Study of The Physical And Mechanical Prop-erties Of Aerogels Obtained From Bacterial Cellulose. *Biomacromolecules* **2019**, *20*, 1401–1411. [CrossRef] [PubMed]
38. Gao, C.; Wan, Y.; Yang, C.; Dai, K.; Tang, T.; Luo, H.; Wang, J. Preparation and characterization of bacterial cellulose sponge with hierarchical pore structure as tissue engineering scaffold. *J. Porous Mater.* **2010**, *18*, 139–145. [CrossRef]
39. Thygesen, A.; Oddershede, J.; Lilholt, H.; Thomsen, A.; Ståhl, K. On the Determination of Crystallinity And Cellulose Content In Plant Fibres. *Cellulose* **2005**, *12*, 563–576. [CrossRef]
40. Ruan, C.; Zhu, Y.; Zhou, X.; Abidi, N.; Hu, Y.; Catchmark, J. Effect of Cellulose Crystallinity On Bacterial Cellulose Assembly. *Cellulose* **2016**, *23*, 3417–3427. [CrossRef]
41. Fernandes, M.; Gama, M.; Dourado, F.; Souto, A. Development of novel bacterial cellulose composites for the textile and shoe industry. *Microb. Biotechnol.* **2019**, *12*, 650–661. [CrossRef]
42. Du, R.; Wang, Y.; Zhao, F.; Qiao, X.; Song, Q.; Li, S.; Kim, R.-C.; Pan, L.; Han, Y.; Xiao, H.; et al. Production, Optimization and Partial Characterization of Bacterial Cellulose from Gluconacetobacter xylinus TJU-D2. *Waste Biomass Valorization* **2020**, *11*, 1681–1690. [CrossRef]
43. Huang, Y.; Zhu, C.; Yang, J.; Nie, Y.; Chen, C.; Sun, D. Recent advances in bacterial cellulose. *Cellul.* **2014**, *21*, 1–30. [CrossRef]
44. Mukaremera, L.; Lee, K.K.; Mora-Montes, H.M.; Gow, N.A.R. Candida albicans Yeast, Pseudohyphal, and Hyphal Morphogenesis Differentially Affects Immune Recognition. *Front. Immunol.* **2017**, *8*, 629. [CrossRef]
45. ISO. *ISO/TC 212 Clinical Laboratory Testing and In Vitro Diagnostic Test Systems, Clinical Laboratory Testing and In Vitro Diagnostic Test Systems—Reference Method for Testing the In Vitro Activity of Antimicrobial Agents against Yeast Fungi Involved in Infectious Diseases*; ISO 16256:2012; ISO: Geneva, Switzerland, 2012; ISO 16256:2012.
46. CLSI. *Reference Method for Broth Dilution Antifungal Susceptibility Testing of Yeasts*; Approved Standard-Third Edition M27-A3; Clinical and Laboratory Standard Institute: Wayne, PA, USA, 2008.
47. CLSI. *Reference Method for Broth Dilution Antifungal Susceptibility Testing of Filamentous Fungi*, 3rd ed.; CLSI Guideline M38; Clinical and Laboratory Standards Institute: Wayne, PA, USA, 2017.
48. Bauer, A.W.; Kirby, W.M.; Sherris, J.C.; Turck, M. Antibiotic susceptibility testing by a standardized single disk method. *Am. J. Clin. Pathol.* **1966**, *45*, 493–496. [CrossRef] [PubMed]
49. CLSI. *Method for Antifungal Disk Diffusion Susceptibility Testing of Yeasts*, 3rd ed.; CLSI Guideline M44; Clinical and Laboratory Standards Institute: Wayne, PA, USA, 2018.
50. CLSI. *Method for Antifungal Disk Diffusion Susceptibility Testing of Non-Dermatophyte Filamentous Fungi*, 1st ed.; CLSI Guideline M51-A; Clinical and Laboratory Standards Institute: Wayne, PA, USA, 2010; CLSI Guideline M51-A.
51. Frone, A.N.; Panaitescu, D.M.; Nicolae, C.A.; Gabor, A.R.; Trusca, R.; Casarica, A.; Stanescu, P.O.; Baciu, D.D.; Salageanu, A. Bacterial cellulose sponges obtained with green cross-linkers for tissue engineering. *Mater. Sci. Eng. C* **2020**, *110*, 110740. [CrossRef] [PubMed]

52. Abral, H.; Chairani, M.K.; Rizki, M.D.; Mahardika, M.; Handayani, D.; Sugiarti, E.; Muslimin, A.N.; Sapuan, S.; Ilyas, R. Characterization of compressed bacterial cellulose nanopaper film after exposure to dry and humid conditions. *J. Mater. Res. Technol.* **2021**, *11*, 896–904. [CrossRef]
53. Singh, A.; Yadagiri, G.; Parvez, S.; Singh, O.P.; Verma, A.; Sundar, S.; Mudavath, S.L. Formulation, characteriza-tion and in vitro anti-leishmanial evaluation of amphotericin B loaded solid lipid nanoparticles coated with vitamin B12-stearic acid conjugate. *Mater. Sci. Eng. C* **2020**, *117*, 111279. [CrossRef]
54. Agafonova, M.N.; Kazakova, R.R.; Lubina, A.P.; Zeldi, M.I.; Nikitina, E.V.; Balakin, K.V. and Shtyrlin, Y.G. Antibacterial activity profile of miramistin in in vitro and in vivo models. *Microb. Pathog.* **2020**, *142*, 104072. [CrossRef] [PubMed]
55. Bañuelos-Valenzuela, R.; Delgadillo-Ruiz, L.; Echavarría-Cháirez, F.; Delgadillo-Ruiz, O.; Meza-López, C.; Bañue-los-Valenzuela, R.; Delgadillo-Ruiz, L.; Echavarría-Cháirez, F.; Delgadillo-Ruiz, O.; Meza-López, C. Chemical composition and FTIR of ethane extracts of Larrea tridentata, Origanum vulgare, Artemisa ludoviciana and Ruta graveolens. *Agrociencia* **2018**, *52*, 309–321.
56. Pagola, S.; Benavente, A.; Raschi, A.; Romano, E.; Molina, M.A.A.; Stephens, P.W. Crystal structure determination of thymoquinone by high-resolution X-ray powder diffraction. *AAPS PharmSciTech* **2004**, *5*, 24–31. [CrossRef]
57. CLSI. *Performance Standards for Antifungal Susceptibility Testing of Yeasts*, 2nd ed.; CLSI Guideline M60; Clinical and Laboratory Standards Institute: Wayne, PA, USA, 2020; CLSI Guideline M60.
58. CLSI. *Performance Standards for Antifungal Susceptibility Testing of Filamentous Fungi*, 2nd ed.; CLSI Guideline M61; Clinical and Laboratory Standards Institute: Wayne, PA, USA, 2020; CLSI Guideline M61.
59. AbuKhader, M. Thymoquinone in the clinical treatment of cancer: Fact or fiction? *Pharm. Rev.* **2013**, *7*, 117–120. [CrossRef]
60. Abdel Azeiz, A.Z.; Saad, A.H.; Darweesh, M.F. Efficacy of Thymoquinone against Vaginal Candidiasis in Predni-solone-induced Immunosuppressed Mice. *J. Am. Sci.* **2013**, *9*, 155–159.
61. Randhawa, M.A.; Gondal, M.A.; Al-Zahrani, A.-H.J.; Rashid, S.G.; Ali, A. Synthesis, morphology and antifungal activity of nano-particulated amphotericin-B, ketoconazole and thymoquinone against Candida albicans yeasts and Candida biofilm. *J. Environ. Sci. Health Part A* **2015**, *50*, 119–124. [CrossRef]
62. Khan, M.A.; Aldebasi, Y.H.; Alsuhaibani, S.A.; Alsahli, M.A.; Alzohairy, M.A.; Khan, A.; Younus, H. Therapeutic potential of thymoquinone liposomes against the systemic infection of Candida albicans in diabetic mice. *PLoS ONE* **2018**, *13*, e0208951. [CrossRef] [PubMed]
63. Cavaleiro, C.; Salgueiro, L.; Gonçalves, M.-J.; Hrimpeng, K.; Pinto, J.; Pinto, E. Antifungal activity of the essential oil of Angelica major against Candida, Cryptococcus, Aspergillus and dermatophyte species. *J. Nat. Med.* **2015**, *69*, 241–248. [CrossRef] [PubMed]
64. Khader, M.; Bresgen, N.; Eckl, P. In vitro toxicological properties of thymoquinone. *Food Chem. Toxicol.* **2009**, *47*, 129–133. [CrossRef]
65. Osmanov, A.; Farooq, Z.; Richardson, M.D.; Denning, D.W. The antiseptic Miramistin: A review of its comparative in vitro and clinical activity. *FEMS Microbiol. Rev.* **2020**, *44*, 399–417. [CrossRef]
66. Uribe, C.; Oliveira, F.D.S.D.; Grossmann, B.; Kretzmann, N.; Da Silveira, T.R.; Giugliani, R.; Matte, U. Cytotoxic effect of Amphotericin B in a myofibroblast cell line. *Toxicol. Vitro* **2013**, *27*, 2105–2109. [CrossRef] [PubMed]
67. Goyal, S.N.; Prajapati, C.P.; Gore, P.R.; Patil, C.R.; Mahajan, U.B.; Sharma, C.; Talla, S.P.; Ojha, S.K. Therapeutic Potential and Pharmaceutical Development of Thymoquinone: A Multitargeted Molecule of Natural Origin. *Front. Pharm.* **2017**, *8*, 656. [CrossRef] [PubMed]
68. Liu, S.-S.; Liu, Z.-X.; Wei, H.; Yin, Y.-Y.; Zhang, Q.-W.; Yan, L.-H.; Wang, Z.-M.; Yang, L.-X. Chemical compositions, yield variations and antimicrobial activities of essential oils from three species of Euodiae Fructus in China. *Ind. Crop. Prod.* **2019**, *138*, 111481. [CrossRef]
69. Sarah, R.; Tabassum, B.; Idrees, N.; Hussain, M. Bio-active Compounds Isolated from Neem Tree and Their Applications. *Nat. Bio-Act. Compd.* **2019**, 509–528.
70. Heard, S.C.; Wu, G.; Winter, J.M. Antifungal natural products. *Curr. Opin. Biotechnol.* **2021**, *69*, 232–241. [CrossRef]
71. Nguyen, H.Q.; Bradley, D.T.; Tunney, M.M.; Hughes, C.M. Development of a core outcome set for clinical trials aimed at improving antimicrobial stewardship in care homes. *Antimicrob. Resist. Infect. Control* **2021**, *10*, 1–11. [CrossRef]
72. Pelfrene, E.; Botgros, R.; Cavaleri, M. Antimicrobial multidrug resistance in the era of COVID-19: A forgotten plight? *Antimicrob. Resist. Infect. Control.* **2021**, *10*, 1–6. [CrossRef] [PubMed]
73. Goodlet, K.J.; Spadafora, K.; Walia, R.; Nailor, M.D. Updates in the Treatment of Breakthrough Mold Infections. *Curr. Fungal Infect. Rep.* **2020**, *14*, 153–165. [CrossRef]
74. Gupta, A.K.; Venkataraman, M.; Renaud, H.J.; Summerbell, R.; Shear, N.H.; Piguet, V. The increasing problem of treatment-resistant fungal infections: A call for antifungal stewardship programs. *Int. J. Dermatol.* **2021**. [CrossRef] [PubMed]
75. Espinel-Ingroff, A.; Cantón, E.; Pemán, J. Antifungal Resistance among Less Prevalent *Candida* Non-*albicans* and Other Yeasts versus Established and under Development Agents: A Literature Review. *J. Fungi* **2021**, *7*, 24. [CrossRef]
76. Esson, M.M.; Mecozzi, S. Preparation, Characterization, and Formulation Optimization of Ionic-Liquid-in-Water Nanoemulsions toward Systemic Delivery of Amphotericin B. *Mol. Pharm.* **2020**, *17*, 2221–2226. [CrossRef] [PubMed]
77. Carolus, H.; Pierson, S.; Lagrou, K.; Van Dijck, P. Amphotericin B and Other Polyenes—Discovery, Clinical Use, Mode of Action and Drug Resistance. *J. Fungi* **2020**, *6*, 321. [CrossRef] [PubMed]

MDPI
St. Alban-Anlage 66
4052 Basel
Switzerland
Tel. +41 61 683 77 34
Fax +41 61 302 89 18
www.mdpi.com

Materials Editorial Office
E-mail: materials@mdpi.com
www.mdpi.com/journal/materials

MDPI
St. Alban-Anlage 66
4052 Basel
Switzerland

Tel: +41 61 683 77 34
Fax: +41 61 302 89 18

www.mdpi.com

ISBN 978-3-0365-3207-3